Chitosan-graphene nanocomposite microneedle arrays for transdermal drug delivery

A thesis submitted to the University of Sheffield for the degree of Doctor of Philosophy

Richard Justin
Department of Materials Science and Engineering,
University of Sheffield

February 2015

Declaration

I declare that I am the sole author of this thesis, and that this thesis has not been submitted to another university in full or in part for another degree or qualification. I declare that the work within this thesis is my own, unless otherwise referenced or acknowledged. Permission has been granted from copyright holders to replicate figures or data within this thesis.

Richard Justin,

Richard Justin

February 2015.

This thesis is dedicated to the memory of my grandfather, Sean Colgan, who passed away the year that I started my Ph.D.

Acknowledgements

First and foremost, I would like to thank my supervisor Dr. Biqiong Chen for the assistance, support, and guidance over the past number of years and for giving me the chance to do the project. I would like to thank my family back in Ireland for their support over the past few years. I would like to thank the other members of the research group who have helped me when I needed help, in particular to Yongzhe Piao and Martin Frydrych who have been good friends to me throughout the past 3-4 years. I would like to thank the University of Sheffield who gave me a stipend during my studies and whose facilities I used to do my research work.

Regarding research and testing, a thank-you must go to the lab technicians who assisted me, so thank you Ben Palmer, Rob Hanson, Dr. Nik Reeves-McLaren, Dawn Bussey, Beverley Lane, Joanna Bates, Dr. Le Ma and Dr. P. Zeng for your assistance. I must thank the researchers from other research groups who we collaborated with during this thesis. I would like to thank Prof. Sheila MacNeil and Dr. Sabiniano Román of the Department of Materials Science and Engineering at the University of Sheffield, who undertook the cell viability testing and optical cell imaging within this thesis. I would like to thank Prof. Kang Sun, Dr. Ke Tao, Miss Dexin Chen, Miss Yawen Xu, and Prof Guangdong Zhou of the School of Materials Science and Engineering at Shanghai Jiao Tong University, who undertook the fluorescent cell imaging, M.R.I. imaging, and photothermal measurements within this thesis. I would like to thank Xiangshuai Geng, for undertaking the graphene biostability images in Chapter 5 and 6, and Richard Grant for undertaking the fluorescent lifetime analysis in the same chapters. I must also thank Prof. David Lidzey of the Department of Physics and Astronomy and Prof. Michael Ward of the Department of Chemistry for allowing me to use their photoluminescent facilities.

Abstract

The project focused on the hypothesis that degradable, polymer microneedle arrays are a promising alternative to traditional drug delivery routes, offering the patient a painless, high concentration, and quick delivery of therapeutics through the skin. This project explored chitosan-graphene nanocomposites as potential materials for microneedle arrays; the addition of graphene to chitosan is believed to yield improved mechanical properties and electrical conductivity over pristine chitosan, which will allow for long and slender microneedles and for electrically stimulated drug delivery, and may positively affect the degradation and drug delivery properties of chitosan.

Graphene derivatives, such as graphene oxide, reduced graphene oxide, graphene quantum dots, and magnetic graphene quantum dots were synthesised and then characterised, before they were used as the filler within chitosan nanocomposites. Their effect at varying concentrations upon the mechanical properties, electrical conductivity, drug release, and enzymatic degradation rate of chitosan were assessed. It was determined that reduced graphene oxide was the optimum nanoparticle to reinforce chitosan, achieving the best mechanical and electrical conductivity properties of the nanocomposites.

Chitosan-graphene nanocomposite microneedle arrays were shown to passively release small molecular weight drugs at a high delivery quantity and rate. Conductive chitosan-graphene nanocomposite microneedles were tested to determine the effect of electrical stimulation on the release of large molecular weight drugs from the nanocomposite, with substantial improvements in the release rate of large molecular weight drugs when compared to passive diffusion. The microneedle arrays were shown to survive the force of insertion through compressive loading. The depth of penetration of the microneedles was determined through cross-sectional analysis of chicken skin.

Contents

List of figures

List of schemes

List of tables

List of abbreviations

AFM	Atomic force microscopy
BSA	Bovine serum albumin
CdS	Cadmium sulphur
CdSe	Cadmium selenium
CdTe	Cadmium telluride
CMC	Carboxymethylcellulose
CNTs	Carbon nanotubes
CT	Computed tomography
DNA	Deoxyribonucleic acid
EDS	Energy dispersive spectrometry
FTIR	Fourier transform infrared
GO	Graphene oxide
GQDs	Graphene QDs
HAI	Haemagglutination inhibition
IO	Iron oxide
MSC	Mesenchymal stromal cells
MQDs	Magnetic QDs
M.R.I.	Magnetic Resonance Imaging
MWt	Molecular weight
NIR	Near infrared
PCL	Poly(ε-caprolactone)
PE	Polyethylene
PEG	Poly(ethylene glycol)
PEI	Polyethylenimine

P.E.T.G.	Positron emission tomography
PET	Polyethylene terephthalate
PGA	Polyglycolic acid
PI	Polyimide
PL	Photoluminescent/fluorescent
PLA	Poly(L-lactide acid)
PLGA	Poly(lactic-co-glycolic acid)
PMMA	Poly(methyl methacrylate)
PNIPAM	poly-n-(isopropyl acrylamide)
PP	Polypropylene
PS	Polystyrene
PVA	Poly(vinyl alcohol)
PVP	Poly(vinyl-pyrrolidone)
QDs	Quantum dots
rGO	Reduced graphene oxide
RNA	Ribonucleic acid
ROS	Reactive oxide stress
SC	Stratum corneum
SEM	Scanning electron microscopy
TEM	Transmission electron microscopy
UTS	Ultimate tensile strength
UV	Ultraviolet
UV-Vis	UV-Visible light
VE	Viable epidermis
XRD	X-ray diffraction

List of symbols

A   Area

$^{\circ}C$ Degree Celsius

C_{init} Initial concentration

C_s Drug solubility

C_{elec} Conductivity

D   Drug diffusion coefficient

Da   Daltons

eV   Electron volt

E   Young's modulus

ε_b Epsilon, symbol for elongation to break

η Eta, symbol for refractive index

g   Gram, often prefixed with n for nano-, μ for micro-, or k for kilo-

G   Giga, used as prefix for International System of Units

h   Hour

k   Kilo, used as prefix for International System of Units

k_H Higuchi constant

K   Diffusion coefficient

l   Litre, often prefixed with n for nano-, μ for micro-, or k for kilo-

l_{rgo} length of rGO

m   Metre, often prefixed with n for nano-, μ for micro-, or k for kilo-

min   Minute

M   Mega, used as prefix for International System of Units

M_t Cumulative amount of drug released

μ Mu, symbol for micro and used as prefix for International System of Units

n_d	Diffusion release exponent
Oe	Oersted
Pa	Pascal (S.I. unit of pressure)
ϕ	Phi, symbol for fluorescence quantum yield
Q_t	The amount of drug released at a specific time
QT	The total amount of drug released
R	Radius of gyration
ρ	Rho, symbol for density
S	Siemens
t	Time
t_{rgo}	Thickness of rGO
θ	Theta, symbol for angle
T	Tera, used as prefix for International System of Units
T_E	Echo time
T_g	Glass transition temperature
T_R	Relaxation time
Vg^e	Effective filler volume fraction
W	Watt
wt.%	Weight percentage
χ_c	Chi, symbol for crystallinity percentage
X	wt.% of rGO within the nanocomposite

List of publications

The following journal papers are based on the work from this thesis:

- R. Justin and B. Chen, "Strong and conductive chitosan-reduced graphene oxide nanocomposites for transdermal drug delivery", Journal of Materials Chemistry B, vol. 2, no. 24, pp. 3759-3770, 2014.

- R. Justin and B. Chen, "Characterisation and drug release performance of biodegradable chitosan-graphene oxide nanocomposites", Carbohydrate Polymers, vol. 103, pp. 70-80, 2014.

- R. Justin and B. Chen, "Body temperature reduction of graphene oxide through chitosan functionalisation and its application in drug delivery", Materials Science and Engineering C, vol. 34, no. 1, pp. 50-53, 2014.

- Richard Justin, Sabiniano Román, Dexin Chen, Ke Tao, Xiangshuai Geng, Richard T. Grant, Sheila MacNeil, Kang Sun and Biqiong Chen, "Biodegradable and conductive chitosan – graphene quantum dot nanocomposite microneedles for delivery of both small and large molecular weight therapeutics", RSC Advances, vol. 5, pp. 51934-51946, 2015.

- Richard Justin, Ke Tao, Sabiniano Román, Dexin Chen, Yawen Xu, Xiangshuai Geng, Ian Ross, Richard T. Grant, Andrew Pearson, Guangdong Zhou, Sheila MacNeil, Kang Sun, and Biqiong Chen, "Photoluminescent and superparamagnetic reduced graphene oxide-iron oxide quantum dots for dual-modality imaging, drug delivery and photothermal therapy", Carbon, vol. 97, pp. 54-70, 2015.

- R. Justin and B. Chen, "Chitosan-magnetic quantum dot nanocomposites for the targeted and monitored release of therapeutics from detachable microneedles", In preparation.

Chapter 1. Introduction

Compared to the 20th century, people in the 21st century are living longer and healthier lives, due mainly to improvements in healthcare [1,2]. This trend has created a boom in the biomedical and healthcare sectors, such that these sectors are very lucrative to the economy; in the UK, the average increase in public healthcare spending was 6.6% a year between 2000 and 2011 [3] and global healthcare expenditure is expected to increase 5.3% a year between 2014 and 2017 [4].

Within the biomedical and healthcare sectors is the therapeutic drug and drug delivery markets. The quantity of therapeutic drugs consumed is increasing; for example, the prescription drugs market increased 6.5% between 2005 and 2006 [5]. Smart drugs are being developed that can remedy malignancies quicker and more effectively than the previous generation of drugs can [6]. These recent developments must be met with improvements in the delivery to the body to fully utilise the therapeutic effect [7,8]; such improvements should be painless, should not be constrained to one therapeutic type, and should deliver the therapeutic efficiently.

Therapeutic delivery systems, such as hypodermic needles and oral tablets, are commonly used but are limited in their application, efficiency and ease of use [9–11], and as such cannot be considered an ideal drug delivery device. This has led to the development of other forms of drug delivery to solve the inadequacies of the current drug delivery methods; one of these methods is transdermal drug delivery [12,13]: the delivery of therapeutics through the dermal layer into the blood circulatory system. Of the many transdermal drug delivery devices that are being developed, the most promising of these is the bio-polymer microneedle array, a series of micrometre-sized projections made from a biocompatible and biodegradable polymer. This system bypasses the hepatic first pass through the stomach, liver and kidney by allowing the drug to enter the blood system through the capillaries within the dermal layers. It

will limit distress to the patient by being painless and it will promote self-administration by being easy to use.

Simultaneous to the development of smart drugs and new drug delivery devices, the application of nanoparticles, such as graphene and iron oxide, in conjunction with therapeutics has been investigated. The crossing of smart drugs and drug delivery systems with nanotechnology could yield very promising results, such as possible improvements in the therapeutic effect of drugs [14], imaging capability [15,16], the ability to track bound drugs *in vivo* [17,18], the ability to target bound drugs to specific sites [19], and the ability to thermally ablate tumours [20].

The overall aim of this project is to develop a new type of microneedle array using nanocomposites of a degradable and biocompatible polymer and functional nanoparticles for targeted and monitored transdermal drug delivery. These nanocomposites will be optimised in terms of their main material properties: an optimised nanocomposite would have increased mechanical properties such as Young's modulus and ultimate tensile strength that would reduce the chance of microneedles buckling or bending under force; it would have a sufficiently increased electrical conductivity relative to pristine chitosan to allow for electrical stimulation of the drug delivery; the nanocomposites would possess similar or higher enzymatic degradation rate properties to pristine chitosan; and the nanocomposites would have quicker and more efficient drug delivery profiles than pristine chitosan, while also offering stimulus-responsive release and monitoring functionalities. There are five objectives associated with this project which are outlined below:

- To prepare chitosan-graphene oxide nanocomposites and investigate the effect of graphene oxide on the mechanical properties, enzymatic degradation rate and drug delivery performance of chitosan.

- To reduce graphene oxide using a green, biocompatible method to restore the electrical conductivity and mechanical strength of graphene for incorporation into chitosan, study the effect of reduced graphene oxide on the mechanical, enzymatic degradation and drug delivery performance of chitosan, and demonstrate the release of a model drug from chitosan-reduced graphene oxide nanocomposite microneedle arrays.

- To develop electrically conductive chitosan-graphene quantum dot nanocomposites with imaging and tracking functionality during drug delivery, and investigate the passive release of small molecular weight (< 1000 Da) drugs and the electrically stimulated release of large molecular weight (>1000 Da) drugs from chitosan-graphene quantum dot microneedle arrays.

- To develop novel iron oxide-reduced graphene oxide quantum dots with intrinsic photoluminescent and superparamagnetic properties that can be used for dual modality imaging/tracking and site specific targeting of bound drugs.

- To prepare electrically conductive chitosan-magnetic quantum dot nanocomposites with dual-modality imaging and targeting functionality, create a novel design of detachable microneedle array, and study the release of drugs from electrically stimulated or detachable chitosan-magnetic quantum dot microneedle arrays.

This research will help advance the fields of transdermal drug delivery and polymer-graphene nanocomposites and lead to new designs of degradable microneedle arrays for targeted and monitored transdermal drug delivery.

Chapter 2. Literature review

2.1 The current therapeutic delivery routes

Currently, the main therapeutic delivery routes used are the hypodermic syringe, the perioral tablet route, and the nasal inhalation route. The standard hypodermic needle is used to administer the therapeutic to either a muscle (intramuscular), into a vein (intravenous), or just under the skin of the patient (subcutaneous) [21]. The advantages of hypodermic syringe include a quick application procedure and the ability to bypass the hepatic first pass. The downsides to hypodermic syringes include poor patient compliance and the risk of blood transmitted diseases [10,11,22–25].

The perioral route of drug administration is achieved through the swallowing of the tablet, digestion through the stomach, and then absorption in the intestines and colon. Metabolism occurs in the liver and the bioavailability of the drug is lowered due to the hepatic first pass, often to a small fraction of the original dose, and can be further lowered by the insolubility of the drug within biological fluids in the intestines and colon [9,26,27]. Further adding to the complexity of drug development, the way that a drug is metabolised within a body will vary from person to person [28], something that must be accounted for during the design phase of the drug. As for advantages of the perioral route, the ease of administration reduces the need for skilled medical staff to administer the therapeutic. The pain associated with oral tablet administration is a lot lower and there is no piercing of the skin with an external device like with a hypodermic syringe and this negates the risk of blood transmitted diseases.

The nasal inhalation route applies the drug through the nostrils to the mucous lining of the olfactory region of the superior turbinate (within the inner nostril cavity) which is densely packed with blood vessels [9,29,30]. This avoids the hepatic first pass through the liver, associated with tablet medications, and allows for easy self-administration of the medicine.

The pH of any solution or powder will have to match the pH of the nasal passage or there is a risk of irritation and degradation of the mucous layers. The permeability of the mucous layers depends on the size of the molecule trying to penetrate, so this limits the size of the molecules in a nasal spray to 1000 Daltons [30].

2.2 Transdermal drug delivery

2.2.1 Introduction

Transdermal drug delivery refers to the administration of drugs through the dermal layer. Transdermal drug patches, chemical or mechanical exfoliants, permeation enhancers and microneedle arrays have all been used to administer therapeutics transdermally [12,31,32]. In the dermis lies a region called the viable epidermis (VE) (Figure 2.1). Within the VE lies a dense network of blood capillaries. Drugs delivered to the VE will diffuse into the blood capillaries and pass into the main blood system, therefore avoiding the hepatic first pass [12]. Once diffused into the main blood vessels from the capillaries, the drug can then be absorbed into the cells within the body. The drug would typically arrive to the cells/tissue from blood vessels, with the drug entering the tissue from the vessels by diffusion and convection means [33]. Once diffused through the vessel wall, the drug will have to move through the lipid membrane, the extracellular matrix, and the cellular wall. The rate that drugs achieve this is dependent upon the molecular weight (MWt) of the drug, the solubility of the drug in bodily fluids (for example, the extra-cellular matrix) or lipids (lipid membrane), the charge of the drug molecule, the therapeutic dose administered and the gradient of the drug level difference between the blood vessel and the tissue [33,34], and as such, the rate at which various drugs enter the cells will differ from drug to drug.

In the VE, there is a dense population of Langerhans cell, dermal dendritic cells, macrophages, and monocytes [35–38]; these will locate and recognise any foreign body that

enters through the stratum corneum (SC), engulf the foreign body and present them to the lymphocytes which initiate a specific and prolonged immune response to the foreign body. By focusing the delivery of therapeutics to the VE, the delivered therapeutics can very quickly initiate a substantial response from the immune system of the patient to any vaccine administered [39,40].
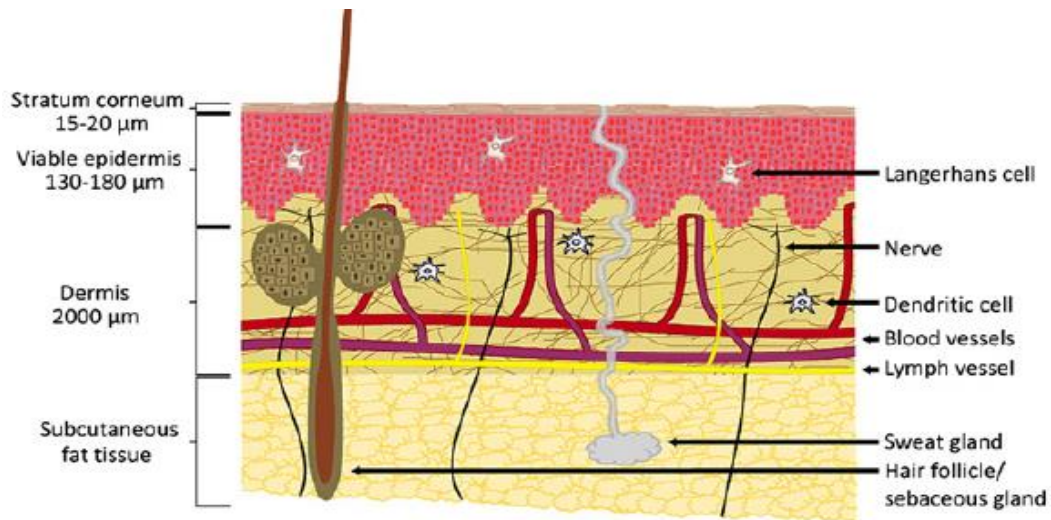
Figure 2.1: Illustration of the layers of the human skin showing the SC and the nerves, veins and arteries deep within the dermis layers. Adapted from Van der Maaden et al. [40] with permission from Elsevier Limited, copyright 2012.

2.2.2 The different types of devices for transdermal drug delivery

This section will briefly review some recent advances in transdermal drug delivery, including topical cream, passive diffusion patches, electroporation, iontophoresis, thermal ablation, magnetophoresis, and sonophoresis. A summary is compiled in Table 2.1 of the key findings, advantages and disadvantages of the current transdermal drug delivery devices. Microneedle arrays will be discussed in Section 2.3.

Topical cream

Topically-applied therapeutics are the most basic form of transdermal drug delivery. One of the first reported studies on transdermal drug delivery was that of topically-applied hydrocortisone dissolved in acetone [41]. Taking the form of therapeutics dissolved in solvents

(e.g. hydrocortisone in acetone [41] or perillyl alcohol in water [42]), dispersed in gels (methoxalen [43] and tazarotene [44]), in a lotion/emulsion (glucose [45] and betamethasone [46]), or in a liposome suspension [47–49], the topically-applied therapeutics are applied directly to the outer dermal layers and have been shown to passively diffuse through the SC and into the VE. The permeation rate of hydrocortisone varied depending on the thickness of the SC at a particular test site and whether there were follicles at the test site [41], but it was shown to permeate through all of the test sites at a therapeutic level. Changing the dispersion agent from an ointment to a liposome increased the amount of triamcinolone found in the VE by 400% [49]. Methoxalen, administered to the patients through a gel, reduced the eczema in ~89% of patients treated, and was shown to be as effective a treatment as UV irradiation in the treatment of eczema [43].

Topical creams can be self-administered by the patient, reducing the cost of the treatment as there is no need for specialist healthcare assistance. There is, however, no control on the permeation rate of the therapeutic through the SC. The permeation is often slow, only milligrams per day [12,35,36]. Due to the low permeability of the SC, the maximum MWt of the drug that can be used is less than 1000 Daltons [12,50]. The drug must also be sufficiently lipophilic as the main diffusion route is through the intercellular lipid domain within the SC [12,51].

Passive diffusion patch

A passive diffusion patch is a device that contains an internal reserve of a topically-applied therapeutic, a diffusion membrane, and an impermeable backing-cover. This device is attached to the outer surface of the skin by an adhesive substance. The diffusion membrane is used to control the release of the drug from the reservoir, and in doing so makes the transdermal patch different to a topical cream where there is no control mechanism [51]. The rate of drug delivery into the skin is dependent on the surface area of the diffusion membrane, the permeability

coefficient of the drug, and the concentration gradient between the internal reservoir and the skin [12,51]. As a passive diffusion patch is, simplistically, an improved version of the topically-applied therapeutic, it has the same advantages and disadvantages as the topically-applied therapeutic, i.e. it may be self-administered and cheap to use, but the drugs that can be used with this system are limited by their MWt and solubility. It can, however, control the rate at which a drug diffuses from the internal reservoir.

Electroporation

Electroporation increases the permeation of the SC by using an external electric field applied to the skin through electrodes; under electrical stimulation, the membrane of a cell will undergo a (reversible) chemical change where its permeability increases temporarily [52,53]. The therapeutic is then applied to the skin through topical cream or a passive diffusion patch; the electrical stimulation and treatment do not occur at same time.

Electroporation increases the quantity of drug permeated through the SC in comparison to passive diffusion. The permeation of the therapeutics dextran, doxorubicin, and fentanyl from a passive diffusion patch were greatly improved when the skin was under electroporation stimulation in comparison to passive diffusion without electroporation stimulation [54]. It was noted that electroporation created less skin damage/side effects than using tape to strip the SC from the test site, which was an alternative route to increase the permeability of the skin [54]. Electroporation increased the delivery rate of calcein fourfold over passive diffusion [55]. Similar improvements were noted for gadolinium-labelled albumin [56] and hormones [57] when they were applied to electroporated skin. Electroporation can be used to administer deoxyribonucleic acid (DNA) vaccines, with a 100% survival rate for mice treated with the pox-virus vaccine [58]. There was a 100 times improvement in the plasmid DNA levels within mice that underwent electroporation treatment than those that did not undergo electroporation treatment [59].

Electroporation offers significantly improved permeation rates when compared to topical cream or passive diffusion, but the equipment required may prohibit its widespread use as it may be more expensive than topical cream or passive diffusion. It may also be too complex for self-administration; stimulation of the nerves and muscles within subjects as well as superficial burning of the SC is possible with electroporation if incorrect parameters are used [52]. If the electrode resistance is too high, the electrode can burn the skin [60,61].

Iontophoresis

Iontophoresis is the stimulation of drug transfer through the SC by the application of an electric current directly to the SC [12,62–64]; the therapeutic reservoir is built into the positive electrode and the electric current transfers the drug from the reservoir through the SC by electro-repulsion for charged molecules and/or by electro-osmosis for molecules with no charge. The stimulation and treatment occur at the same time, contrary to electroporation treatment.

Iontophoresis increased the quantity of hydroxocobalamin delivered through the skin in test patients, with 1469 μg delivered over 4 h with iontophoresis stimulation and 181 μg delivered by passive means [65]. Similarly, dexamethasone phosphate and gentamicin sulphate could be transdermally delivered via iontophoresis, and dexamethasone phosphate had a ~2.5 times higher delivery quantity than the value achieved by passive diffusion [66]. Lidocaine hydrochloride (LH) administered by electroporation and iontophoresis achieved local anaesthesia [61], but it was noted that iontophoresis obtained the greater depth of anaesthesia. A linear relationship (Figure 2.2) between the drug delivery of ketorolac and the current density applied via iontophoresis was found, showing that the delivery was current dependent and could be controlled to achieve a specific delivery rate [67]. The therapeutic effect of methylprednisolone sodium succinate was noted by 88% of test subjects that were treated with iontophoresis [68].
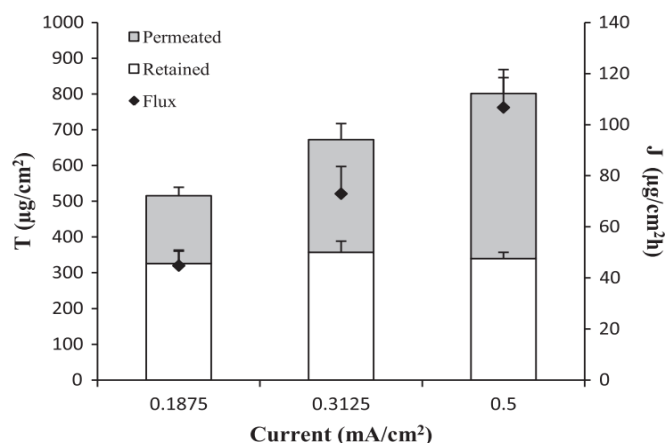
Figure 2.2: Effect of current density on the transferred amount ("permeated") of ketorolac across a membrane under iontophoresis stimulation. Adapted from Gratieri et al. [67] with permission from Elsevier Limited, copyright 2014.

The advantages (improved and controllable drug delivery) and disadvantages (possibility of skin irritation and the cost/complexity of the device) of the electroporation device are relevant to the iontophoretic device. Skin irritation and damage was noted in patients whilst using an iontophoretic device to stimulate drug delivery [12,61,65].

Magnetophoresis

Magnetophoresis is the process of using an external magnetic field to force a drug through the SC [62,69]; this is achieved through magneto-repulsion which induces the movement of diamagnetic drugs and magneto-hydrokinesis which induces the movement of the solvent constituent of the topical cream through the pores in the SC.

The transfer of LH through skin over 8 h was shown to be dependent on the density of the magnetic flux used [69]. The drug transfer using a 300 µTesla magnetophoresis device transferred 12 times the amount that passive diffusion could achieve in the same time frame [69]. A 3 fold increase in LH transfer was recorded for a magnetophoresis patch in a similar experiment [70]. Krishnan et al. [71] researched the drug delivery profile of naltrexone using a 250 µTesla magnetophoresis device compared to a passive patch, reporting a 5-6 times increase in the drug concentration levels for magnetophoresis when compared to a passive patch. The main problem with magnetophoresis is that for the drug to be transferred across by

magneto-repulsion, the drug needs to have a stronger diamagnetic tendency than a paramagnetic tendency, which is not always feasible.

Sonophoresis

Sonophoresis is the process of increasing the permeability of the SC by using ultrasonic energy to induce gas cavitation, heat, convection currents, and pressure differences in the SC [13,36,62]. Sonophoresis can be achieved by low or high frequency ultrasound [72,73], and the equipment required would typically consist of a signal generator, ultrasound transducers, and possibly an amplifier to increase the signal from the generator.

A sonophoresis device will deliver one standard dose of insulin in less than 20 min, whereas by passive diffusion the same dosage will take just under 3 h [74]. The quantity of cyclosporine A transferred when under sonophoresis stimulation was 7 fold higher after 30 min than the amount transferred under passive diffusion [75], whilst heparin was transferred with a 21 fold higher flux than passive diffusion over 25 h [76]. The quantity of salicylic acid transferred when under high frequency sonophoresis was 4 times higher than for passive diffusion [73]; in this work, the author claims that a lower frequency sonophoresis device did not noticeably improve the transfer of salicylic acid across the SC. Other therapeutics that were investigated were BSA [77], insulin [78], sulforhodamine B [79], and calcein [80]. A comprehensive list of therapeutics tested and that showed promising drug permeation behaviour when under sonophoresis stimulation is compiled in the work of Polat et al. [81].

Similar to electroporation and iontophoresis, the equipment required to use sonophoresis may be prohibitively expensive and complex for widespread use. Joshi et al. [36] noted that as the gas level in the SC decreases, the permeability of the SC decreases as well. This implies that there is a maximum usage level per application site, meaning that a new administration site will have to be found on the patient when the previous site becomes

unusable. This may be a hindrance for patients who require frequent drug administration, for example diabetics.

Thermal Ablation

Thermal ablation is the selective removal of the SC by localised, controlled extreme heat sources, subsequently followed by the application of therapeutics in the form of passive diffusion patches or topical cream [82–84]. The skin exposed to the heat field is vaporised and pores are temporarily created through the SC. Thermal ablation of the SC can be achieved by running a current through a highly resistive material [85] or via laser induced thermal ablation [86].

The antigen response after vaccination was stronger when administered through thermally ablated skin than through intact skin [82]. The delivery of BSA through full thickness human cadaver skin was studied [87], with the amount released from passive diffusion ($\sim$0 µg ml^{-1}) increasing to $\sim$650 µg ml^{-1} through the use of thermal ablation on the SC. Similar results were achieved for sulforhodamine B. Human growth hormone [88] could permeate through thermally ablated skin but not through intact skin, and the bioavailability of the therapeutic was measured as 75% in rats and 33% in guinea pigs, when compared to the subcutaneous injected therapeutic. The thermal ablation of skin increased the permeation of granisetron hydrochloride ($\sim$30 times higher than passive) and diclofenac sodium ($\sim$9 times higher than passive) [89].

Similar to iontophoresis and electroporation, there are a lot of variables to consider when applying thermal ablation to the skin and this could be a limitation regarding its widespread use; if the procedure is not undertaken properly, if the time of application is too long, or the temperature is not controlled adequately, then heat damage could potentially occur to the skin layers, the blood vessels, the nerves and the muscle/tissue around the treatment site.

Table 2.1: Comparison table of transdermal drug delivery devices

Type	Method	Advantages	Disadvantages
Topical cream	Passive diffusion	Cheap Simple to build and operate	Limited to < 1 kDa drugs No control over diffusion rate Low diffusion rate
Passive diffusion patch	Passive diffusion	Cheap Simple to build and operate Diffusion of drugs can be controlled	Limited to < 1 kDa drugs Low diffusion rate
Electroporation	Electrical stimulation	No drug size limits Control over diffusion rate	Costly Poor design or operation can harm patients
Iontophoresis	Electrical stimulation	No drug size limits Control over diffusion rate	Costly Poor design or operation can harm patients
Magnetophoresis	Magnet stimulation	No drug size limits Control over diffusion rate No risk of harm to patient	Costly Not all drugs are suitable for use
Sonophoresis	Sound-energy mediated delivery	No drug size limits Control over diffusion rate No risk of harm to patient	Costly Sites on body can be used for a limited time
Thermal ablation	Thermal removal of skin layers	No drug size limits Control over diffusion rate	Costly Poor design or operation can harm patients

2.3 Microneedle arrays

2.3.1 Introduction to Microneedle Technology
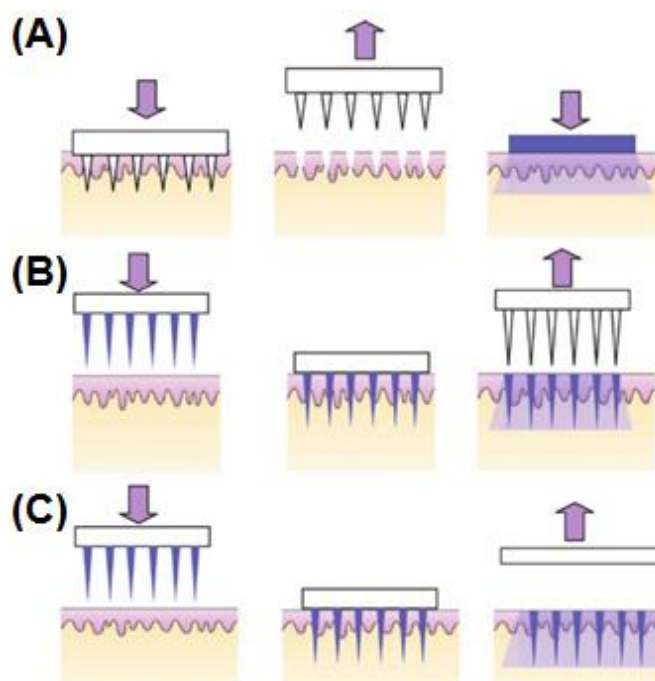
Figure 2.3: An illustration of first and second generation microneedle arrays. The first generation microneedle arrays are made from non-biodegradable material and the drug is delivered (A) through a transdermal patch and (B) through a powder coating on the external surfaces of the array. (C) Second generation microneedles that are made from a biodegradable polymer can deliver their encapsulated drug payload through biodegrading into the tissue. Adapted from Arora et al. [84] with permission from Elsevier Limited, copyright 2008.

The simplest design of a microneedle patch is an array of solid, conical micrometre-sized projections (Figure 2.3 and Figure 2.4) that pierce through the SC to create micro-channels for drugs to permeate through to the VE where there is both a dense network of blood capillaries to diffuse into and a dense population of immune system cells for vaccines to utilise (Section 2.2.1). Transdermal drug delivery with a microneedle array can offer an improvement in the delivery of vaccines and therapeutics over conventional drug delivery methods like hypodermic needle delivery [38,90–92]. Another advantage over hypodermic syringes is that microneedle arrays have a high level of patient compliance, with minimal pain or irritation recorded in previously reported tests compared to hypodermic syringes [37,93,94].

14

Of the current transdermal drug delivery devices, microneedle arrays offer the best mixture of cost effectiveness, ease of use, and delivery performance [84,94–96]. Microneedle arrays can be cheap, requiring no additional electrical equipment to operate, unlike electroporation, iontophoresis or sonophoresis devices. Microneedle arrays can be used to deliver a wide range of therapeutics of various molecular sizes and solubility, from vaccines like the human-papillomavirus vaccine [97], the recumbent anthrax protective antigen [29], and the "Chimera-Vax" vaccine [98], to therapeutics like plasmid DNA [99], desmopressin [100], calcein [35], naltrexone [101], methyl nicotinate [102], insulin [103], ovalbumin [37], lysozyme [104], sulforhodamine [104,105], bovine serum albumin (BSA) [104,105] and β-galactosidase [105].

2.3.2 First generation microneedle arrays

The first practical study on microneedle drug delivery was calcein delivered via reactive ion etched silicon microneedle arrays [35]. This design and other microneedle arrays made from metals and silicon are often termed "first generation". These simple devices are often produced using the same low cost, high production manufacturing processes as for microchips in the computer industry (e.g. microlithography and etching, see Section 2.3.5). The drug is applied after the piercing of the SC by the microneedle array through a topical cream, a transdermal patch (see Figure 2.3A), or a dried therapeutic powder applied to the exterior of the microneedle projections themselves (see Figure 2.3B).

The delivery of therapeutics have been tested with first generation microneedles, such as desmopressin (mean bioavailability of microneedle delivered therapeutic was 85%, compared to 0.1% for oral and 3.4% for nasal administration) [100], calcein (with higher quantities delivered through microneedle administration than through passive diffusion) [35], as well as tests that confirm that naltrexone [101], methyl nicotinate [102], LH [106], insulin [103], and ovalbumin [37], can all be delivered via a first generation microneedle.
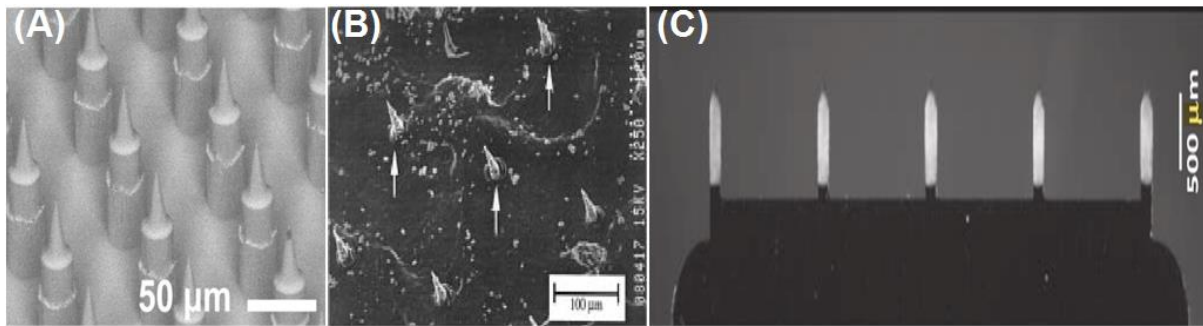
Figure 2.4: Images showing first generation microneedles; (A) Metal conical microneedle projections, adapted from Corbett et al. [97] with permission from PLOS under the Creative Commons Attribution License 2010; (B) Penetration of metal microneedles through the SC, adapted from Henry et al. [35] with permission from John Wiley and Sons, copyright 2000; (C) In-plane microneedle array coated with a Hepatitis C (Hep C) vaccination powder, adapted from Gill et al. [107] with permission from Nature Publishing Group, copyright 2010.

First generation microneedles were tested in conjunction with vaccinations, DNA or ribonucleic acid (RNA) gene therapies, proteins and other molecules. Vaccinations against various threats to humans (for example human influenza virus [38,90,91], human-papillomavirus [97], anthrax [29], and Japanese Encephalitis, Dengue Haemorrhagic fever and Yellow fever [98]) would be ideal therapeutics to be administered through microneedle array technology, due to ease of administration and the heightened immune response from delivering a drug to the VE [35–38]. Koutsonanos et al. [38] showed that for a similar 10 µg dose of the vaccine, mice in the microneedle administered group had higher haemagglutination inhibition (HAI) and lgL titers (which are both signs of an efficient influenza specific immune response to a vaccine) than the intramuscular injected group. Alarcon et al. [90] showed higher influenza specific titer counts for all intradermal microneedle doses than the traditional intramuscular injection route in blood samples taken 3 weeks, 6 weeks and 8 weeks after administration. Zhu et al. [91] recorded comparable titer levels for subjects administered with an inactivated influenza virus through a microneedle and a hypodermic syringe.

First generation microneedle delivery of gene therapies have interested people as large molecular treatments may be tough to administer with standard transdermal techniques and oral delivery is limited as the hepatic first pass may damage the therapeutic. A low dose of a

plasmid DNA therapeutic administered through microneedles (3.2 µg) was comparable to a high dose administered through an intramuscular hypodermic syringe injection (100 µg) in reducing the size of tumours in mice [107]. Other reports have shown that gene therapies can be successfully transported into the test subject, such as β-galactosidase [108], and plasmid DNA encoded firefly luciferase [109].

Despite the many advantages of the first generation microneedle array over hypodermic syringes and other transdermal drug delivery devices like iontophoresis and electroporation, it does have disadvantages due to the materials that they are made from. For example, first generation microneedle arrays made from metal, ceramics, or silicon do not biodegrade and are sharp and therefore they must be disposed of properly; if improperly disposed of, (for example, in a landfill site) the microneedle array may prove to be a blood borne pathogen risk to people who come into contact with the microneedle array [11] or if someone reuses the microneedle array [110].

A second issue with the material is that the therapeutic must be applied to the outer surface of the array, or administered after the microneedle array has been inserted (see Figure 2.3). Neither of these methods of therapeutic application is optimised; for example, coating the therapeutic onto the outer surface of the microneedle array means that the therapeutic might either break off or rub off of the array and onto the outer stratum layers during initial insertion. Also, as only a thin layer on the outer surface of the microneedle can be used, the quantity of drug that can be applied with each microneedle array is limited in comparison to the volume within the microneedle itself. This issue can be partially solved through the development of hollow microneedle arrays, such as those created from glass [111], silicon [112], or from metal [103], where liquid solutions of drugs can be stored in reservoirs to flow through the shaft when the SC is perforated by the microneedle arrays themselves. This type of microneedle array solves the problem of limited drug quantities, but the first problem (disposal of the microneedle

17

array) remains unsolved for this generation. The hollow microneedle array are often used in conjunction with a piezoelectric pump [113,114], which may add to the price and complexity of the microneedle array and may limit the widespread use of these types of microneedle arrays.

2.3.3 Second generation microneedle arrays

A second generation of microneedles (Figure 2.3C and Figure 2.5) were designed from biodegradable and biocompatible polymers to alleviate the problems of the first generation, e.g. no biodegradation and limited therapeutic-loading capacity. Some polymers can be biodegraded through enzymes within the body, such as chitosan [115] and poly(glycerol sebacate) [116]. Others by environmental conditions, such as poly(acrylic acid) [117]. Some polymers are water soluble, such as poly(vinyl alcohol) (PVA)[118]. This aids in the post-administration waste treatment of the second generation microneedle array. These new microneedle arrays also have the advantage where the drug can be encapsulated within the polymer; this means that more drug can be stored per microneedle array than would be possible if the drug was coated on the microneedle exterior, and the drug release is now dependent on the drug diffusing from the polymer and the drug is released straight into the VE.
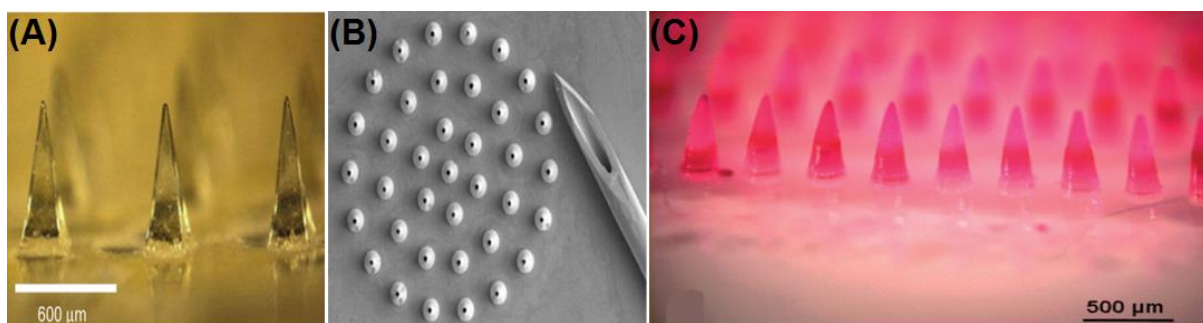
Figure 2.5: Images showing second generation microneedles; (A) Polymer microneedle projections made from amylopectin to allow for biodegradation, adapted from Lee et al. [104] with permission from Elsevier Limited, copyright 2008; (B) An array of polymer microneedles beside a 26 gauge hypodermic syringe needle allowing for a comparison in size, adapted from McAllister et al. [95] with permission from National Academy of Sciences of the United States of America, copyright 2003; (C) Poly(vinyl-pyrrolidone) (PVP) microneedles with the encapsulated drug sulforhodamine to allow for transdermal drug delivery, adapted from Sullivan et al. [105] with permission from John Wiley and Sons, copyright 2008.

Biocompatible polymers such as poly(l-lactide) acid (PLA) [95], poly(glycolic acid) (PGA) [95], poly(lactic-co-glycolic acid) (PLGA) [95], poly(vinyl-pyrrolidone) (PVP) [92], and carboxymethylcellulose (CMC) [104] have been used in the development of microneedle arrays. PLA and CMC microneedles were used to deliver sulforhodamine B (see Figure 2.6), BSA, and lysozyme [104]. The enzymatic activity of lysozyme that was added into a CMC microneedle array and stored at room temperature for 2 months was shown not to be substantially degraded in comparison to fresh lysozyme, which is an important result as therapeutics may be stored in microneedles for a substantial amount of time prior to use. The delivery of sulforhodamine into the skin by CMC microneedles can be seen in Figure 2.6, where the sulforhodamine can be seen under fluorescent light to have diffused from the surface into the VE layers under the SC. Similar diffusion results were achieved for the delivery of sulforhodamine B and BSA with PVP microneedles [105]. PLGA microneedles were used for the delivery of ovalbumin [119], silk protein microneedles were used for the encapsulation of the enzyme horseradish peroxidase and tetracycline [120], and for BSA and sulforhodamine [121], and hyaluronic acid microneedles were used for the delivery of fluorescein isothiocyanate labelled dextran [122]. Dextrin microneedles were used to deliver heparin and insulin [123,124]. A microneedle made from starch/gelatin (1:1 weight ratio) was used for the release of insulin, with the microneedle treated rats exhibiting a similar hypoglycaemic effect as subcutaneous injected rats [125]. It was also noted that the insulin retained a 92% bioavailability and was delivered in a pharmacologically suitable quality [125].
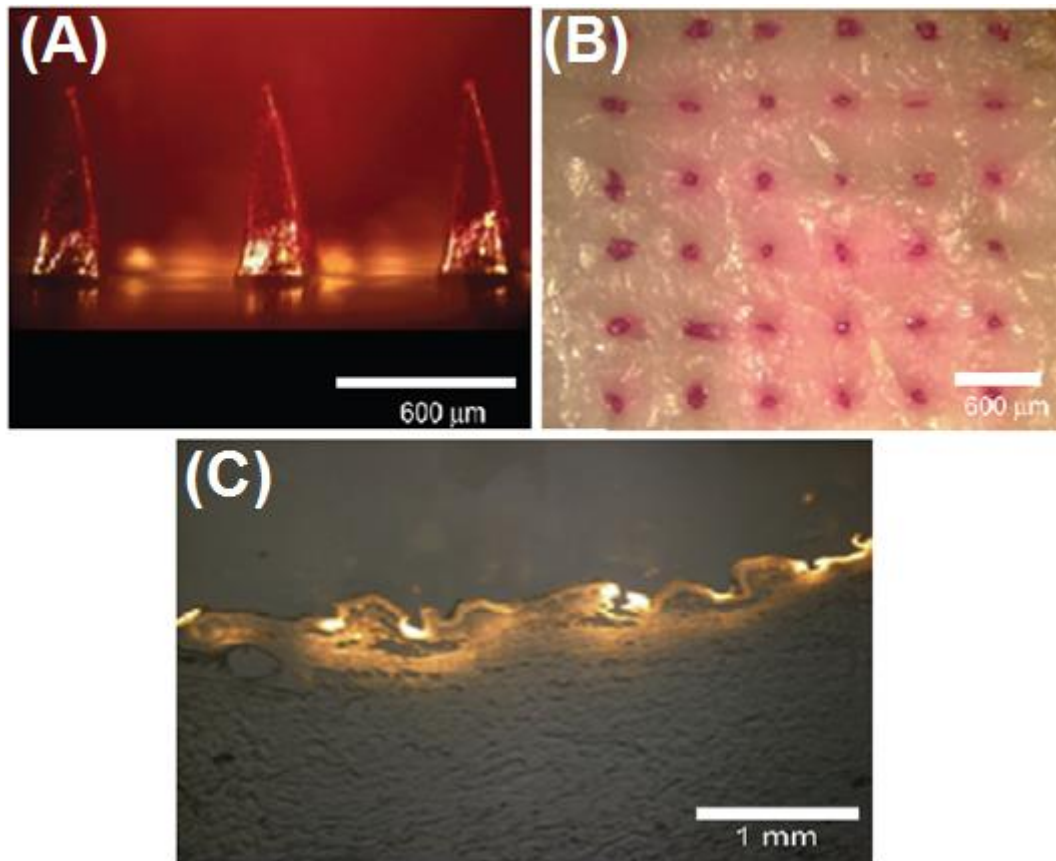
Figure 2.6: (A) image of the microneedle array, (B) sulforhodamine staining of the skin after application, and (C) histological cross section of skin showing fluorescence. Adapted from Lee et al. [104] with permission from Elsevier Limited, copyright 2008.

A vaccination against the PR8 influenza virus was administered by PVP microneedle arrays into mice, with the humoral immune response titer levels found to be statistically similar between microneedle and hypodermically administered groups [92]. CMC microneedles were used to deliver an influenza vaccine, with strong immune response recorded 102 days post application via the microneedle [126]. Vaccinations against tetanus were encapsulated within thermoplastic starch microneedles [127], as well as the encapsulation of goat anti-human IgG antibodies into maltose microneedles [128]. Microneedles made from PVA, trehalose and maltitol (2:3:3 weight ratio) were used to administer recombinant protective antigen to rats, with higher titer counts noted after microneedle application than after intramuscular or intradermal injection [129].

PLA microneedles were coated with a poly(o-nitrobenzyl-methacrylate-co-methyl-methacrylate-co-poly(ethylene-glycol)-methacrylate) film which was left within the dermal layers upon application of the PLA microneedle; this film was used to deliver DNA and RNA therapeutics into the dermal layers of *(in vivo)* mice and *(ex vivo)* macaque monkeys [130]. Plasmid DNA encoded with firefly luciferase was successfully administered to mice via PLGA microneedles, with a rapid delivery shown by an increase in luciferase activity after 5 minutes post application [99]. β-galactosidase was encapsulated and subsequently released from PVP microneedles [105].

While second generation microneedles made from PLA, PVP, PLGA, etc., have many advantages over the first generation microneedles, they are not fully optimised for transdermal drug delivery. A problem with standard second generation microneedle arrays is that the diffusion of the drug from the polymer depends on a number of things such as the rate of water uptake into the polymer, the dissolution rate, MWt and solubility of the drug, and the rate that the polymer is degraded by enzymes within the body or dissolved by the bodily fluids [131,132].

2.3.4 Electrically-stimulated microneedle arrays

Recently, there has been an increase in the studies of microneedle arrays that work in unison with another transdermal drug delivery system to improve the drug release performance relative to either separate device. An example of such a system is a combined iontophoresis–microneedle array system for the delivery of various drugs, such as insulin where the stainless steel microneedles were both the positive electrode for the iontophoresis device and the means of perforating the skin to create microchannels in the SC [133]. Using iontophoresis increased the quantity of insulin transferred by 3-5 times the value transferred without iontophoresis stimulation [133]. The delivery of BSA into the skin was ~3 times higher when a microneedle was combined with an iontophoresis device than without [134]. Small MWt drugs can

passively diffuse from microneedle arrays into the SC, and as such there was no noticeable increase in drug delivery rate when the microneedle array was combined with iontophoresis compared to passive diffusion [134,135].

Another possible combination is the electroporation-microneedle array combination that can have hollow microneedles to allow for therapeutic flow from an internal reservoir [136,137] or have the therapeutic applied to the outer surface of solid microneedles [58,138]. Such devices can be used for the electroporation of specific cells [138,139] or for the electroporation of the SC [140]. Therapeutics that were delivered successfully and in a higher quantity than the amount achieved by passive diffusion include dextran [140], calcein and BSA [139] and DNA vaccines [58,138]. There was a 140 fold increase, in comparison to passive diffusion, in the quantity of dextran that permeated the skin when an electroporation-microneedle array was used; this compares favourably to microneedle only (7 fold increase) and electroporation only (20 fold increase) [140]. It was found that increasing the voltage to the device when electroporating prostate cells would increase the uptake of calcein and BSA into these cells [139].

Electrically-stimulated microneedle arrays have improved drug delivery performance over standard first generation microneedle arrays and over passive diffusion, as well as the ability to modulate the delivery by varying the electrical stimulus, but they are more expensive than standard microneedle arrays (due to the equipment required) and are liable to the same problems as those discussed for electroporation/iontophoresis machines and first generation microneedles on their own (Section 2.2).

2.3.5 Manufacture of microneedle arrays

Microneedle arrays have been designed in their first and second generation forms for almost two decades, and in that time several different manufacturing processes have been used to manufacture the microneedle arrays. For second generation microneedle arrays, an original

version of the design is often produced from a metal/silicon/ceramic material initially. This original microneedle array would be replicated using silicone and a vacuum oven to create numerous female moulds; these female moulds would then, in turn, be filled with the chosen polymer and the drug to create second generation microneedle arrays [141]. The different processes used to create microneedle arrays can be summarised as microlithography, etching, laser fabrication, and 3D printing, of which brief descriptions of the processes are included below.

Microlithography

Microlithography was conceived to transfer complex shapes onto wafers by the selective removal of photo resist polymer material. Microlithography is mainly used in the computer chip, electronics, and semiconductor industries. Microlithography has been used previously in microneedle array projects [92,95,105].

Microlithography can be split into two classifications; (1) parallel and (2) serial. Parallel lithography refers to photolithography, where the UV light source is used to change the material properties of the photo resist material, allowing for selective removal by "developer" solvents. Serial lithography refers to either "electron beam direct write" lithography or focused ion beam lithography [142,143]. For an electron beam direct write lithography device, the beam is focused on a polymer material that is chemically changed by electrons passing through it. Upon the application of a developer solution, the undesired polymer is removed. A focused ion beam lithography device works either to remove a layer or to construct a layer. The ion beam has enough power to impinge and remove a small section of the wafer down to a certain depth. The ion beam also has the power to reduce the environmental gas within the chamber to a solid at specific points, allowing for the precise placement of solid material to form upright objects [144].

Etching

Etching uses the selective removal of a sacrificial material to form objects of high resolution for use within the electronics and semiconductor industries. Etching relies on the chemical reaction of etchants like sodium hydroxide and hydrofluoric acid with a sacrificial material coating. Wet etching uses solvents to achieve a controlled removal of specific material from a substrate wafer. This level of control is afforded by the use of a mask made from a material that is resistant to the solvent and by knowing the etch rate of the etchant. Silicon wet etching has been used previously to create microneedle arrays [145,146].

Reactive ion etching achieves higher resolution by using radical particles to remove the chemically reactive sacrificial material not protected by a reaction inhibitor mask. The radical particles are created by the ionisation of the gas within the chamber by a combination of low pressure and radio frequency electromagnetic stimulation. The ions from the gas plasma bombard the substrate, both reacting chemically with the sacrificial material and forcibly ejecting (sputtering) any material with a lower binding energy than the kinetic energy of the ion. These two processes combine to etch away the desired pattern [142]. Reactive ion etching has been used previously to create microneedle arrays [95,146].

Laser Microfabrication

UV laser cutting or drilling is a dry micromachining process [147]. UV laser microfabrication was used in previous literature to create microneedle arrays [38,99,103]. Light energy from the laser is targeted at specific points on the target material and the material is melted and ejected by a shockwave from its original position. By modifying the laser power and by knowing the thermal properties of the target material, the depth of each penetration impact can be changed to allow shallow or deep impacts.

3D printing

Two-photon photo-polymerisation relies on the raising of the photo-initiator molecules within a photo-curable resin from the ground state to a higher energy state via the absorption of photons, with the polymerisation occurring at the focal point of a highly focused laser of sufficient wavelength. Femtosecond direct laser writing was used to produce 3D scaffold structures for cell growth, with feature sizes 50 μm high and 7 μm wide achieved [148,149]. Similarly sized features, this time in the form of cantilevers and pyramids, were created by picosecond laser pulses for use as optical data storage devices [150].

Additive polymer printing techniques require the local heating of a polymer filament and the extrusion of the melted polymer through a fine nozzle, with horizontal layers of deposited polymer building up to form 3D structures. These printers do not provide the same resolution or size of detail as two-photon polymerisation can, often with limits of 0.1 mm resolution, but produce objects much quicker.

Replication procedures for the microneedle arrays

Typically, the initial microneedle array that was produced by 3D printing, microlithography, etching, or other methods, would be replicated using silicone and a vacuum oven to create numerous female moulds. This can be achieved by inserting the original microneedle array fully into uncured silicone, using a vacuum oven to remove bubbles and voids, and then subsequently curing the silicone.

Once the mould has been replicated, commonly the mould is filled by using either a vacuum oven or a centrifuge; either method will ensure that the voids will be filled and that the microneedle will be fully formed. In some instances, it is easier to use a vacuum oven to fill the voids, for example filling the mould with molten polymer [141] or filling it with a photo-curable resin [105]. In other circumstances, such as those where heat is not required, a

centrifuge can be used to fill the voids of the mould [104,119,151,152], which is the process employed in this thesis.

2.4 Functional Nanoparticles

In this section, recent publications will be discussed that report on nanoparticle-assisted drug delivery, bio-imaging, and thermal ablation applications; the nanoparticles of particular interest are carbon nanotubes (CNTs), graphene, iron oxide (IO), hybrids of graphene-IO, and other nanoparticles such as gold and quantum dots (QDs).

In this project, the drugs will be bound to graphene and subsequently released from the nanocomposite into the body in this form, so it is important to study the literature on nanoparticle-assisted drug delivery. Publications on nanoparticle-assisted drug delivery focus on the interactions between the drug and the nanoparticle, the potential for targeting the nanoparticle to a specific site, and the diffusion of the drug from the nanoparticle once at the target site. Studies on the imaging potential of nanoparticles have assessed their applicability to various imaging modes such as magnetic resonance imaging (M.R.I.), computed tomography (CT), positron emission tomography (P.E.T.G.), fluorescent and optical microscopy, and photo-acoustic. Studies on thermal ablation applications investigate the interaction between nanoparticles and external stimulations such as NIR irradiation or an AC magnetic field, and the efficiency that the nanoparticles convert the stimulating energy to heat in order to damage tumours and cancer cells [153].

The biocompatibility of nanoparticles will also be discussed in their sections, as it is important for future biomedical applications. It is well known that ultrafine particulate matter in the air have adverse effects on the humans and animals that inhale them, ranging from cardiovascular, pulmonary, respiratory, and cancer problems [154–156]. The effect that CNTs,

graphene, IO, hybrids of graphene-IO, gold, and QDs have on the body must be checked for similar effects.

2.4.1 Carbon Nanotubes

CNTs are carbon allotropes that are in essence "rolled up" sp^2 carbon nanosheets (Figure 2.7). CNTs have recently been researched as potential drug delivery systems [157], as imaging agents [158], and as thermal ablation agents [159].
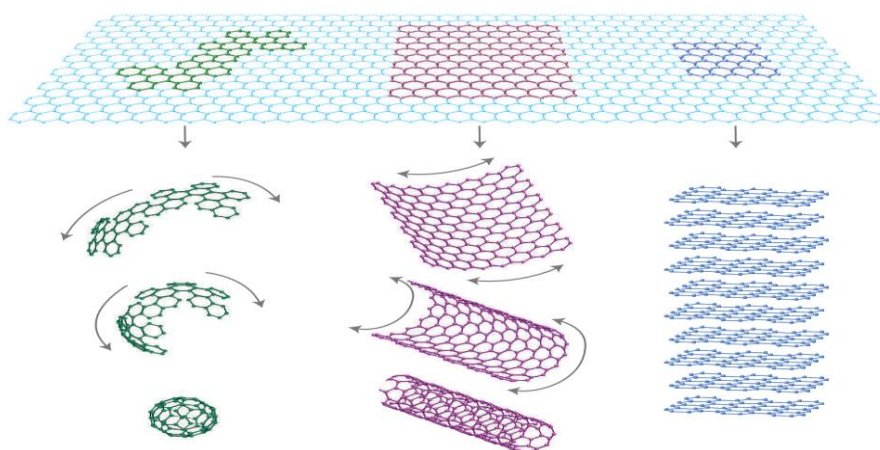
Figure 2.7: A sheet of carbon atoms, arranged in a hexagonal arrangement, can be formed into other carbon nanostructures like CNTs, fullerenes and graphite. Adapted from Geim et al. [160] with permission from Nature Publishing Group, copyright 2007.

CNTs were coated with a Platinum IV anticancer drug and were shown to have a pH sensitive release of the drug after the CNTs had entered cancer cells [157]. The presence of the free drug itself did not notably decrease the cell viability (with a maximum decrease of ~10% with a 0.5 μM concentration), but when delivered by CNTs the drug reduced the cell viability by ~85% at a 0.5 μM concentration of the drug. The drug, per mg of protein, was measured at 23 ng within the cytosol region and 36 ng within the nucleus after 3 h, values that were twice as high as for free Platinum IV [157]. Fluorescein labelled RNA attached to CNTs were used to target HeLa cells in mice [161], with the RNA working within one week to reverse the growth and reduce both the size and weight of the tumours when compared to control mice tumours.

CNTs can be used to image tumours in mice [158]. By coating the CNTs with a copper isotope (to allow for P.E.T.G. imaging) and an antagonist of integrin (to provide targeting functionality), CNTs were able to target and image with high resolution the tumours within the mice. Welsher et al. [162] used functionalised CNTs and NIR light stimulation to monitor the flow of blood through a mouse. Figure 2.8 shows the progression of the PEG coated CNTs from the insertion point at the tail vein to the lung and then from the lung to the spleen via the kidney and the liver, demonstrating that these nanoparticles can be used to monitor blood flow and to determine if there are any blockages within the veins.
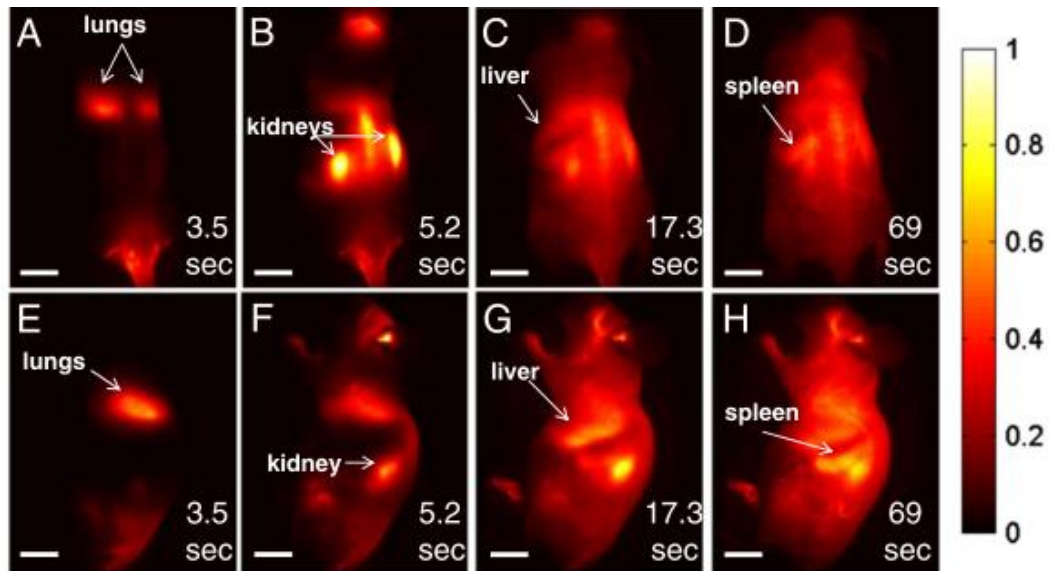
Figure 2.8: The path of blood flow through the lung, kidney, liver and then to the spleen. Upper row is in the plan view and lower row is in the side view. Adapted from Welsher et al. [162] with permission from National Academy of Sciences of the United States of America, copyright 2011.

CNTs were used to photothermally ablate 4T1 tumours in mice using NIR irradiation [159]; this would only occur when CNTs were used in conjunction with NIR irradiation and not with CNTs or irradiation on their own. Similarly, PEG coated CNTs achieved photothermal ablation of mice, with those treated with CNTs and laser irradiation surviving the duration of the study: their tumours decreased in size and mass unlike the control mice that died from tumour growth after thirty days [163].

The biocompatibility of CNTs can depend on whether there are any impurities on the CNTs after production, which may limit the usefulness of CNTs in biomedical applications. Shvedova et al. [164] applied CNTs, containing trace amounts of iron derivatives, to human epidermal keratinocytes. The unpurified CNTs damaged the cells when introduced in doses from 0.06-0.24 mg ml^{-1} through OH free radical interaction with cells. Reactive oxide species (ROS) can lead to oxidative stress which may lead to cell apoptosis [165–168], DNA damage [169], and some diseases of the brain [170] and the cardiovascular system [171]. The ROS in the unpurified CNTs is from the manufacturing process and can lead to changes to the structure of the cells (nucleus, mitochondria and the tonofibril) after 18 h [164]. Monteiro-Riviere et al. [172] assessed purified CNTs (without any iron derivatives present) with human epidermal keratinocytes; the cell viability reduced to 70% with a high dose (0.4 mg kg^{-1}). This shows that if the impurities of CNTs can be reduced to negligible levels, the cell viability can be maintained. Radomski et al. [173] noted that CNTs at concentrations of 0.2-300 μg ml^{-1} induced platelet activation and clotting of the blood. Li et al. [174] suggested that CNTs administered in doses of 10 to 40 μg per mouse can inflict ROS damage on the mitochondrial DNA and that this led to an increase in atherosclerosis in the mice. Yokoyama et al. [175] recorded that granulomas surrounded implanted CNTs after 1 week and these granulomas developed to fibrous tissue formations after four weeks. These results suggest that the CNT manufacturing process and the concentration of CNTs within the body must both be carefully monitored in order to avoid cytotoxicity.

2.4.2 Graphene

Graphene is a carbon allotrope in the form of a sheet of sp^2 carbon atoms arranged in a hexagonal arrangement that can be formed into other carbon nanostructures like CNTs, fullerenes and graphite, as demonstrated in Figure 2.7 [160]. Graphene possesses the highest ultimate tensile strength (UTS) (130 GPa) and Young's modulus (E) (1 TPa) of any natural

substance, as well as a theoretical surface area of 2,630 m^2 g^{-1}, an electron mobility greater than 10,000 cm^2 v^{-1} s^{-1}, resistance value of 6 kΩ, conductivity of 20 x 10^3 S cm^{-1}, and a thermal conductivity value of ~4,000-5300 W mK^{-1} [160,176–182]. Pristine graphene was originally isolated by Geim and Novoselov in 2004 via mechanical exfoliation of graphite [178], but other methods have been developed such as growing graphene via chemical vapour deposition onto substrates and epitaxial growth [183], or the solvent exfoliation of graphite [184,185]. Pristine graphene was not used in this project and therefore these methods will not be discussed further.

Graphene oxide (GO) is created by oxidising graphite and exfoliating the resultant graphitic oxide to create single layer GO (the structure of which is shown in Figure 2.9) [186–188]. The degree of oxidation can change many aspects of the structure of GO [189], with an increase in oxidation often met with an increase in the ratio of sp^3 to sp^2 carbon domains and an increase in the quantity of hydroxyl, carboxyl, and epoxide groups present. The oxidation process gives GO ample functional groups that improve the bonding of GO to other molecules [190] and excellent dispersibility within many solvents [191], though the defects within the structure caused by the oxidation do reduce the mechanical properties; as the degree of oxidation varies, so too does the regularity of defects that interfere with and reduce the sp^2 domains [189]. The idealised sp^2 carbon structure gives pristine graphene its strong E value, and as such, GO which has limited sp^2 domains may not match the E of pristine graphene. The reported E of GO varies in the literature from 207 GPa [192] to 380-470 GPa for ordered and 290-430 GPa for amorphous GO [193], but the values are always less than the value associated with pristine graphene. GO has an electrical conductivity value 6 orders of magnitude lower than pristine graphene, with conductivity values of 1-5 x 10^{-3} S cm^{-1} [194] and resistance values of ~1 x 10^{12} Ω [195] due to the defects in and the reduction of the size of the sp^2 domains; the conductivity is so low that GO is often considered an electrical insulator [196,197].
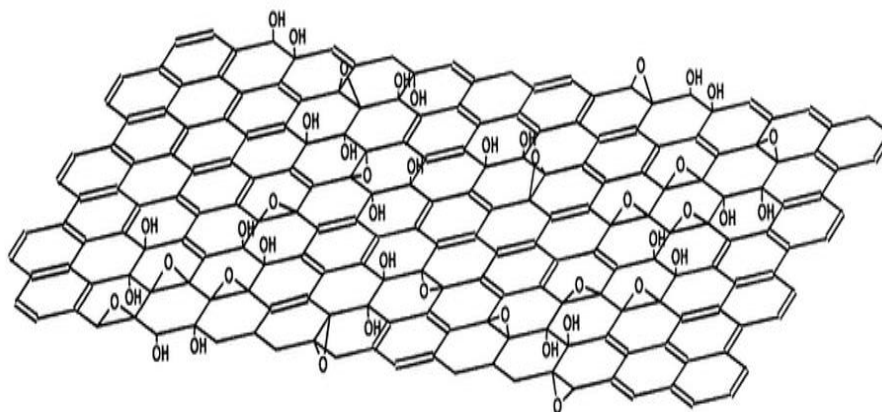
Figure 2.9: Illustration of the perceived chemical structure of GO [198,199]. Adapted from He et al. [198] with permission from Elsevier, copyright 1998.

Typically, the method of producing GO is to oxidise graphite through the Hummers method [186] or a modification of that method [187,200]. A standard Hummers oxidation reaction would involve the addition of graphite to an agitated mixture of sulphuric acid H_2SO_4, sodium nitrate $NaNO_3$, and potassium permanganate $KMnO_4$ [186]. Some modifications to the Hummers method include the addition of phosphoric acid H_3PO_4 when adding the sulphuric acid [187], or a pre-oxidisation step where a 80 ^{o}C mixture of sulphuric acid, potassium persulfate $K_2S_2O_8$, and phosphorus pentoxide P_2O_5 was used to oxidise the graphite before the main Hummers method [200]. Once a sufficient amount of time has passed (predetermined by the method used) the graphite oxide slurry is typically either diluted with water [186] or poured onto ice [187], before treatment with hydrogen peroxide H_2O_2.

To partially restore the excellent properties of graphene to GO whilst maintaining the dispersibility of GO, the GO can be reduced to "reduced graphene oxide" (rGO) by removing the functional groups created during the oxidation of graphite [201–203]. Reduction can be achieved by a number of methods, such as using toxic chemicals such as ammonia, hydrazine and diazene [204–206], by using biomolecules, or by hydrothermal reduction. The biomolecules route uses biomolecules such as glucose that contains hydroxyl groups [207,208], green tea polyphenol that contains pyrogallol and catechol groups [209], gelatin that contains

amine groups [210], ascorbic acid that contains hydroxyl groups [211–213], chitosan that contains amine groups [214], and BSA that contains phenolic groups [215] to reduce the GO. The usage of biomolecules to reduce the GO to rGO is ideal for the biomedical industry as it will often coat the rGO with the biomolecule by chemical grafting, which will improve the biocompatibility of the rGO [216].

The hydrothermal reduction route uses a supercritical solvent, for example water, to reduce the functional groups of GO [217]. At supercritical temperatures, water behaves like a strong electrolyte with a high diffusion coefficient and a high dielectric constant comparable to polar organic solvents [218]. The proposed method of hydrothermal reduction of GO is through heterolytic bond cleavage, where both of the electrons involved in the bond remain with the most electronegative of the oxidation-reduction pair [218]. The hydrothermal reduction route is advantageous in comparison to other methods such as hydrazine reduction as it is environmentally friendly with no toxic chemicals, is a 'one pot' procedure requiring just the addition of a suspension to an autoclave, and the end product can be fine-tuned easily by varying the reduction temperature and time.

Graphene, GO and rGO have found use in biomedical applications such as drug delivery, imaging and thermal ablation of tumours [219,220]. A popular application for GO and rGO is therapeutic delivery, where it has been shown that using graphene based nanoparticles as the drug carrier can increase the efficiency of the drug that is delivered, relative to free/unbound drug [216,221,222]. GO bound with the anti-cancer drug ethyl-hydroxycamptothecin (SN38) showed a 50% cell viability reduction at a drug concentration of 6 nanomoles, which was comparable to the control of Irinotecan (CPT-11, the oral administration version of SN38) at a concentration of 10 μmoles [14]. Zhang et al. [223] found that the cytotoxicity for GO-doxorubicin or GO-campothecin was much higher than for either free standing drug on its own. Hypocrellin A and SN-38 were bonded together onto GO, and

this combined treatment showed a better cytotoxic effect to A549 cells than either drug bonded to GO on its own, showing the benefit of dual-therapeutic treatment [224]. The pH sensitive release of Ibuprofen or 5-fluorouracil in either the stomach or a tumour could be achieved from chitosan coated GO [216]. Similar pH sensitive release was noted for epirubicin bonded to hyaluronic acid-GO, with this pH sensitivity allowing for an increased release of the drug into the nucleus of the cells [225]. The pH of the solution is a critical factor on the successful loading onto and the release of doxorubicin from GO, with a neutral solution shown to be the best for loading and an acidic solution best for the release of doxorubicin [226]. Other therapeutics that were studied include resveratrol [227] and chlorin e6 [228], while there were further studies on doxorubicin with rGO-PEG-poly(ethylenimine) (PEI) [229], PEI-poly(sodium 4-styrenesulfonate) coated GO [230], hyaluronic acid-rGO [231], and PEG alginate-GO [232].

Once bonded to graphene, the drug will gradually diffuse from the graphene nanoparticle. The manner of the diffusion type, i.e. Fickian (molecular diffusion), non-Fickian/anomalous, or case II relaxation controlled transport [233–235], can vary in the literature as the type of drug (and therefore the type of bonding to graphene) and the pH of the release medium may vary the release rate and release profile of the drug [234]. Changing the pH of the release medium changed the type of diffusion that occurred when rhodamine B was released from GO from case II (pH = 7.4) to anomalous diffusion (pH = 4.5) [234]. The authors believed that the pH sensitivity is due to the changes in the hydrogen bonding between the graphene and the rhodamine B due to the protonation of the COOH group. In the case of gentamicin and graphene, the pH (either pH = 3, 7.4 or 10) of the release medium did not change the diffusion type (Fickian) when analysed, suggesting that the bonds between that particular drug and graphene were not pH sensitive; similarly, the diffusion type of rhodamine B from carbon black or CNTs remained Fickian, regardless of the pH of the release media [236], due to the different type of bonding (π-π) used between those nanoparticles and

rhodamine B in comparison to the aforementioned study on GO and rhodamine B (hydrogen bonding) [234].
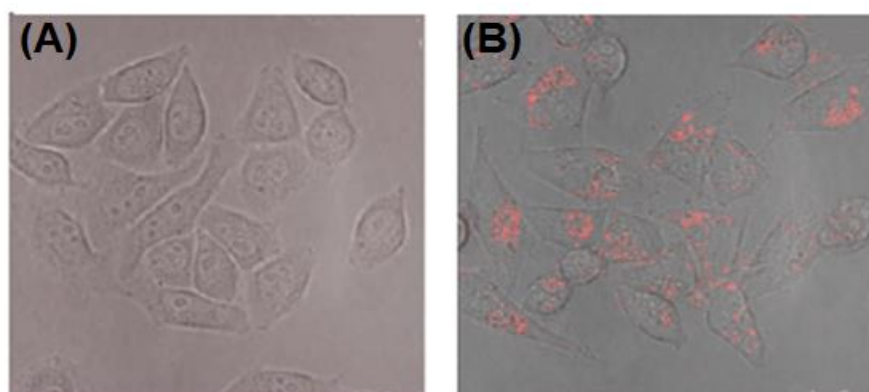
Figure 2.10: (A) Free molecular beacons and (B) graphene - molecular beacons, showing the difference in transfection of the cells due to the presence of graphene. Images are fluorescent microscopy images overlayed onto bright field optical microscopy images. Adapted from Lu et al. [237] with permission from The Royal Society of Chemistry, copyright 2010.

Gene therapies can also be delivered in conjunction with GO, with the loading of DNA onto GO found to be dependent on certain factors, with higher loadings achieved when the DNA helix was short, the solvent had a low pH and a high ionic strength [238]. Plasmid DNA and siRNA were transferred via PEG-PEI coated GO [239,240], with both papers noting that the transfection of the cells with the gene therapies could be improved by using NIR laser irradiation. Similar transfection rate increases into HeLa cells were noted for DNA and RNA gene therapies that were bonded to graphene than for the free therapeutic [221]. Zhang et al. [222] used GO functionalised with PEI to transfer short interfering RNA therapeutics into BcL-2 cancer cells during an in vitro experiment. GO bonded to trimethyl-chitosan was conjugated to folic acid, which acted as a targeting mechanism against cancer cell lines with folate receptors, and the GO could then be used to deliver doxorubicin or plasmid DNA into HeLa cells [241]. The imaging of cells could be achieved by using molecular beacons bonded to graphene; the successful transfection of the cells with the gene therapy could be determined through fluorescence imaging as shown in Figure 2.10 [237]. Graphene increased the transfer of the therapeutic to the cells, as shown by the stronger fluorescence for cells treated with the

graphene bound therapeutic than for the free molecular beacon solution. The delivery of molecular beacons by GO was similarly noted by Lu et al. [237], who also showed that the GO could prevent the enzymatic cleavage of the molecular beacon by preventing the cleaving enzyme from binding to the molecular beacon. Cells could also be probed by a molecular probe consisting of aptamer-carboxyfluorescein coated GO [242].
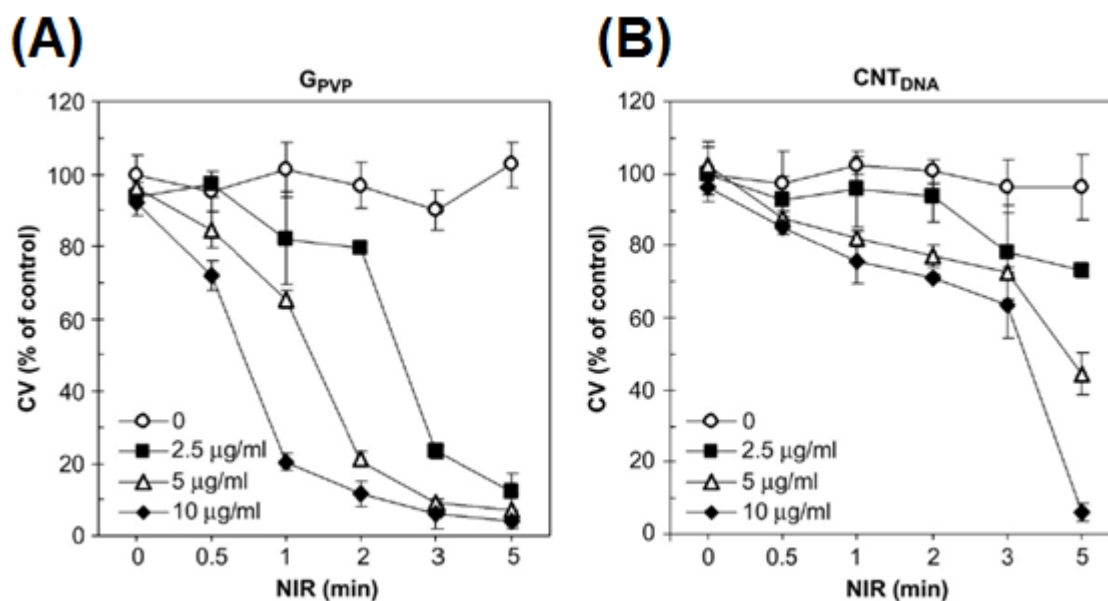
Figure 2.11: (A) GO and (B) CNTs under NIR laser stimulation, showing a reduction in the cell viability of cancer cells. The time required to achieve ~80% photothermal ablation of the cells was less for GO than for CNTs, showing GO to be a better photothermal ablation agent. Adapted from Markovic et al. [243] with permission from Elsevier Limited, copyright 2011.

Markovic et al. [243] tested GO as a thermal ablation agent for the treatment of cancer cells. Within 3 minutes of NIR stimulation, at least 75% of the cells had been killed for each concentration of graphene. After 5 minutes, all concentrations of graphene (2.5 µg ml^{-1}, 5 µg ml^{-1}, and 10 µg ml^{-1}) had killed between 80-100% of the cells present (Figure 2.11). Yang et al. [244] used PEG coated GO and a NIR laser to thermally ablate tumours in mice, similar to Robinson et al. [245] who used GO coated with PEG and the targeting ligand RGD to target U87MG cancer cells for thermal ablation. Robinson achieved an 80-90% reduction in cancer cell viability.
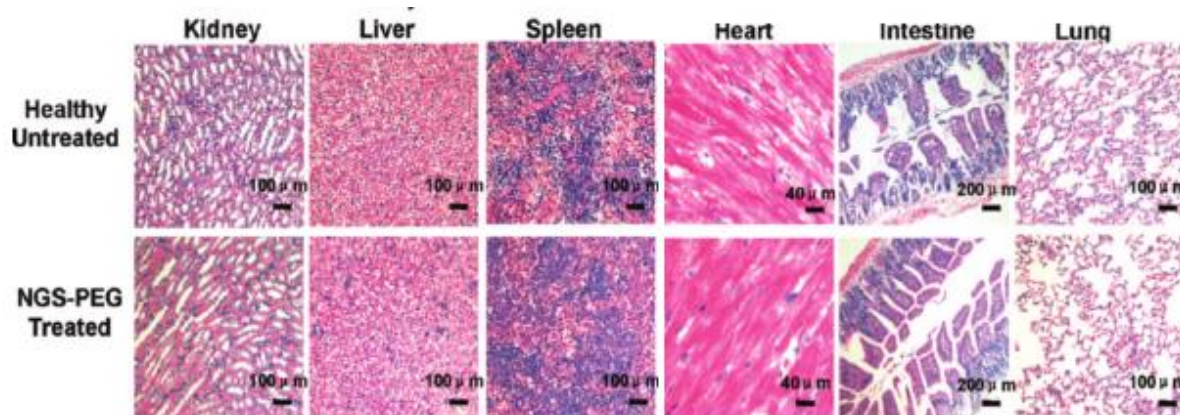
Figure 2.12: Light micrograph after 40 days showing no damage to the kidney, liver, spleen, heart, intestine, or the lung after treatment with 20 mg kg^{-1} of PEG coated GO. Adapted from Yang et al. [244] with permission from American Chemical Society, copyright 2010.

Wang et al. [246] analysed the effects of GO on human fibroblast cells and mice. Doses of 20 µg ml^{-1} or lower did not induce toxicity in the human fibroblast cells, but doses of 50 µg ml^{-1} or higher induced severe toxicity through a decrease in cell adhesion and an increase in cell apoptosis. Below the concentration of 0.4 mg per mouse, there was no notable toxicity within the mice, but at 0.4 mg per mouse there were signs of severe chronic toxicity, including granuloma formations within the lung, liver, spleen and kidney of the mice. Similarly, Zhang et al. [247] noted no toxicity in the liver, spleen or the kidney in mice treated with 1 mg kg^{-1} or 10 mg kg^{-1} of GO over a 2 week time span. It was noted, however, that there was granuloma formation and inflammation within the lungs for the higher dosage of GO. A haemolysis assay showed that there was no ill effect at doses of 10 and 80 µg ml^{-1} on haemoglobin and that GO did not harm red blood cells [247]. The aspiration of 50 µg per mouse of graphene nanoplatelets formed granulomas in the bronchiolar lumen and inflammation in the chest wall, and ultimately resulted in cell apoptosis through ROS [248].

Coating GO or rGO with biomolecules can improve the biocompatibility of the nanoparticles [222,249–252]. After a treatment of 20 mg kg^{-1} of PEG coated GO, there was no obvious signs of chronic toxicity after 40 days within mice (Figure 2.12) [244]. Human mesenchymal stem cells [253] and osteoblasts [254] were shown to proliferate when in the

presence of chitosan coated graphene. Mice treated with 20 mg kg^{-1} of PEG coated GO did not suffer hepatic nanotoxicology after 3 months, with white blood cell, red blood cell, platelet, and haemoglobin counts similar to control samples of untreated mice [249]. Yang et al. [249] analysed the whole body biodistribution of PEG-GO and its concentration in the liver, spleen, urine and faeces, showing that the majority of the GO was excreted though urine within 2 days and that the main congregation point within the body was the spleen.

2.4.3 Iron oxide

IO nanoparticles, such as magnetite Fe_3O_4 and maghemite γ-Fe_2O_3, have use within biomedicine as imaging contrast agents, drug delivery systems, thermal ablation agents and filtering agents for biological assays [255–257]. Their small size allows them to migrate through blood vessels and into tumours. Typically, IO nanoparticles such as magnetite and maghemite are superparamagnetic, a phenomenon where they hold no residual magnetic force (they will not aggregate together through their own magnetic force), but can be manipulated by external forces.

IO nanoparticles have been used before as targeted drug delivery carriers as IO can be manipulated by external magnetic fields to collect in specific sites [19,258]. Alexiou et al. [19] attached the anti-cancer drug mitoxantrone to IO and used an external magnetic field to attract the IO to tumours within rabbits. Within the tumour, 4.71 µg ml^{-1} of mitoxantrone was measured when a treatment of 5 mg m^{-2} IO-mitoxantrone was administered to the rabbit, compared to 0.58 µg ml^{-1} of mitoxantrone when 10 g m^{-2} of free mitoxantrone was administered. This showed that a substantial increase could be achieved in the amount of drug delivered to a tumour when the drug is targeted to a specific site. IO loaded with doxorubicin could be manipulated by an external magnet to aggregate close to the magnet [259]; cell viability analysis confirmed that the cell viability was lower closer to the magnet site than it was far from the magnet, which was attributed to the presence of IO-doxorubicin. Hu et al.

[258] researched polyallylamine nanocapsules encapsulating IO and doxorubicin hydrochloride. Purushotham et al. [260] used poly-n-(isopropyl acrylamide) (PNIPAM) to form a polymer layer around magnetic IO and doxorubicin. Other drugs that have been bonded to IO for drug diffusion and drug release tests include vitamin B2 [261], vitamin B12 [262], fluorescein sodium [263], and theophyllinec [118]. Gene therapies have been investigated for use with IO; the Sendai virus, a RNA virus that can be used as a gene therapy vector, was bound to maghemite nanoparticles and was shown to effectively transfer luciferase plasmid into BHK-21 cells without an increase in cell cytotoxicity (when compared to unbound gene therapy vector) [264].
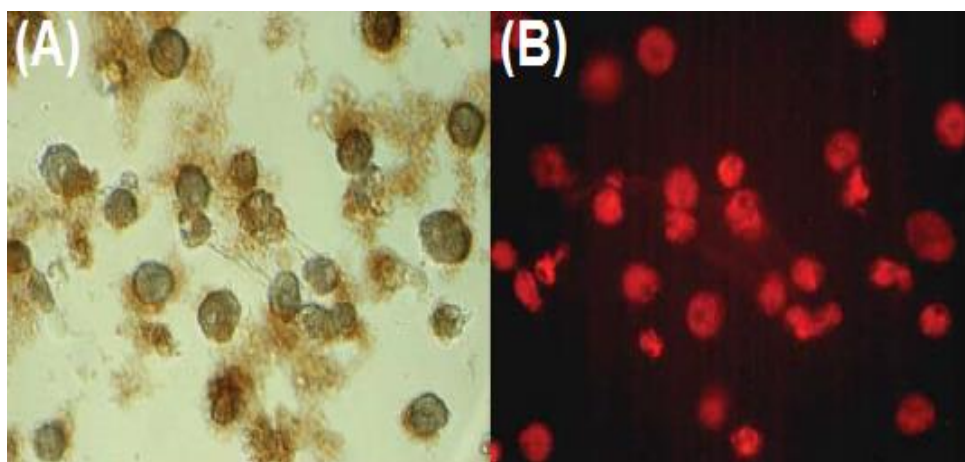
Figure 2.13: (Left) A transmitted light microscopy image and (right) fluorescent light microscopy image of IO NPs within phagocytic cells. Adapted from Corr et al. [265] with permission from The Royal Society of Chemistry, copyright 2006.

IO can be used for M.R.I. of tumours and the circulatory system [266,267]. Cheong et al. [16] showed that IO could successfully image the liver, the spleen and the inguinal region of mice, while Lim et al. [268] imaged metastatic breast cancer cells within mice. Park et al. [269] imaged tumours and vital organs in mice, and determined that smaller IO nanoparticles are removed from the body quicker than larger nanoparticles, a finding that could be beneficial in optimising the ability of IO as a contrast agent. These results show that IO is an effective contrast agent for body organs for imaging purposes. Corr et al. [265] investigated whether IO,

bonded to fluorescent markers, could be consumed by osteoblast cells and phagocytic cells, and the cells can be seen very clearly in Figure 2.13.

The use of IO in thermal ablation is owed to the superparamagnetic behaviour; if manipulated by an AC magnetic field, the IO will revolve on their primary axis and generate heat [270], with chitosan coated IO nanospheres used in cancer ablation therapy [20,271]. Babincov et al. [272] tested IO coated with cisplatin to reduce the cell viability of sarcoma cells (Figure 2.14). Thermal ablation reduced the cell viability by ~20%, while free cisplatin would reduce cell viability by 20-25%. When the effects of the thermal ablation and bound drug were combined into one nanohybrid, the cell viability was reduced by 75-80%
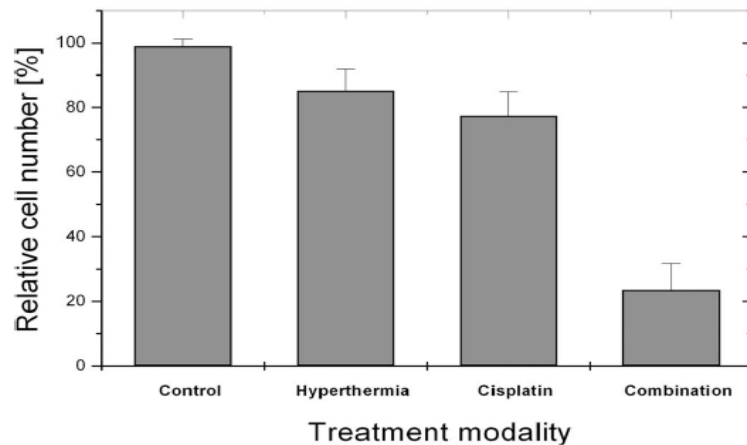
Figure 2.14: Reduction in cell numbers of control, hyperthermia on its own, cisplatin on its own, and a combination of cisplatin and hyperthermia. Adapted from Babincov et al. [272] with permission from IEEE, copyright 2008.

Brunner et al. [273] found that pristine IO had a high level of cytotoxicity to human mesothelioma cells when exposed to a concentration of 10 µg ml^{-1} or higher, which they suggested was due to ROS toxicity of pristine IO. This ROS toxicity did not affect all cell types, as mice fibroblast cells had a 75% cell viability up to the dose of 30 µg ml^{-1}. Zhang et al. [274] showed that IO nanoparticles with and without a surface coating of PEG can enter both mouse macrophage and human breast cancer cells. Uptake by macrophage cells was lower for the PEG coated IO than for the uncoated IO, but this trend was reversed for human breast cancer cells. Similar results for the increase in cell viability by the passivation of IO by

biomolecules coating were noted for pullulan coated IO [275], dimercaptosuccinic acid coated IO NPs [276], and for silica coated cobalt ferrite nanoparticles [277]. Park et al. [269] analysed the biodistribution of IO nanoparticles within the body of mice. The highest concentrations of the IO were found in the lymph nodes and in the spleen, suggesting that the body was removing the IO from the blood through the reticuloendothelial system (RES) and the macrophages within it. A high concentration, around 13%, was still in the blood. Low uptake in the brain and the lungs shows that, in this case, the nanoparticles did not accumulate to dangerous levels in two very sensitive areas of the body. Weissleder et al. [266] recorded similar biodistribution patterns after 24 h for IO in mice, showing high uptake in the lymph nodes and the spleen, similar to the findings of Park et al. [269]. Weissleder et al. [278] noted no body weight loss, no reduction in food consumption, no increase in mortality or morbidity when rats were injected with a maximum of 160 µg kg^{-1} of IO. No tissue damage was noted in the liver, spleen or the lymph nodes, though the level of haemoglobin in the blood slightly increased as both the dose and the time of the test increased.

2.4.4 Graphene-iron oxide nanoparticles

IO can be chemically deposited onto GO to form a nanohybrid GO-IO [279–281]. If the GO has been reduced to rGO during the deposition process, it may become rGO-IO [282]. These nanohybrids combine the interesting functions of IO and GO/rGO; namely the superparamagnetic properties of IO and the abundant functional groups/high surface area of GO. GO-IO have found use in biomedicine as targeted drug carriers, imaging agents, and photothermal agents [279–282].

GO-IO was bonded with PEG and doxorubicin to create a targeted drug delivery carrier [280]; the GO-IO-PEG-doxorubicin could be manipulated and aggregated by the presence of a magnet, and subsequent fluorescent imaging of the bound doxorubicin showed a higher quantity of doxorubicin within cells close to the magnet than there was farther away. This

reduced the cell viability of the cancer cells close to the magnet, in comparison to cells farther away, showing the possibility to target a drug to a specific site. GO-IO loaded with doxorubicin could be manipulated to aggregate at a specific spot by a magnet [279]. The anti-cancer drug 5-fluorouracil was bonded to rGO-IO and the nanohybrid was shown to be capable of entering HepG2 cells, into which it would use pH sensitive drug release to release the drug [283]. The degree of pH sensitivity was such that in a pH = 4 environment, there was a ~55% release of the drug after 8 h, but in a neutral environment the release was only ~15%. The nanohybrid was also shown to be biocompatible, with a ~100% cell viability achieved with rGO-IO concentrations up to 80 μg ml^{-1}. GO-IO was also bound to 5-fluorouracil, with similar results [284]. Insulin was bonded to GO-IO and was shown to have a pH sensitive release, high biocompatibility, and similar enzymatic properties to free insulin [285]. The delivery of doxorubicin using GO-IO has been studied before [286–288], with additional targeting mechanisms such as folic acid [286,289] reported as well as chitosan functionalisation to improve biocompatibility [287].

Tri-modal imaging was achieved with rGO-IO [282], with photo-acoustic and M.R.I. imaging from the rGO-IO and fluorescent imaging achieved through bonding the rGO-IO with a cyanine dye. The rGO-IO achieved within 1 day the full ablation of 4T1 tumours in mice using the strong NIR absorbance of the rGO-IO and a NIR laser (5 min exposure at 0.5 W cm^{-2} power) [282]. GO-IO-PEG was used as a photothermal ablation agent [280]. Once imaged using M.R.I., the nanohybrid could be targeted to a site in the body for thermal ablation using NIR irradiation [280]. The nanohybrid achieved a ~90% cell viability reduction using 5 min of 2 W cm^{-2} irradiation. Campothecin and methotrexate were both bound to GO-IO as an anti-cancer nanohybrid, which achieved a high cell reduction for HepG2 and L02 cell lines and a tumour volume reduction of ~40% without NIR irradiation and ~74% with NIR irradiation [290].

2.4.5 Other nanoparticles

As well as the carbon and iron oxide based nanoparticles, other nanoparticles such as gold and quantum dots (QDs) have been used for drug delivery, bio-imaging and thermal ablation applications.

Gold

Nanoparticles of gold can be used as both drug delivery carriers, imaging agents and as photothermal ablation agents in the bioengineering sector [291–294]. Rhodamine B was bonded to and subsequently released from gold nanoparticles under NIR laser irradiation [295]. The co-application of gold nanoparticles with rhodamine B aided the permeation of the drug through the SC [296]. The liver specific release of amino-coumarin was achieved with gold nanoparticles that had both lactose and the drug bonded to the surface [291]; the lactose was used to target the nanoparticles at hepatic stellate cells in the liver. PEG functionalised gold nanoparticles had an improved ability to enter into and deliver oxaliplatin to the nucleus cells than either the free drug or non-functionalised, pristine gold delivering the drug [297]. Similarly, glutathione functionalised gold achieved the cellular uptake and release of a fluorescent dye; this was not achievable for the free dye [298]. PEG functionalised gold could deliver the drug silicon phthalocyanine 4 into tumours at a higher quantity than the free drug achieved by itself [299]; the PEG-gold also increased the water solubility of the hydrophobic drug. Gold nanoparticle drug delivery was also studied with paclitaxel [300], nitric oxide [301], and with phthalocyanine [302].

Gold nanoparticles have been investigated as a gene transfer agent [292,303,304]. Takahashi et al. [292] showed that plasmid DNA can be absorbed onto the surface of gold nanorods and subsequently released from the gold nanorods by near-infrared (NIR) laser irradiation, allowing for the possibility of targeted release of therapeutics at specific sites, similar to other studies on NIR laser irradiation stimulated release of DNA attached to gold

nanoparticles [303,304]. The intracellular release of RNA from gold nanoparticles could be achieved in the presence of glutathione [305]; there was minimal release of the RNA when the gold nanoparticles were in a solution with glutathione concentration at that of the extracellular matrix, but the RNA was released at therapeutic levels when the glutathione was at a intracellular concentrations.
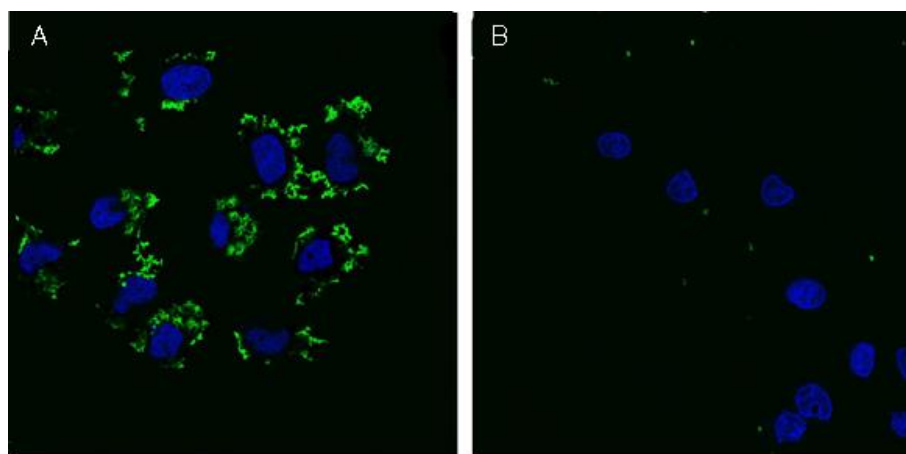
Figure 2.15: Confocal image of (A) HeLa and (B) A549 lung cancer cells showing specificity in nanoparticle targeting. Adapted from Zhang et al. [293] with permission from Elsevier Limited, copyright 2010.

Zhang et al. [293] bonded folic acid targeting ligands to gold nanoparticles to provide a means to image specific cancer cell lines, such as targeting HeLA cells but not A549 lung cancer cells. Figure 2.15 shows a confocal microscopy image of (At) HeLa cells and (B) A549 lung cancer cells. There is a clear difference in the concentration of gold nanoparticles surrounding the HeLa cells and the A549 cells, which shows that this cell specific targeting does work. Huang et al. [294] used a targeting ligand to target malignant cells with gold nanoparticles, successfully imaging malignant oral epithelial HOC 313 and HSC cell lines and then thermally ablating the cells with a NIR laser.

Gold nanoparticles (4 nM concentration) could achieve the photothermal ablation of cancer cells when irradiated with a 800 nm laser for 2 min at a relatively low power level of 1.1 mW, compared to 22.2 mW to photothermally ablate cells without a gold nanoparticle treatment [306]. Gold nanoparticles bonded to doxorubicin were used to kill breast cancer cells

under NIR laser irradiation [307]. The gold nanoparticles alone under NIR laser irradiation achieved a ~10% reduction in cell viability, but with doxorubicin this dropped to ~55%. Peptides were used to selectively target gold nanoparticles, with bonded doxorubicin, against specific cell types [308], with a focus on targeting HeLa and A549 cells more efficiently.

Quantum dots
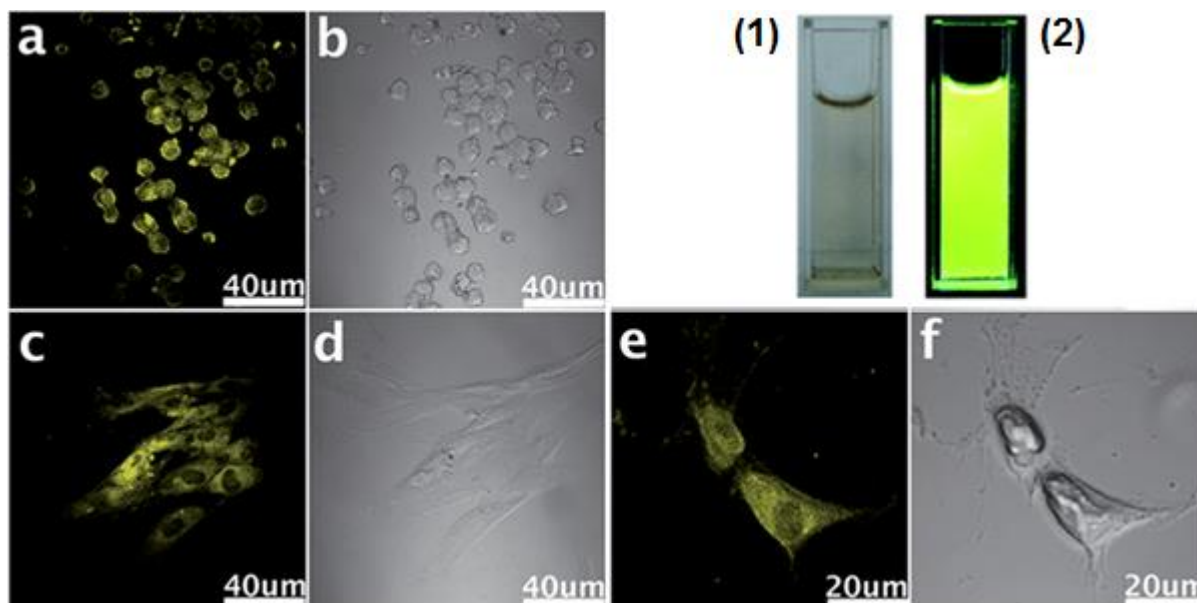
Figure 2.16: Main image: Fluorescent (A, C, E) and optical (B, D, F) microscopy images of GQDs (diamter of 5-10 nm) within cells under 405 nm light. Inset: (1) GQD suspension in water and (2) GQD suspension under 405 nm light. Adapted from Zhang et al. [309] with permission from The Royal Society of Chemistry, copyright 2012.

QDs are semiconductor nanocrystals that emit a dimension-dependent luminescence due to quantum confinement effects, and semiconductor QDs would typically be <10 nm in radius [310–313]. These semiconductor QDs, without a polymer or biomolecule passivation coating, are of little use for biomedical applications as QDs like cadmium selenide (CdSe), cadmium sulphide (CdS) or cadmium telluride (CdTe) are cytotoxic during *in vitro* cell tests due to the photolysis release of cadmium ions whilst also being shown to uncoil DNA helical strands [314–317]. Alternatives to CdSe or CdTe are QDs made from silver-selenide (700-820 nm emission) or silver-sulphur (1060 nm emission) or sulphur-zinc sulphide (1155 nm emission) [318–320], indium-arsenic with zinc-selenide or CdSe (all 700-900 nm emission) [321–323],

or (indium-phosphorous)-(zinc-sulphide) (emission 620 nm) [324,325]. These alternatives are not as common as the CdSe or CdTe QDs though, and since CdSe or CdTe are cytotoxic an in depth discussion of these types of QDs are not included in this work; CdSe or CdTe will only be discussed briefly in terms of magnetic QDs (MQDs), where CdSe and CdTe are very important.

MQDs can be synthesised by either doping conventional QDs (for example CdSe, indium phosphorous or CdTe) with metal elements (for example with manganese [326], chromium [327], cobalt [328], nickel [329], or gadolinium [330]) or by encasing conventional QDs with magnetite [331] or maghemite [332] in silica spheres. These MQDs possess the photoluminescent (PL) properties of conventional QDs and the magnetic properties of the doping agent or the encapsulated IO, but they contain the cytotoxic compounds CdSe or CdTe and therefore cannot be called biocompatible without a passivation coating. An example of passivation would be the amino-PEG and carboxyl-PEG used on Ni doped CdTeSe-CdS that greatly improved the biocompatibility of the QDs, allowing for the MQDs to be used for cell sorting and imaging [329]. MQDs were shown to be suitable for M.R.I. imaging, with studies on Mn doped CdSe-ZnS [333] and Gd doped CdSe [330] showing that they were a suitable M.R.I. contrast agent as well as possessing PL properties (emission ~570-580 nm). MQDs were investigated as drug delivery carriers, with MQDs consisting of magnetite and CdSe-ZnS in a silica sphere bonded to ibuprofen, with the drug released fully over 80 h [334].

A second type of QDs are those derived from carbon, such as carbohydrates [15], nanodiamonds [335], and graphene [217,336–338]. Graphene QDs (GQDs) can be created by ultrasonication [336], chemical reduction [337], photo-reduction [338], and hydrothermal cutting [217]. These carbon QDs emit the same level of luminescence as the cadmium QDs, but do not carry the same cytotoxic risk and therefore can potentially be used by the biomedical industry.

The main use for QDs in the biomedical industry is for *in vivo* imaging. It has been shown that GQDs could enter cells but did not enter the nucleus of stem cells during *in vitro* tests; they maintained a high (80%) viability for neurosphere and pancreas progenitor cells up to 100 µg ml^{-1} after 72 h, and could image neurospheres (Figure 2.16 A-B), pancreas progenitor cells (Figure 2.16 C-D), and cardiac progenitor cells (Figure 2.16 E-F) successfully under 405 nm wavelength irradiation [309]. *In vitro* imaging of HeLa cells have been reported from carbohydrate derived carbon dots [15], as well as *in vitro* imaging of N1H-3T3 cells using nanodiamond derived carbon dots, in which the author noted that they entered cells and stayed in the cytoplasm [335]. GQDs were also shown to enter the cell membrane and cytoplasm of A549 cells during *in vitro* imaging [338]. Carboxylated GQDs caused no acute toxicity to rats after 22 days post injection at a concentration of 10 mg kg^{-1} and were shown to image *in vitro* KB cancer cell lines and *in vivo* KB tumours in mice, which allowed for the imaging of the tumour as well as the liver, kidney, spleen, heart and lung [339]. The carboxylated GQDs maintained a high (80%) cell viability of various cell lines up to a concentration of 500 µg ml^{-1} and noticed no acute toxicity within rats when haemoglobin, white blood cells, and platelet levels as well as urea levels were analysed after 22 days post injection with 10 mg kg^{-1} of GQDs [339]. Carbon QDs can be excreted rapidly from the body after being administered through intravenous, intramuscular or subcutaneous injections [340].

Further protection for cells against the effects of QDs can be acquired from passivation; the cell viability of nanoparticles can be improved upon by coating with a biocompatible organic compound. Polydopamine coated GQDs were shown to be distributed into the main organs (liver, lung, heart, spleen and the kidney) after 4 h and to circulate longer in the system than uncoated GQDs allowing for longer *in vivo* imaging [341]. Amine functionalised GQDs [337] significantly improved the cell viability of GQDs. Passivation of conventional QDs has reduced their cytotoxicity, with CdSe QDs being treated with lactose [342] and with PEG [343–

346] to lower cytotoxicity. Lactose coated CdSeS-ZnS QDs showed no noticeable cytotoxic effect after 24 h when HeLa cells were treated with 0.5 mg ml^{-1} [342].

2.5 Polymer nanocomposites

2.5.1 Introduction to polymer nanocomposites

A good definition of a composite is given by Hull et al. [347] in their book, which states that a composite consists of at least two (i.e. the matrix and the filler) physically distinct and mechanically separable materials which, when combined together by dispersing the filler in the matrix, gives the composite material optimised properties that are superior to or distinctive from the properties of either of the individual constituents. An example of a property that might be improved is the mechanical properties of a polymer by using strong and stiff carbon fibre to reinforce the polymer [348].

A "nanocomposite" is a composite where the filler component is a nanoparticle, such as GO [190], montmorillonite clay [349], CNTs [350], or IO [351]. These nanocomposites have found use as structural materials, in biomedical applications such as drug delivery and scaffolds, and as conductive materials for energy storage or electromagnetic interference shielding [352–358]. Nanoparticles can make highly effective fillers for polymer composites for a number of reasons: as they are exfoliated, nanometre size nanoparticles, they possess a much larger specific surface area than the micro-scale fillers [359–361], allowing for a much larger interfacial zone than what can be achieved with a micro-scale filler, therefore maximising the interactions between the filler and the matrix as well as the load transfer between the matrix and the filler. Nanoparticles can have their functional groups tailored to specific polymers, in order to increase the bond strength between the polymer and the nanoparticle [362].

Improvements in mechanical properties can be achieved with a lower weight percentage (wt.%) of nanofiller than with micro-scale filler, making the resultant nanocomposite lighter

than a conventional composite [360,361]. The addition of a small amount of nanoparticles may also improve the thermal and electrical conductivity and/or the barrier properties of the polymer matrix [363–365].

2.5.2 Processing of polymer nanocomposites

There are three main ways to prepare nanocomposites; solvent processing, melt processing, and in-situ polymerisation. Solvent processing of nanocomposites involves the stirring and dispersion of nanoparticles into a solvent, mixing this solvent-nanoparticle suspension under high shear stresses into a low-viscosity polymer-solvent solution, casting the suspension into a mould of the required shape, and the subsequent drying of the suspension and hot pressing where necessary to form the desired form (i.e. a film, test specimens, etc.) [366]. Polymers that have been used to create nanocomposites through this method include PVA [367,368], gelatin [369–371], thermoplastic polyurethane [372,373], polystyrene (PS) [374], and poly(methyl methacrylate) (PMMA) [375].

Melt processing involves the dispersion by shear mixing of nanoparticles in powder form into a molten polymer within a heated extruder [366]. The resultant nanocomposite can then be processed using other means, like injection moulding. Due to the higher viscosity of the molten polymer, the dispersion of the nanoparticle within the matrix may be poorer than what was achieved with solvent processing, but melt processing is quicker, easier to scale up to industrial levels of production and does not involve the use of solvents [366]. Examples of nanocomposites formed by melt processing are poly(ethylene terephthalate)-clay (PET) [376], polyamide-clay [377], polyester-GO [378], polycarbonate-GO [379], and thermoplastic polyurethane-clay [380]. Nanoparticles such as GO may, however, be unintentionally reduced to rGO by the high temperatures used within melt processing, limiting the functional groups of the GO/rGO available for bonding between the polymer and the graphene in some cases [381].

In-situ polymerisation can be used to prepare nanocomposites, where the nanoparticles are dispersed within the monomers or precursor polymer and an initiator/curing agent is added [366]. Typically, energy in the form of heat (or light for photo polymerisation) is a requirement for the polymerisation to occur. Examples of in-situ polymerisation nanocomposites are PMMA-GO [382], PS-GO [383], PS-clay [384], or PVA-clay [385] nanocomposites. Thermosetting polymer-graphene nanocomposites can also be produced using this method. For example, epoxy-graphene nanocomposites were prepared by adding curing agents to a suspension of epoxy resin and GO [386].

Depending on the application of the nanocomposite, some of these production methods may not be suitable. For example, if the nanocomposite is to be used for drug delivery purposes such as in this thesis, then the use of high temperatures may damage the drug that was present. In this instance, the best production method might be to use a thermoplastic polymer that is soluble in water or another suitable non-toxic solvent, preferably at a low temperature.

2.5.3 Polymer-graphene nanocomposites

The benefits of using nanoparticles as the nanofiller for a nanocomposite were discussed in Section 2.5.1. Polymer-graphene nanocomposites can have improved mechanical properties (such as improved Young's modulus (E), ultimate tensile strength (UTS), elongation to break (ε_b), and energy to break), electrical conductivity (C_{elec}), thermal conductivity, and permeability properties than their pristine polymer counterparts [352,366]; this is because graphene and its derivatives make promising nanofillers as they have high aspect ratios, high surface area and a high E, high electrical conductivity, and high thermal conductivity [160,176–179].

Table 2.2: Percentage improvements in mechanical properties of polymer-graphene nanocomposites relative to the pristine polymer

Polymer	Graphene (wt.%)	E / %	UTS / %	ε_b / %	Ref.
PVA	rGO (0.7 wt.%)	48.4	46.7	-39.3	[387]
PVA	GO (3.5 wt.%)	44.7	324	-78.8	[388]
PVA	GO (5 wt.%)	46.1	290	-33.1	[367]
Cellulose	GO (0.2 wt.%)	7.2	50.0	-	[389]
Polycarbonate	rGO (0.25 wt.%)	11.1	3.8	-	[390]
Polyimide (PI)	GO (5 wt.%)	1761	1211	-76.3	[363]
PI	rGO (5 wt.%)	1265	985	-73.5	[363]
PI	rGO (5 wt.%)	803	699	-71.3	[363]
PI	rGO (5 wt.%)	635	450	-78.2	[363]
Bisphenol-A epoxy	Graphene (0.1 wt.%)	33.9	45.5	-	[386]
E44 epoxy	GO (2 wt.%)	116	-	-	[391]
Epon 828 epoxy	GO (0.4 wt.%)	59.9	54.1	-	[392]
Polyethylene (PE)	GO (0.5 wt.%)	-	0.5	1.8	[393]
PET	Graphene (0.08 wt.%)	22.9	42.3	19.0	[394]
PCL	rGO (5 wt.%)	109	30.1	-74.4	[395]
Chitosan	GO (1 wt.%)	18.3	36.0	110	[396]
Chitosan	GO (2.5 wt.%)	33.0	36.1	51.2	[396]
Chitosan	GO (1 wt.%)	51.3	92.7	40.4	[397]
Chitosan	GO (1 wt.%)	64.3	122	57.0	[398]
Chitosan	rGO (1 wt.%)	61.5	20.6	-55.3	[209]
Chitosan	rGO (1 wt.%)	17.2	3.3	-10.5	[399]
Gelatin	GO (1 wt.%)	64.9	83.9	47.2	[369]
Gelatin	GO (2 wt.%)	100	86.7	43.2	[369]
PLA	GO (1 wt.%)	20.5	51.9	18.7	[400]
PLA	GO (2 wt.%)	59.6	27.5	-21.8	[400]

Table 2.2 shows some examples of changes in E, UTS, and ε_b for polymer-graphene nanocomposites at their optimum wt.% of graphene, relative to their pristine polymer. In general, the highest E and UTS occur for a nanocomposite when there is a good dispersion of graphene within the polymer, a strong interface between the graphene and the polymer, and the

optimum wt.% of graphene has been achieved, as discussed in Section 2.5.1. An example of where the importance of dispersion and a strong interface to mechanical properties is the study on PI-GO and PI-rGO nanocomposites [363]; Ha et al. [363] state that the better mechanical properties of the PI-GO in comparison to PI-rGO are due to the higher concentration of functional groups on GO that creates a strong interface between the two constituents and can also improve the dispersion of the nanoparticles within PI by restricting phase separation of the two constituents. As the reduction degree increases for the different types of rGO used in that study, the percentage improvement relative to pristine for the mechanical properties decreases [363].

Also of importance to the mechanical properties of a nanocomposite is the E of graphene, with the different graphene derivatives having different mechanical properties, as discussed in Section 2.4.2. Istrate et al. [394] report that a very low concentration (0.08 wt.%) of pristine graphene can improve the mechanical properties of PET, with a 22.9% increase in E, 42.3% increase in UTS, and a 19.0% increase in ε_b relative to pristine PET. A similar increase in E and UTS for GO/rGO nanocomposites typically required a higher wt.%, such as 1 wt.% GO [396,400] or 0.7 wt.% rGO [387].

Within a nanocomposite, stresses applied to the polymer matrix can be transferred to the graphene when there is a strong interfacial bond between the polymer matrix and the graphene [401], utilising the superior mechanical properties of the graphene. For polymer-graphene nanocomposites, the ε_b may change relative to the pristine polymer. An increase of the ε_b may be explained by the ability of the graphene to realign and translate with the polymer chains when the nanocomposite is under stress [369,400]; the graphene within the nanocomposite has retained its mobility within the matrix. A decrease in the ε_b may be explained by the inability of the graphene to translate and realign with the chains [369,400], a

51

poor bonding interface between the graphene and the polymer [363,402], or by possible

aggregation of the graphene in the polymer matrix.

Table 2.3: The electrical properties of polymer-graphene nanocomposites.

Polymer	Graphene	0 wt.% C_{elec} / S m^{-1}	Max. obtained C_{elec} / S m^{-1}	Percolation threshold / wt.%	Ref.
PMMA	rGO	-	0.1 at 1 wt.%	0.2	[382]
Polypropylene (PP)	rGO	-	0.3 at 4.9 wt.%	4.9	[403]
PP	rGO	1×10^{-9}	0.08 at 0.2 vol.%	0.033 (vol.%)	[404]
PS	rGO	6.7×10^{-14}	3.49 at 1.1 vol.%	0.0075 (vol.%)	[405]
PS	rGO	1×10^{-10}	0.029 at 2 wt.%	2.0	[383]
PE	rGO	2×10^{-13}	2.11 at 3 vol.%	0.47 (vol.%)	[406]
PCL	rGO	1×10^{-11}	1×10^{-4} at 8 wt.%	0.5	[407]
PI	rGO	1×10^{-13}	1.4×10^{-4} at 5 wt.%	-	[363]
PI	rGO	1×10^{-13}	3.3×10^{-2} at 5 wt.%	-	[363]
PI	rGO	1×10^{-13}	3.3×10^{-1} at 5 wt.%	0.45 (vol.%)	[363]
PI	GO	1×10^{-13}	6.2×10^{-5} at 5 wt.%	0.45 (vol.%)	[363]

Graphene can improve the electrical conductivity of a nanocomposite, in comparison

to the pristine polymer. Pristine graphene has excellent electrical properties, as discussed

previously in Section 2.4.2, and a relatively small wt.% of graphene is capable of forming a

conductive network through the polymer matrix to turn an insulating, pristine polymer into a

conductive nanocomposite; this wt.% is termed the percolation threshold, p_c [366,408]. Potts

et al. [366] state that the percolation threshold for a nanocomposite is dependent on the

nanoparticle shape and size, the quality of its dispersion/distribution within the polymer, and

the volume fraction of the nanoparticle. A review of electrical conductivity increases is shown

in Table 2.3 that shows considerable increases in conductivity for nanocomposites containing

graphene derivatives, when compared to the pristine polymer. The highest increases in

conductivity were achieved by using conductive rGO that were well dispersed within the

polymer at a high enough concentration to establish a percolation network. For example, 0.2

vol.% of rGO increased the conductivity of polypropylene by about seven orders of magnitude, with a percolation threshold at 0.033 vol.% [404]. Similarly, 5 wt.% of ascorbic acid reduced rGO increased the conductivity of PI by about twelve orders of magnitude [363]. In the same work, the less-conductive GO also increased the conductivity of PI at a 5 wt.% loading of GO by about eight orders of magnitude over pristine PI, showing that the electrically conductive rGO nanoparticle increased the conductivity of the polymer by more than GO. As discussed previously in Section 2.4.2, GO has a significantly lower conductivity value than pristine graphene or rGO, being effectively an electrical insulator.

A dispersion of large-aspect ratio nanoparticles within a nanocomposite may decrease the permeability of the nanocomposite to gases and liquids, in comparison to pristine polymers [409–412]. This dispersion of nanoparticles may reduce the permeation through polymers courtesy of the "tortuous path" model [413]; the nanoparticles impede the permeation of molecules directly through the polymer matrix and the molecules must go around the nanoparticles in order to permeate fully through the nanocomposite. To improve the barrier properties of a nanocomposite, nanoparticles should possess a high aspect ratio and should be well exfoliated and dispersed throughout the polymer matrix [364,413]. The permeability of nitrogen through polyurethane decreased by 90% with the addition of 3 wt.% rGO [372], the permeability of hydrogen through PEI with the addition of rGO [414], and the permeability of moisture through PI from 181 g mm^{-2} day^{-1} to 31 g mm^{-2} day^{-1} with the addition of 0.001 wt.% GO [415]. The permeation of oxygen and water vapour reduced by 98% and 68%, respectively, for PVA-GO at 0.72 vol.% GO loading in comparison to pristine PVA [364]. A PS-GO nanocomposite of 0.02 vol.% GO could reduce the permeability of oxygen by ~35% in comparison to pristine PS [416]. A loading of 2.27 vol.% reduced oxygen permeability from ~1000 cm^3 m^{-2} day^{-1} to 380 cm^3 m^{-2} day^{-1}.

2.5.4 Polymer-iron oxide nanocomposites

IO is not a common nanoparticle for use within a nanocomposite, but the previous work suggests that polymer-IO nanocomposites retain the superparamagnetic properties of the IO nanoparticles, as noted with PMMA-polypyrrole-IO [417], 'Nafion 117'-IO [418], PMMA-IO [351], and PVA-IO [419] nanocomposites. The encapsulation of IO can increase the electrical conductivity of the nanocomposites such as poly(3,4-ethylenedioxythiophene)/poly(styrene sulfonate)-IO [420,421] and PMMA-polypyrrole-IO [417].

Limited studies of polymer-IO nanocomposites for structural applications exist, but it was shown that a polyphenylene oxide-IO nanocomposite with a 10 wt.% loading of IO had a 10.4% higher UTS than the pristine polymer [422]; the ε_b decreased at this loading in comparison to the pristine polymer by 26.5%, which the authors believe was due to the restricted movement of the polymer chains due to the increasing adherence of the polymer chains to the IO. Similar decreases (~20%) in the ε_b were noted for PI-IO nanocomposites of 1-3 wt.%, in comparison to pristine PI, but contrary to the previous report, the UTS also decreased by ~8% [423]. The authors suggested that the poorer mechanical properties may be because of IO aggregation and a poor interfacial interaction between the IO and the PI [423]. PVA-IO nanocomposites of 1.2 wt.% and 2.4 wt.% possessed the same E as pristine PVA, but had lower ε_b and energy to break than the pristine polymer [424]. The ε_b decreased by 20% for the 1.2 wt.% nanocomposite, and ~60% for the 2.4 wt.% nanocomposite, similar to the other reviews of polymer-IO nanocomposites [422,423]. The UTS of the 2.4 wt.% nanocomposite did not change in comparison to the pristine polymer, but the 1.2 wt.% nanocomposite reduced by ~10% [424]. The storage modulus of ethylene vinyl acetate-IO nanocomposites and the resistance to thermal degradation both increased as the loading of IO increased, relative to the pristine polymer [425].

2.5.5 Polymer-quantum dot nanocomposites

Polymer composites containing QDs focus mainly on the PL properties of the QDs within the nanocomposite. Polymer-QDs nanocomposites retain the PL behaviour of the QDs, such as CdS in PET [426], CdTe in PVA [427,428], CdSe/zinc-sulphur in PVA [428], and other polymer-QDs nanocomposites [429–433], allowing for the transparent and PL films to be used for optoelectronic devices. McDonald et al. [434] reported that lead-sulphur QDs in poly(2-methoxy-5-(2'-ethylhexyloxy-p-phenylenevinylene)) can be used to convert NIR light into energy and act as a nanocomposite photovoltaic device, with a 3 fold increase in internal quantum efficiency over previous thin film studies. Zhu et al. [435] demonstrated a temperature-dependent fluorescent emission from a flexible and transparent poly(ether ether ketone)-CdSe/zinc-sulphur nanocomposite film.

PVA nanocomposites containing 6 wt.% zinc-oxide QDs possessed 3.9 times higher E, a 2.8 times higher toughness to break, a 87% increase in the ε_b, and a 86% higher UTS than the pristine PVA [436]. Poly(styrene-butadiene-styrene)-1 wt.% CdTe QDs nanocomposites possessed a 4% increase in the ε_b and a 27% higher UTS than the pristine poly(styrene-butadiene-styrene), whilst retaining the PL behaviour of the QDs [437]. PMMA with a 6 wt.% CdS QDs loading possessed a 47% higher E and a 57% higher UTS than the pristine PMMA [438]. Contrary to the previous results, the presence of CdSe-CdS QDs in PLA affected the mechanical properties of the nanocomposite [439], which the authors suggest is due to a poor interface between the PLA and the QDs. A 3.6 wt.% loaded PLA nanocomposite possessed 23% lower E, a 9% lower toughness to break, a 20% increase in the ε_b, and a 35% lower UTS than the pristine PLA [439]. The PLA-(CdSe-CdS) QD nanocomposites did, however, retain the PL behaviour of the CdSe-CdS QDs.

2.6 Chitosan and chitosan-graphene nanocomposites

2.6.1 Introduction to chitosan
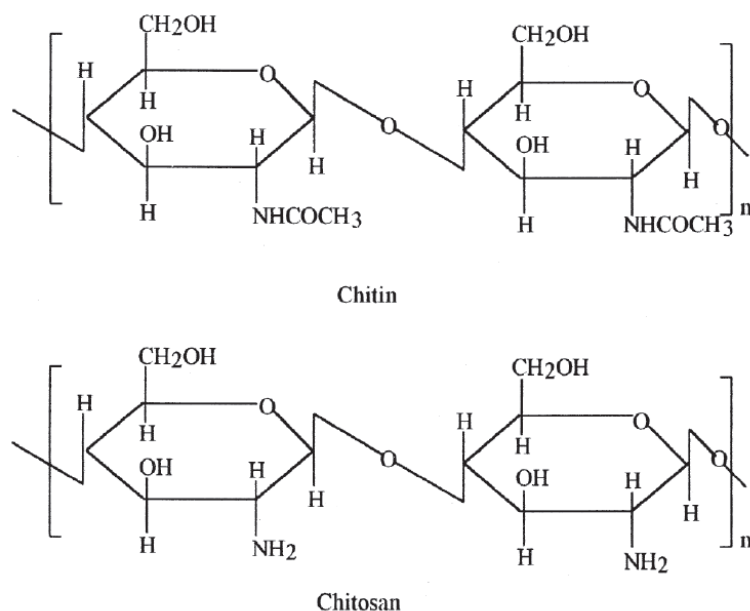
Figure 2.17: Chemical structure of the polymer chitin and the derivative chitosan. Adapted from Ravi Kumar et al. [440] with permission from Elsevier Limited, copyright 2000.

The polymer used within this project is chitosan, chosen because it is strong, biocompatible, enzymatically degradable, and simple to process into a desired shape without extreme heat or toxic solvents [441,442]. Chitosan, commonly denoted as linear (1-4)-2-amino-2-deoxy-β-D-glucan, is a cationic polysaccharide and a derivative of chitin (the material that makes up the shells and exoskeletons of some sea crustaceans and of some insects) [441,443,444]. Chitosan is processed from chitin by a deacetylation process using concentrated sodium hydroxide [441]. Figure 2.17 shows the chemical structure of chitosan, with NH_2 amine and CH_2OH hydroxy-methyl groups visible. Chitosan possesses an orthorhombic unit cell structure, with four glucosamine units per unit cell [441,445]. The dimensions (a, b, c) of the unit cell are 0.828 nm, 0.862 nm, and 1.043 nm [441,446]. Chitosan is soluble in certain acidic solutions (such as acetic, lactic, citric, and ascorbic acid), due to the protonation of the amine group when exposed to an acidic solution [440,441,443,444]. This gentle manufacturing process is important if the

56

chitosan is to be used for drug release applications like microneedle arrays. Extreme heat, toxic chemicals or irradiation may damage delicate drugs, like DNA/RNA gene therapeutics, within the microneedle arrays.

Chitosan is a polymer that can be degraded by *in vivo* conditions [447]. Degradation of polymers can occur through photo-degradation, thermal degradation, mechanical degradation, or through chemical degradation and typically result in bond scission or chemical transformations of the polymer [448]. Photo-degradation occurs through the absorption of UV light or γ-irradiation by the polymer, which can raise the electrons of molecules within the polymer to a higher electronic state; this can cause the oxidation of the polymer and bond cleavage. Thermal degradation can lead to the scission of polymer bonds along the polymer chain. Mechanical action, such as stretching or bending, can cause the mechanical degradation of the polymer and lead to crazing, cracking and delamination of the polymer. Chemical degradation, an important degradation route for *in vivo* application, occurs via the hydrolysis scission of the polymer backbone through ingression by water or it can be catalysed by acid [448]. The degradation of chitosan can be catalysed by acids that can use either free radical or oxidation routes to degrade chitosan [447], but more commonly chitosan is degraded through enzymes (either lysozyme or chitosanases) via the hydrolysis of the β-glycosidic linkages between the acetyl units [447]. Lysozyme can be found naturally in blood plasma and urine [449]. Funkhouser et al. [450] reported that the human DNA has 8 glycoside hydrolase 18 (GH18) chitanases / chitosanases that can degrade chitosan or chitin in the body. The presence of molecules that can degrade chitosan is important as the chitosan within the microneedle array may enter the body and may need to be degraded and excreted.

Onishi [451] showed that chitosan could be excreted from the body, with the excreted chitosan of a reduced MWt relative to the original chitosan. Chitosan was found not to accumulate in the liver, spleen, or blood plasma. The chitosan was excreted through the kidney

via urine and complete excretion was achieved within 12 h of the chitosan dose being administered. Richardson et al. [452] also reported rapid clearance from the blood, with only 32.2% of the original dose remaining after 1 h. Chitosan showed no cytotoxicity to human lymphoblastic leukaemia and human embryonic lung cells in an *in vivo* experiment and no haemolysis effect within solutions of chitosan and red blood cells [452]. Blood tests by Rao et al. [442] showed that no haemolysis effect was noted during their tests; also, a skin and eye irritation test showed no irritation to the chitosan solution for the test animal.

Chitosan has been studied for biomedical applications such as to stimulate the formation of blood clots [441,442]. Chitosan nanoparticles have delivered the drugs tamoxifen [453,454], endoxifen [453], paclitaxel [455], and epirubicin [456], as well as others [457–461] and have been studied as a potential gene transfer agent [462]. In these works, it was noted that chitosan nanoparticles could enter and be retained within cells [455,457,458] and that the nanoparticles have a pH sensitive release of the therapeutic [454,455,460]. Methotrexate, bonded to chitosan nanoparticles, could be delivered to the brain through the blood-brain barrier [463]. Chitosan microspheres containing furosemide [464], mitoxantrone [465] and sodium diclofenac [466] were studied, with the chitosan-sodium diclofenac microspheres showing pH sensitive release that would allow for colon specific release of the drug. Chitosan micelles were used to contain the hydrophobic drug paclitaxel [467] and 6-mercaptopurine [468]; the 6-mercaptopurine release from the chitosan micelle was dependent on the local concentration of glutathione, a feature that made it effective against HL-60 human promeloytic leukaemia cells [468]. Chitosan chains could also be directly conjugated to drugs like exendin-4 [469], insulin [470], and paclitaxel [471] for oral administration and with the anti-HIV drug d4T Stavudine [472].

Chitosan hydrogels were used to study the release of lidocaine and LH [473], and the encapsulation of BSA [474], methotrexate [463], heparin sodium, LH, metronidazole,

hydrocortisone, clotrimazole, estradiol, progesterone and piroxicam [475]. BSA had a pH sensitive release from a chitosan hydrogel that would allow for the site specific delivery of the drug into the intestines [474]. Ishihara et al. [476] used a chitosan hydrogel to encapsulate fibroblast growth factors and heparin, and showed that the therapeutics could be released from the hydrogel into mice. Chitosan films were created that encapsulated nifedipine [477] and calcein and BSA [478]. Oral tablets made from compressed, powdered chitosan were developed with pH sensitivity for the delivery of timolol maleate, ephedrine, propranolol hydrochloride, acetylsalicylic acid, naproxen, sulphadiazine, indomethacin and pindolol [479], insulin [480], and indomethacin [481].

2.6.2 Chitosan-graphene nanocomposites

Chitosan has been used previously as the polymer matrix to form chitosan-graphene nanocomposites [209,396,397,399,482]. The processing of the chitosan-graphene nanocomposites would typically involve the dispersion of the nanoparticles in water to form a suspension; this suspension is then stirred into a dilute acetic acid suspension [209,396,397,399,482]. Chitosan is fully soluble in acidic solutions (such as acetic, lactic, citric, and ascorbic acid) [440,441,443,444]. This chitosan-graphene suspension is then poured into a mould and allowed to dry and solidify to the required shape.

Chitosan-graphene nanocomposites show improved mechanical strength over pristine chitosan [209,396,397,399,482]. Section 2.5.1 discussed the properties that make graphene an efficient nanofiller, i.e. high aspect ratios, high surface area and a high E, and Section 2.5.3 discussed previous studies on polymer-graphene nanocomposites and how graphene could improve the properties of the nanocomposites. It can be seen from Table 2.2 that chitosan-GO nanocomposites show increases in E, UTS and ε_b over pristine chitosan [396–398]; chitosan-rGO nanocomposites show increases for E and UTS but a decrease for the ε_b [209,399], which will be discussed below.

The increases in E and UTS vary from report to report presumably due to the different types of chitosan used, with MWt and deacetylation degrees varying for each work. For example, chitosan of 95% deacetylation and MWt of 600,000 Da was used in a nanocomposite that showed 18.3%, 36.0% and 110% increases in E, UTS and ε_b respectively [396], but chitosan with 87% deacetylation and MWt of 186,000 Da showed 51.3%, 92.7% and 40.4% increases in E, UTS and ε_b respectively [397], despite the nanocomposites containing the same 1 wt.% of GO and using the same preparation procedure to make the nanocomposite. This can make the comparison between chitosan-based nanocomposites difficult as the molecular weight and crystallinity can affect the material properties, such as mechanical strength [483], electrical conductivity [484], and degradation behaviour [115,447,485,486]. Nevertheless, it can be seen from the increases in E and UTS that graphene can act as a suitable stress transfer agent within chitosan when there is a strong bond interface (in the case of chitosan-GO, the bonding was hydrogen bonding [396,397,482]) between the two and there is an adequate dispersion of the graphene.

For the chitosan-GO nanocomposites, the increase in ε_b can be associated with the mobility of the GO within the chitosan; the GO can realign and translate within the chitosan when the nanocomposite is under stress [369,400]. For the chitosan-rGO nanocomposites, the rGO cannot realign under stress and the nanocomposites become more brittle than the chitosan-GO nanocomposites, which possibly is due to a reduction in the quantity of functional groups on rGO compared to GO which will reduce the bonding interaction between a polymer and the rGO [363].

It was reported that the addition of GO to chitosan would afford the chitosan nanocomposite better mechanical rigidity and a better resistance to solubility when submerged in water than pristine chitosan [482]; this was attributed by the authors to GO increasing the stability of the film by decreasing the interaction between water molecules and the hydroxyl

groups of chitosan. Chitosan-rGO showed a higher resistance to acidic conditions than pristine chitosan by resisting dissolution in acetic acid conditions that caused the dissolution of pristine chitosan [209]; this was attributed by the authors to the rGO acting as a physical cross linker between the chitosan chains, stopping the chains from entering solution despite the protonation of the amine groups. Decreasing the susceptibility of the nanocomposite to water/acid ingression and weakening is important if chitosan-GO nanocomposites are to be used for structural purposes.

Other notable studies on chitosan-GO nanocomposites have shown that the nanocomposites are biocompatible and are not cytotoxic; chitosan-GO nanocomposites with up to 6 wt.% GO were shown to be biocompatible with murine osteoblasts, with the addition of GO improving the proliferation of the cells and lowering the cytotoxicity to the cells, relative to pristine chitosan [398]. Similar results were noted for chitosan and pristine graphene nanocomposites, where the cell viability tests showed that nanocomposite with a 0.6 wt.% loading of graphene has a similar cytotoxicity to pristine chitosan when incubation times were 48 h [487], and where a chitosan-PVA-GO nanocomposite with 1 wt.% GO loading showed similar biocompatibility to pristine chitosan and the proliferation of the cells after 7 days was highest for the nanocomposite containing 6 wt.% GO [488]. A chitosan-GO aerogel was created by freeze-drying an aqueous solution of chitosan-GO, and this aerogel possessed a high porosity (a nanocomposite aerogel with 3 wt.% GO had a porosity of ~80%) and could be used to absorb doxorubin [489]. The subsequent release of doxorubicin was found to be pH sensitive, with a faster release in acidic conditions. Chitosan-GO nanocomposites could potentially work as an electrochemical biosensor, with the cyclic voltammetry results dependent upon the wt.% of GO [490].

2.7 Characterisation techniques

During this thesis project, the nanoparticles and the nanocomposites were characterised in terms of mechanical properties, chemical properties, physical properties, and biological properties.

2.7.1 Mechanical properties

Chitosan-graphene nanocomposites, cut into dog-bone shaped specimens, were tensile tested to determine their Young's modulus, their elongation to break, and their ultimate tensile strength. Microneedles were compression tested between two metal platens to determine the force required to fail the microneedle arrays.

2.7.2 Chemical properties

The chemical properties, such as bond type and chemical analysis, were studied for chitosan-graphene nanocomposites and for graphene nanoparticles through molecular spectroscopy, the study of how the internal energy of a molecule is affected by the absorption or emission of an applied, external electromagnetic radiation [491]. Fourier transform infrared (FTIR) spectroscopy is the study of the change in vibration-induced electric dipole moment of a molecule [492]. Raman spectroscopy is the study of the change in polarisability of a molecule, caused by a rotational-vibrational motion [491]. UV-Vis spectroscopy is a measure of the electronic changes of a molecule when a valence electron increases its orbit due to it absorbing an irradiation source in the visible or UV region (190 to 800 nm wavelength) [491,492]. PL spectroscopy is the study of electronically excited molecules that lose vibrational energy but maintain acquired electronic energy, and subsequently proceed to release this electronic energy to return to the ground electronic state; this electronic energy is released as a longer wavelength radiation energy than the original radiation energy [491]. Energy dispersive spectrometry (EDS), a by-product of transmission electron microscopy imaging, is the identification of

characteristic x-ray emissions from an irradiated atom due to inelastic scattering of an incident electron by an electron in an atom in a sample [493].

2.7.3 Physical properties

The physical properties, such as crystalline structure, nanofiller dispersion and the surface topography, of chitosan-graphene nanocomposites and graphene nanoparticles were assessed. X-ray diffraction (XRD) was used to investigate the crystalline structure of nanoparticles and chitosan nanocomposites; this was achieved by identifying the angles of incidence (Bragg angles, θ) that were produced by constructively interfered waves of irradiation passing through the test sample [493]. TEM uses a beam of condensed and focused electrons to irradiate and pass through a thin specimen, during which the TEM can selectively allow only transmitted electrons through to the imaging apparatus to give a brightfield image of the test specimen, the type of imaging used in this thesis [493,494]. In scanning electron microscopy (SEM), the condensed and focused electron beam does not pass through the sample but is simply scanned over the sample surface in a raster fashion, interacting with the atoms on and just below the surface within an "interaction volume" and producing the secondary electrons that are used to image the surface of the sample [494,495]. AFM measures the physical interaction of a tip with the specimen surface while the tip is scanned along the surface of the sample in a raster fashion, i.e. the tip moves along a horizontal scan line [496].

2.7.4 Biological properties

Biological properties, such as the enzymatic degradation of polymers and the cytotoxicity of graphene nanoparticles, were studied. The enzymatic degradation of chitosan and chitosan-graphene nanocomposites by an aqueous lysozyme solution was studied [497]. The cytotoxicity of graphene towards specific cell lines were analysed by MTT (3-[4,5-dimethylthiazol-2-yl]-2,5- diphenyltetrazolium bromide) assay; cells that were incubated with graphene were treated with the tetrazolium salt solution which metabolises in the presence of

viable cells to a formazan, the concentration of which can be measured through UV-Vis spectroscopy.

2.8 Summary of the literature review

Currently, the main therapeutic delivery devices used are hypodermic syringes and perioral tablets; these devices have disadvantages that include poor patient compliance, poor bioavailability and poor delivery performance. A very promising alternative was shown to be transdermal drug delivery. This is the delivery of drugs through the dermal layers to the viable epidermis, an area rich in blood vessels and antigen presenting cells that can provide a strong immune response to therapeutics. The microneedle array was shown to be particularly promising as a transdermal drug delivery device as it is painless when compared to most other delivery routes and it can offer both dose sparing and a quicker immune response when compared to the current therapeutic routes. Recent developments in microneedle array design, such as the change from metal/ceramic based arrays to biodegradable polymer based arrays, were reviewed and the studies on their drug delivery performance were promising, therefore microneedle arrays were chosen to be developed further in this project.

After reviewing the microneedle array, it was determined that microneedle arrays currently lack functionality, such as the ability to encapsulate drugs within the microneedle array itself and to stimulate/control their release, the ability to target the drug to key sites within the body to maximise efficiency, and the ability to track/monitor the drug *in vivo* once released from the microneedle array. It was determined that nanoparticles, when bound to the drug and encapsulated within a polymer, would add these abilities to microneedle arrays. Recent advances in nanoparticle-assisted drug delivery were critically analysed, in which nanoparticles have been used to intelligently deliver drugs to specific sites of the body. Of particular interest within this thesis were graphene and iron oxide, with graphene of interest to drug delivery applications because of the large specific surface area and abundant functional

groups to bond drugs to. Iron oxide is of interest due to its intrinsic magnetic properties that allow for M.R.I. imaging and targeting by an external force. The effect that nanoparticles can have *in vivo* was examined, with key findings from recent papers on nanoparticle cytotoxicity, the distribution of the nanoparticles during the treatment, and the excretion route discussed. As these drug-bound nanoparticles will be encapsulated within a polymer, the ability of nanoparticles to improve the mechanical and electrical conductivity properties of polymers was researched.

The polymer chosen for use within a microneedle array needed to be degradable, with a desired degradation timescale of 1 or 2 months, to allow for safe disposal after use, biocompatible to prevent complications during use, easy to process to avoid excessive heat or toxic solvents, and mechanically strong as the microneedle array needs to survive insertion into the skin layers. The chosen polymer, chitosan, was analysed for its potential use as the polymer in microneedle arrays and as the matrix within a chitosan-graphene nanocomposite; previous studies on chitosan-graphene nanocomposites were reviewed, as well as recent publications on the toxicity, biodistribution, and excretion paths of chitosan within the body.

Chapter 3. Chitosan-graphene oxide nanocomposites

3.1 Introduction

The focus of this chapter is the development of chitosan-GO nanocomposites that have improved mechanical (with an E of 1-1.5 GPa) and drug release properties (an increase in efficiency and delivery rate), relative to pristine chitosan. The addition of GO to chitosan should improve the mechanical properties of chitosan due to the large aspect ratio of GO and the functional groups on the surface of GO which should promote a strong interface between the chitosan and the GO. The functional groups of GO allow for the bonding of therapeutics to the surface of GO and will aid in the dispersion of GO and bound drug within fluids, which may improve the release of the drug from chitosan.

GO was synthesised by a modified Hummers method and then characterised to determine the functional groups, the crystal structure, and the dimensions and thickness of the nanosheets. A chitosan-GO nanocomposite was created by dispersing GO into water and then dispersing the suspension into a dilute acetic acid suspension. The effects of GO on the mechanical properties and enzymatic degradation rate of chitosan-GO nanocomposites relative to pristine chitosan were investigated. The effect of GO on the drug release profile of chitosan was analysed, as well as the effect of varying the drug loading ratio onto GO. The model drug chosen for this chapter was fluorescein sodium (FL), selected due to its good dispersibility within aqueous mediums and distinct absorption peaks between 450 to 500 nm that would aid with quantitative analysis. The drug was used to study the release rate of small MWt drugs from chitosan-GO nanocomposites.

3.2 Experimental section

3.2.1 Materials

Chitosan powder (MWt = 100,000-300,000, Acros Organics, deacetylation degree $\geq$ 90% as determined by free amine groups) and phosphate buffered saline (PBS) were used as purchased from Fisher Scientific. The following chemicals were used as purchased from Sigma Aldrich; acetic acid (> 99.7%), sulphuric acid (95-98%), hydrogen peroxide (29-32% in H_2O), potassium permanganate (97%), sodium nitrate (> 99%), fluorescein sodium, lysozyme (from chicken egg white, ~100,000 units mg^{-1}) and graphite powder ($\leq$ 20 µm).

3.2.2 Preparation of graphene oxide

GO was synthesized from a modified Hummers method and subsequently purified, exfoliated and freeze dried [186,187]. Briefly, graphite (3 g) was added to sulphuric acid H_2SO_4 (69 ml) and sodium nitrate $NaNO_3$ (1.5 g). The mixture was stirred vigorously for 30 min in an ice bath. Potassium permanganate $KMnO_4$ (9 g) was added slowly, and when fully added the mixture was heated to 35 °C and stirred for 12 h. Potassium permanganate (9 g) was added to the mixture and stirred for 12 h before being poured over a mixture of ice (400 ml) and 30% hydrogen peroxide H_2O_2 (3 ml). The graphite oxide suspension was centrifuged at 8000 rpm for 1 h in an Eppendorf 5804 with the supernatant being discarded. The graphite oxide was dispersed in fresh distilled water for a total of five cycles to remove residue chemicals from the production process. Graphite oxide was dried in a vacuum oven and stored in powder form in a desiccator. When required, graphite oxide was exfoliated in distilled water for 2 h by a Fisherbrand sonication bath (230 V, 50 Hz) and centrifuged at 8000 rpm for 30 min to remove larger than desired particles. The supernatant dispersion was collected and lyophilized in a Labconco FreeZone Triad freeze-dryer to be stored in powder form in a desiccator

3.2.3 Loading of drug onto graphene oxide

Fluorescein sodium powder was added to a 2 wt.% solution of GO in water and stirred for 24 h. Unbound FL in the supernatant was removed from the solution through intense centrifugation at 8000 rpm for 1 h. This process was repeated to ensure the removal of all unbound FL. The FL coated GO (GO-FL) was then re-dispersed in distilled water by stirring for 1 h.

3.2.4 Preparation of chitosan-graphene oxide nanocomposites

Chitosan powder was added to a solution of 2 wt.% acetic acid in distilled water and stirred for 24 h to prepare the chitosan solution. Then, the required concentration (0.25, 0.5, 1, 2, and 5 wt.%) of nanoparticle filler was added to the chitosan solution and mixed for 12 h. The resultant dispersion was degassed in a sonication bath for 30 min. The dispersion was poured into a Teflon mould and allowed to air dry. Prior to testing, film was conditioned in an oven for 1 h at 50 $^{\circ}$C. Drug loaded GO was also used to produce nanocomposites of GO-FL and chitosan using GO-FL nanohybrids containing 2 wt.% GO and various amounts of FL.

3.2.5 Structural characterization of graphene oxide and nanocomposites

FT-IR spectroscopy of nanocomposite films and GO-FL powder was achieved through a Perkin Elmer Spectrum 100 with ATR at a resolution of 1 cm^{-1} and an accumulation of 5 scans. XRD analysis of the crystal structure was achieved by using a Stoe Stadi P with Cu-K$_{\alpha 1}$ irradiation (0.154 nm wavelength) with an Imaging Plate detector. A Veeco Dimension 3100 AFM with Olympus AC160TS probes was used in tapping mode at 0.5 Hz to analyse the thickness and dimensions of GO sheets laid on a mica substrate. Laser scattering (LS) particle sizing of particles from 0.1 to 900 μm was achieved through a Coulter LS130 using 3 one minute runs of nanoparticles in a dispersion of GO (0.4 mg ml^{-1}). TEM analysis was achieved using a F.E.I. Tecnai Biotwin using bright field imaging at an accelerating voltage of 80 kV. TEM samples were prepared using a Reichert-Jung Ultracut E microtome. UV-Vis was performed on

dispersions of nanoparticles by a Perkin Elmer Lambda 900 spectrometer between 200-800 nm at a resolution of 1 nm. A Horiba Fluoromax 4 with excitation source of 480-500 nm (max excitation shown to be 495 nm) and emission readings from 500-600 nm was used for PL spectroscopy (using solutions of 45.6 wt.% loaded GO-FL at 1 mg ml^{-1}, GO at 0.545 mg ml^{-1}, and unbound FL at 0.456 mg ml^{-1}). Zeta potential was measured using a Brookhaven ZetaPALS, with solution concentrations of 1 mg ml^{-1} and 5 cycles of 10 runs per sample. SEM analysis of the gold sputter coated fracture surface of the nanocomposite films was achieved with an F.E.I. Inspect F50 with an accelerating voltage of 5 kV.

3.2.6 Tensile testing of nanocomposites

Tensile testing was performed on a Zwick Roell Z005 twin column tensometer using a 5 kN load cell and a 1 mm min^{-1} strain rate in accordance with ISO-527. Specimens (number (n) = 10) were created using a punch of a dog-bone shape with the narrow test section between grips measuring 22 mm in length, 2.7 mm in width and 1 mm in thickness. The tensometer was calibrated against a stainless steel specimen of the same dimensions as the polymer specimens (Figure 3.S1).

3.2.7 Drug release from nanocomposites

Nanocomposite specimens (n = 5) were placed in a phosphate buffered saline (PBS) solution (30 ml) at 37 $^{\circ}$C to simulate *in vivo* conditions and gently agitated at 100 rpm in a Stuart SI500 shaking incubator. A known quantity (2 ml) of solution from the container was removed after every time step, making sure to replace it with the same amount of fresh PBS solution. UV-Vis in a Perkin Elmer Lambda 900 determined the release rates of the drug from the nanocomposite in neutral (pH = 7.4) and acidic (pH = 2, 5.5, and 6.5) conditions. The quantity of FL was determined by comparing the absorbance peak at 450 nm of the test samples with solutions of

free FL of known concentration (from 0.001 to 1 mg ml^{-1}) in water, similar to the procedure used to measure the quantity of FL in solution during the loading of the drug onto the GO.

3.2.8 Enzymatic degradation tests

Enzymatic degradation tests have been described elsewhere [497,498]. Briefly, the polymer films were submersed in a PBS solution (pH = 7) at 37 $^{\circ}$C containing the enzyme lysozyme at a natural concentration within the body, 1.5 µg ml^{-1} [449,499]. Samples were maintained at 37 $^{\circ}$C and were gently agitated. At regular intervals, each specimen was removed from the beaker, washed with distilled water, dried in a vacuum oven, and the mass measured. The sample was placed into fresh PBS and lysozyme solution to maintain constant enzymatic activity. For each sample type, there were 5 specimens for mass analysis and two sacrificial specimens for characterization analysis.

3.2.9 Statistical analysis

Statistical analysis (standard deviation and 95% confidence intervals) were calculated using MatLab 2012a software.

3.3 Results and discussion

3.3.1 Characterisation of GO
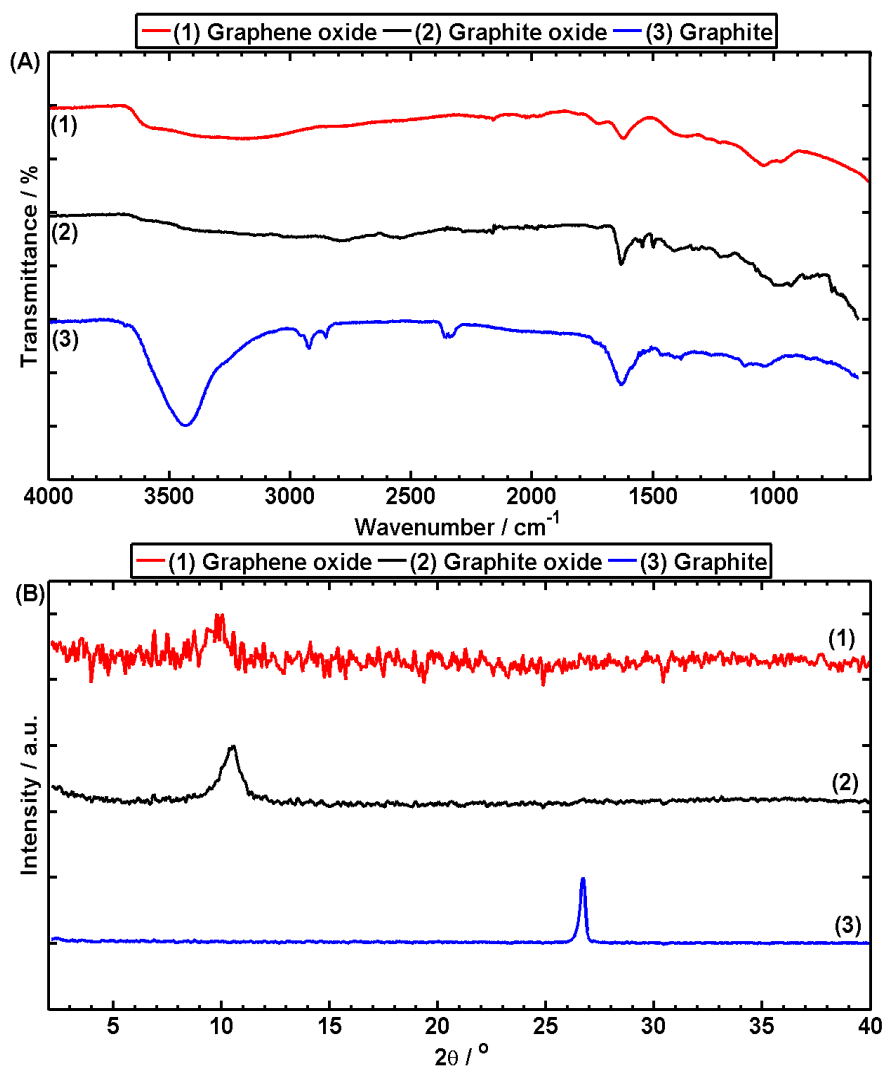
Figure 3.1: (A) FT-IR spectra and (B) XRD traces for GO, graphite oxide and graphite.

GO, produced through exfoliation of graphite oxide created from a modified Hummers method, was characterized by FTIR, XRD, AFM, and LS to confirm the chemical bonds present, the interlayer spacing, and the dimensions of the GO respectively. The process of oxidation introduces additional functional groups to graphite; these can be identified by FTIR to verify the successful oxidation. The graphite curve has two main peaks, one at 3400 cm^{-1} (O–H bonds) from absorbed, free water and a second at 1640 cm^{-1} (C=C bonds). The process of oxidation introduces a peak at 1043 cm^{-1} (C–O bonds) and at 1727 cm^{-1} (C=O bonds) on the graphite

71

oxide and GO curve, as well as the 1628 cm^{-1} for C=C bonds and at 3400 cm^{-1} for O–H bonds from retained free water in the sample [187,210]. The oxidation process should change the chemical structure of graphite and will increase the interlayer spacing; the changes can be identified through XRD (Figure 3.1B). The (002) peak of graphite oxide is at $2\theta = 11^\circ$ corresponding to an interlayer spacing of 0.8 nm and the (002) peak of graphite is at $2\theta = 26^\circ$ corresponding to an interlayer spacing of 0.34 nm, similar to the published literature [214]. This shows that the oxidation procedure has increase the interlayer spacing of graphite. The low intensity of the peak at $2\theta = 10^\circ$ on the GO curve shows that the majority of nanosheets were exfoliated from graphite oxide to GO nanosheets [352,397].
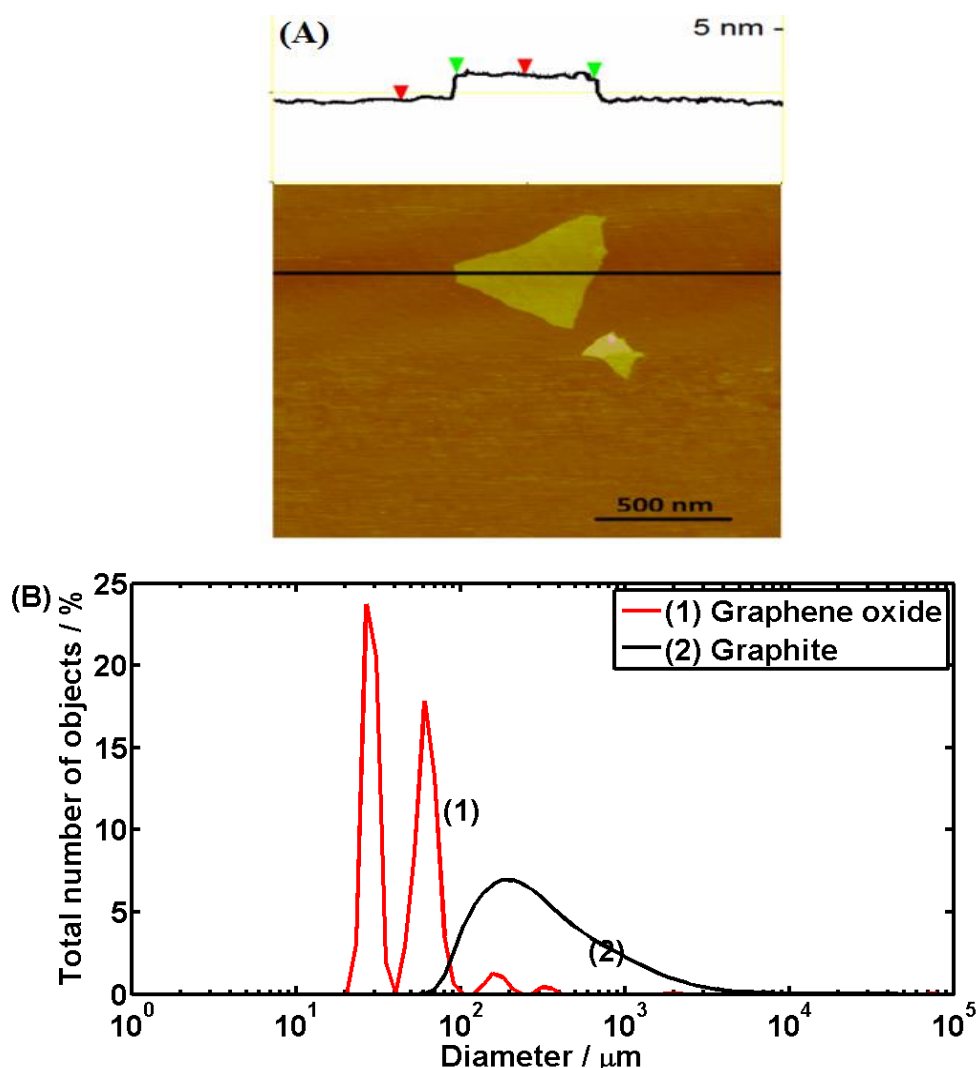
Figure 3.2: (A) AFM image and height profiles of GO nanosheets and (B) laser scattering particle sizing profiles of GO nanosheets and graphite in an aqueous solution.

An AFM image of single layer thick GO nanosheets is shown in Figure 3.2A. The thickness of each layer is around 1.0 nm thick, as determined from several AFM images, showing the exfoliation of graphite oxide into single layer GO nanosheets [397]. The thickness of GO is thicker than the reported thickness of graphene (0.37 nm [500]), showing that the oxidation process has increased the thickness of GO relative to pristine graphene.

The lateral size of GO nanosheets can be measured as approximately between 0.2 to 0.6 μm. This is a representative of a small sample size of the GO sheets. The LS size distribution of a greater sample size of GO sheets is shown in Figure 3.2B, showing that the majority of sheets range in size from 0.6 to 2 μm. The difference in size range between the AFM and LS values can be attributed to the fact that LS analysis measures the hydrodynamic diameter of GO particles and that it assumes these particles are spherical in shape. Graphite powder measured in size between 1 to 20 μm, showing that the oxidation and dispersion processes have successfully led to the production of smaller GO.

3.3.2 Characterisation of chitosan-GO nanocomposites

Chitosan nanocomposites of 0.25, 0.5, 1, 2, 5 wt.% GO were created by dispersing known quantities of GO in chitosan solution and air drying to form a film. Characterization of the nanocomposites will allow for an analysis of the interfacial interactions (FTIR), the crystallinity of the nanocomposites (XRD), and the GO dispersion (TEM). An FT-IR analysis of chitosan nanocomposites containing 0-5 wt.% GO is shown in Figure 3.3A. Prominent peaks show strong $C = C$ (1620 cm^{-1}), $C = O$ (1720 cm^{-1}) and O–H bonds (3300 - 3400 cm^{-1}). An additional range of peaks can be seen at 2400-3200 cm^{-1}, which are N–H bonds from ammonium ions created by the deacetylation process, and at 1530-1540 cm^{-1}, which are amino groups from the chitosan [466]. At 1400 cm^{-1}, C–OH bonds can be seen and at 1000-1100 cm^{-1} C–O bonds can be seen [482]. The C–O bonds (from 1018 to 1012 cm^{-1} and 1088 to 1084 cm^{-1} for pristine chitosan and the nanocomposites respectively) and the amino group (from

1539 to 1531 cm^{-1} for pristine chitosan and the nanocomposites respectively) have shifted significantly, indicating a strong hydrogen bonding between these two groups and the functional groups in GO [396,482], implying a strong interface between the chitosan and the GO..
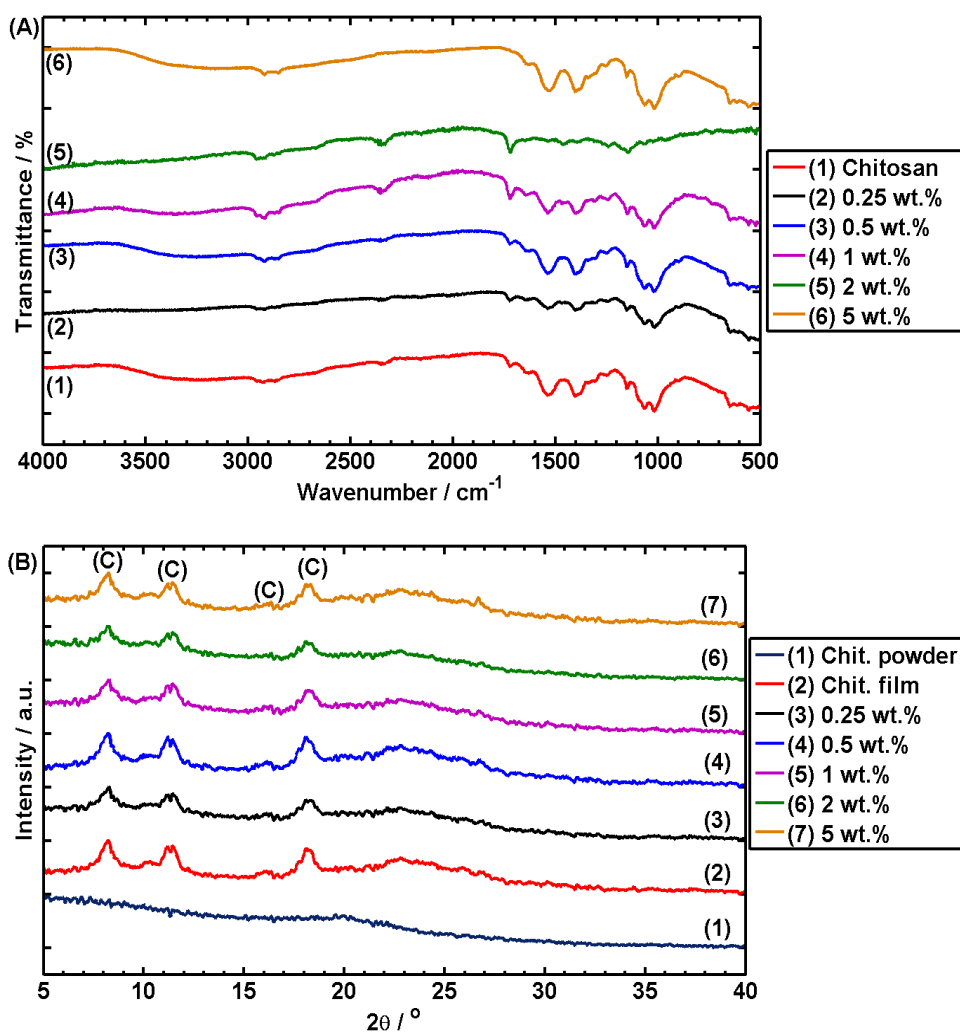
Figure 3.3: (A) FT-IR spectra, (B) XRD traces of chitosan nanocomposites containing 0-5 wt.% GO.

Crystallinity can affect the degradation of chitosan, and as such it is important to analyse the effect that GO can have on chitosan crystallinity. This can be acquired from XRD analysis of the nanocomposites. An XRD analysis of the nanocomposites containing chitosan and GO is shown in Figure 3.3B. An amorphous structure for the chitosan powder can be identified as the broad peak at 20° [216]. Diffraction peaks for all nanocomposites can be seen

at 8, 11, 16, 18 and 23°, in keeping with the literature [396,397]. Peaks at 8, 11 and 18° are the result of a crystalline structure in chitosan while 16° and 23° are due to an amorphous structure in chitosan film [396]. Assuming no peaks for GO were present in the nanocomposite due to their low content and the strong interaction between GO and chitosan which may lead to nearly full exfoliation [396], the crystallinity percentage, χ_c, of nanocomposites can be determined from analysing the diffraction peaks of chitosan, as shown in Equation 3.1 [501,502].

$$\chi_c = \frac{I_c}{I_c + I_a} \tag{3.1}$$

where I_c is the peak area of the crystalline region and I_a is the peak area of the amorphous region. The crystallinity values of chitosan nanocomposites are 30.5, 32.0, 23.3, 25.4, 27.3, and 21.5% for pristine chitosan and chitosan nanocomposites of 0.25, 0.5, 1, 2, 5 wt.% GO respectively.
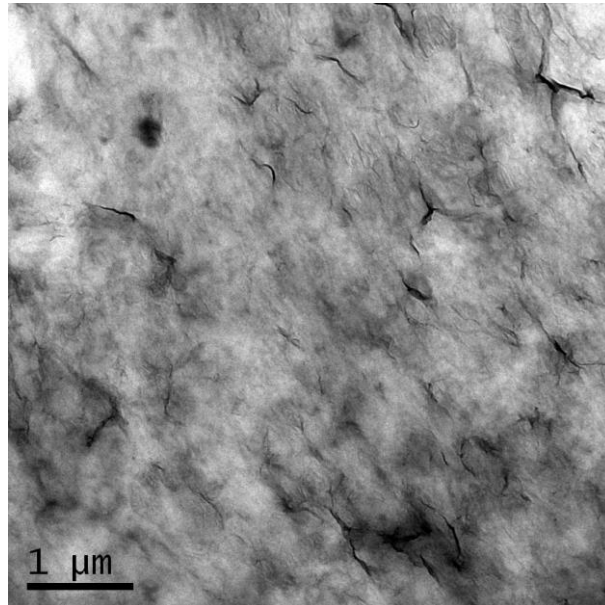
Figure 3.4: TEM micrograph of 2 wt.% GO chitosan nanocomposite, showing a good dispersion of GO nanosheets.

The TEM micrograph in Figure 3.4 shows a good dispersion of GO nanosheets (shown as black lines within the matrix, as per the literature [362,503]), within the 2 wt.% GO chitosan nanocomposite, the majority of which are exfoliated, confirming the validity of the assumption of a good dispersion. Solution casting has created crystalline regions within the chitosan film,

which differentiates from the amorphous chitosan powder (curve 1, Figure 3.2B). The presence of 0.25 wt.% GO slightly increased the crystallinity, owing to its nucleation effect [504]. However, nanocomposites of higher GO contents have lower crystallinity than pristine chitosan films. Presumably, GO reduces the crystal growth by hindering the mobility of the chitosan chains, which outweighs the nucleation effect [504]. The lowest crystallinity was measured for the sample with 5 wt.% GO.
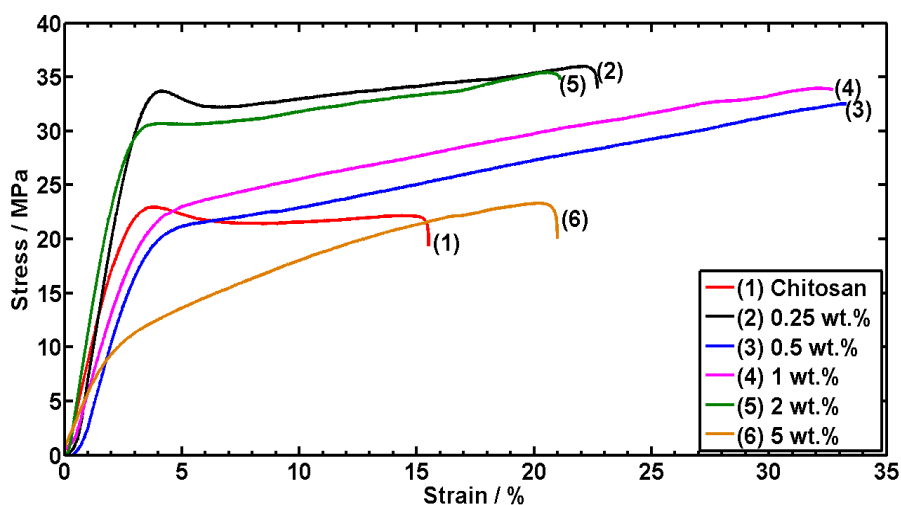
Figure 3.5: Representative tensile stress versus strain curves for chitosan nanocomposites containing 0-5 wt.% GO.

The nanocomposites can use GO as a structural reinforcement to improve mechanical properties as well as a drug carrier. Mechanical testing will allow for a determination of the optimum GO concentration to be used for the nanocomposite-based transdermal drug delivery devices which will require mechanical strength during application, such as microneedle arrays. The representative tensile stress-strain curves for chitosan and GO nanocomposites are shown in Figure 3.5. The behaviour of the nanocomposites under strain varies depending on their GO content. Pristine chitosan samples undergo elastic deformation, yielding and necking without strain hardening. Chitosan-0.25 wt.% (curve 2) and chitosan-2 wt.% (curve 5) strain soften and then proceed to work harden before failing. The nanocomposites containing 0.5 wt.%, 1 wt.% and 5 wt.% do not strain soften after yielding but proceed straight to work hardening before

failing. The introduction of GO increases the ductility and ability of the samples to work harden when compared to the pristine chitosan sample.

The mechanical properties are summarized in Table 3.1. The pristine chitosan film fails at an average strain of 14.5%. The samples containing 0.25 to 5 wt.% GO fail at between 17.7-35.1% strain, demonstrating substantial increases in ductility of chitosan which are attributable to the orientation and delamination of graphene sheets under tension [505]. Chitosan-0.25 wt.% and chitosan-2 wt.% have the highest E value of the sample range, with average E values of 1.23 GPa and 1.30 GPa respectively. GO has a higher E than chitosan, 207 GPa versus 1 GPa [192], and a high aspect ratio, a large specific surface area and abundant functional groups, thus acting as an effective reinforcement filler in these two cases. In contrast, the chitosan-0.5 wt.% and chitosan-1 wt.% present lower modulus values. Both the effective volume fraction of GO and the effect of GO on polymer crystallinity affect the E of the final nanocomposite [506]. The former takes into account the contribution from the interfacial region and is therefore dependent on both the GO content and the dispersion degree of GO [506]. Lower GO contents, e.g. 0.25 wt.%, are expected to lead to better dispersion and therefore more efficient reinforcements.

Table 3.1: The mechanical properties of chitosan-GO nanocomposites.

GO content / wt.%	E / GPa	UTS / MPa	ε_b / %
0	1.00 ± 0.10	24.2 ± 1.4	14.5 ± 2.7
0.25	1.23 ± 0.12	34.5 ± 1.4	19.0 ± 2.2
0.5	0.86 ± 0.08	30.4 ± 1.8	25.9 ± 4.2
1	0.93 ± 0.13	32.4 ± 1.2	35.1 ± 2.6
2	1.30 ± 0.14	33.2 ± 2.2	17.7 ± 2.6
5	0.46 ± 0.11	21.9 ± 1.1	22.4 ± 3.3

In comparison, the lower moduli exhibited by chitosan-0.5 wt.% and chitosan-1 wt.% nanocomposites can be attributable to their lower crystallinities. Chitosan-5 wt.% shows the

lowest modulus, presumably due to the presence of defects and aggregates in addition to the low crystallinity, which is further discussed below. With the exception of chitosan-5 wt.%, the addition of GO increased the UTS. Again, chitosan-0.25 wt.% and chitosan-2 wt.% present the highest tensile strength among the materials tested, with increases of 43% and 37% compared to the value for their polymer counterpart. The strong bonding between GO and chitosan has allowed for an efficient transfer of stress from the chitosan to the GO nanosheets. Similar increases are expected for flexural modulus, flexural strength, and fracture toughness for the nanocomposites as the GO content increases [507].
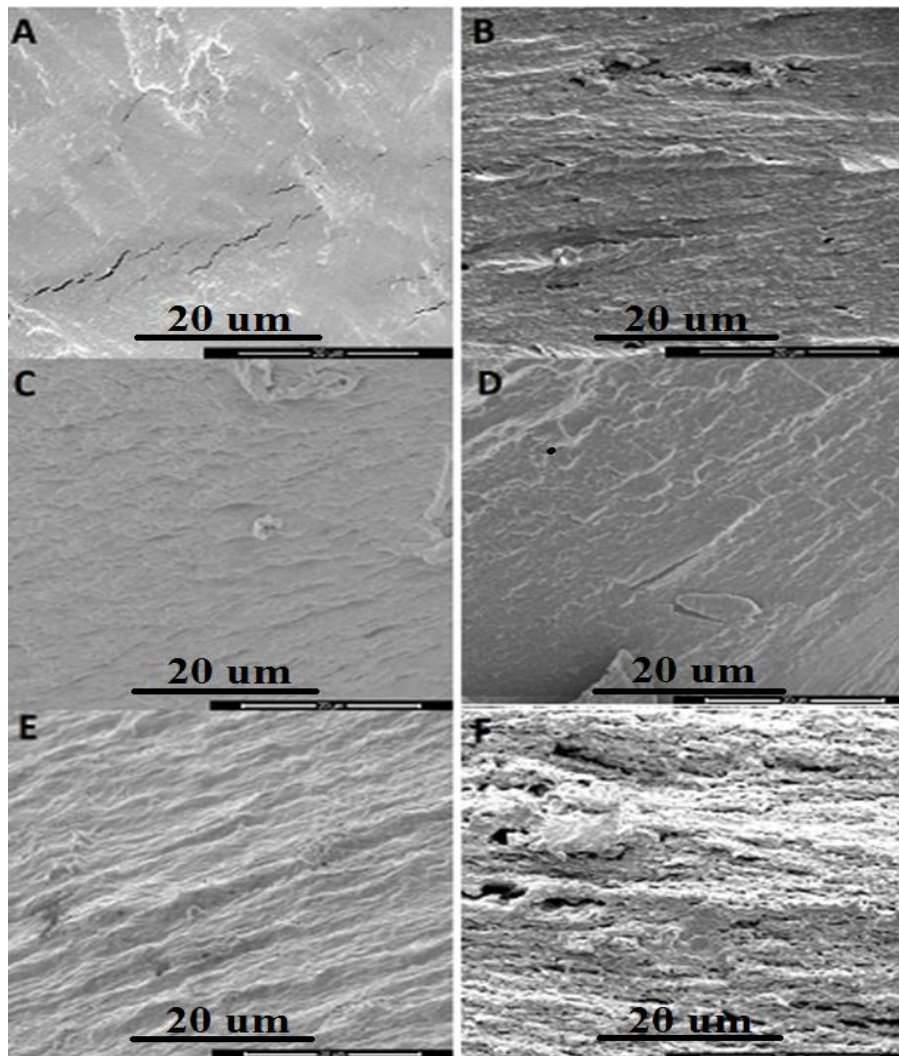
Figure 3.6: SEM micrographs of the tensile fracture surface of chitosan GO nanocomposite films containing (A) 0 wt.%, (B) 0.25 wt.%, (C) 0.5 wt.%, (D) 1 wt.%, (E) 2 wt.%, and (F) 5 wt.%. (Scale bar = 20 μm)

An analysis of the fracture surface of tensile specimens (Figure 3.6) shows that the nanocomposites containing 0-2 wt.% GO show a uniform morphology throughout the fracture surface which suggests that there were no voids or aggregations in these nanocomposites, while voids and aggregations can be seen in the image for the sample with 5 wt.% GO which may explain its inferior mechanical properties.

Based on the above mechanical results, the two nanocomposites that possess the best mechanical properties are chitosan-0.25 wt.% and chitosan-2 wt.%. As a higher concentration of GO allows for a higher quantity of drug to be loaded onto GO than would be achievable with a lower concentration, the optimum nanofiller concentration for load-bearing drug delivery devices such as microneedle arrays is considered to be 2 wt.% and therefore it is used for subsequent drug delivery and enzymatic degradation tests.

3.3.3 Drug loading and release analysis

Drug coated GO was created through a mixing procedure and the removal of excess drug. The successful bonding of FL onto GO surface can be confirmed by UV-Vis, FT-IR, photoluminescence spectroscopy and AFM. Figure 3.7A shows the UV-Vis spectra of GO at the concentration of 0.4 mg ml^{-1} to allow for an analysis of absorption peaks. The peak at 230-235 nm can be attributed to $\pi \rightarrow \pi^*$ conjugations of $C = C$ bonds and the peak at 300 nm is the $n \rightarrow \pi^*$ conjugation of $C = O$ bonds [187]. A comparison of unbound FL, GO-FL hybrid, and GO nanosheets in Figure 3.7A shows that the characteristic peaks of FL at 450 and 480 nm are present with a shift to 445 and 475 nm on the GO-FL hybrid curve while a shoulder peak at 270-275 nm of the FL curve has been transposed onto the GO-FL curve but is not present on the GO curve.
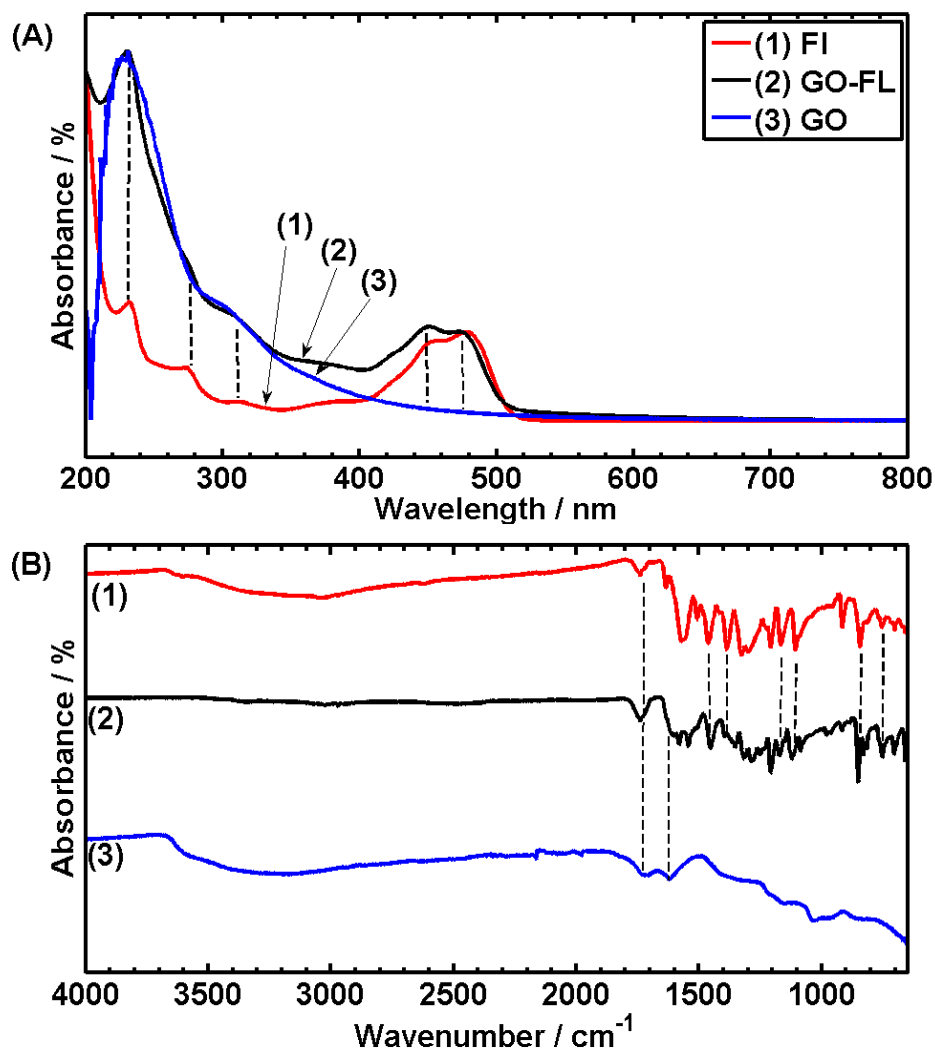
Figure 3.7: (A) UV-Vis spectra, (B) FT-IR spectra of unbound FL, GO, and 45.6 wt.% loaded GO-FL hybrid.

FT-IR spectroscopy analysis of GO-FL and FL powders are shown in Figure 3.7B. In this figure, peaks characteristic of GO can be seen (C=O at 1720 cm^{-1}, C=C bonds at 1600 cm^{-1} and C–O bonds at 1000-1100 cm^{-1}) for the 45.6 wt.% FL loaded GO-FL nanohybrid. Peaks characteristic of FL can be seen on the GO-FL curve below 1600 cm^{-1} and there is a shift in wavenumber on peaks (from 1738 for FL to 1726 cm^{-1} for GO-FL, from 1572 to 1530 cm^{-1}, and from 1088 to 1066 cm^{-1}) which can be attributed to both physical absorption of the drug onto the surface and an overlapping of FL peaks with GO peaks. The bonding between GO and FL is $\pi\rightarrow\pi$ stacking (electrostatic and hydrogen bonding), as reported in the literature [508].

80
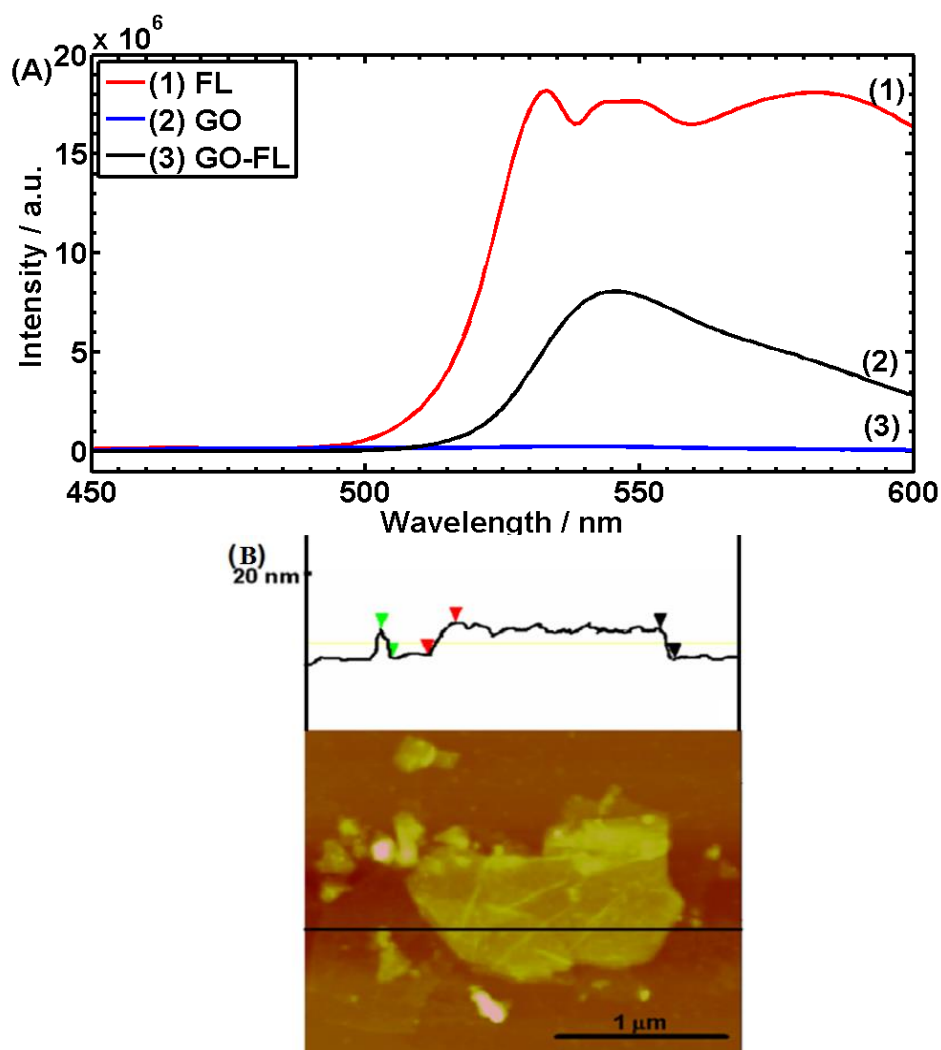
Figure 3.8: (A) Photoluminescence spectroscopy of unbound FL, GO, and 45.6 wt.% loaded GO-FL hybrid. (B) AFM image of a GO-FL sheet from the 45.6 wt.% loaded GO-FL solution, showing a sheet of 8.3 nm, 9.4 nm, and 8.7 nm thick at the green, red and black arrow points.

Photoluminescence spectra are shown in Figure 3.8A, showing the quenching effect of GO on GO-FL in comparison to free FL. The solutions of unbound FL and pristine GO were of a concentration equal to the quantity of FL or GO on the GO-FL in the 45.6 wt.% FL loaded GO-FL nanohybrid solution. GO-FL has a PL property courtesy of the FL, as can be seen by comparing to the GO, again suggesting successful bonding of FL onto GO. An AFM image of a single GO-FL sheet from the 0.84:1 solution is shown in Figure 3.8A. It shows a sheet of an approximate thickness of 8.7 nm. The increase in thickness from 1 nm for GO is due to the coating of FL on the surface, which can be seen to be rough and uneven across the surface (for further images, see Figure 3.S2 in S.I.). Zeta potential readings were taken before and after the

synthesis of the 0.84:1 ratio solution, with values of -53.58 (± 0.96) mV for GO and -54.54 (± 0.76) mV for GO-FL, implying both have good stability in aqueous solutions and that the electrical charge of GO is only slightly decreased by the addition of FL.
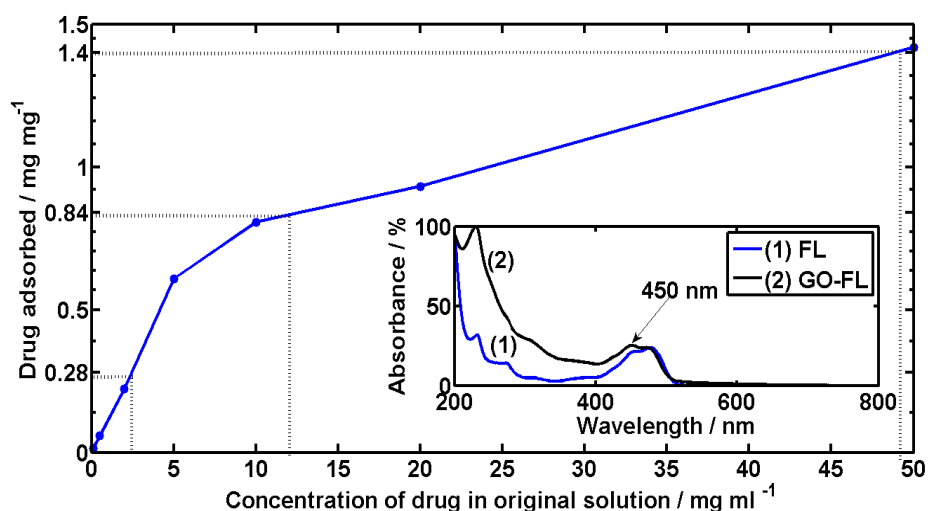
Figure 3.9: Drug loading chart of fluorescein sodium onto GO nanosheets as a function of initial FL concentration after 24 h of bonding. Inset: UV-Vis Spectroscopy analysis of FL in water solution.

The quantity of FL was determined by UV-Vis spectroscopy analysis by measuring the absorbance percentage of the characteristic peak (450 nm) of FL (Figure 3.9 inset). To calculate the drug loading ratio (FL:GO), the amount of unbound FL present in the supernatant prior and after to absorbing onto GO was measured against the spectra of standard FL solutions with a known concentration. Drug loading ratio was calculated by Equation 3.2:

$$Drug\ loading = \frac{Original - unbound\ FL\ (mg)}{Quantity\ of\ GO\ (mg)} \qquad (3.2)$$

The drug loading ratio of FL to GO is dependent on the original concentration of the drug in the solution within the experiment time frame of 24 h. Figure 3.9 shows the increase in drug loading ratio when the original concentration of FL is varied from 0.1 mg ml^{-1} to 50 mg ml^{-1}, allowing for the selection of initial concentrations to make GO-FL powders with defined loading ratios. Initial concentrations of FL of 2.5 mg ml^{-1}, 12.5 mg ml^{-1} and 49 mg ml^{-1} were

used to create nanohybrids with the loading ratios (FL:GO) of 0.28:1 (21.9 wt.%), 0.84:1 (45.6 wt.%), and 1.4:1 (58.3 wt.%), respectively.
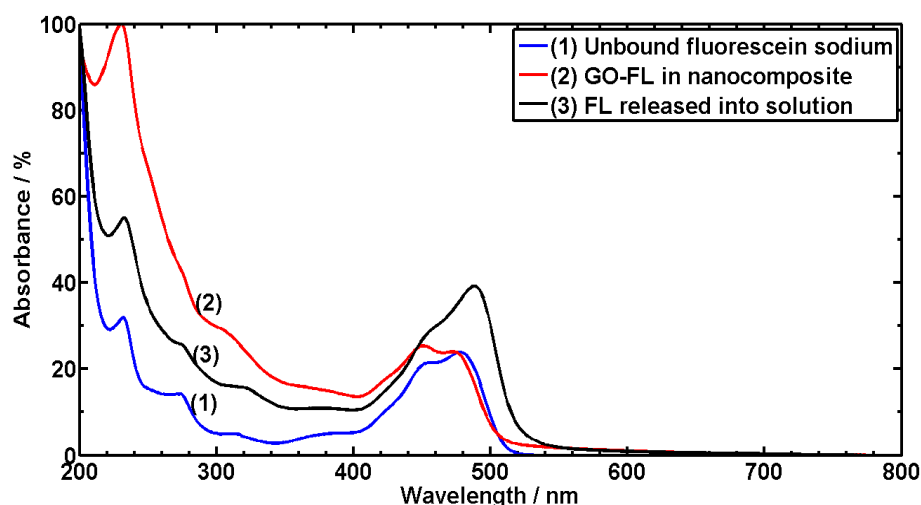
Figure 3.10: UV-Vis spectra of free FL, GO-FL loaded into the nanocomposites and FL released into PBS during drug release testing.

The release rate and quantity released are important to determine for a drug delivery mechanism, which can be analysed using UV-Vis spectroscopy. Figure 3.10 shows a comparison of free FL, GO-FL encapsulated nanocomposites and the FL released during testing. The characteristic peaks of the FL at 450 nm and 480 nm in the free FL have shifted back from 445 nm and 475 nm for the GO-FL after being released from the nanocomposite into the PBS medium, which indicates a possible unbinding of FL from GO after release and is coincident with previous speculation of drug diffusing away from GO [509]. The peaks at 450 nm were used to calculate the drug release amounts according to the method described in the experimental section, and the results are discussed subsequently.
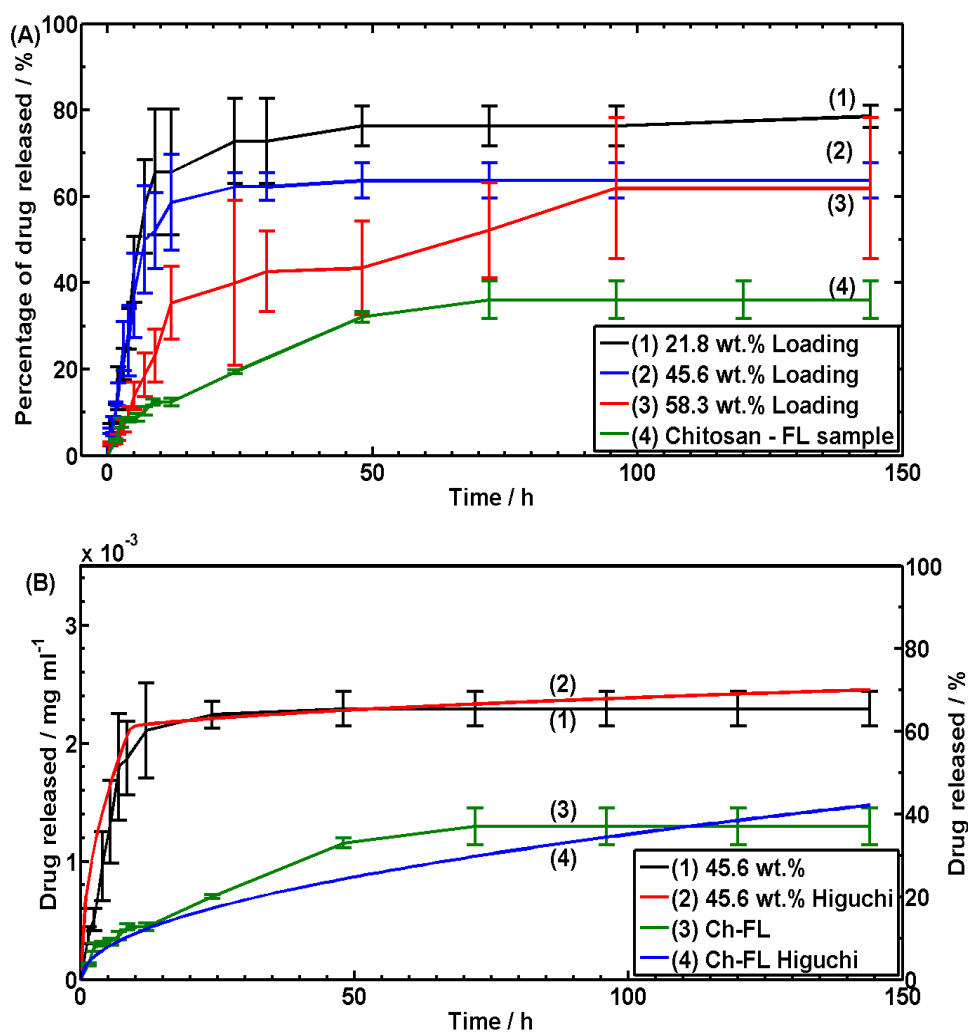
Figure 3.11: (A) Percentage of drug released from chitosan-2 wt.% GO-FL nanocomposites in comparison to a non-GO Chitosan-FL hybrid in a neutral (pH = 7.4) environment as a function of drug loading. (B) Higuchi equation simulation of drug release from chitosan-FL and chitosan GO-FL nanocomposite.

Figure 3.11A shows the cumulative quantity (%) released in a neutral environment (pH = 7.4) over 144 h. There are different release profiles for the samples containing the following loading ratios; FL equal to 21.8 wt.%, 45.6 wt.%, and 58.3 wt.% of the GO-FL nanohybrid while the GO content in the nanocomposite is fixed at 2 wt.%. The sample containing a 21.8 wt.% loading reaches a drug level plateau after 9 h of 66% of the drug in the sample, or 75 μg ml^{-1}. The sample containing a 45.6 wt.% loading is slower to reach the plateau, achieving maximum release at 24 h, 62% of the drug in the sample or 2.2 μg ml^{-1}. After 12 h, a 59% release has been achieved, showing the possibility of a rapid but strong drug delivery system

of 2 µg ml^{-1} in 12 h. The nanocomposite containing a 58.3 wt.% drug loading took 96 h to reach the maximum release level (60% of total available drug or 3.75 µg ml^{-1}). There is a relationship between the degree of drug loading and the time taken to reach the plateau that can be explained by the drug concentration gradient. Initially, the release medium has 0% drug concentration and therefore the diffusion from the nanocomposite to the release medium is fast. As the drug concentration in the release medium increases, the diffusion of the drug from the nanocomposite decreases. By varying the loading of the drug onto the GO the drug release rate can be altered to suit the application (i.e. fast release of anaesthetic for pain relief or sustained release of a therapeutic drug). The 45.6 wt.% loading percentage sample was chosen to undergo further analysis in acidic drug release conditions and enzymatic degradation analysis as it offered the optimum combination of strong, efficient and fast delivery of a drug as well as drug loading efficiency. The incomplete release of the drug can be attributed to the incomplete release of the GO from the chitosan matrix. The drug is attached to the GO and therefore cannot be released into the medium. There is a strong hydrogen bonding between the chitosan and the nanoparticles, as shown in Figure 3.5, which shows a shift in the 1539 and 1018 cm^{-1} peak for pristine chitosan to 1530 and 1016 cm^{-1} for 58.3 wt.% loaded GO-FL in chitosan. This strong bonding restrains the nanoparticles and restricts their movement and subsequent dissolution from the chitosan. A similar effect is noted in the enzymatic degradation analysis later in this paper.

A hybrid of chitosan and unbound FL was created that contains the same mass of FL as the nanocomposite sample containing a 45.6 wt.% loading of FL in GO-FL hybrid (Figure 3.11A). This sample was used to investigate the improvement that bonding a drug to GO can have on the drug release performance. The sample of free FL encapsulated in chitosan has a plateau after 72 h at 36% of the drug in the sample or 1.2 µg ml^{-1}. The unbound FL was unable to diffuse fully through the polymer film and out into the release medium within the 150 h,

presumably due to the strong hydrogen bonding between FL and chitosan. In contrast, the nanocomposite sample containing the same amount of FL has both a quicker and more substantial (62% versus 36%) delivery of the drug than the sample of free FL. The hydrophilic GO sheets may have increased the diffusion coefficient of the GO-FL in comparison to unbound FL (see below), raising the speed and the amount of the drug release. Similar to the case in chitosan film, the incomplete release of the drug from the nanocomposite film may be attributed to the strong bonding between GO-FL and chitosan. This strong bonding restrains the GO-FL hybrid from being released into the PBS medium.

To further understand the improvement in drug delivery performance that grafting to GO offers, release profiles of drugs in the polymer and nanocomposite were estimated by drug diffusion equations that are commonly used such as the Higuchi equations [510,511]. The standard Higuchi equation defines the cumulative amount of drug released, M_t, as:

$$M_t = k_H \times \sqrt{t} \qquad (3.3)$$

where t is the time elapsed and k_H is the Higuchi constant, defined as:

$$k_H = A \times \sqrt{2 \times C_{init} \times D \times C_s} \qquad (3.4)$$

where C_{init} is the initial concentration of the drug within the matrix, A is the cross sectional area of the diffusion matrix, C_s is the drug solubility and D is the drug diffusion coefficient in water, namely 500 mg ml^{-1} and 0.42×10^{-5} cm^2 s^{-1} respectively for pristine FL [512]. The result of the modelling analysis for unbound FL and its release from chitosan is shown in Figure 3.11B, showing a close correlation to the experimental results and confirming the accuracy of the experimental data. However, they do not model the experimental results for the GO-FL chitosan nanocomposite due to the variations in the drug diffusion coefficient. Using the Higuchi equation, an approximation of the diffusion coefficient for FL in the nanocomposite can be made, with an initial value of 0.22×10^{-3} cm^2 s^{-1} up to 10 h and then a lower diffusion value of 0.1×10^{-5} cm^2 s^{-1} until the end of the test. The ability to increase the diffusion

coefficient could allow for drugs with poor diffusivity in water to be released more efficiently than they would be as an unbound drug. A quicker and more substantial release of these drugs would improve the therapeutic effect of treatments.

GO-FL might have been released together from the nanocomposite into the PBS medium, which can be identified by the change of the colour of the PBS, thereby increasing the initial diffusion coefficient of the drug. After having been released into the PBS, FL gradually detached from GO and presented as free FL, as determined from the UV-Vis spectra (Figure 3.10). This suggests that the free released FL can then diffuse into the cell membranes, leaving the GO to be excreted from the body through the renal system [244]. The above calculations consider FL as the drug. If GO-FL is considered as a single drug entity, the C_s x C_{init} will remain the same because the new C_s for GO-FL is 45.6% of the original C_s while the new C_{init} is the 1/45.6% of the original C_{init}, which means the above theoretical values for D will stand.
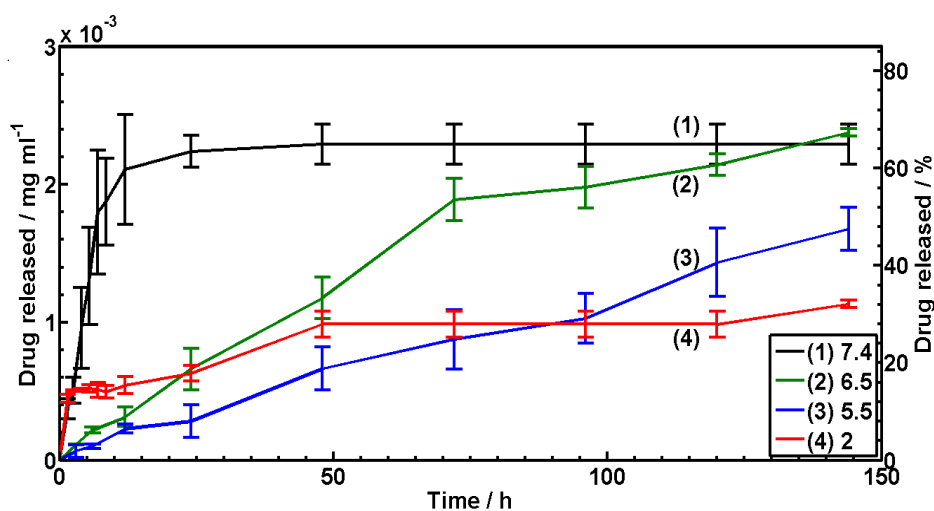
Figure 3.12: Percentage of drug released from GO-FL nanocomposites in an environment with differing pH.

Figure 3.12 shows the cumulative quantity of drug released in an acidic environment (pH = 2, 5.5 and 6.5) from a nanocomposite containing a 45.6 wt.% loading of FL in GO-FL hybrid. The nanocomposite placed in the pH = 2 solution released the drug initially in a profile

similar to the profile for neutral conditions. A steady release of drug was recorded until a plateau was reached at 48 h (27% of drug within the test samples or 0.84 µg ml^{-1}). The pH = 5.5 and 6.5 samples released the drug slowly but steadily, where final release quantities were 46% (1.43 µg ml^{-1}) at 144 h and 59% (1.84 µg ml^{-1}) at 120 h respectively. Presumably the pH =2 conditions rapidly dissolved the surface of the test specimens which then released the drug that was encapsulated in that region, but then the layers did not exfoliate and the hydrophilic GO became hydrophobic and tended to aggregate together, presumably through electrostatic attractions [513,514], thus hindering the release of FL. In the neutral environment, chitosan swelled in the medium; the presence of the hydrophilic GO facilitated the release of FL as discussed above. The surface dissolution did not occur as rapidly when the specimens were placed in solutions of pH = 5.5 and 6.5, and neither did the specimens exfoliate as rapidly as the specimens in the neutral solution. The slower dissolution and exfoliation hindered the rapid release of drug, but the higher pH values did not cause as strong an electrostatic attraction as for the pH =2 specimens, and therefore did not hinder the release of FL. A reduction in the maximum drug release amount when in an acidic medium offers the possibility of a selective release device with limited release in gastric juices (pH of 1-2) and then a more substantial release when in the neutral media of the intestines (pH = 6-7) or in a targeted disease area where the pH is 5.5-7.4.

The bonding of FL onto GO increases the maximum drug release amount by 72% when compared to unbound FL from a chitosan matrix. The drug release tests show that the drug release behaviour can be altered by varying the drug loading ratio onto the GO. The release profile is sensitive to the pH of the release medium, with the quantity of drug released reduced substantially (by 48%) when in an acidic medium.

3.3.4 Enzymatic degradation analysis of chitosan-GO nanocomposites
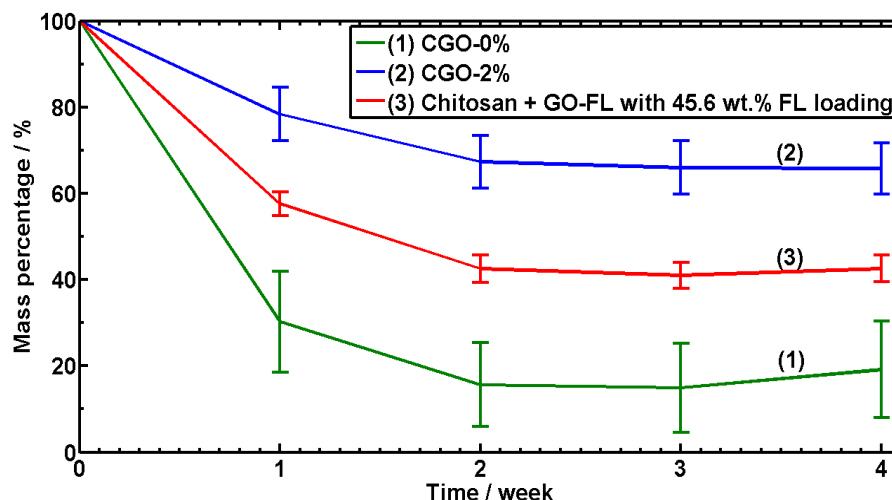
Figure 3.13: Mass change during enzymatic analysis of nanocomposites containing prisitne chitosan, 2 wt.% GO, and GO-FL with 45.6 wt.% FL loading over 4 weeks.

The effect that GO will have on the enzymatic degradation rate of a polymer has not been analysed in the literature. Pristine chitosan and specimens of nanocomposites containing 2 wt.% GO and 2 wt.% GO-FL with 45.6 wt.% FL loading were submerged in a solution of hen egg white lysozyme and PBS to simulate in vivo conditions. Hen egg white lysozyme possesses a similar main chain formation and binding sub-sites as human lysozyme [515]. The by-product of the degradation process is a lower MWt chitosan [516,517].

During the enzymatic degradation analysis, the mass of the samples dropped at different rates (Figure 3.13). Pristine chitosan showed the quickest degradation rate of those tested, losing 70 wt.% of their initial mass after one week compared to 22 wt.% for chitosan-2 wt.% and 43 wt.% for the GO-FL with 45.6 wt.% FL loading samples. A change in the colour of the PBS solution containing the GO-FL with 45.6 wt.% FL after one week confirmed the release of the drug into the medium containing the enzyme during the enzymatic degradation test. The initial high degradation rate for all the profiles can be attributed to the lysozyme reaction to the abundant chitosan chains containing at least 3 acetyl units [516,517]. Lysozyme degrades polysaccharides like chitin and chitosan through enzymatic hydrolysis of the β-(1→4)

glycosidic linkages through the hexameric sugar ring binding sites of lysozyme [497,516]. Once the number of suitable sites has been reduced, the rate of degradation slows between week one and week two and then again between week 2 and week 3 for all specimens. Pristine chitosan reduced to 15 wt.% of their original mass after 2 weeks, compared to 67 wt.% and 43 wt.% respectively for chitosan-2 wt.% and the GO-FL with 45.6 wt.% FL loading samples. The degradation rate for all samples plateaued around week 2, after which the mass of samples varied no more than 2%. The mass loss curve for pristine chitosan is similar to the literature [497].

The difference in mass loss between the samples can be explained by the presence of the nanoparticles GO and GO-FL. Nanoparticles like graphene and GO are impermeable to most molecules [410]. They may decrease the rate at which the enzymes permeate through a nanocomposite through the tortuous path model that predicts an increase in the barrier properties of nanocomposites (as discussed in Chapter 2, Section 2.6). Furthermore, the adsorption of the chitosan molecular chains to the GO via strong hydrogen bonding and electrostatic forces can restrict the chain movement, similar to the physical crosslinking effect of the oxygen groups of GO on polyacrylamide hydrogels [518]. Crosslinking can act to slow down the cleaving and enzymatic degradation of these macromolecules [519], hence the mass loss is lower for the nanocomposites than for the pristine chitosan. The difference in mass loss between chitosan-2 wt.% and GO-FL with 45.6 wt.% FL loading can be attributed to the presence of the drug coating in the latter which limited the bonding sites between GO and chitosan dissolved in the solution.
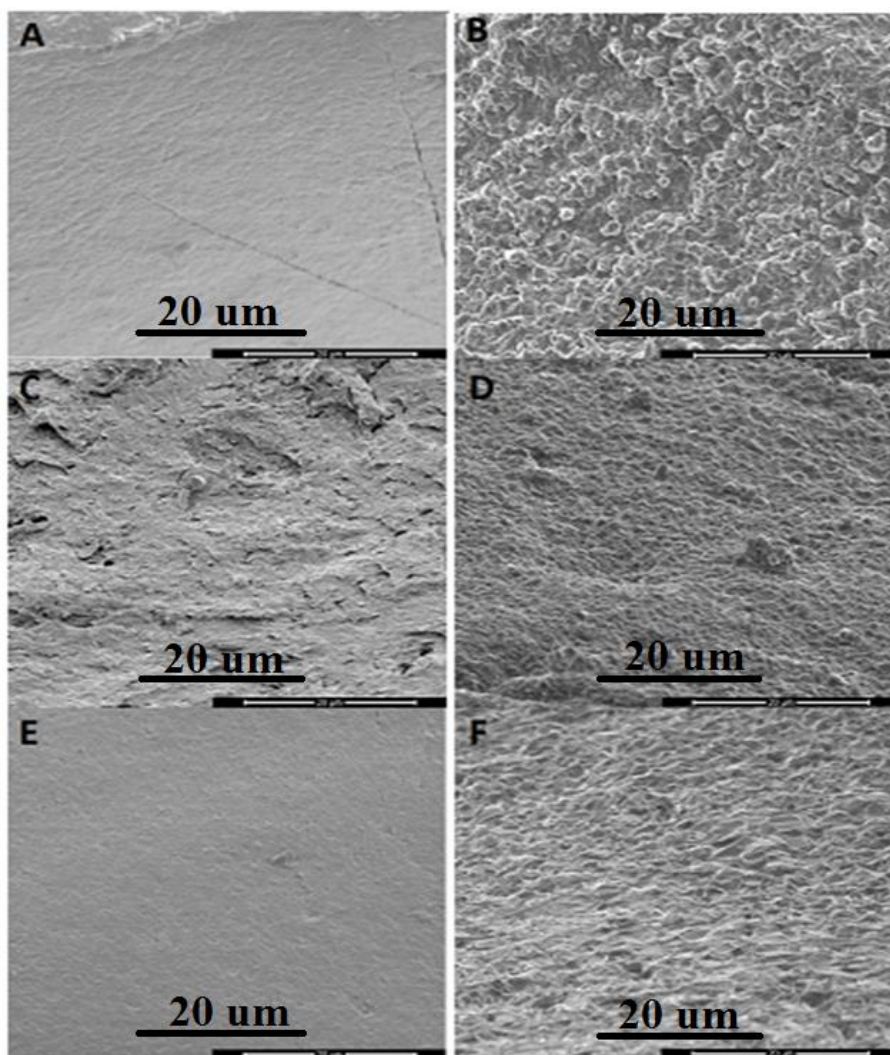
Figure 3.14: SEM images of the top surface of (A-B) chitosan, (C-D) chitosan and 2 wt.% GO, and (E-F) chitosan and GO-FL with 45.6 wt.% FL loading. The images A, C, and E were taken before the test and the images B, D, and F were taken after one week of the enzymatic degradation test. (Scale bar = 20 μm)

The effects of GO and GO-FL on the enzymatic degradation of chitosan can also be seen in Figure 3.14, which shows the surface morphology of the films before the enzymatic degradation test began and 1 week after the test. Among the three samples analysed, chitosan-2 wt.% GO-FL suffered the least pitting and crevassing on the surface during enzymatic degradation, confirming its enhanced resistance to enzymatic activity. As the chitosan-2 wt.% GO-FL nanocomposite is degraded, it is eroded by the dissolution of the chitosan into solution. This will leave chitosan-coated GO-FL nanosheets partially exposed which are still anchored

in the chitosan. High aspect ratio extrusions appear in the sample for chitosan-GO-FL (Figure 3.15) which are chitosan-coated GO-FL nanosheets.
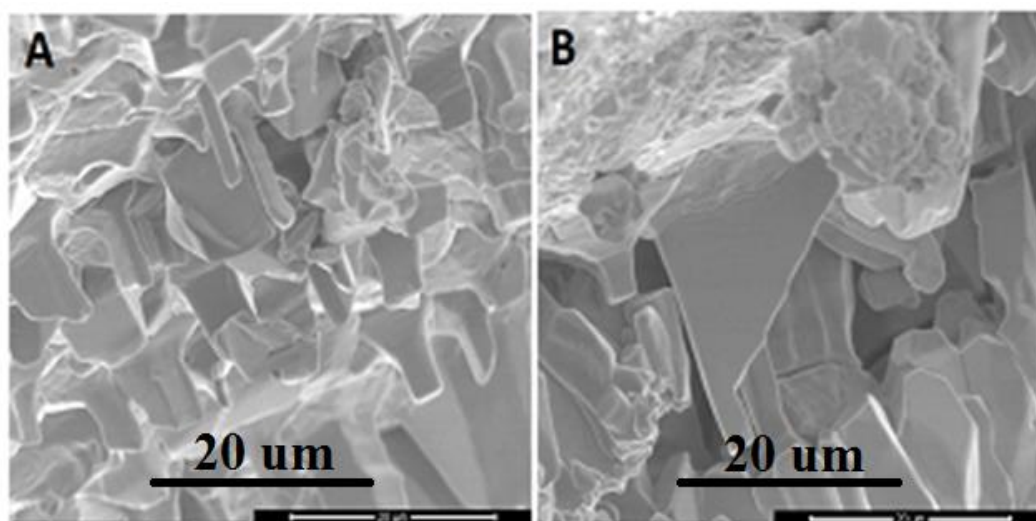
Figure 3.15: SEM images of the fracture surface of chitosan GO-FL nanocomposite showing chitosan coated GO sheets. (Scale bar = 20 μm)

There is no correlation between enzymatic degradation rate and the release rate of the drug as the pristine chitosan film was the fastest to degrade over the course of the first week during which it lost more mass (70%) than the nanocomposite of GO-FL, but in the form of a drug eluding polymer it had the slowest release rate and a lower efficiency of delivery with a plateau of delivery after 72 h. The difference between drug delivery performance and enzymatic degradation rate can be explained by the tortuous path that slowed the enzymes progression into the nanocomposite containing GO-FL and by the chitosan chains that are bound onto the GO surface, making them more difficult to break. The mass loss curve for the sample containing 45.6 wt.% FL in GO-FL hybrid over 4 weeks is important to consider when studying drug release from nanocomposites. Over the first week, the nanocomposite lost 43% of its original weight (Figure 3.13) and released 62% of the available drug (Figure 3.11(A)). The nanocomposite will stay intact within the body long enough for a steady and controlled drug delivery to occur before degrading and being excreted, as can be seen in SEM analysis after one week (Figure 3.14 and Figure 3.15).

3.4 Conclusions

GO was synthesised by a modified Hummers method and the characterisation studies on GO in this chapter served as a benchmark for changes in chemical/physical structure, dimensions and functionality of other graphene derivatives through this thesis. Enzymatically degradable chitosan and chitosan nanocomposite films with 0.25 to 5 wt.% GO were prepared by solution casting. The nanocomposite containing 2 wt.% GO exhibited the best combination of mechanical properties and drug loading capacity, with the Young's modulus raising from 1 to 1.3 GPa, UTS from 24 to 34 MPa, and ε_b from 14.5% to 17.7% compared to the pristine chitosan. Improvements of the mechanical properties were attributable to the high stiffness, strength, specific surface area and ample functional groups as well as the mobility of GO sheets under tension.

Drug release tests show that the release profile of the drug from the polymer matrix is dependent on two key factors: the loading ratio of the drug to GO and the pH of the solution that the drug is being released into. In a comparison to chitosan with the same amount of FL, the GO-FL nanohybrid containing 45.6 wt.% FL loading released 72% more of the drug and achieved maximum delivery in a shorter timespan than the conventional composite sample. Different drug release profiles were noted during testing in neutral and acidic media with a decrease in release rate and a reduction of release quantity by 48% during the acidic test, showing a pH sensitive release functionality. Nanocomposites of GO and GO-FL degraded slower than pristine chitosan, with about 70% and 45% of their original mass remaining at week 2 compared to 18% for chitosan, due to the strong bonding of the GO with chitosan and the effect of the tortuous path model on the permeability of the enzyme.

In conclusion, chitosan-2 wt.% GO nanocomposites showed improved mechanical properties and drug release properties in comparison to pristine chitosan, while also showing pH and drug-loading-ratio sensitive release. These improvements could allow for chitosan-GO

nanocomposites to be used for drug delivery applications such as microneedle arrays, where the increased strength would be needed to maintain microneedle rigidity and the drug release properties would allow for a quicker release of the drug into the body in comparison to what a pristine chitosan microneedle could achieve.

Chapter 4. Chitosan-reduced graphene oxide nanocomposites

4.1 Introduction

The chitosan-GO nanocomposites from Chapter 3 possessed improved mechanical properties and drug release rates over pristine chitosan, but the presence of GO did not impart new functionality, such as electrical conductivity, to the nanocomposite. As discussed in Section 2.4.2, the electrical conductivity of GO is around 6 orders of magnitude lower than pristine graphene and so did not increase the conductivity of the resultant chitosan-GO nanocomposites. The focus of this chapter was on improving both the electrical conductivity and mechanical properties of chitosan-graphene nanocomposites by synthesising a reduced graphene oxide that is suitable for use for drug delivery purposes such as microneedle arrays. Central to this chapter is the facile and biocompatible manufacturing process of the rGO, achieved by mixing a chitosan solution and a GO dispersion at 37 $^{\circ}$C for 72 h (see Scheme 4.1), which allows for the reduction of GO into rGO. This process does not require excessive heat, toxic solvents, or irradiation yet allows for the pre-loading of drugs into the material.

Once synthesised, the rGO was characterised to compare it to GO and the effectiveness of the reduction technique is analysed. The rGO was used as the nanofiller for a chitosan nanocomposite, chitosan-rGO, which is enzymatically degradable and possesses the mechanical strength and controlled drug delivery required for potential uses in microneedle arrays. The effects of rGO addition and rGO concentration on the structure, glass transition temperature (T_g), crystallinity, mechanical properties, electrical properties, drug delivery performance and enzymatic degradation rate of chitosan were investigated and the optimised nanocomposite was subsequently used to form microneedle arrays.
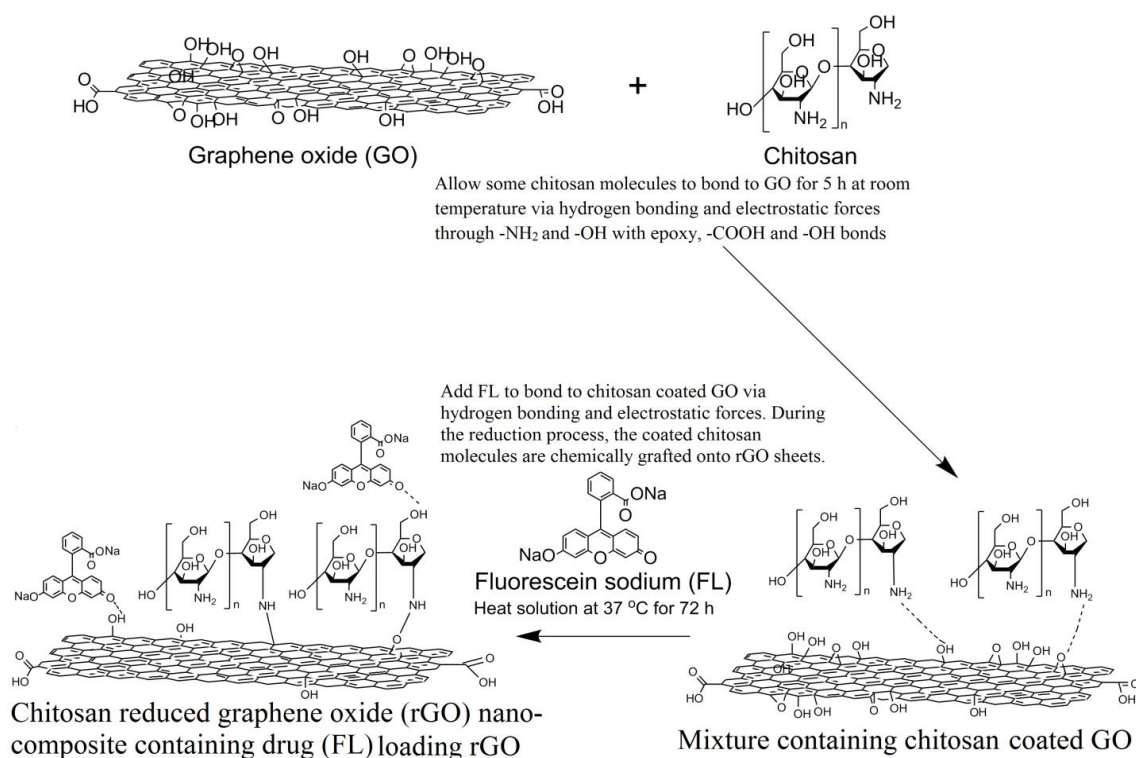
Scheme 4.1: The experimental procedure to prepare chitosan-reduced graphene oxide (rGO) nanocomposites with the drug (FL) loaded onto the rGO nanosheets. During the reduction process, GO is dispersed in a chitosan solution; this promotes hydrogen and electrostatic bonding between the amine and hydroxyl groups of chitosan and the epoxy, carboxyl and hydroxyl groups of GO. The reduction procedure chemically grafts the chitosan onto the now-reduced rGO. A drug, such as fluorescein sodium, can be introduced to the chitosan-GO mixture before reduction and loaded onto the chitosan-coated GO through hydrogen bonding or electrostatic forces [508].

4.2 Experimental section

4.2.1 Materials

The following chemicals were reagent grade and used as purchased from Sigma Aldrich; acetic acid, sulphuric acid, hydrogen peroxide, potassium permanganate, sodium nitrate, fluorescein sodium, phosphate buffered saline, and graphite powder ($\leq$ 20 mm). Chitosan powder (Mw ¼ 100 000–300 000) was used as purchased from Fisher Scientific. Foetal calf serum (FCS) was kindly provided by Dr. Ingunn Holen of the University of Sheffield.

4.2.2 Preparation of graphene oxide

The method for making GO has been described before in Chapter 3. Briefly, GO was synthesized from a modified Hummers method [186,187]. Graphite (3 g) was added to

sulphuric acid H_2SO_4 (69 ml) and sodium nitrate $NaNO_3$ (1.5 g). The mixture was stirred vigorously for 30 min in an ice bath. Potassium permanganate $KMnO_4$ (9 g) was added slowly, and when fully added the mixture was heated to 35 °C and stirred for 12 h. Potassium permanganate (9 g) was added to the mixture and stirred for 12 h before being poured over a mixture of ice (400 ml) and 30% hydrogen peroxide H_2O_2 (3 ml). The graphite oxide suspension was centrifuged at 8000 rpm for 1 h in an Eppendorf 5804 with the supernatant being discarded. The graphite oxide was dispersed in fresh distilled water for a total of five cycles to remove residue chemicals from the production process. Graphite oxide was dried in a vacuum oven and stored in powder form in a desiccator. When required, graphite oxide was exfoliated in distilled water for 2 h by a Fisherbrand sonication bath (230 V, 50 Hz) and centrifuged at 8000 rpm for 30 min to remove larger than desired particles. The supernatant dispersion was collected and lyophilized in a Labconco FreeZone Triad freeze-dryer to be stored in powder form in a desiccator

4.2.3 Preparation of reduced graphene oxide

1 g of chitosan was added to a 100 ml solution of 2 wt.% acetic acid in water and stirred overnight to allow for complete dissolution of the chitosan. 1 g of GO was dispersed in 100 ml of distilled water by intense stirring and sonication. The two solutions were combined and heated at 37 °C for 72 h under constant stirring. This solution was centrifuged at 8000 rpm for 1 h in an Eppendorf 5804 to separate the reduced graphene oxide (rGO) flakes from the aqueous chitosan solution and then washed with 2% acetic acid solution for three cycles to remove the excess chitosan. The rGO was dispersed in the distilled water by a Fisherbrand sonication bath (230 V, 50 Hz).

4.2.4 Drug loading onto reduced graphene oxide

One gram of GO was dispersed in 100 ml of distilled water by intense stirring and sonication. Simultaneously, 1 gram of chitosan was added to a 100 ml solution of 2 wt.% acetic acid in

water. The two solutions were combined and stirred intensely for 5 h at room temperature to ensure bonding has occurred. FL powder (0.84 g) was added to the mixture and heated at 37 °C for 72 h under stirring. Unbound FL and free chitosan in the supernatant were removed from the solution through intense centrifugation at 8000 rpm for 1 h in an Eppendorf 5804 and the rGO-FL powder was then washed with distilled water and acetic acid solution twice.

4.2.5 Preparation of chitosan-graphene nanocomposites by in-situ reduction

Chitosan was added to a solution of 2 wt.% acetic acid in water and stirred for 24 h (Scheme 4.1). The required concentration (0.25, 0.5, 1, 2, 5, 7 and 10 wt.%) of GO was added to the chitosan and acetic acid solution. The temperature of the resultant suspension was then raised to 37 °C for 72 h under stirring to allow for the interaction of chitosan and GO and to reduce the GO. The suspension was degassed in a sonication bath for 30 min. The suspension was poured into a mould and allowed to air dry. Prior to testing, film was placed in an oven for 1 h at 50 °C.

To prepare drug loaded rGO chitosan nanocomposites, the same procedure was applied with the required concentration (1 or 2 wt.%) of GO in water added to the chitosan and acetic acid solution and stirred for 5 h. After this, FL (1.2 wt.%) was added into the suspension which was subsequently heated at 37 °C for 72 h under stirring for the reduction of GO and bonding of FL onto the rGO. Due to the amounts of GO used to prepare the chitosan-rGO nanocomposites, the terms 1 wt.% and 2 wt.% rGO nanocomposites were used subsequently in this paper.

4.2.6 Structural characterisation

A Perkin Elmer Lambda 900 spectrometer was used for UV-Vis spectroscopy (1 nm resolution). A Perkin Elmer Spectrum 100 with a diamond attenuated total reflectance (diamond-ATR) unit was used for FT-IR spectroscopy at a resolution of 1 cm^{-1}. A Stoe Stadi P with Cu Ka$_1$ irradiation (0.15406 nm wavelength) was used for XRD. Measurements were

taken from 2–40 º (2θ) with a scanning speed of 1º min^{-1} at 40 kV and 35 mA. Atomic force microscopy of rGO sheets laid on a mica substrate was achieved through a Veeco Dimension 3100 atomic force microscope with Olympus AC160TS probes in tapping mode at 0.5 Hz. A Coulter LS130 was used for laser scattering particle sizing from 0.1 to 900 μm, with particles analysed using 3 one minute runs of nanoparticles in an aqueous solution. Powders were tested in a Perkin Elmer Pyris 1 between 40 to 600 ºC at 5 ºC min^{-1} for thermogravimetric analysis under a nitrogen atmosphere. Raman spectroscopy was achieved using a Renishaw inVia Raman microscope at a wavelength of 785 nm between 50-4000 cm^{-1} with a 0.5 cm^{-1} resolution, with laser power reduced to 5% to avoid laser induced heating. A Perkin Elmer DSC 6 was used to analyse the glass transition temperatures of chitosan nanocomposites. Samples were initially raised from 30 ºC to 200 ºC at a rate of 30 ºC min^{-1} in a nitrogen environment before cooling to 30 ºC at a rate of 20 ºC min^{-1} to remove the thermal history of the specimens. Thermographs were measured from the second heating which was identical to the first stage. The density of specimens (preheated at 60 ºC in a vacuum oven for 6 h) was determined by gas pycometry using a Micromeritics AccuPyc II 1340 using 50 purge cycles of helium gas and 10 density calculation cycles.

4.2.7 Tensile testing

Tensile testing was achieved with a Hounsfield twin column tensometer using a 1kN load cell and a 1 mm min^{-1} strain rate in accordance with ISO-527 (1 and 2). Specimens (n = 5) were of a dog bone shape with the narrow test section between grips measuring 22 mm in length, 2.7 mm in width and 1mm in thickness.

4.2.8 Electrical testing

Chitosan nanocomposites of 0, 0.25, 0.5, 1, 2, 5, 7, 10 wt.% rGO were measured using a Thurlby DMM 1905a. Silver paint (RS 186-3600) was applied to the ends of test samples (n =

5) to form contact points. The device was calibrated using metal wire (steel, copper and aluminium).

4.2.9 Drug release testing

rGO-FL nanoparticles (40 mg) was placed in PBS solution (20 ml, pH = 7.5 or 4) at 37 °C. This solution was added to a dialysis bag (Fisher Scientific Biodesign Dialysis tubing DO14, M_w cut off = 14 kDa) which was then submerged in 100 ml of PBS of the same pH as within the dialysis bag. A known quantity of solution from the container was removed after every time step, making sure to replace it with the same amount of fresh PBS solution. UV-Vis spectroscopy in a Perkin Elmer Lambda 900 determined the release rates of the drug. The quantity of FL was determined by comparing the absorbance peaks at 320 nm with solutions of free FL of known concentration.

Nanocomposite specimens (n = 5) were placed in a phosphate buffered saline (PBS) solution (30 ml) at 37 °C and gently agitated at 100 rpm in a Stuart SI500 shaking incubator. A known quantity (2 ml) of solution from the container was removed after every time step, making sure to replace it with the same amount of fresh PBS solution. UV-Vis in a Perkin Elmer Lambda 900 determined the release rates of the drug from the nanocomposite in neutral (pH = 7.4) and acidic (pH = 2, 5.5, and 6.5) conditions. The quantity of FL was determined by comparing the absorbance peak at 450 nm of the test samples with solutions of free FL of known concentration (from 0.001 to 1 mg ml^{-1}) in water, similar to the procedure used to measure the quantity of FL in solution during the loading of the drug onto the GO.

4.2.10 Enzymatic degradation analysis

Enzymatic degradation tests have been described elsewhere [497,498]. Briefly, the polymer films were submersed in a PBS solution (pH = 7) at 37 °C containing the enzyme lysozyme at a natural concentration within the body, 1.5 μg ml^{-1} [449,499]. Samples were maintained at 37 °C and were gently agitated. At regular intervals, each specimen was removed from the beaker,

washed with distilled water, dried in a vacuum oven, and the mass measured. The sample was placed into fresh PBS and lysozyme solution to maintain constant enzymatic activity. For each sample type, there were 5 specimens for mass analysis and two sacrificial specimens for characterization analysis. The stability of rGO and GO suspensions in biological mediums was tested by visual analysis of rGO and GO suspensions (concentration of 0.3 mg ml^{-1}) in FCS, PBS and distilled water over 28 days.

4.2.11 Microneedle preparation and analysis

Microneedles containing 2 wt.% rGO-FL were created to assess the performance of rGO nanocomposites in transdermal drug release applications. Microneedle male moulds were designed through finite element analysis modelling using Autodesk Inventor Professional 2014 and then produced on our behalf by Shapeways (USA). Microneedles were a 10 by 10 array of 100 microneedles, with each microneedle consisting of a cylindrical base (starting diameter of 310 µm tapering to 200 µm and a height of 150 µm), a main shaft (diameter of 200 µm and height of 300 µm), and a cone (tapering from 200 to 40 µm and a height of 150 µm) (Scheme 4.2). Microneedles were prepared by filling female silicone moulds with excess amounts of high viscosity 2 wt.% rGO-FL chitosan mixture (Scheme 4.2), centrifuging the moulds at 8000 rpm for 1 h and cleaning away the excess suspension from the mould [152]. The mould was allowed to air dry. The process of filling the mould and centrifuging was repeated twice more to guarantee that the cavities were fully filled.
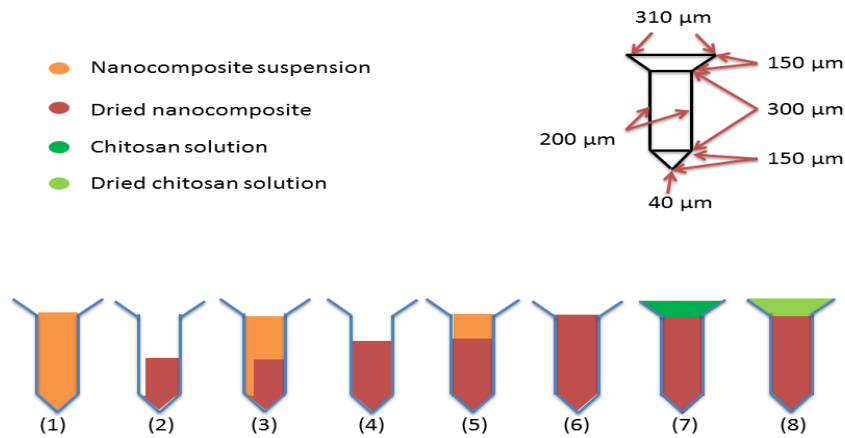
Scheme 4.2: Procedure to create chitosan - 2 wt.% rGO-FL microneedle arrays.

Microneedles were mechanically tested for structural rigidity under compressive loads with a Hounsfield twin column tensometer using a 10 N and a 1 kN load cell with a 1 mm min^{-1} strain rate. Images were taken of the compression testing with a Veho VMS-001 digital microscope under normal white light. The dissolution of FL from microneedles was visualized using pseudo-*in vivo* methods [120], with microneedles inserted into a hydrogel of gelatin (4.5 g in boiling water (40 ml) and allowed to set before the upper surface was covered with paraffin tape). Images were taken of the dissolution of FL through the hydrogel with a Veho VMS-001 digital microscope under normal white light and UV light (365 nm).

4.3 Results and discussion

4.3.1 Characterisation of reduced graphene oxide
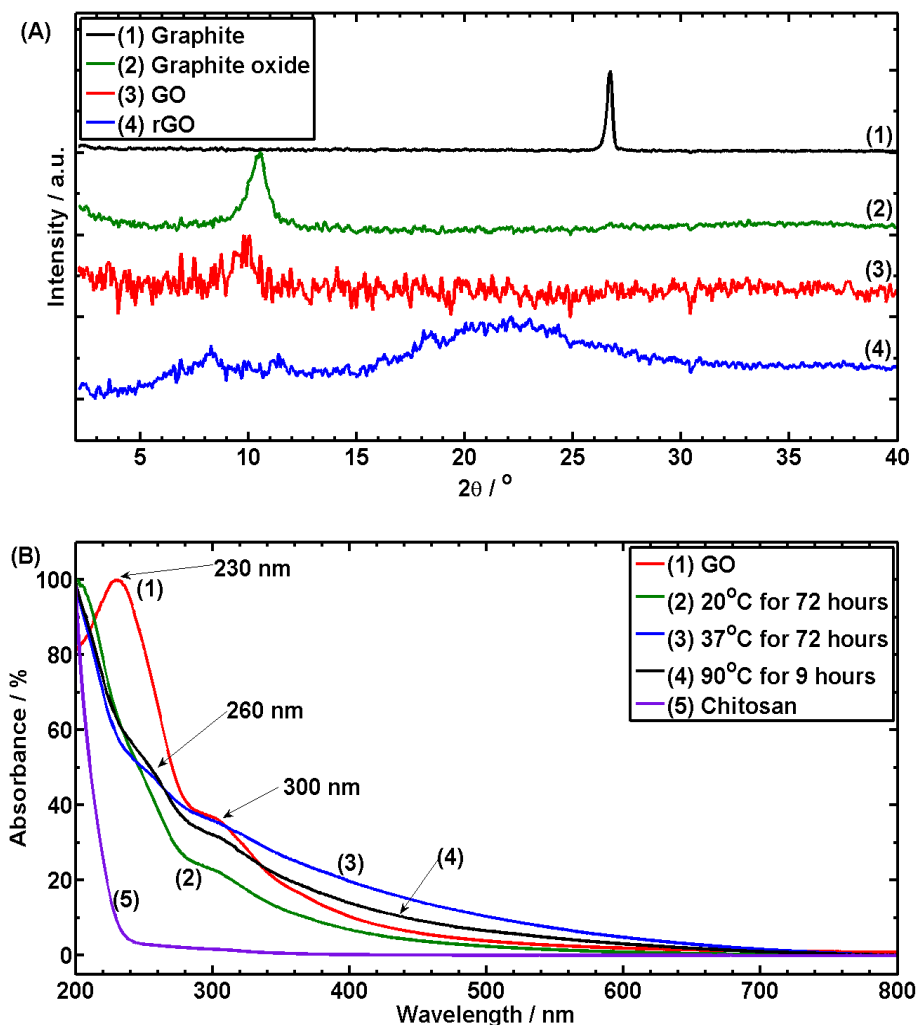
Figure 4.1: (A) XRD curves for graphite, graphite oxide, GO, and rGO. (B) UV-Vis absorption spectra for GO, rGO created at 20 °C or 37 °C for 72 h or 90 °C for 9 h, and chitosan.

As discussed in Section 2.4.2 (page 29), the oxidation procedure to create GO creates ample functional groups that improve the bonding of GO to other molecules [190] and give it excellent dispersibility within many solvents [191], though the oxidation procedure does reduce the mechanical and electrical conductivity properties [192–194]. By partially restoring the structure to that of pristine graphene by removing the functional groups created during oxidation, rGO can maintain the dispersibility of GO but also restore some of the material properties of pristine graphene. Figure 4.1A shows the XRD curves for graphite, graphite

oxide, GO, and rGO. Graphite, graphite oxide, and GO have been discussed in Chapter 3, Figure 3.1B. The creation of a broad peak for rGO at $2\theta = 23°$ is synonymous with the creation of partially reduced rGO, where the crystalline structure has nearly returned to that of pristine graphene or graphite ($2\theta = 26°$), which is in keeping with the literature [399].
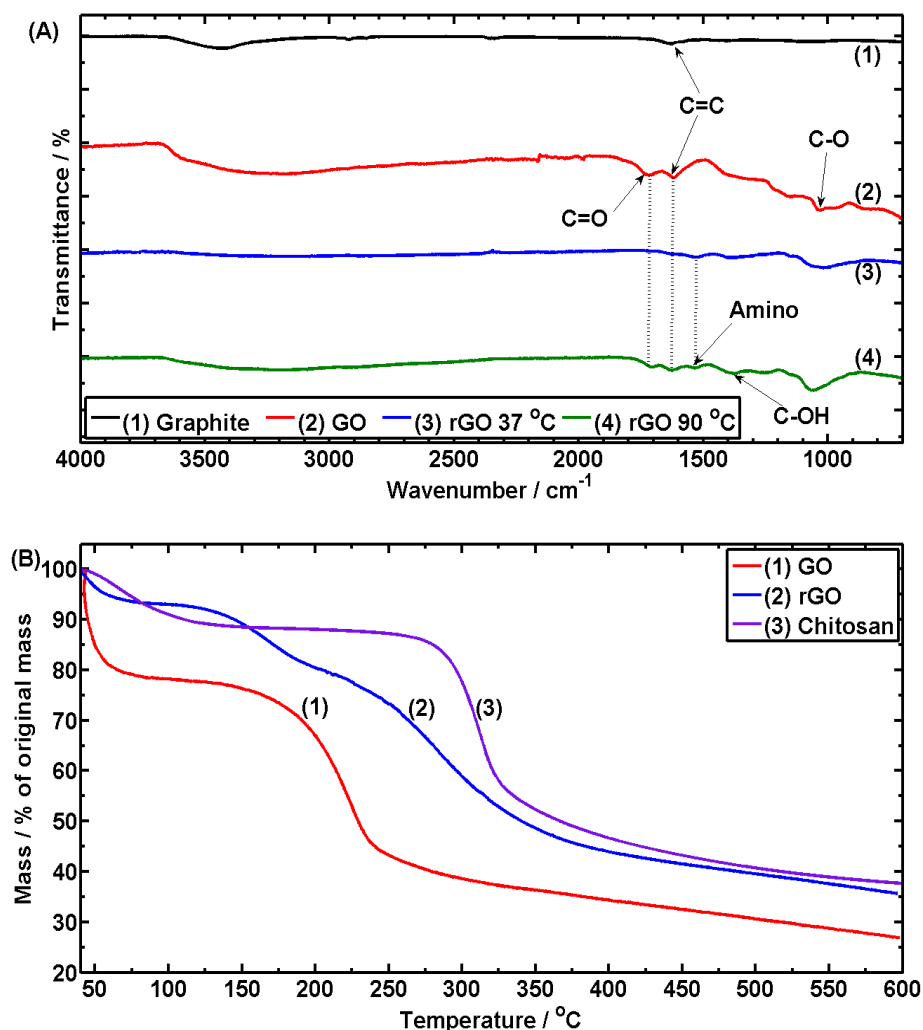
Figure 4.2: (A) FT-IR spectra for GO and rGO created at 37 °C for 72 h or 90 °C for 9 h. (B) TGA of GO, chitosan reduced rGO, and chitosan.

Figure 4.1B shows the UV-Vis spectra of GO, rGO created at 20 °C or 37 °C for 72 h or 90 °C for 9 h, and chitosan. For GO, there are two noticeable peaks; the peak at 230-235 nm corresponds to the change in electronic state level from $\pi \rightarrow \pi^*$ for C = C bonds, and the peak at 300 nm corresponds to the change in electronic state level from $n \rightarrow \pi^*$ for C = O bonds [187,520]. The successful reduction can be seen for the rGO curve created at 37 °C for 72 h as

the shoulder peak of C = O bonds at 300 nm has been reduced and is no longer a noticeable feature of the curve. A shift has also occurred of the wavelength attributed to the $\pi \rightarrow \pi^*$ change of C = C bonds, shifting to 260 nm due to the restoration of the π transition network that is seen in graphene nanosheets and CNTs [210]. These changes are similar to the rGO created by heating at 90 °C for 9 h, showing that body temperature reduction is a suitable alternative to high temperature reduction processes. There was no such shift in the peaks for the rGO curve created at 20 °C for 72 h suggesting this temperature did not reduce the GO in this time frame. The UV-Vis spectra for GO treated at 20 °C and 37 °C at different time steps (Figure 4.S1, Appendix 1) highlight the gradual reduction of GO when treated at 37 °C over 72 h. There is no change in the curve for GO treated at 20 °C which shows the importance of both the use of temperature and the functionalisation with chitosan to the reduction process.

Figure 4.2A shows the FT-IR spectra of GO and rGO created at 37 °C for 72 h or 90 °C for 9 h. The rGO created at 37 °C or 90 °C possesses the same peaks, again showing the similarity between the two reduction processes and the effectiveness of the body temperature reduction method. The peak intensities of C-O bonds (1050-1060 cm^{-1}), the C=O bonds (1700-1750 cm^{-1}) and the O-H bonds (3400 cm^{-1}) from GO decrease significantly after reduction. The C=C bonds can be seen at 1600-1650 cm^{-1} with amino groups and C-OH bonds from the chitosan (1530 cm^{-1} and 1400 cm^{-1}). The amino (-NH$_2$) groups of chitosan react with the oxygenated groups (C=O and C-O) of GO to reduce the GO in rGO in a direct "redox" reaction, where chitosan is chemically grafted onto rGO sheets [214]. Besides chemical bonding, hydrogen bonding and electrostatic forces are also present between the remaining oxygenated functional groups of rGO and the amino and hydroxyl groups of chitosan [214]. This is shown in Scheme 4.1.

Figure 4.2B shows the thermogravimetric analysis (TGA) curves of GO, chitosan and rGO which allows for a determination of the reduction in oxygen groups present on rGO and

the content of chitosan. Eliminating free water that was removed below 100 °C for all samples, the GO powder lost 45% of its mass during the first decomposition stage at 195-230 °C, while rGO lost 13% of its mass. This represents a 73% reduction in oxygen functional groups through the facile reduction process. The mass loss (33%) for the rGO between 280 and 320 °C can be mainly attributed to the degradation of the glucosamine in the chitosan coating [214], similar to pristine chitosan (mass loss of 39% between 280 to 320 °C). Taking into account these two mass losses, the mass loss of GO at this temperature range (3.2%), and the oxygen reduction degree, the chitosan content in the original rGO was estimated at 85%.
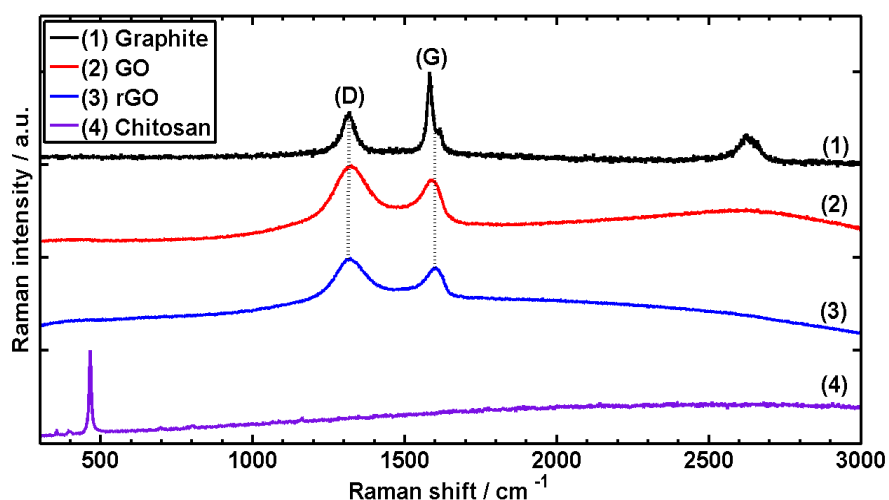
Figure 4.3: Raman intensity curves for graphite, GO, and rGO.

Raman spectroscopy, Figure 4.3, further confirms the successful reduction of GO into rGO at 37 °C. Transition for the G band from 1581 to 1590 to 1597 cm^{-1} for graphite, GO, and rGO respectively show a change in the e_{2g} mode of sp^2 [210,216]. Similarly, the D band shifts from 1318 to 1322 to 1313 cm^{-1} for graphite, GO, and rGO respectively show a change in the breathing mode of a_{1g} symmetry [208]. The blue shift in the G band for rGO can be attributed to the partial reduction of oxide groups and the strong interaction between the rGO and chitosan [210,214,216].
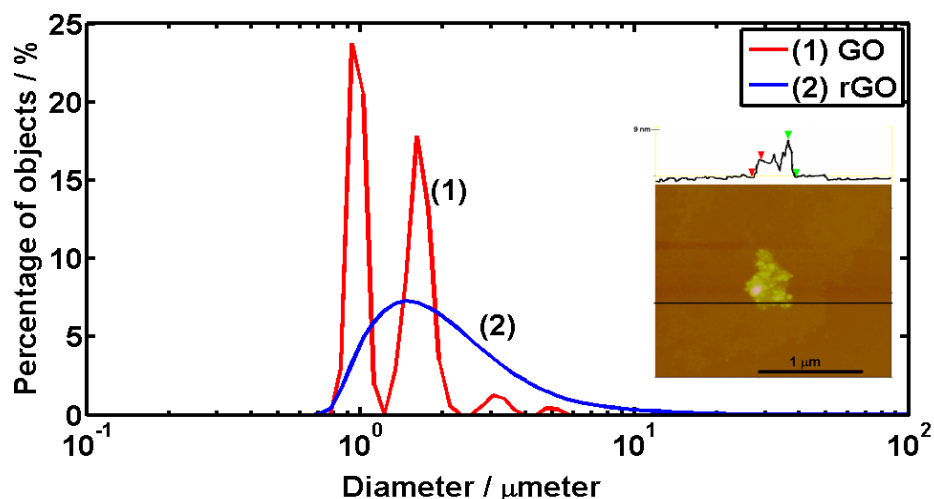
Figure 4.4: Laser scattering particle sizing of rGO nanosheets in an aqueous solution. (Inset) AFM image of a rGO nanosheet on a mica substrate The height profile for the AFM image shows a thickness of 3.5 nm for a single layer sheet, the edge of which is highlighted by red arrows.

The hydrodynamic diameter of rGO was determined as 0.85 to 5 μm from laser sizing analysis (Figure 4.4), noting that the latter assumed the particles were spherical rather than in sheet form. As identified through AFM (Figure 4.4 (Inset)), the thickness of each rGO nanosheet is ~3.5 nm, confirming the formation of a protective chitosan coating on graphene nanosheets as each nanosheet of GO is around 1 nm (Figure 3.1).
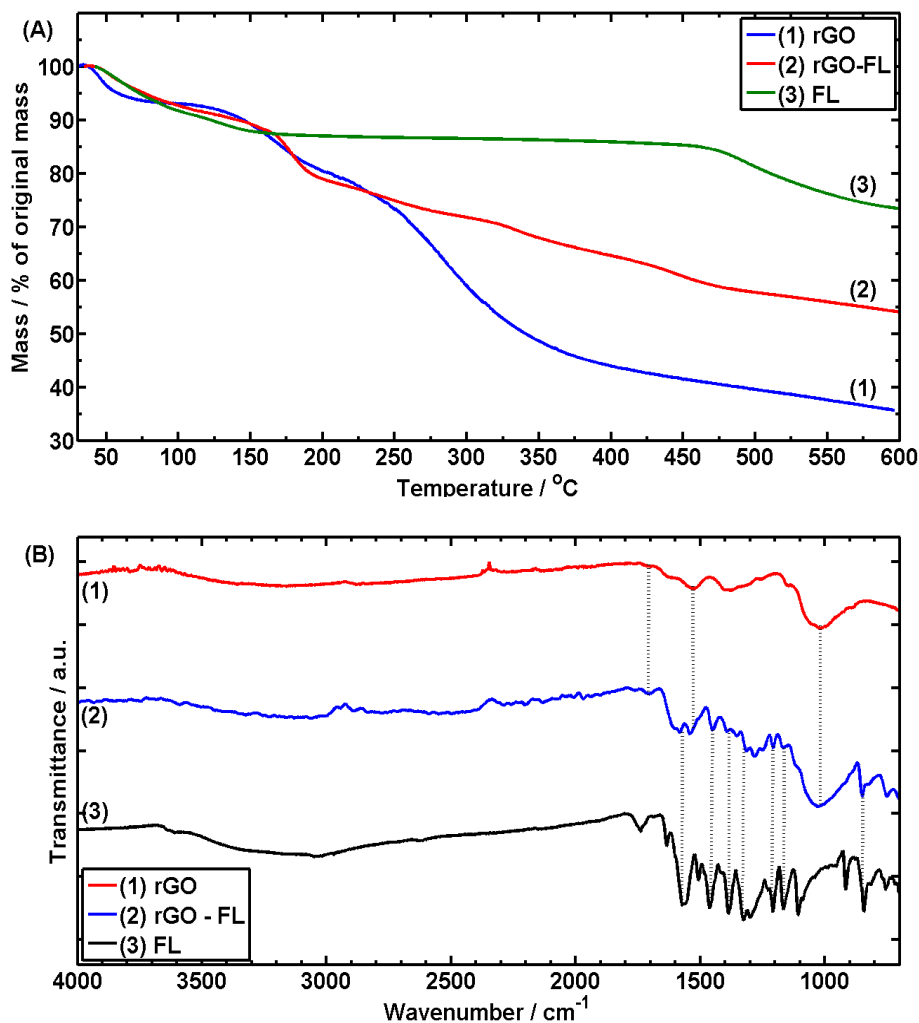
Figure 4.5: (A) TGA spectra for rGO, rGO-FL and FL powder showing the loading ratio of FL:rGO to be 0.26:1, once free water has been eliminated. (B) FT-IR spectra for rGO, rGO-FL and FL powder.

Drug grafted rGO nanohybrids (rGO-FL) were created through mixing chitosan with GO for 5 h initially and then subsequently mixing with FL at ambient temperature, followed by reduction at 37 °C for 72 h and removal of the unbound FL. Bonding is through the carboxyl groups of FL with the amine and hydroxyl groups of chitosan and the epoxy, carboxyl and hydroxyl groups of GO. The loading ratio of FL:rGO was determined by TGA to be 0.26:1 (Figure 4.5A). The success of the combined drug grafting and reduction procedure can be confirmed by FT-IR analysis (Figure 4.5B) that shows that characteristic peaks of both rGO (1050 cm^{-1}, 1400 cm^{-1}, 1530 cm^{-1}) and FL (840 cm^{-1}, 1100 cm^{-1}, 1450 cm^{-1}) are present on the rGO-FL curve. The peak intensities of C=O (98% for both rGO and rGO-FL) and C-O (87%

for rGO and 92% for rGO-FL) were similar for both rGO and rGO-FL when the curves were normalised, which demonstrates that the reduction process was not hampered by the grafting of the drug and worked to create the rGO-FL hybrid.
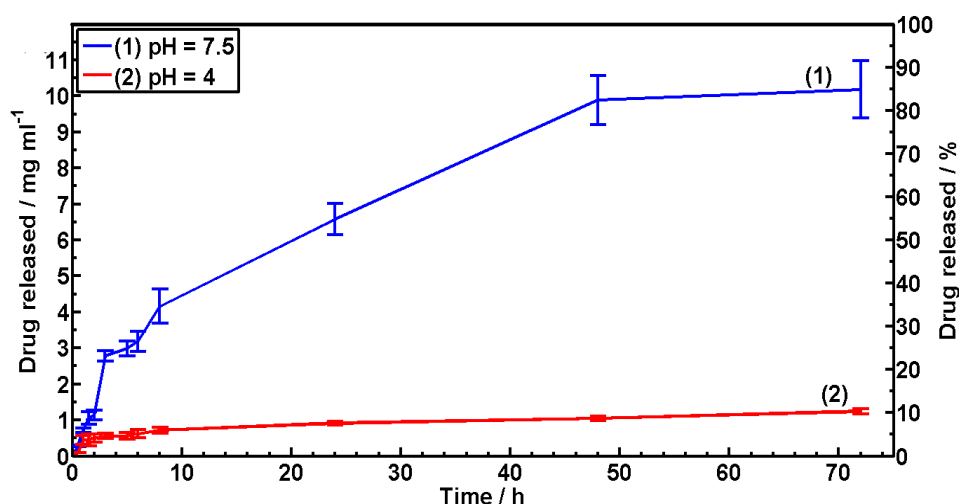
Figure 4.6: Drug release from rGO-FL powder in PBS solution (pH = 4 or 7.4) over 72 h.

The cumulative release of FL from rGO-FL in PBS (pH = 4 and 7.4) over 72 h is shown in Figure 4.6. FL can be seen to diffuse from the rGO nanosheets in a PBS solution, with the maximum value of 10.2 mg ml^{-1} (91%) occurring around 72 h in a pH = 7.4 release medium. There was a quick initial release, with 2.78 mg ml^{-1} (25%) and 4.16 mg ml^{-1} (37%) released after 3 h and 8 h respectively, potentially allowing rGO bound drugs to be used for applications where a quick release is necessary. This initial release rate lowered until a plateau of 10.2 mg ml^{-1} (91%) was reached around 72 h. In an acidic medium, the release rate is much lower, achieving a maximum value of 1.2 mg ml^{-1} (11.1%) after 72 h. This compares to a value of 3.18 mg ml^{-1} released in a neutral medium after 6 h. This pH sensitivity can be explained by the change of rGO dispersion in the medium. When in the neutral release medium, rGO nanosheets were well dispersed and stable in the medium due to electrostatic repulsion from the amine groups of its coating material chitosan as previously discussed [216]. When in the acidic release medium, chitosan is dissolved and so the electrostatic repulsion decreases, and

the electrostatic attraction, caused by the carboxyl and hydroxyl groups in GO and the salt in PBS, prevails. This leads to the aggregation of rGO sheets in the medium which prevents the efficient release of FL [513]. This pH sensitivity will allow for the drug grafted-rGO to be used for applications such as site specific drug delivery to regions like the colon, and prevent undesirable side effects by limiting the release of the drug in acidic areas like the stomach (gastric acid has a pH of ~2 [521]).
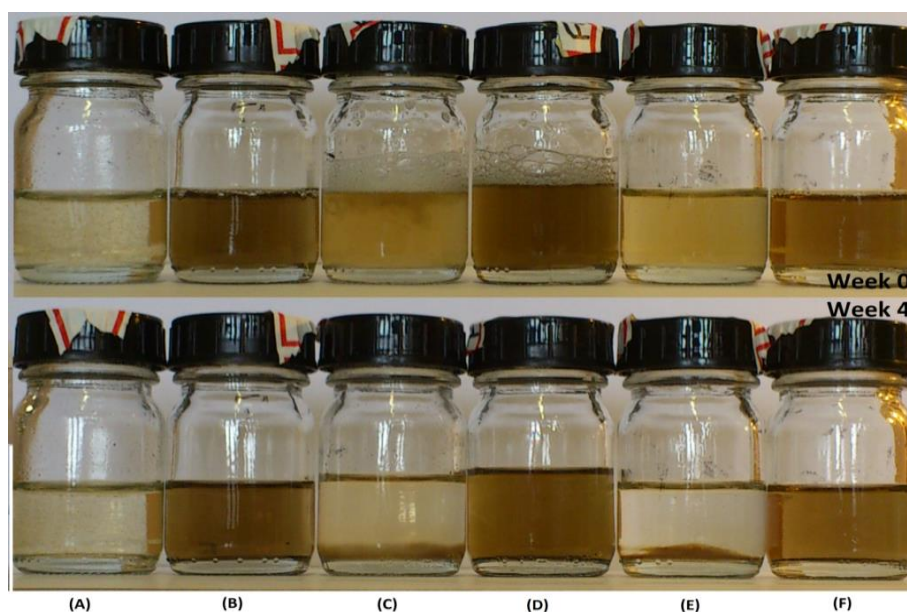
Figure 4.7: The biostability of the (A, C, E) GO and (B, D, F) rGO nanosheets in solutions of (A-B) distilled water, (C-D) foetal calf serum, and (E-F) phosphate buffered saline (pH = 7.4).

For the rGO to be used for drug delivery *in vivo*, the rGO will have to be stable within bodily fluids. If it is not stable, it may aggregate and this will hinder the release of drug. The biostability (Figure 4.7) of the GO and rGO nanosheets in solutions of distilled water, foetal calf serum (FCS, pH = 7.4), and phosphate buffered saline (PBS, pH = 7.4) is shown over the course of 4 weeks. The rGO sheets remain stable and in dispersion within all of the fluids (B, D, F) , which is attributed to the chitosan coating. The GO sheets without a chitosan coating aggregated in the FCS (C) and PBS (E) which can be seen at the bottom of the containers, though they were stable in distilled water (A). Presumably the GO aggregated in the FCS solution due to the physical crosslinking of GO by proteins in the FCS and in PBS due to

110

electrostatic forces caused by the salt in PBS [210,522]. Chitosan maintained an electrostatic repulsion through the positively charged amine groups, allowing the rGO nanosheets to remain well-dispersed when in biological fluids [216].

4.3.2 Characterisation of chitosan-rGO nanocomposites
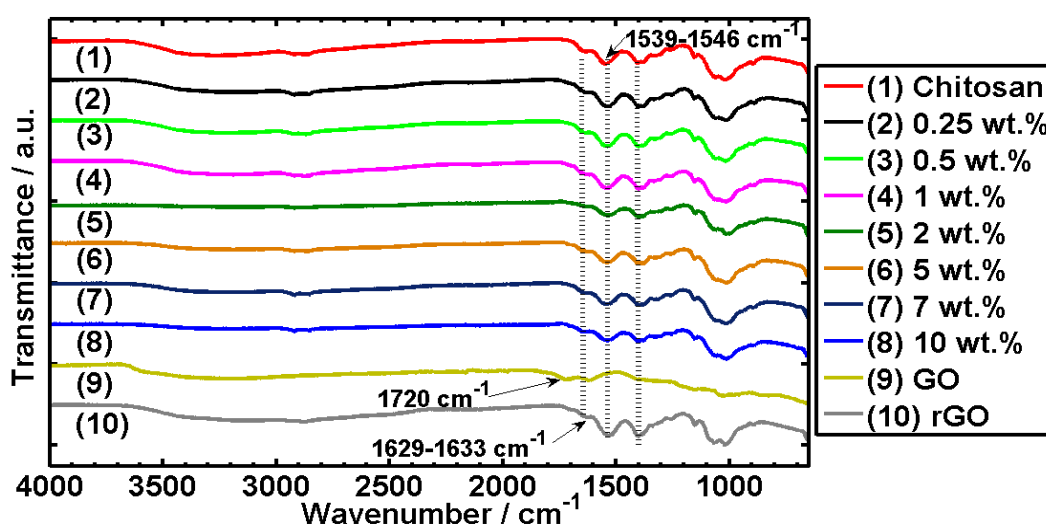
Figure 4.8: FT-IR spectra of chitosan nanocomposites containing 0-10 wt.% rGO.

The results from Section 4.3.1 show that GO was reduced by the body temperature reduction process, and so chitosan nanocomposites of 0, 0.25, 0.5, 1, 2, 5, 7, and 10 wt.% rGO were prepared by the same in-situ reduction process, i.e. the reduction of known quantities of GO in chitosan solution at 37 °C for 72 h and subsequent air drying. Figure 4.8A shows the FT-IR spectra of chitosan nanocomposites and their control samples of GO and rGO nanosheets. For the nanocomposites, strong peaks from the chitosan can be seen at 2800 cm^{-1} (N-H), 1633 cm^{-1} (C=C), 1400 cm^{-1} (C-OH), 1000 - 1100 cm^{-1} (C-O), and at 1530 cm^{-1} (amino groups) [466,482], similar to the rGO control sample in Figure 4.2A. In comparison to chitosan-GO nanocomposites at the same concentrations, the spectra of these nanocomposites have a much weaker peak of the 1720 cm^{-1} C=O bonds (which can be clearly identified in the spectrum for GO), confirming successful reduction of GO into rGO. Chitosan-GO nanocomposites possess a prominent 1720 cm^{-1} C=O peak, even at low concentrations. The C=C peaks have shifted

111

from 1633 cm^{-1} for pristine chitosan to 1629 cm^{-1} for the nanocomposites due to the presence

of rGO and the peak for amino has shifted from 1546 cm^{-1} for pristine chitosan to 1539 cm^{-1}

for the nanocomposites. This is presumably due to the strong covalent bonding between the

chitosan and the graphene nanosheets (Scheme 4.1) during the reduction process which utilizes

the amino groups of chitosan and the hydroxyl and epoxy groups of GO [214].
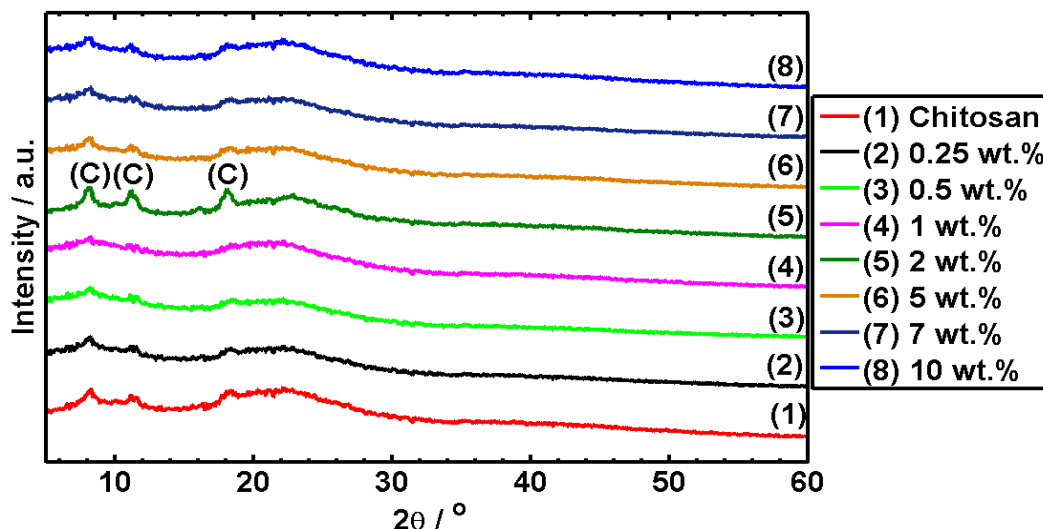
Figure 4.9: XRD traces of chitosan nanocomposites containing 0-10 wt.% rGO with crystalline peaks highlighted with the symbol "C".

Figure 4.9 shows the XRD analysis of chitosan-rGO nanocomposites. Chitosan can be

identified by the crystalline peaks at $2\theta = 8$, 11, and 18° and the broad, amorphous peaks at 2θ

$= 23°$ [396,397]. Crystallinity can be determined from Equation 3.1 (Chapter 3). The results of

the crystallinity analysis are shown in Table 4.1, showing that the presence of rGO increases

the crystallinity of the nanocomposites in relation to pristine chitosan (15.3%). The crystallinity

increased in general as the rGO concentration increased to 7 wt.% (18.9%), before decreasing

at 10 wt.% (17.7%). On one hand, the presence of rGO increased the nucleation of crystals

within the chitosan matrix [504], while on the other hand it limited the mobility of polymer

chains restricting rearrangements of the polymer chains into ordered crystalline structure. In

these cases, the former was the dominant factor. In the case of the 10 wt.% rGO, the decrease

in crystallinity in comparison to the 7 wt.% rGO nanocomposite may be due to the partial

aggregation of the rGO within the nanocomposite, thereby decreasing the number of viable nucleation points that would be possible if the rGO was fully exfoliated. The crystallinity data of chitosan-rGO nanocomposites are lower than those of chitosan-GO nanocomposites (Chapter 3) at the same graphene concentrations (32.0, 23.3, 25.4, 27.3, and 21.5% for 0.25-5 wt.% GO), presumably due to the reduction process decreasing the chain mobility of the chitosan more substantially, arising from the covalent bonding in comparison to hydrogen bonding and electrostatic forces (chitosan-GO nanocomposites).

Table 4.1: Crystallinity and glass transition temperature of chitosan-rGO nanocomposites

rGO content / wt.%	Crystallinity / %	Glass transition temperature / $^{\circ}$C
0	15.3	134.1
0.25	16.5	134.7
0.5	18.1	138.5
1	17.8	144.2
2	18.1	160.9
5	18.5	165.6
7	18.9	171.9
10	17.7	173.5
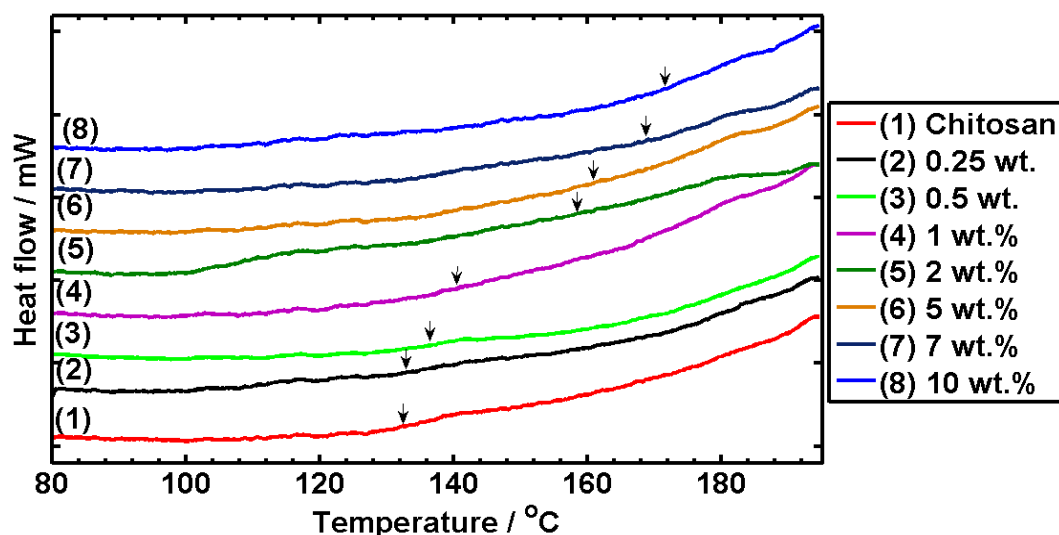
Figure 4.10: DSC traces of chitosan nanocomposites containing 0-10 wt.% rGO.

Figure 4.10 and Table 4.1 show the results of the DSC analysis of chitosan-rGO nanocomposites of varying rGO concentration. The presence of rGO significantly alters the

glass transition temperature (T_g) of chitosan, with a maximum increase of 39 °C achieved for the 10 wt.% nanocomposite (173 °C versus 134 °C). The value for pristine chitosan is similar to the reported literature (140 °C) [523]. Similar large (30 °C) increases in T_g were observed in PMMA and were attributed to a good dispersion of graphene and to a strong bonding interaction between the graphene and the polymer [359]. The chemical bonding of the polymer chains to the rGO surface can restrict the movement of the polymer chains, increasing the temperature at which the polymer changes from a brittle state to a softer, rubber-like state. As well as the quality of bonding, the degree of exfoliation of the nanoparticles (higher degree of exfoliation equals a higher surface area and more bonding sites per gram) and the degree of the dispersion within the polymer matrix also affect the T_g [524,525].
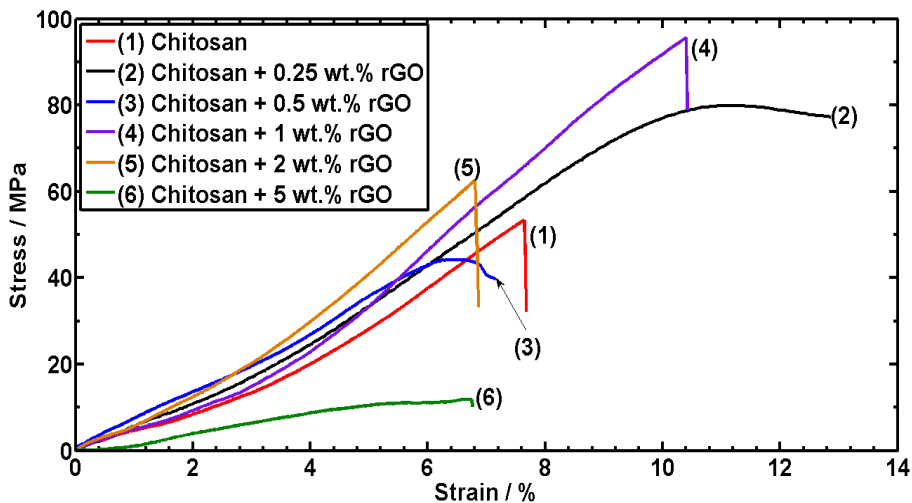
Figure 4.11: Tensile stress versus strain curves of chitosan nanocomposites containing 0 - 5 wt.% rGO.

Representative curves for chitosan and rGO nanocomposite specimens of 0, 0.25, 0.5, 1, 2 and 5 wt.% rGO are shown in Figure 4.11. Pristine chitosan undergoes a brittle failure, which is attributable to the mild heating process applied to prepare the chitosan film in the same manner as used to produce the chitosan-rGO nanocomposites. The heating process might cause the thermal crosslinking of the amino groups in chitosan [526], leading to an increase in

the E from 1 to 1.38 GPa, UTS from 24.2 MPa to 55.4 MPa and a small reduction in the ε_b from 14.5% to 8.2% in comparison to the values recorded in Chapter 3.

Table 4.2: The mechanical properties of chitosan-rGO nanocomposites.

GO content / wt.%	E / GPa	UTS / MPa	E_b / %
0	1.38 ± 0.15	55.4 ± 3.9	8.2 ± 1.7
0.25	1.75 ± 0.25	73.6 ± 4.2	11.6 ± 1.2
0.5	1.95 ± 0.26	41.1 ± 5.4	8.0 ± 1.7
1	2.64 ± 0.15	80.9 ± 20.8	10.8 ± 1.0
2	2.25 ± 0.43	65.6 ± 4.6	6.7 ± 0.6
5	0.69 ± 0.28	9.5 ± 3.3	5.3 ± 2.0

The introduction of rGO into chitosan has improved the Young's modulus recorded for samples of 0.25-2 wt.%, from 1.38 GPa up to 2.64 GPa (Table 4.2). This is due to rGO being an effective nanofiller, with a high Youngs modulus over 180 GPa [527,528], a high aspect ratio and a high surface area. The UTS values of the nanocomposites of 0.25-2 wt.%, are in general higher than the pristine chitosan, increasing from 55.4 MPa up to 80.9 MPa, apart from the 0.5 wt.% nanocomposite that has a UTS of 41.1 MPa. Enhancements of the UTS may be attributed to the high strength of rGO and effective stress transfer originated from the strong covalent bonding between chitosan and rGO. Samples containing 0.25 and 1 wt.% rGO have a higher ε_b (11.6% and 10.8% respectively) and the 0.5 wt.% sample has a similar ε_b (8%) than pristine chitosan (8.2%), presumably due to a good dispersion of rGO within the nanocomposites and the mobility of rGO nanosheets during testing [369,400]. This is presumably due to the covalent bonding between rGO and chitosan which prevents the realignment of the chitosan chains when the nanocomposite is placed under strain, similar to other chitosan-rGO nanocomposites [209]. Samples containing 2 wt.% rGO failed at a slightly lower ε_b than pristine chitosan, which may be attributable to a poorer dispersion of rGO within the nanocomposite because of the higher rGO concentration.

The 5 wt.% rGO nanocomposite was brittle due to the inadequate dispersion of rGO within the nanocomposite and failed at a low E, UTS and ε_b. Nanocomposites with even higher rGO concentrations (7 wt.% and 10 wt.%) were too brittle to form into test specimens using the current procedure, and were therefore not tested.
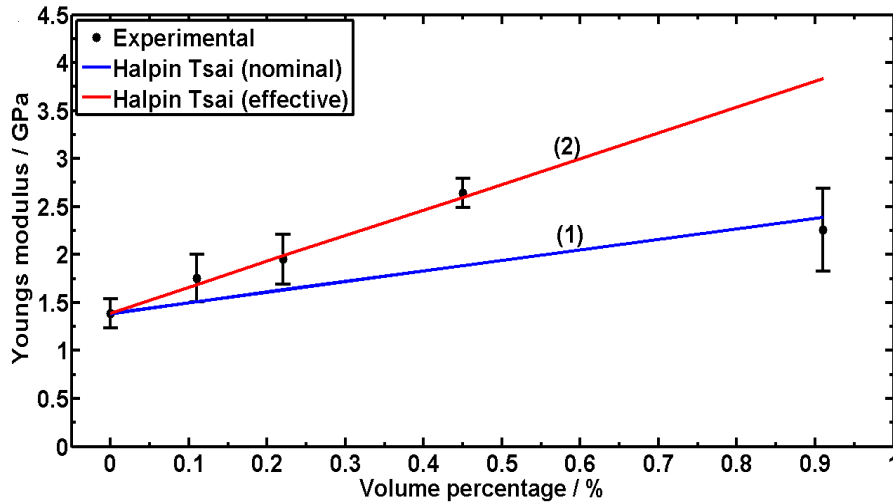
Figure 4.12: Halpin-Tsai modulus prediction estimates of chitosan nanocomposites, using both nominal and effective volume fractions of rGO in comparison with the experimental data.

The modified Halpin-Tsai method (Equations 4.2 to 4.5) allows for the calculation of the Young's modulus of nanocomposites with randomly orientated nanosheets [529,530].

$$E = \frac{1 + \frac{2l_{rgo}}{3t_{rgo}} \times \eta_1 \times V_g}{1 - \eta_1 \times V_g} \tag{4.2}$$

where:

$$\eta_1 = \frac{\frac{E_g}{E_p} - 1}{\frac{E_g}{E_p} + \frac{2l_{rgo}}{3t_{rgo}}} \tag{4.3}$$

The nominal filler volume fraction, V_g, can be determined from:

$$V_g = \frac{\frac{X}{\rho_g}}{\frac{X}{\rho_g} + \frac{100 - X}{\rho_p}} \tag{4.4}$$

116

where E_g and E_p are the Youngs modulus of chemically reduced GO (217.5 GPa, taken from the average Young's modulus of rGO reported in two papers, 185 GPa [527] and 250 GPa [528]) and chitosan (1.38 GPa) respectively, X is the wt.% of rGO within the nanocomposite, l_{rgo} and t_{rgo} are the length (1 μm) and thickness (3.5 nm) of the single rGO nanosheets taken from AFM and laser sizing analysis (assuming the nanocomposites are fully exfoliated within the matrix), and ρ_g and ρ_p are the densities of rGO and chitosan (3,120 kg m^{-3} and 1,458 kg m^{-3} from gas pycometry of rGO and chitosan powder, respectively). The effective filler volume fraction, V_g^e, which takes into account the contribution of the adsorbed or attached polymer chains, can be determined from [506]:

$$V_g^e = V_g \times \left(1 + \left(k_c \times R \times A \times \rho_g\right)\right) \qquad (4.5)$$

where k_c is a constant relevant to the ratio of the modulus of the adsorbed chitosan to the modulus of rGO and the thickness of the adsorbed layer (assumed as 0.22) [369,400,506], A is the specific surface area of chemically reduced GO (determined as 466 m^2 g^{-1} by B.E.T. surface area analysis) [203], and R is the radius of gyration of chitosan chains (52.5 nm) [531]. The results of the calculations are shown in Figure 4.12. It can be seen that in general the modified Halpin-Tsai model for randomly aligned nanocomposites using the nominal volume fraction underestimated the nanocomposites with lower rGO concentrations while the theoretical values calculated using the effective volume fraction show good correlation, which is consistent with previous studies on polymer-graphene nanocomposites [369,400]. Unlike the effective volume fraction method, the nominal volume fraction method did not consider the contribution of the interface to the modulus, thus giving lower theoretical values. At higher rGO concentrations (2 wt.%), the model with the effective volume fraction overestimated the experimental value, presumably due to the poorer dispersion of rGO sheets in the matrix. As previous described, this method assumes that the graphene sheets are fully exfoliated within the polymer matrix, which may not be the case for the 2 wt.% nanocomposite.

A high Young's modulus and a high mechanical strength are both important for microneedles as they are key parameters to determine the buckling and bending force failure values. Another key parameter is a high content of rGO which will allow for a considerable quantity of bonded drug to be included into the microneedle. The strongest nanocomposite contained 1 wt.% rGO, with increases of 95.6% for UTS to 80.9 MPa and 91.3% for Young's modulus to 2.64 GPa in contrast to pristine chitosan, whilst enhancing the ductility of pristine chitosan by 31.7%. The nanocomposite containing 2 wt.% rGO had an increase of 63.0% for Young's modulus and a 18.4% higher UTS than the pristine chitosan, which are lower than the increases found for the 1 wt.% nanocomposite. The higher content of rGO in the 2 wt.% nanocomposite, however, offers a higher drug loading capacity relative to the 1 wt.% nanocomposite. So, both nanocomposites were chosen for drug release and enzymatic degradation analysis.
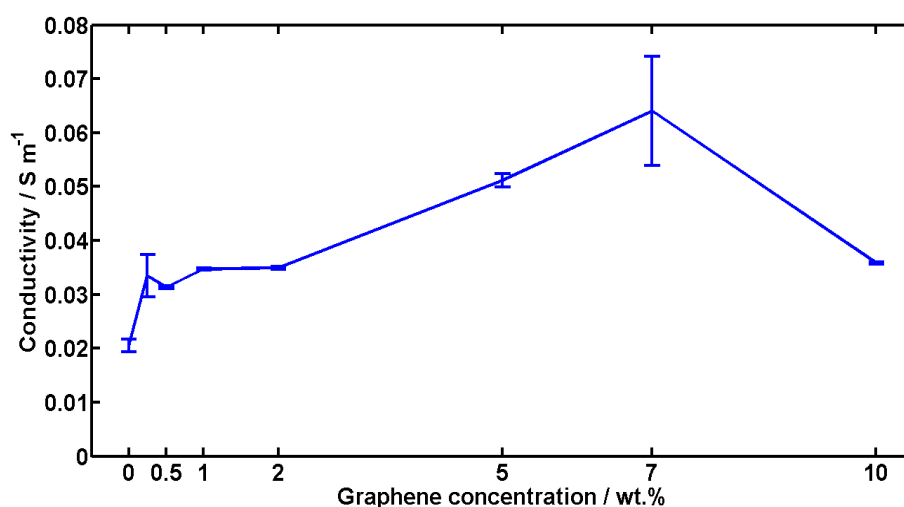
Figure 4.13: Conductivity versus rGO concentration of chitosan nanocomposites containing 0-10 wt.% rGO.

The electrical conductivity of chitosan and rGO nanocomposites of 0, 0.25, 0.5, 1, 2, 5, 7 and 10 wt.% rGO are shown in Figure 4.13. It has been shown previously that the diffusion of therapeutics from microneedle arrays can be improved by the process of iontophoresis [133–135,532], which is the electro-repulsion of charged molecules by an electrical field from

one electrode towards the other electrode [62]. If the chitosan-rGO nanocomposites are suitably conductive, they may be used as combined iontophoresis-microneedle array devices with improved drug delivery, relative to conventional microneedle arrays. Conductivity can be measured by calculating the inverse of resistivity, shown in Equation 4.6. There is a significant increase in conductivity between the pristine chitosan and the 0.25 wt.% rGO nanocomposite, with similar values between the nanocomposites of 0.25 wt.% to 2 wt.% rGO, and further increases between 2 wt.% and 7 wt.% rGO. The initial, major conductivity increase is at 0.25 wt.% rGO, therefore this concentration is presumed to be the percolation threshold [403]. The maximum conductivity of 0.06 S m^{-1} was achieved at 7 wt.% rGO, with conductivity dropping at 10 wt.% rGO to 0.03 S m^{-1}. All of the nanocomposites have a conductivity value similar to or higher than other conductive polymer-GO or rGO nanocomposites (Chapter 2, Table 2.3).

$$\text{Resistivity } (\Omega \, m) = \text{Resistance } (\Omega) \times \frac{\text{area (m}^2)}{\text{length (m)}} \qquad (4.6)$$

The reason behind the increase in conductivity is that graphene has a high electrical conductivity (electron mobility of 10,000 cm^2 v^{-1} s^{-1}) [179]. The dispersion and the degree of exfoliation are also important in order to avoid the formation of aggregates of graphite within the nanocomposites. With this in mind, the reduction in conductivity of the 10 wt.% in comparison to the 7 wt.% nanocomposite, despite having a higher concentration of rGO, can be attributed to a poorer dispersion and/or a lower degree of exfoliation within the 10 wt.% nanocomposite.
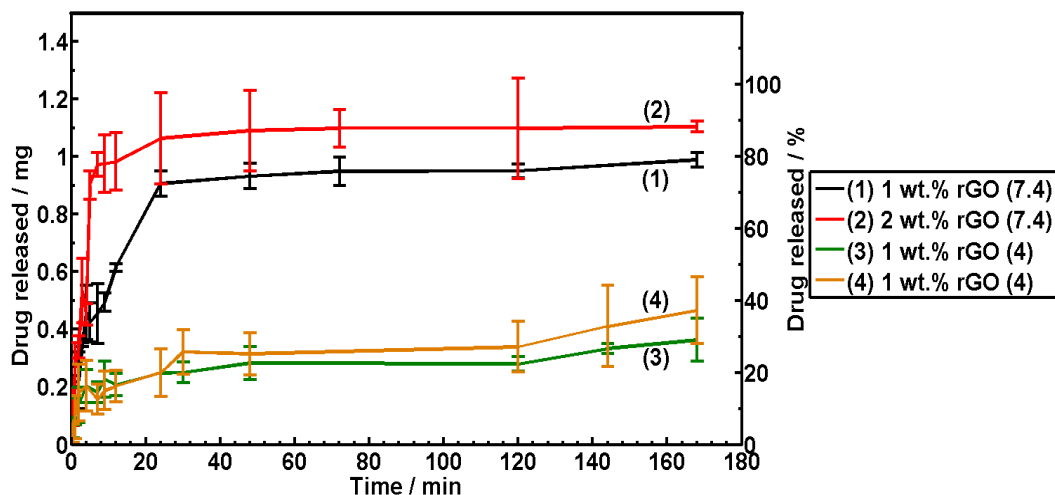
Figure 4.14: Cumulative drug release (mg) and percentage drug release (%) from rGO-FL nanocomposites (1 and 2 wt.% rGO) in a neutral (pH = 7.4) and acidic (pH = 4) environment. (B) Cumulative drug release (mg) from rGO-FL nanocomposites and Higuchi equation simulation of FL release from 1 wt.% and 2 wt.% rGO nanocomposites in pH = 7.4 PBS solution.

Figure 4.14 shows the cumulative and percentage of total drug released in a neutral environment (pH = 7.4) and an acidic environment (pH = 4) over 168 h. Similar to the chitosan-GO nanocomposites in Chapter 3, bonding rGO to FL within chitosan improves the drug release performance in comparison to pristine chitosan. This can be seen by comparing the chitosan rGO-FL nanocomposites to a hybrid of chitosan and free FL (Chapter 3) with the same quantity of FL. The chitosan-FL hybrid has a plateau after 120 h at 0.39 mg or 36% of the drug in the sample. The nanocomposites have both a quicker and more substantial delivery of the drug than the hybrid of chitosan and free FL, with the 2 wt.% nanocomposite achieving a maximum release of 91% of the available drug (1.09 mg) after 48 h and the 1 wt.% nanocomposite achieving a release of 75% (0.91 mg) after 24 h. The drug release from the nanocomposites plateaued and the cumulative release values remained effectively consistent until the end of the test.

The nanocomposites of 1 wt.% and 2 wt.% rGO with a loading of 1.2 wt.% FL were tested for their pH responsive drug release performance (Figure 4.14). When submerged in acidic solution (pH = 4), the release of FL from the nanocomposites was reduced in comparison

to release profiles in neutral conditions (69.2% reduction for the 1 wt.% and 69.5% reduction for the 2 wt.% nanocomposite). Samples of pristine chitosan fully dissolved within less than 12 h in the acidic medium which did not occur with the chitosan-rGO nanocomposites, showing that the presence of rGO nanosheets improves the resistance of chitosan to acid. Similar to the neutral condition test, rGO concentration affected the release performance of the nanocomposite with the 2 wt.% nanocomposite releasing 0.32 mg (or 27% of the available drug in the tested specimens) after 30 h and the 1 wt.% nanocomposite achieving a release of 0.28 mg (or 24% of the available drug) after 48 h.

The decrease in the release of FL from the rGO-FL into the acid medium compared to the case with the neutral medium, despite the low pH assisting in the swelling and presumably the partial dissolution of the chitosan nanocomposite, allows for pH sensitivity that will limit the release of the drug in areas of low pH, such as the stomach, and will increase the release in areas of neutral pH (e.g. the targeted disease area). The pH sensitivity of the nanocomposites is presumably due to the amine group in the chitosan coating of rGO when the rGO-FL is in the release medium. The amine group is important as it provides an electrostatic repulsion that prevents aggregation when in a neutral medium [216]. When this chitosan coating is partially dissolved in the low pH solution, the electrostatic repulsive forces are decreased substantially due to the degradation of the amine group to the point where the electrostatic attraction forces, between the carboxyl and hydroxyl groups on the rGO surface and the salt in PBS, are dominant and cause the rGO sheets to aggregate and hinder the release of FL [513,514].
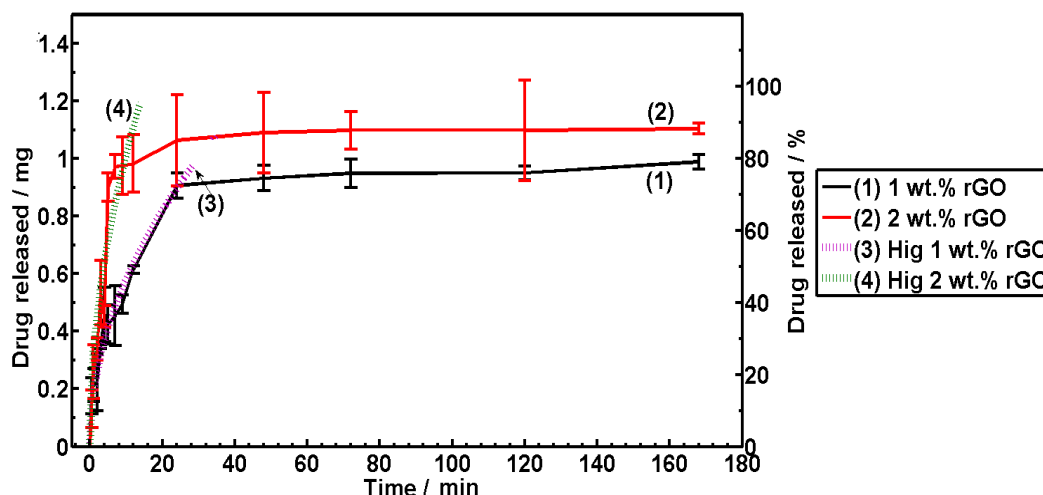
Figure 4.15: Cumulative drug release (mg) from rGO-FL nanocomposites and Higuchi equation simulation of FL release from 1 wt.% and 2 wt.% rGO nanocomposites in pH = 7.4 PBS solution.

The increase in drug release performance between the pristine chitosan and the chitosan-rGO nanocomposites may be explained by the effect that bonding FL to rGO has on the diffusion coefficient in water of FL, similar to the effect that was noted in Chapter 3 for the chitosan-GO nanocomposites. The hydrophilic chitosan reduced rGO sheets may have increased the diffusion coefficient of the rGO-FL in comparison to unbound FL. The Higuchi equation (Equation 3.3 and 3.7 from Chapter 3) simulation of FL release from pristine chitosan and from 1 wt.% and 2 wt.% rGO nanocomposites is shown in Figure 4.15. rGO-FL was released together from the nanocomposites into the PBS releasing medium due to physical adsorption of the FL onto rGO, where subsequently the FL will separate from the rGO as shown previously. When considering rGO-FL as the releasing agent, the Higuchi equations (Equations 3.3 and 3.4) can be used to model the initial drug release from the rGO nanocomposites, with the diffusion coefficient rising from 0.42×10^{-5} cm^2 s^{-1} for pristine FL to 0.27×10^{-4} cm^2 s^{-1} and 0.42×10^{-4} cm^2 s^{-1} for the rGO-FL in the 1 wt.% and 2 wt.% nanocomposite respectively.

As the FL content is constant but the rGO content varies from 1 wt.% to 2 wt.%, the drug loading ratio of FL onto rGO is presumably the cause of the different release profiles, similar to the chitosan-GO-FL nanocomposites in Chapter 3. The initial ratio of FL to GO in

122

the preparation of the nanocomposite is 0.55 for the 1 wt.% nanocomposite while it decreases to 0.38 for the 2 wt.% nanocomposite. Based on the maximum loading ratio of FL to rGO (0.26:1) and the amount of chitosan in the rGO (~ 85 wt.%), it can be considered that all the FL has been loaded onto the rGO sheets. So, the drug loading ratio in the 2 wt.% nanocomposite is lower than in the 1 wt.% nanocomposite. The higher rGO wt.% and the lower drug loading ratio of the 2 wt.% nanocomposite allows for a quicker diffusion of the FL from the rGO-FL nanohybrid. Drug loading ratio affects the bonding between the rGO and the drug, with lower drug loading ratios increasing the number of bonding sites between the rGO and the drug at a fixed mass of the drug.

Chitosan and chitosan-rGO nanocomposites containing 1 wt.% and 2 wt.% rGO had their enzymatic degradation characteristics tested in a solution of lysozyme and PBS to simulate *in vivo* conditions (Figure 4.16A). After 7 days, pristine chitosan samples were at 49% of their original mass, while the 1 wt.% rGO nanocomposite was at 64% and the 2 wt.% rGO nanocomposite was at 62% of their original mass. As with the chitosan-GO nanocomposites of Chapter 3, initially the enzymatic degradation rate is rapid as there is an abundance of ideal acetyl units for lysozyme to degrade through the β-glycosidic linkages [497,516]. When these ideal degradation sites are consumed, the degradation rate slows down and plateaus. This can be seen by the decrease in enzymatic degradation rate, with the remaining mass for pristine chitosan dropping to 46, 44 and 40% after 2, 4, and 6 weeks. Similarly, the mass for 1 wt.% dropped to 60, 55, and 53% and the mass for 2 wt.% dropped to 59, 55, and 49% after 2, 4 and 6 weeks respectively.
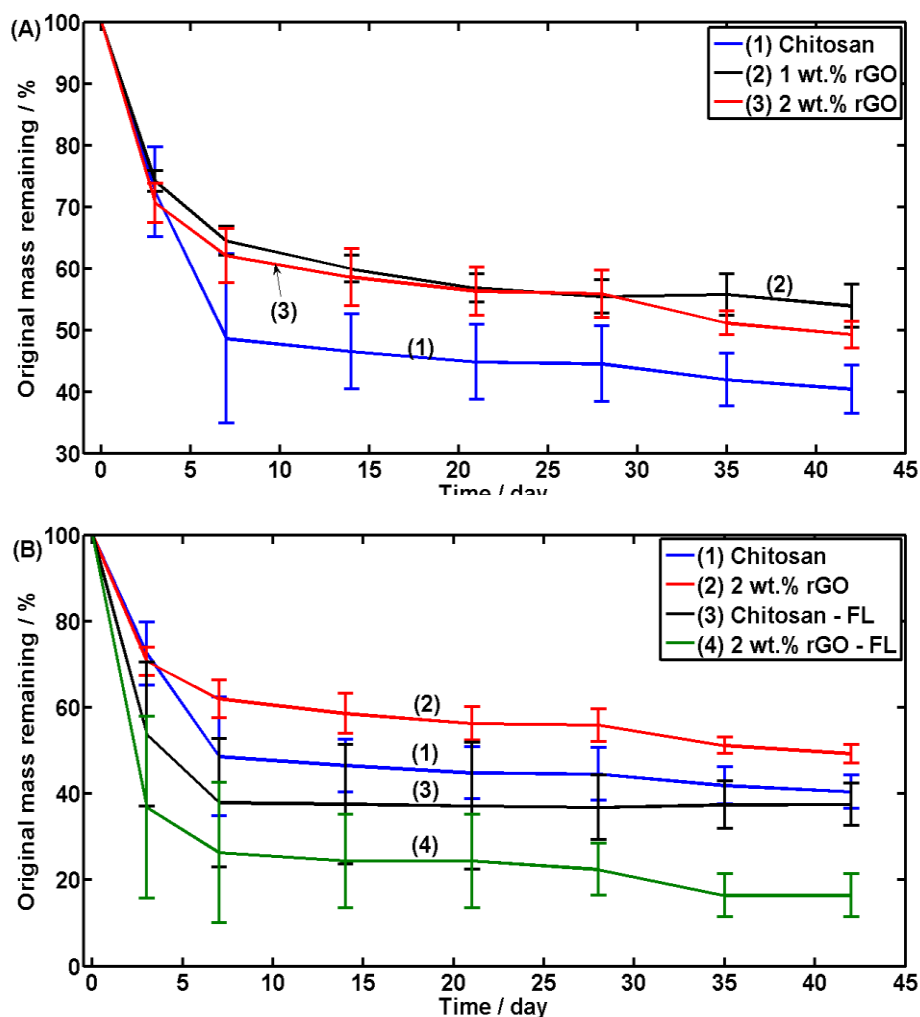
Figure 4.16: Mass change during enzymatic analysis of chitosan-rGO nanocomposites containing (A) 0 wt.% rGO, 1 wt.% rGO, and 2 wt.% rGO, and (B) chitosan-FL, and 2 wt.% rGO-FL nanocomposites over 4 weeks.

The difference in mass loss between the pristine chitosan and the rGO nanocomposites can be explained by the "tortuous path" model explained in Chapter 3. The presence of the rGO improved the barrier properties of the nanocomposites. The enzymatic degradation is also hindered by the strong covalent bonding forces between the amine and hydroxyl groups of chitosan and the epoxy, carboxyl and hydroxyl groups of rGO that can restrict the chitosan chain movement, as shown in the DSC and XRD analysis, and hence slow the cleaving of the chains by the lysozyme. It is interesting to note that the barrier properties of the nanocomposites are not dependent on the rGO concentration in this case, with both nanocomposites possessing a similar enzymatic degradation path, presumably due to the decrease in dispersion and

exfoliation quality for the 2 wt.% nanocomposite negating the effect of the increased rGO weight percentage in comparison to the 1 wt.% nanocomposite.

The inclusion of the drug into a nanocomposite also affects the enzymatic degradation rate, shown in Figure 4.16B. The inclusion of the drug quickens the enzymatic degradation rate and decreases the remaining mass at each time step in comparison to the nanocomposites without the drug. The difference can be attributed to both the dissolution of the drug from the samples and also the reduction in the bonding between the rGO and the bulk chitosan due to the presence of the drug. The remaining mass for 2 wt.% rGO-FL dropped to 27% after 1 week and plateaued at 23% after 4 weeks. At the end of the test there was only 16% of the original mass remaining, compared to 37% for the chitosan-FL.

4.3.3 Chitosan-rGO Microneedle performance

Microneedles were produced that contain chitosan-2 wt.% rGO-FL and these were subjected to compression and drug release tests. Figure 4.17 shows the microneedles successfully created by centrifuging highly viscous suspensions into female moulds.
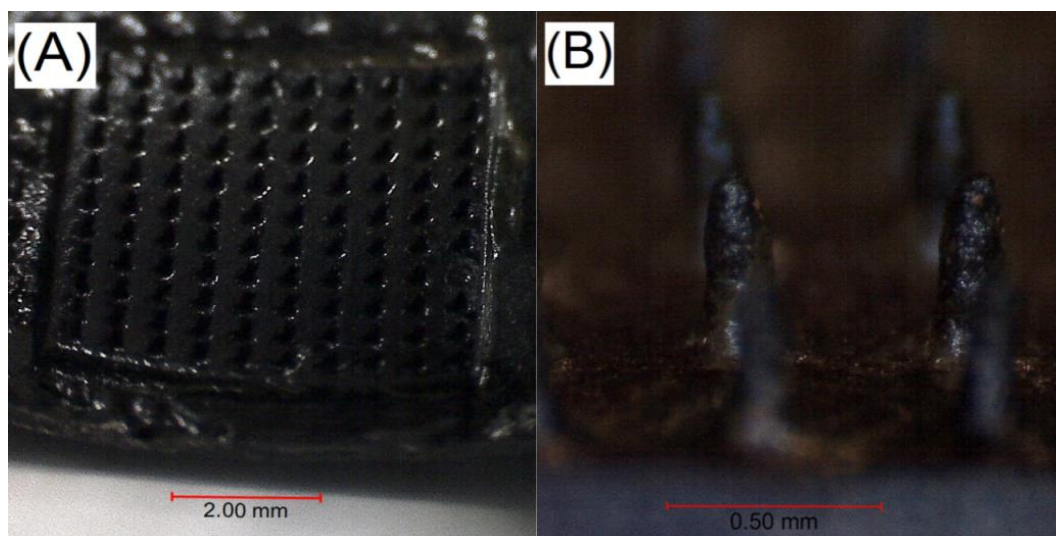
Figure 4.17: Optical microscopy images of the microneedles created from chitosan and 2 wt.% rGO-FL nanocomposites; (A) Overview of a microneedle array and (B) a close up which shows the shape of the individual microneedles.
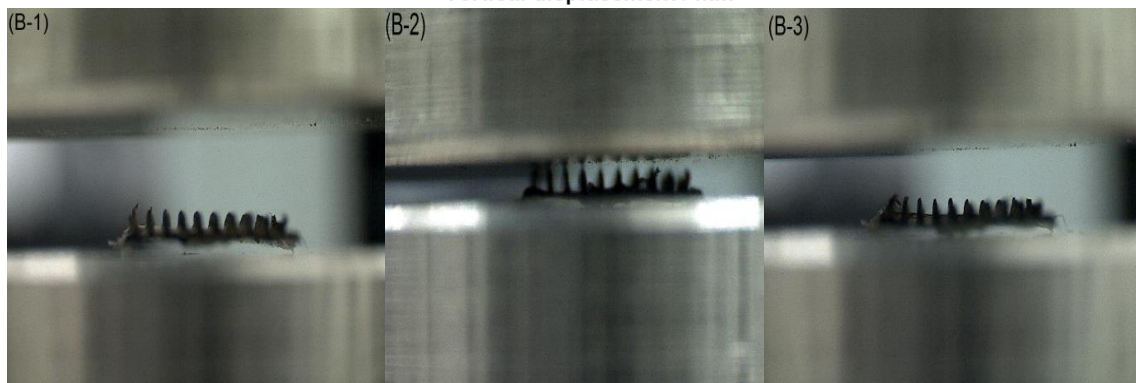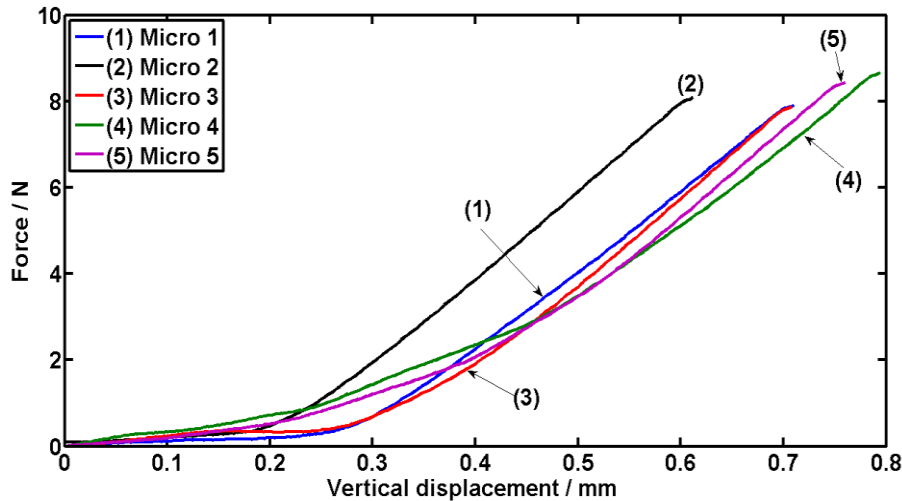
Figure 4.18: (A) Compression test results for six microneedle arrays created from chitosan and 2 wt.% rGO-FL nanocomposite material tested up to 10 N or a minimum distance between the two platens of 0.1 mm. (B) The images of the microneedle array on the stationary platen, (B-1) before the compression test, (B-2) during the compression test with a load of 10 N, and (B-3) after the compression test, showing no damage to the structure.

Microneedles were tested for their structural rigidity under compressive loads, as shown in Figure 4.18. The microneedle tip design has a radius of 20 μm in order to guarantee that the microneedle is sharp enough to puncture the SC (which requires a pressure of 3.18 MPa [533]); by considering the radius of the microneedle and the pressure required, each individual microneedle needs to withstand 0.016 N of force without failing due to bending or buckling, or 1.6 N for the entire microneedle array. All the microneedle arrays tested survived the compressive force of 1.6 N without failing, as shown in Figure 4.18A. The sudden increase in force on the curve is taken as the point where the compressive platen is meeting resistance from the microneedle shaft as it tries and fails to buckle or bend to microneedle shaft. Up to this point, the platen was compressing the microneedle tip, slightly deforming it from its original

126

shape. A failure of the microneedle would be seen as a sudden drop in the force required to displace the platen vertically. Figure 4.18 B1-B3 shows a series of images taken before, during and after the compression testing of a microneedle array to 10 N, showing that the microneedles can survive a compressive cycle designed to simulate insertion into human skin.

To test the force required to fail a microneedle, Figure 4.S2 shows compressive testing curves for microneedles using a 1 kN load cell with no limitation on maximum loads or minimum depths. The microneedles began to yield at a mean compressive force value of 37 N, the point at which is indicated by the relevant arrow on the curve. After this point, the individual microneedles are being crushed to a horizontal position after having failed by bending means (shown in the inset image). The compression testing indicates that the chitosan-rGO-FL microneedles are strong enough to withstand the force of insertion without the fear of buckling or bending of the individual microneedle shafts.
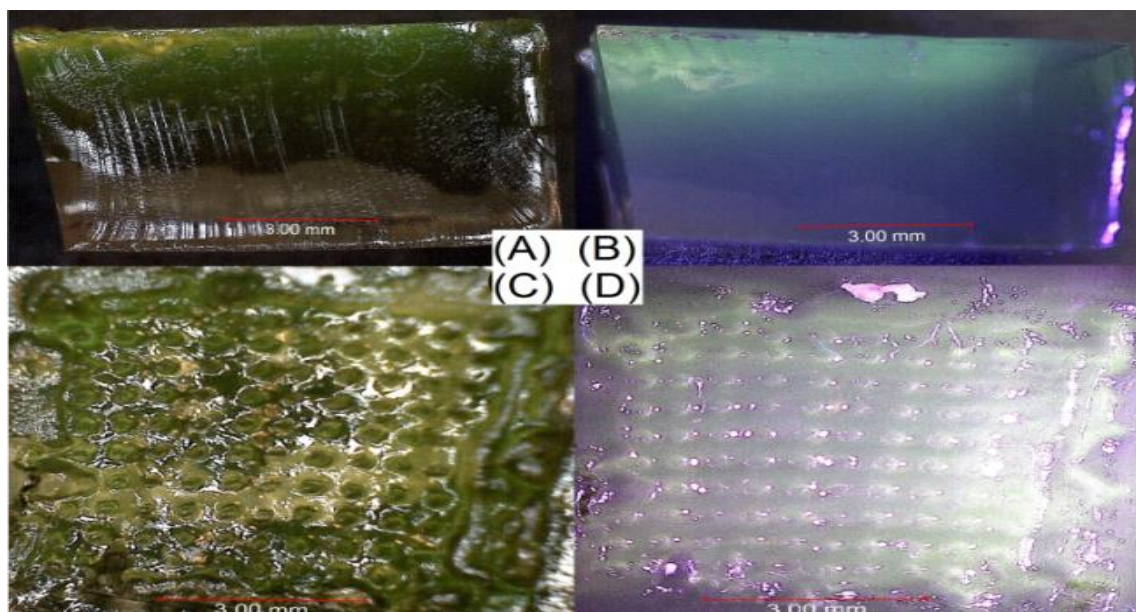
Figure 4.19: Optical microscopy images of the dissolution of rGO-FL from microneedle arrays after insertion into a gelatin hydrogel for 6 h. (A-B) Cross section of the hydrogel after the microneedle array has been removed. The diffusion of rGO-FL can be seen by the presence of the green-yellow color which shows the depth and width of diffusion through the hydrogel. In (C-D), the holes left behind when the microneedle array pierced the hydrogel can be seen in the plan view of the hydrogel. Images (B) and (D) are under UV light (400 nm) which was used to better highlight the fluorescence of FL In contrast to gelatin.

Figure 4.19 shows optical microscopy images of the dissolution of rGO-FL from microneedle arrays after 6 h into paraffin film (simulating the SC) and a gelatin hydrogel (simulating the VE) [120]. The hydrogel contains water that will allow the drug to diffuse, much like the bodily fluids between cells in the VE. Once the microneedle array was removed with tweezers and the hydrogel cross-sectioned with a knife, the diffusion of rGO-FL can be seen in Figure 4.19 A-B as the green-yellow colour from which one can see the depth of diffusion (about 2 mm) through the hydrogel. Figure 4.19 C-D is a plan view of the upper surface of the hydrogel and the characteristic green-yellow colour of rGO-FL can be seen on the surface following diffusion of the rGO-FL from the microneedle into the hydrogel. Images (B) and (D) are under UV light (400 nm), which was used to better highlight the fluorescence of FL in contrast to gelatin. Of note in images (C) and (D) are the holes left behind by the microneedle points after insertion on the surface of the hydrogel sample. This confirms that the microneedles were sufficiently designed to withstand insertion and to penetrate the synthetic layers of the SC (paraffin film) and into the VE (the hydrogel). The microneedles also successfully released the rGO-FL into the hydrogel medium, showing that the chitosan rGO-FL nanocomposites can potentially be used in microneedle arrays for transdermal drug delivery.

4.4 Conclusions

GO was successfully reduced to rGO by hydrogen and electrostatic bonding chitosan to GO in an aqueous suspension, followed by heating the chitosan-coated GO suspension at 37 $^{\circ}$C for 72 h. This biocompatible body temperature reduction process is comparable in reduction effectiveness to higher temperature (90 $^{\circ}$C) processes; the lower temperature allowed for the reduction of GO in the presence of drugs and cells for the development of drug delivery systems and tissue constructs within biomedical and biological applications. The rGO produced was

stable in water, PBS and cell culturing media, and demonstrated pH-sensitive drug release profiles.

The introduction of rGO to chitosan improved the mechanical properties and the conductivity of pristine chitosan, with the strongest nanocomposite containing 1 wt.% rGO showing an increase of 47% for Youngs modulus and 39% for UTS over pristine chitosan whilst maintaining the ε_b at 11.8%. The maximum electrical conductivity of 0.06 S m^{-1} was achieved at 7 wt.% rGO and the percolation threshold was found to be 0.25 wt.%. Similar to chitosan-GO nanocomposites, the chitosan-rGO nanocomposites had improved drug delivery properties over pristine chitosan in neutral conditions, and the nanocomposites showed a pH responsive release of the drug. The presence of rGO reduced the enzymatic degradation rate in comparison to pristine chitosan, due to a decrease in the permeability of the enzyme through the nanocomposite. Chitosan-rGO nanocomposites were formed into microneedle arrays and were shown to be strong enough in compression testing to survive the force of insertion through the SC. The microneedles could release the drug FL when inserted into a hydrogel, used to simulate the dermal layers of the body.

The in-situ body temperature reduction of GO provides an efficient reduction method for the use of polymer-graphene composites in the biomedical sector. The enhancement of the mechanical, electrical, and the drug release performance attributed to the inclusion of rGO means that chitosan-rGO nanocomposites have high potential for use in enzymatically degradable microneedle arrays for transdermal drug delivery. The conductivity of the chitosan-rGO nanocomposites may allow them to be used for electrically stimulated drug delivery applications, i.e. iontophoresis. Combining a microneedle made out of the chitosan-rGO nanocomposite with iontophoresis stimulation may increase the release of large MWt drugs from the nanocomposite relative to passive diffusion.

Chapter 5. Chitosan-graphene quantum dot nanocomposites

5.1 Introduction

In Chapters 3 and 4, GO and rGO have been used as the nanoparticles within the chitosan nanocomposites. GO and rGO have improved the mechanical properties of the chitosan, imparted pH sensitivity to the drug release, and in the case of rGO, increased the electrical conductivity to the nanocomposite. The addition of pH sensitivity and electrical conductivity to chitosan-graphene nanocomposites can make the nanocomposites useful for drug delivery, i.e. pH sensitive release within the bowels and electrically-stimulated, iontophoretic release, but neither nanoparticle can add the functionality of imaging/tracking of the bound drug *in vivo*. Graphene quantum dots (GQDs) have the potential to add this extra ability to chitosan-graphene nanocomposites. The GQDs have intrinsic PL properties that allow for the GQDs to be imaged under fluorescent light for the potential tracking of the GQDs (and any bonded drugs) through the body. They have a low cytotoxicity, unlike the semiconductor QDs discussed in Section 2.3.5.

As well as being PL, GQDs are highly reduced rGO nanoparticles and were therefore thought to be an excellent choice for a filler within a nanocomposite; as discussed in Section 2.4.2, reducing GO to rGO can help to partially return some of the excellent properties of pristine graphene nanoparticles, such as electrical conductivity and mechanical strength, whilst keeping the functional groups that aid in the dispersion of GO. Increasing the conductivity of chitosan is important if the nanocomposites are to be used for iontophoretic/electrically stimulated drug release, and as such, the GQDs are an interesting nanoparticle to do so. For use as a microneedle array, the nanocomposite will need to be mechanically strong; this requirement will make use of the improved mechanical properties of the rGO-based GQD.

GQD were synthesised using previously reported methods [217] and characterised to determine their PL properties. Chitosan-GQD nanocomposites were assessed to determine the optimal wt.% of GQD to maximise the electrical conductivity, mechanical and enzymatic degradation properties. Microneedle arrays were formed from nanocomposites of chitosan and drug-coated GQDs. The nanocomposite microneedles were tested for mechanical integrity under simulated skin insertion conditions. Their ability to release small MWt drugs through passive diffusion and large MWt drugs through electrically stimulated iontophoresis was assessed.

5.2 Experimental section

5.2.1 Materials

Chitosan powder (MWt = 100,000-300,000, Acros Organics), isopropanol alcohol (reagent grade), and phosphate buffered saline (PBS) tablets (pH = 7.4) were purchased from Fisher Scientific. The following chemicals were purchased from Sigma Aldrich: hydrochloric acid (36.5%), hydrogen peroxide (29-32% in H_2O), acetic acid (> 99.7%), potassium permanganate (97%), sodium nitrate (> 99%), lysozyme (from chicken egg white, ~100,000 U mg^{-1}), sulphuric acid (95-98%), fluorescein sodium (FL), graphite powder (≤ 20 μm), rhodamine B, norharmane (β-Carboline), lidocaine hydrochloride (LH, > 99%), trypsin from porcine (BioReagent grade), fluorescein sodium labelled – bovine serum albumin (BSA, BioReagent grade), 3-[4,5-dimethylthiazol-2-yl]-2,5-diphenyltetrazolium bromide (MTT) solution (1 mg ml^{-1} in PBS) and ethylenediaminetetraacetic acid (EDTA, BioReagent grade). Dulbecco's modified eagle medium (DMEM), penicillin, streptomycin, and fungizone were purchased from Gibco Invitrogen (Paisley, UK). Fetal bovine serum was purchased from Advanced Protein

131

Products (Brierley Hill, UK). All chemicals were used as received unless otherwise described.

5.2.2 Preparation of graphene quantum dots

Graphene oxide was synthesized from a modified Hummers [187] method and subsequently purified, exfoliated and freeze dried as outlined before in Chapter 3. The aqueous GO suspension (with a raised pH of 8, ~ 3 mg ml^{-1}) was treated in a Parr Series 4000 autoclave at 200 $^{\circ}$C for 10 h (pressure of boiling water at 201 $^{\circ}$C = 1.6 MPa) to generate reduced graphene oxide quantum dots (GQDs), as described in the literature with some modifications [217]. The suspension was placed in a dialysis bag (Fisher Scientific Biodesign Dialysis tubing, Mw cut off = 3.5 kDa) and the residua chemicals were allowed to diffuse into the distilled water surrounding the dialysis bag. The GQD were collected in an aqueous suspension from the dialysis bag and lyophilised in a Labconco FreeZone Triad freeze-dryer to be stored as a powder in a desiccator.

5.2.3 Cell viability

All human skin and fat were collected and used on an anonymous basis with ethical permission from patients undergoing abdominoplasties or breast reductions from the Department of Plastics, Burns and Reconstructive Surgery, Sheffield Teaching Hospitals under a Human Tissue Authority research bank tissue license number 08/H1308/39. From the collected fat, mesenchymal stromal cells (MSC) were isolated and cultured in DMEM (containing foetal bovine serum, streptomycin (100 µg ml^{-1}), fungizone (630 ng ml^{-1}) and penicillin (100 units ml^{-1}) [534].

When the culture reached a 50% confluence, the cells were treated with a trypsin solution for 10 min to detach, collected and then the cell solution was centrifuged at 1000 rpm for 5 min to form a pellet (Hettich Rotafix 32A centrifuge). Cells were counted, with cells

seeded (10,000 per well) in a 48 well plate. Cells were incubated overnight in DMEM to allow for cell reattachment, after which the DMEM medium was replaced with MGQD suspensions (20, 50, 100, 200, 500 µg ml^{-1} in DMEM) for 6 h and 24 h incubation times (each testing iteration was tested in triplicate). At the end of each incubation time, cells were washed with PBS and then incubated in fresh DMEM until 72 h post-treatment when cells were assessed by the MTT-EDTA. Cells were incubated for 40 min at 37 ^{o}C, after which the formazan salt was eluded by acidified isopropanol. The optical densities of the resultant solutions were measured with a plate reader at 540 nm with a reference filter of 630 nm (Bio-Tek ELx800). Control samples of untreated cells in DMEM were taken as 100% viable, and the optical densities of the MGQD treated cells were compared to these values. An Olympus CK40 microscope was used for cell imaging.

5.2.4 Cell viability and imaging

Dermal fibroblast cells were isolated and cultured in DMEM in a 37 ^{o}C and 5% CO_2 environment [534]. After the cell culture was 50% confluent, the cells were separated from the well plates by a trypsin solution for 10 min and collected by centrifugation of the cell suspension at 1000 rpm for 5 min to form a pellet. Cells were seeded at 10,000 cells per well into a 48 well plate. To allow for reattachment, cells were incubated in DMEM overnight. The DMEM was replaced and the cells were incubated with GQD suspensions (50 µg ml^{-1} or 100 µg ml^{-1} in DMEM) for an incubation time of 12 h. Cells were washed with PBS and then fixed with glutaraldehyde. A Leica TCS SP8 two-photon confocal microscope (excitation source 690 nm, emission filter 360 nm) was used for imaging of cells.

5.2.5 Drug loading onto graphene quantum dots

LH or BSA was bonded to GQDs as follows: 0.3 mg ml^{-1} of GQDs was dispersed in distilled water through stirring and sonication. To this suspension, 0.3 mg ml^{-1} of LH or

BSA was added and stirred for 24 h before centrifugation (8000 rpm for 1 h) separated the GQD-LH or GQD-BSA from the supernatant containing the unbound drug. This GQD-LH or GQD-BSA was lyophilized in a freeze-dryer and then stored in a desiccator until further use.

5.2.6 Preparation of nanocomposites

Chitosan powder was dissolved in 2 wt.% acetic acid – water solution (15 mg ml^{-1}) at room temperature for 24 h under stirring. The required amount of GQDs (0.25 wt.% - 2 wt.%) was dispersed in distilled water and the suspension was added under stirring to the chitosan solution. The suspension was left to stir in a fume hood to evaporate most of the solvent until it became a viscous nanocomposite suspension of chitosan – GQD (~80 mg ml^{-1}). The mixture was degassed in a vacuum oven for 1 h at room temperature and then poured into a petri dish to air dry. Chitosan film without GQDs was prepared in parallel.

5.2.7 Characterisation of GQDs and chitosan-GQD nanocomposites

A Veeco Dimension 3100 with Olympus AC160TS probes in tapping mode at 0.5 Hz was used for atomic force microscopy (AFM). A Brookhaven ZetaPALS (660 nm wavelength) was used for dynamic light scattering (DLS), with 3 cycles of 2 min runs on suspensions of 1 mg ml^{-1} MGQD in KNO$_3$ buffer (10 µM concentration). UV-Vis spectrometry (0.3 mg ml^{-1}) was achieved using a Perkin Elmer Lambda 900 spectrometer with a 1 nm resolution. PL spectroscopy was conducted using a Horiba Fluoromax 4 with excitation sources from 300-400 nm and emission readings from 360-600 nm with a wavelength resolution of 2 nm. Photoluminescence quantum yield measurements used fluorescein sodium in 0.1 sodium hydroxide, rhodamine B in ethanol and 0.01% hydrochloric acid, and norharmane in 0.1 M

sulphuric acid as reference standards. Quantum yield measurements were taken by using Equation 5.1 [535], shown below:

$$\phi_{qd} = \phi_{st} \times \frac{Grad_{qd}}{Grad_{st}} \times \frac{\eta_{qd}^2}{\eta_{st}^2}$$

(5.1)

where "ϕ" is the fluorescence quantum yield, "Grad" is the gradient of the curve of emission versus absorbance, "η" is the refractive index for the solvent used in the solution, and "qd" and "st" are QDs and the standards used.

PL lifetime analysis (1 mg ml^{-1}) was achieved through Time Correlated Single Photon Counting (TCSPC): a Mira 900 Ti-Sapphire laser (10 W), with the wavelength halved through an A.P.E. Second Harmonic Generator, was used as the laser source, a Becker and Hickl SPC-830 was used as the single photon counting module with a Becker & Hickl GmbH PHD-400-N High Speed Photodiode Module as an electronic trigger, and an ID Quantique ID100-50 single photon detection module was used to detect the emission from the sample. Perkin Elmer Spectrum 100 with a diamond attenuated total reflectance unit was used for Fourier transform infrared (FT-IR) spectroscopy between 400-4000 cm^{-1} with a resolution of 1 cm^{-1}. A Stoe Stadi P was used for X-ray diffraction (XRD) analysis with Cu K$_\alpha$ irradiation (0.154 nm wavelength), with operating parameters of 40 kV, 35 mA, and a scanning speed of 1 $^{\circ}$ min^{-1}. A Micromeritics AccuPyc II 1340 was used to measure the density of the GQDs, achieved at room temperature (24 $^{\circ}$C) by using 10 purge cycles and 10 calculation cycles of helium gas.

Electrical conductivity (number of samples = 5) was measured using an Agilent Technologies 34401A digital multimeter, with contact points painted using silver paint (RS Components, RS 186-3600) and using a two probe method. The multimeter was calibrated by testing with various metals of known conductivity. The mechanical properties of chitosan nanocomposites were tested on a Hounsfield universal

mechanical testing machine using a 1 kN load cell and a 1 mm min^{-1} strain rate in accordance with ISO-527. Dog bone shaped test specimens (number = 5) were used, measuring 22 mm in length, 2.7 mm in width and 1 mm in thickness. Enzymatic degradation tests were carried out by placing nanocomposite film samples (number = 5) into 30 ml of 37 °C PBS solution (pH = 7.4) with a 1.5 µg ml^{-1} concentration of lysozyme [499]. Samples were maintained over the course of 8 weeks at 37 °C and agitated at 100 rpm in a Stuart SI500 bioincubator. After each time step, specimens were removed, washed with distilled water, and dried before being weighed and placed into 30 ml of fresh PBS and lysozyme solution.

Thermogravimetric (TGA) was achieved using a Perkin Elmer Pyris 1 with a nitrogen atmosphere with a flow rate of 20 ml min^{-1} from 40 to 700 °C at 5 °C min^{-1}. A Perkin Elmer Lambda 900 spectrometer was used for UV-visible (UV-Vis) spectroscopy from 200-800 nm with a 1 nm resolution.

5.2.8 Production of nanocomposite microneedles

The production of microneedle arrays has been described before [151,152]. Briefly, the procedure consists of two parts: the filling of the main needle shaft with a nanocomposite containing a therapeutic and the filling of the needle base with a conventional nanocomposite. Female silicone moulds were filled with an excess amount of a highly viscous nanocomposite suspension of chitosan – GQD (~80 mg ml^{-1}), with and without a therapeutic drug for testing of drug release and compression testing respectively. Centrifugation at 8000 rpm for 1 h was used to fill the microneedle-shaped cavities, with excess suspension cleaned from the surface. The microneedle arrays were placed inside a fume hood to air dry. This cycle was repeated 3 times to fill the needles. Once the needles were filled, the base of the needles was filled with high viscosity nanocomposite suspension (without drug), centrifuged for 1 h at 8000 rpm and dried in

a vacuum oven overnight at 40 ºC. Upon drying, the exposed side of the microneedle array was gently sanded with fine sandpaper to remove spurs and gently removed from the female mould. Microneedles were stored in desiccators and prior to use were dried further at 40 ºC overnight in a vacuum oven. Pristine chitosan microneedles were also fabricated for comparison.

5.2.9 Compression testing of microneedles

The microneedles were tested using a Hounsfield universal mechanical testing machine using a 10 N load cell and a 1 mm min^{-1} compression rate. Microneedle arrays were fixed to a steel plate and a second steel plate was used to uniformly compress the microneedle arrays (number = 5).

5.2.10 Therapeutic release from microneedles

Quantitative analysis of LH drug release was achieved through the use of UV-Vis spectroscopy (Perkin Elmer Lambda 900 operating at a resolution of 1 nm). Microneedle arrays (chitosan-1 wt.% GQD-LH, number = 5) were placed in 10 ml, 37 ºC PBS solution (pH = 7.4) and tested over 6 h whilst being agitated at 100 rpm. The UV-Vis spectra of the released solutions were compared to the spectra of free LH in distilled water of known concentrations.

5.2.11 Therapeutic release from microneedles with iontophoresis

Microneedle arrays were created from a chitosan-1 wt.% GQD nanocomposite, with the GQDs coated with BSA. These microneedle arrays were used for iontophoretic release of the high MWt drug. The electrical circuit for the microneedle array was based on a prototyping circuit board (PCB). The power to the PCB was supplied by a PP3 9 V 280 mAH nickel-metal hydride (Ni-MH) battery, with the battery snap-on connector linked to the PCB by solder-less jumper wires and an on-off switch (Scheme 5.1). A 2 kΩ

resistor was added to the circuit between the switch and the microneedle to lower the voltage across the circuit.
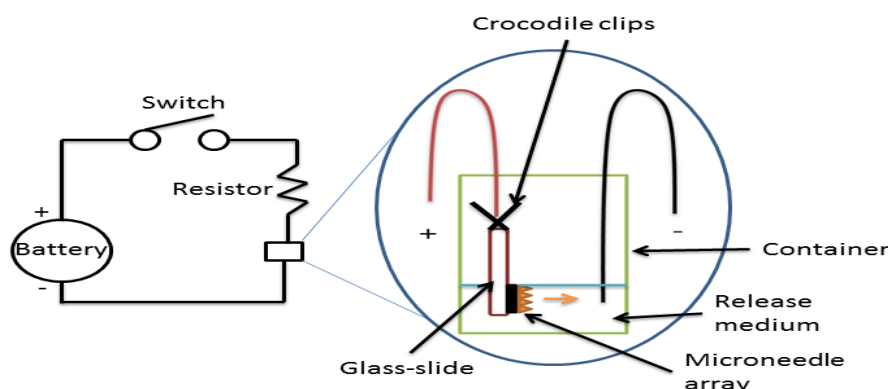
Scheme 5.1: Schematic of the system used to analyse the effect that Iontophoresis has on the therapeutic release from a microneedle array.

Electrically stimulated microneedles were created by mounting the chitosan-GQD microneedle array to a microscopy glass-slide using double-sided tape. One jumper wire, feeding from the positive terminal, was arranged that its exposed end was fixed in contact with one side of the microneedle array. This was achieved by soldering the jumper wire to a crocodile clip; silver paint was applied from the microneedle array edge to the side of the glass-slide where the crocodile clip grasped the glass-slide. The second jumper wire, leading to the negative terminal, was submerged in the receiving medium (distilled water) into which the drug was to release. The glass-slide was submerged vertically in water up to the fixed microneedle array, with the crocodile clip and silver paint out of the water. This method ensured that the electrical flow was through the microneedle into the receiving medium.

5.2.11 Biostability of GQDs and drug-loaded GQDs

Suspensions of GQD, GQD-LH and GQD-BSA (0.3 mg ml^{-1}) were dispersed in distilled water, PBS and FBS, and digital images were taken after 5 min, 2 h, 4 h, and 24 h.

5.3 Results and discussion

5.3.1 Characterisation of graphene quantum dots
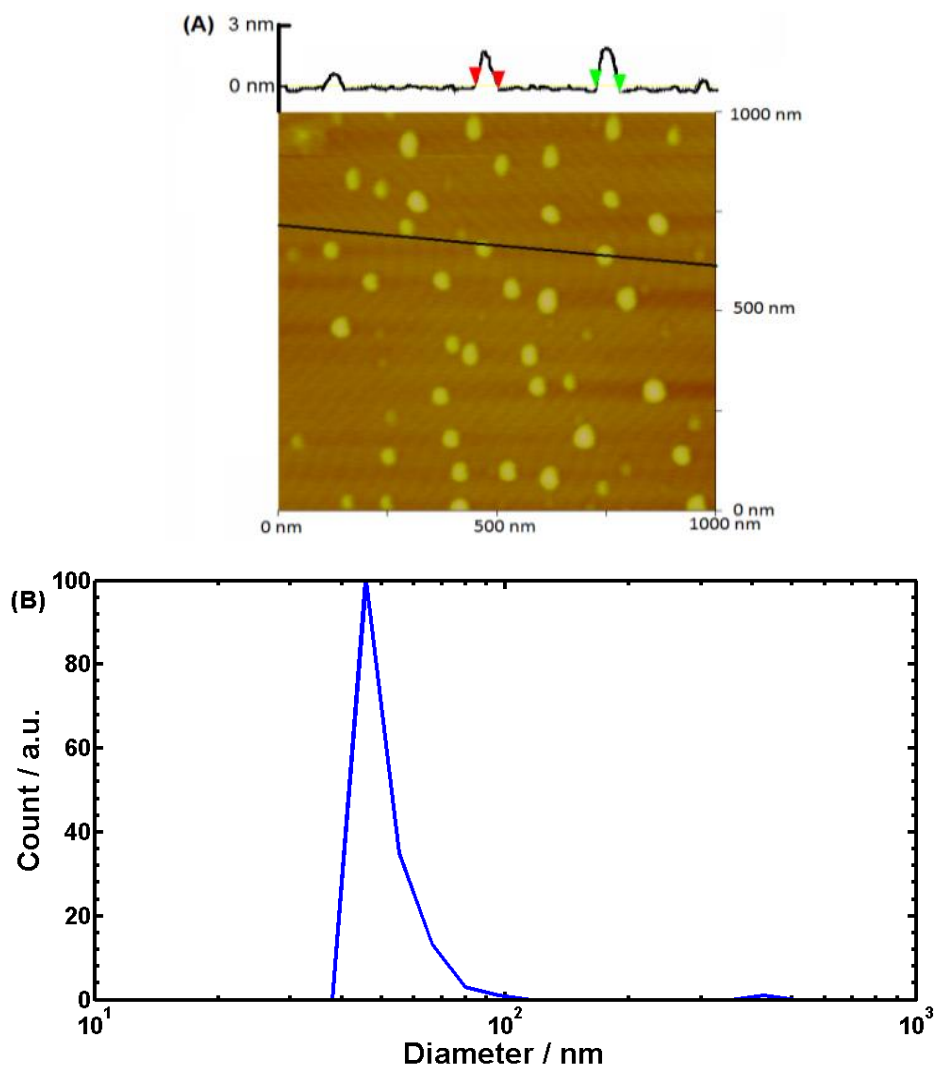
Figure 5.1: (A) AFM image and height profile of GQDs, (B) DLS data of GQDs, showing a large count in the 40-60 nm region.

GQDs were prepared through a hydrothermal reduction procedure (see Scheme 5.1).

Figure 5.1A is an AFM image of the GQDs on a mica substrate, demonstrating that the

GQDs are in general 50-55 nm in diameter, with an average diameter of 51.9 nm and an

average height of ~1.5 nm. The GQDs are thinner than the chitosan-reduced rGO in

Chapter 4 (3.5 nm) due to the hydrothermal route of reduction, i.e. no biomolecules were

used. The GQDs are thicker, however, than the GO from Chapter 3 (~1 nm) that served

as the precursor to GQD and pristine graphene that is estimated at ~0.34 nm thick

139

[536,537]. Presumably the thickness of the GQDs is due to the stacking of two or more of the rGO sheets together after the hydrothermal reduction due to aggregation as there was a substantial decrease in functional groups on the GQD surface compared to GO. This may lower the solubility in solvents, compared to GO, and therefore there may have been partial restacking. Figure 5.1B shows DLS analysis of the hydrodynamic diameter of GQDs, showing a large count of GQDs in the 40-60 nm region and a mean diameter of 54.8 nm.
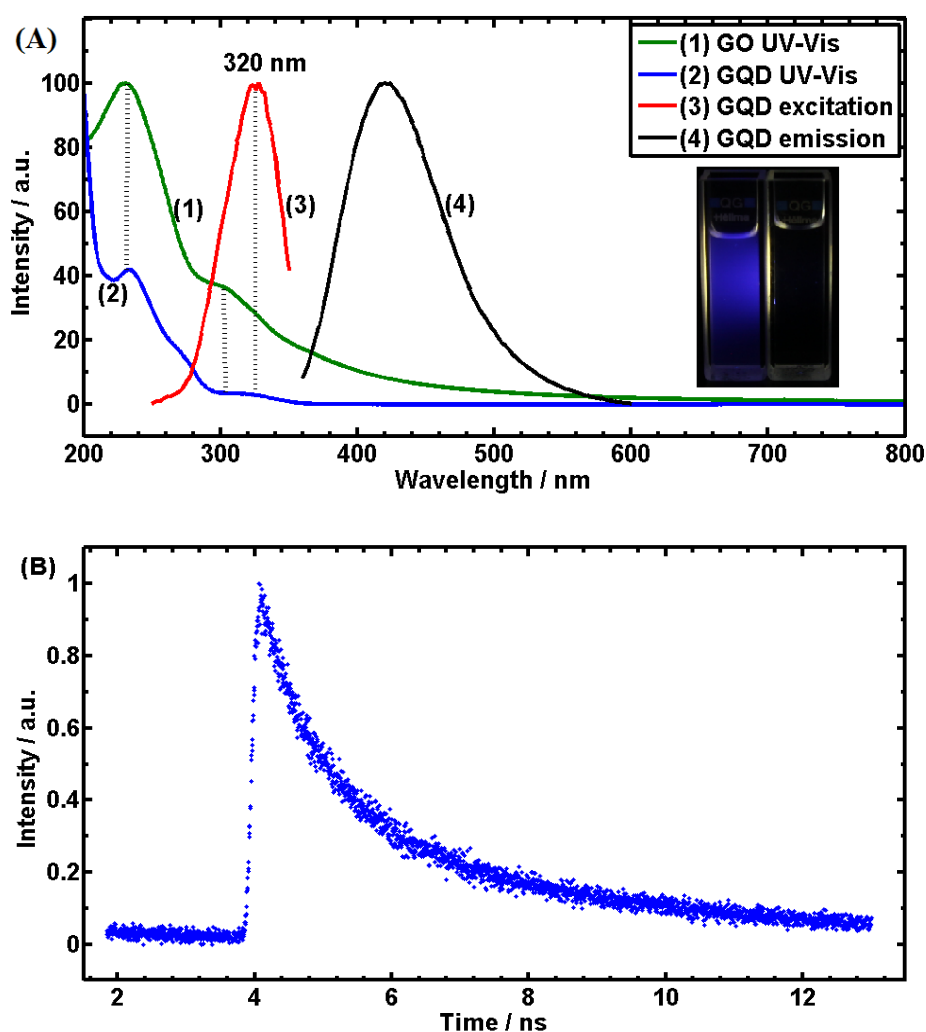
Figure 5.2: (A) PL and UV-Vis spectra showing the UV-vis absorption for GO and GQD, and PL excitation and emission wavelengths for GQD dots, and inset: (left) GQD in distilled water and (right) distilled water, showing the photoluminescent properties of GQDs under UV light (365 nm), and (B) PL lifetime data for GQD aqueous dispersion.

The UV-Vis spectra of GO and GQD show that the 230 nm peak of GO (Figure 5.2A, curve 1) remains for GQD (Figure 5.2A, curve 2), attributed to the $\pi \rightarrow \pi^*$ conjugations of C=C [187], but GQD has an additional peak at 265 nm attributed to the π transition network of graphene being restored [210]. The GQDs also possess an absorption peak at 320 nm, in contrast to the 300 nm peak of GO, similar to other hydrothermally reduced GQDs [217]. This initially indicates GO has changed to rGO in the GQDs during the hydrothermal reduction and cutting process. The PL spectra of the GQDs are also shown in Figure 5.2A, showing the maximum excitation at 320 nm and the maximum emission at 420 nm, indicating a Stokes shift of 100 nm which is similar to previously reported values [217]. The excitation peak at 320 nm is linked to the triple carbenes in the zigzag structure of the GQDs [217,538]. The quantum yield for the GQDs is calculated at 9.4% (data shown in Figure S5.1 in S.I.), again similar to the published literature for GQDs (5.5-14%) [337,338,539]. The selectiveness of the GQDs to the excitation wavelength is depicted in Figure 5.S2, which confirms the strongest emission at the excitation wavelength of 320 nm, with the emission intensity reducing at other wavelengths. The inset to Figure 5.2A shows the GQDs fluoresce under UV light (365 nm) as opposed to no fluorescence for the control sample of distilled water. Figure 5.2B shows PL lifetime data for GQDs, showing that a 1 mg ml^{-1} aqueous suspension has a lifetime of 2.3 ns. This value is similar to other GQDs in the literature (1-10 nanoseconds) and to that of conventional QDs of CdSe/ZnS QDs[540–542] and CdTe QDs [18].
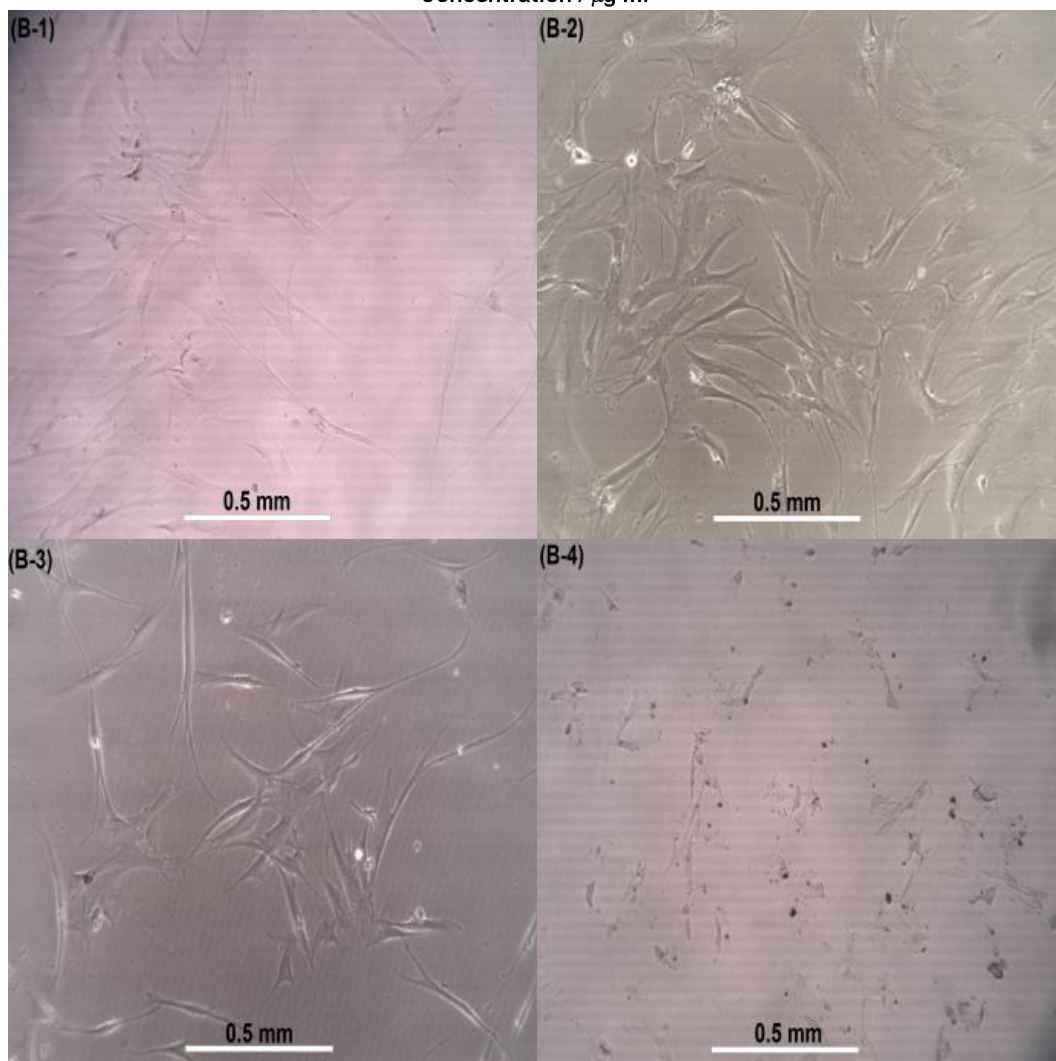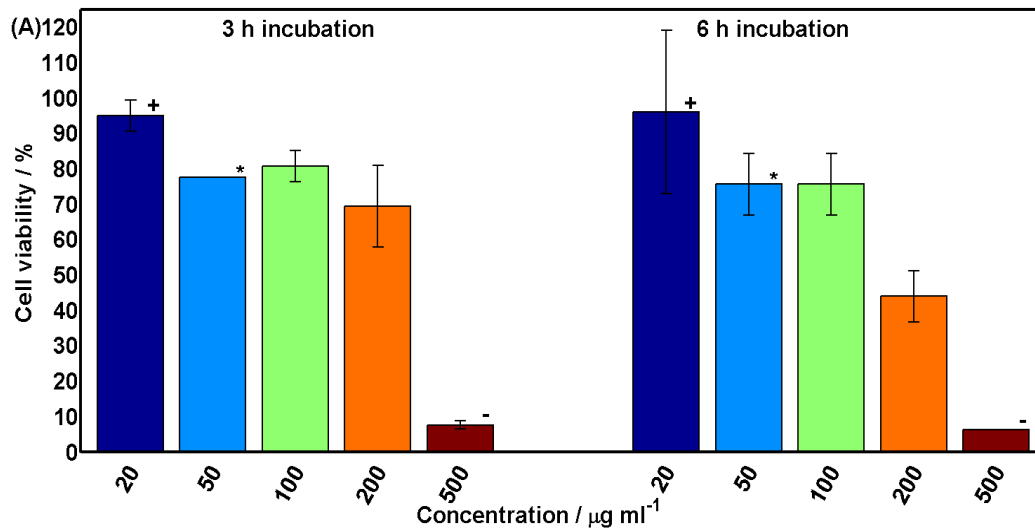
Figure 5.3: (A) MTT-ESTA cell viability results for GQD treated MSC. Concentrations were 20, 50, 100, 200, and 500 μg ml^{-1} and the incubation times were 3 h and 6 h. Results that are statistically similar (p < 0.05) to one another are shown with symbols (*, +, -). (B) Optical microscopy images for samples treated with (1) 0 (control), (2) 20, (3) 100, and (4) 500 μg ml^{-1}. Images were taken 72 h after the 24 h incubation time.

142

MTT cell viability results for MSC treated with GQD concentrations of 20, 50, 100, 200 and 500 µg ml^{-1} in DMEM for 3 and 6 h are shown in Figure 5.3A. For the 3 h samples, the concentrations of 20-200 µg ml^{-1} are within 69-95% cell viability range, comparable to other GQD reports (70-80%) [15,309,338,339], with a dose dependent cytotoxic effect only occurring at 500 µg ml^{-1}. Samples treated with 20 µg ml^{-1} for 3 h and 6 h had a cell viability of 95% and 96% respectively, with these values dropping to 75-80% for 50 and 100 µg ml^{-1} for 3 h and 6 h. For the 200 µg ml^{-1} sample, the cell viability for 3 h is 69% but this drops to 43% for the 6 h incubation time, showing a time dependent cytotoxic effect. Figures 5.3 B1-B4 show optical microscopy images of MSC treated with 0-500 µg ml^{-1} GQDs for 24 h incubation time. It can be seen by comparing the control sample with no GQDs and the 20 µg ml^{-1} sample that the morphology, size and quantity of the MSC are consistent. However, the quantity of cells in the 100 µg ml^{-1} sample has decreased in comparison to the first two samples. The quantity of cells in the 500 µg ml^{-1} sample is even lower compared to the 100 µg ml^{-1} sample, while the size and morphology of the cells have also changed compared to all the samples with lower concentrations. These results confirm that GQDs have limited cytotoxicity up to 100 µg ml^{-1} for 3 h or 6 h, but when exposed to 200 µg ml^{-1} or higher for 6 h or more the cells show signs of apoptosis and are reduced in size and quantity.

Figure 5.4 shows optical and fluorescent microscopy images of dermal fibroblast cells cultured with GQD concentrations of 50 µg ml^{-1} and 100 µg ml^{-1} for a 12 h incubation time. By overlapping the fluorescent images with the optical images, it can be seen that some cells are fluorescent due to the presence of photoluminescent GQDs within the cells. The PL emission is stronger for the cells treated with 100 µg ml^{-1} of GQD, with the higher concentration of GQDs allowing more of the GQDs to be endocytosed into the cells, relative to the lower concentration sample. These results

confirm that the GQDs can potentially be used for *in vivo* cell imaging [309,543], as well as for tracking drugs when they are loaded onto the nanoparticles. Using fluorescent imaging, QDs have previously been tracked migrating through the vasculature in the body [17] and have been tracked during drug delivery [18].
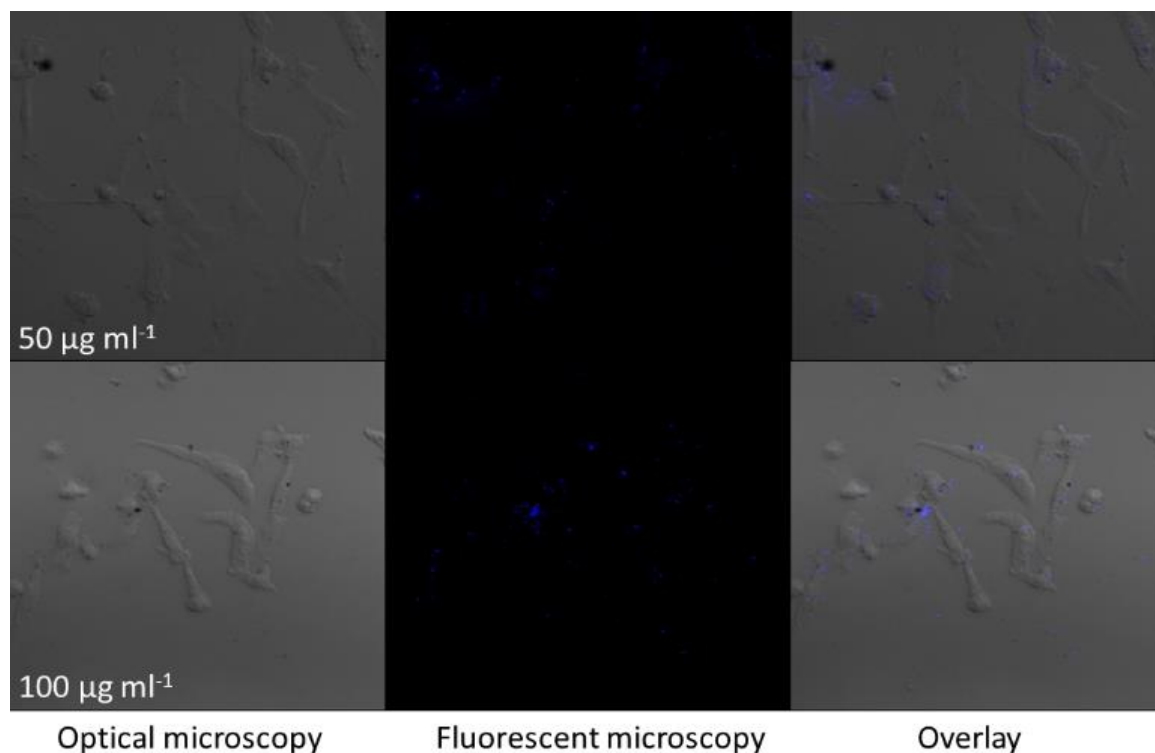
Figure 5.4: Optical and fluorescent microscopy images of fibroblast cells treated with 50 µg ml^{-1} and 100 µg ml^{-1} GQDs for a 12 h incubation time, showing the use of GQDs as fluorescent imaging agents.

5.3.2 Characterisation of chitosan-GQD nanocomposites

Figure 5.5A shows the FT-IR spectra of chitosan-GQD nanocomposites, from which chitosan can be identified through the N-H peaks at 2800 cm^{-1}, C=C at 1640 cm^{-1}, amino at 1535-1546 cm^{-1}, C-OH at 1405 cm^{-1} and C-O at 1050-1100 cm^{-1} [482]. The amino peak shifts from 1535 cm^{-1} for pristine chitosan to 1546 cm^{-1} for the 1 wt.% chitosan-GQD nanocomposite, and the C-O peaks shift from 1065 cm^{-1} and 1021 cm^{-1} for pristine chitosan to 1059 cm^{-1} and 1017 cm^{-1} for 1 wt.% chitosan-GQD due to hydrogen bonding between the amino groups of chitosan and the remaining oxygenated functional groups

on the GQDs [396,482]. The intensity of the main peaks, apart from a slight decrease in the amino and C-OH peaks, did not alter by a notable degree when the GQDs were introduced to chitosan, due to the relatively low content of GQDs within the nanocomposites relative to chitosan.
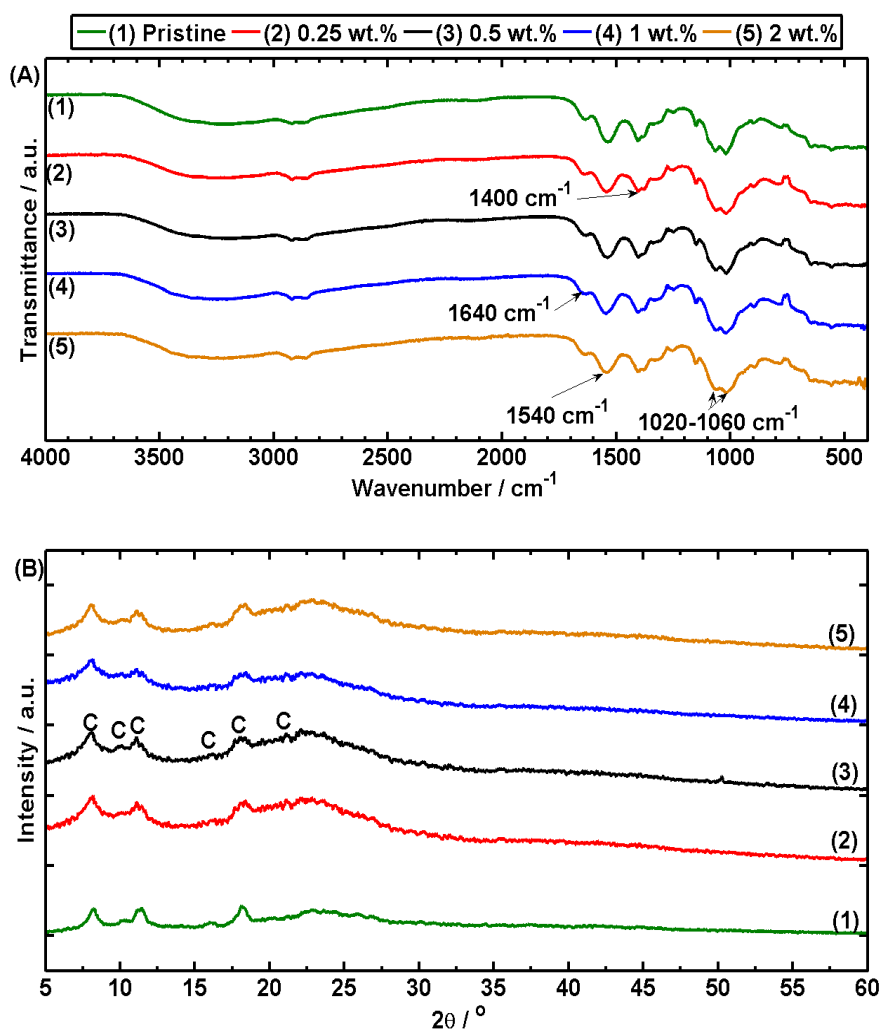
Figure 5.5: (A) FT-IR spectra, (B) XRD traces of chitosan-GQD nanocomposites. The C's in Figure 5.3B denote crystalline peaks from chitosan.

XRD traces (Figure 5.5B) allow for the crystallinity of chitosan to be measured as 59.9%, 51.1%, 54.6%, 56.1%, and 56.4% for chitosan and nanocomposites containing 0.25-2 wt.% GQDs, respectively, by using Equation 3.1 (Chapter 3). The presence of GQDs within the polymer presumably limits the mobility of some chitosan chains due to surface adsorption, hence restricting rearrangement of chitosan chains into

ordered chains to form crystallites and reducing the crystallinity [504], similar to the effect of GO within chitosan-GO nanocomposites in Chapter 3. The significant difference in crystallinity levels between chitosan-rGO (Chapter 4) and chitosan-GQD (Chapter 5) is presumably due to the deacetylation and the treatment procedure of the chitosan solution. As a reference, the crystallinity of the pristine chitosan for the chitosan-rGO series is much lower than the crystallinity of the pristine chitosan for the chitosan-GQD (15.3% versus 59.9%, respectively). The thermal treatment of the chitosan solution by heating at 37 $^{\circ}$C for 72 h has decreased the crystallinity, due to thermal crosslinking as previously reported [544].
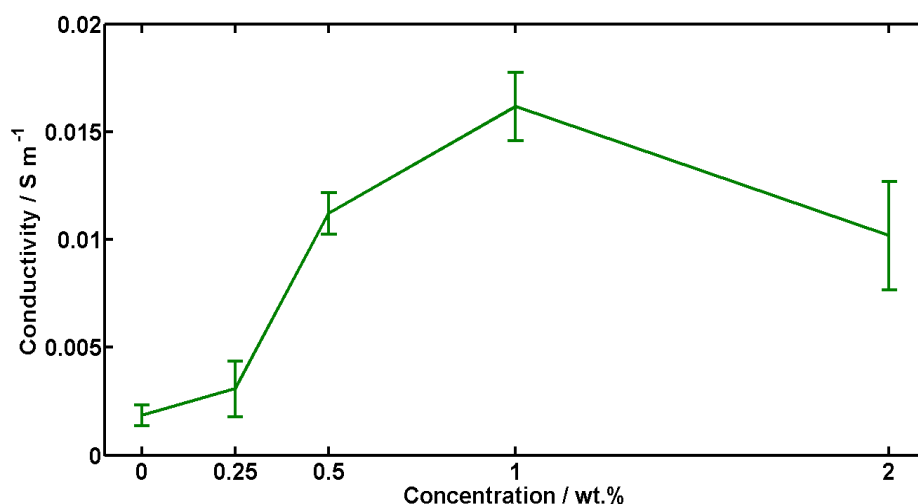
Figure 5.6: Electrical conductivity of chitosan-GQD nanocomposites as a function of GQD concentration.

Figure 5.6 shows the electrical conductivity of the nanocomposites, with peak conductivity occurring at 1 wt.% GQDs and a percolation threshold occurring at around 0.25 wt.%, similar to the percolation threshold of chitosan-rGO nanocomposites in Chapter 4. The low percolation threshold and the increase in conductivity for the nanocomposites compared to the pristine chitosan are due to the high reduction degree and the low thickness of the GQDs, which may have a conductivity close to that of pristine graphene [179]. The conductivity of the nanocomposite containing 1 wt.%

GQDs is 8.9 times of the original value for chitosan (0.0161 S m^{-1} versus 0.0018 S m^{-1}), and is comparable to other polymer-graphene nanocomposites with similar concentrations (0.001 to 0.01 S m^{-1}) [209,545,546]. The decrease in conductivity for the 2 wt.% GQD nanocomposite in contrast to the 1 wt.% GQD nanocomposite may be explained by the partial aggregation of GQDs within the nanocomposite. The difference in conductivity levels between chitosan-rGO (Chapter 4 and chitosan-GQD (Chapter 5) is presumably due to the crystallinity of the chitosan; it has been shown that the conductivity of chitosan films decreases with increased crystallinity [484]. The difference in crystallinity between the two chapters was previously discussed. Due to its relatively high conductivity and high GQD content which would facilitate a high drug loading within the nanocomposite, the 1 wt.% nanocomposite was chosen to undergo further analysis.
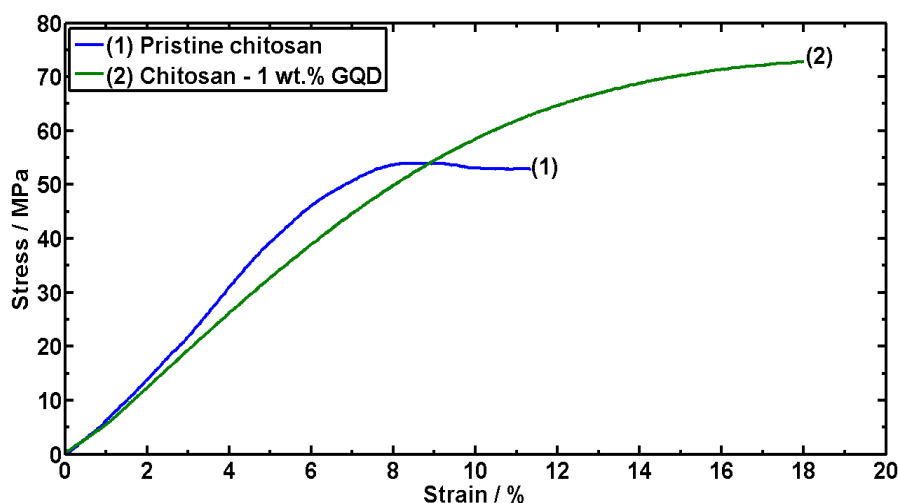
Figure 5.7: Representative tensile stress-strain curves for chitosan and chitosan-1 wt.% GQD nanocomposite.

Figure 5.7 shows representative tensile testing curves for pristine chitosan and chitosan-1 wt.% GQD nanocomposite. The ε_b increase by ~37% from 15.5 ($\pm$ 4.2) % for pristine chitosan to 21.2 ($\pm$ 3.2) % for the 1 wt.% GQD nanocomposite, presumably because of both the orientation of GQDs towards the tension direction which absorbs

energy [400,505,547] and the change in crystallinity as previously discussed. The UTS

for pristine chitosan is 62.5 ($\pm$ 9.4) MPa, which increased by ~36% to 84.8 ($\pm$ 11.8) MPa

for the 1 wt.% GQD, courtesy of the strong interfacial interactions between chitosan

matrix and GQD filler. Similarly, increases in the ε_b (4%) and UTS (27%) were noted

for nanocomposites of poly(styrene-butadiene-styrene) with 1 wt.% CdTe QDs,

attributed to the strong interfacial bond between the polymer and the QDs [437]. The E

has remained similar despite the inclusion of 1 wt.% GQDs, with 1.48 ($\pm$ 0.38) GPa for

pristine chitosan compared to 1.45 ($\pm$ 0.14) GPa for the nanocomposite. The similar E

values may be attributed to the cancelling out of two opposing factors: the reinforcing

effect of GQD nanofiller and the decreased crystallinity of the chitosan. GQD can have

a reinforcing effect on chitosan arising from its high modulus [527,528] and high surface

area, but it is not as effective a nanofiller as GO (Chapter 3) and chitosan-reduced rGO

(Chapter 4) because of its smaller lateral size, lower aspect ratio, and the reduction in

surface functional groups [548]. Countering this expected improvement from the

presence of GQD, a lower crystallinity can result in a lower E value [483], thus causing

the actual E value to remain effectively the same between the pristine chitosan and the

nanocomposite.

The enzymatic degradation profile of the 1 wt.% nanocomposite in a PBS

solution containing the enzyme lysozyme is shown in Figure 5.8. Within the first week,

the enzymatic degradation rate was higher for the 1 wt.% GQD nanocomposite than for

the pristine chitosan, as can be seen by the lower remaining mass for the former. This

initially quicker enzymatic degradation rate of the nanocomposite, relative to pristine

chitosan, may be due to the lower crystallinity of the chitosan-GQD nanocomposite

which promotes faster enzymatic degradation [486]. The effect that crystallinity has on

enzymatic degradation can be seen by comparing the mass losses for pristine chitosan

between Chapter 4 (~50% loss) and Chapter 5 (~23%), with the lower crystallinity chitosan degrading faster.
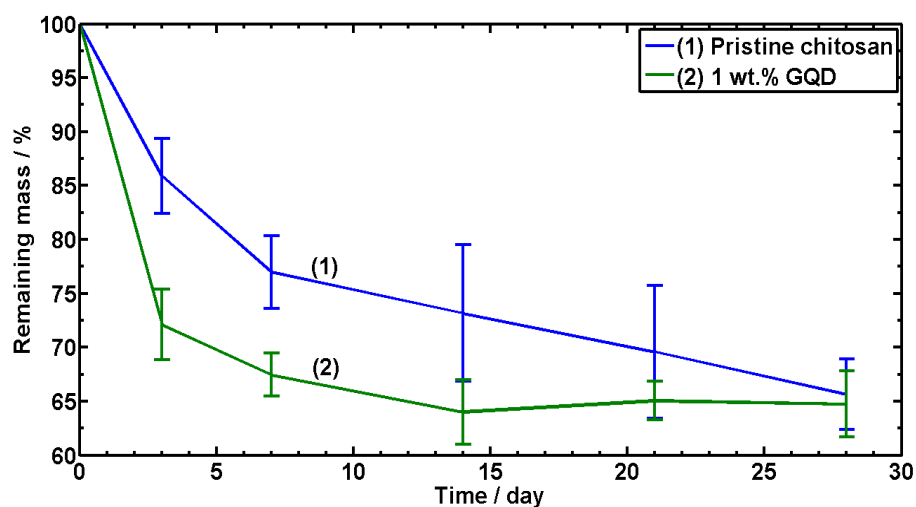
Figure 5.8: Enzymatic degradation profiles for chitosan and chitosan-1 wt.% GQD nanocomposite.

After 28 days, both the pristine chitosan and the 1 wt.% chitosan-GQD nanocomposite were reduced to around 65% of their original mass. The similarity between the remaining mass of the pristine chitosan and the nanocomposite is due to the relatively low loading of GQD within the nanocomposite (just 1 wt.%) and the limited effect that the GQD had upon the permeability of the nanocomposite; it is reported that exfoliated, large aspect ratio nanoparticles can reduce the permeability of a nanocomposite due to the previously explained "tortuous path model" and this effect was evident in the enzymatic degradation studies in Chapter 3 and Chapter 4, but the GQDs have a low aspect ratio, as discussed in previously, and therefore have a limited effect on the permeability of the nanocomposite when present at this low wt.% loading.

5.3.3 Chitosan-GQD nanocomposite microneedles

Microneedle arrays of chitosan-1 wt.% GQD nanocomposite were formed by solution casting into moulds and subsequently drying. Optical microscopy images of chitosan-1 wt.% GQD-LH microneedles can be seen in Figure 5.9A and 5.9B, showing the

alignment of the microneedles within an array as well as the main shaft and conical tip. As shown in Figure 5.9C, the five microneedle arrays tested can all withstand a compressive force of at least 10 N, showing that they are strong enough to withstand the compressive force of insertion into human skin. The microneedle arrays have not broken or bent noticeably after the tests (Figure 5.9C Inset) in comparison to their shape before the test (Figure 5.9B).
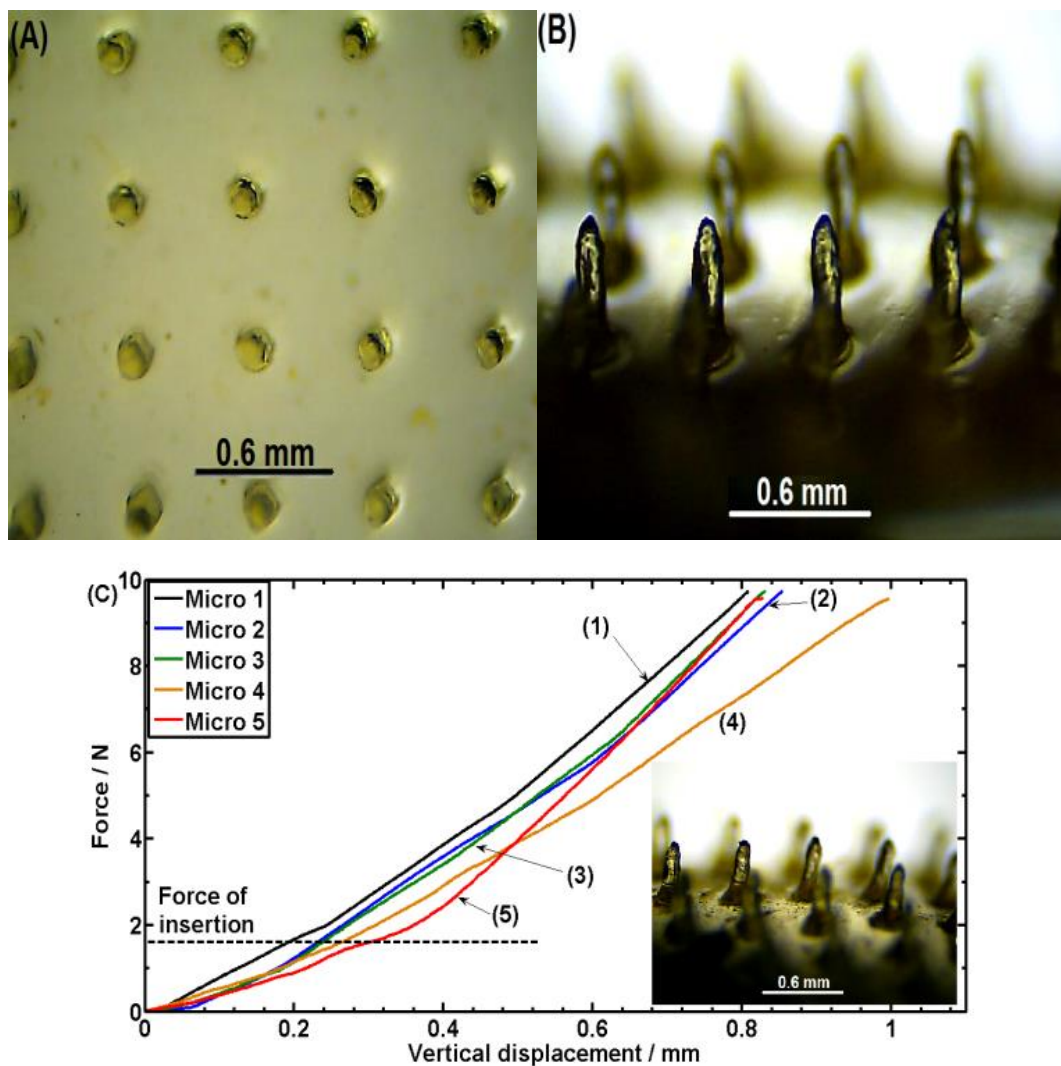
Figure 5.9: (A) Vertical and (B) side view optical microscopy images of chitosan-1 wt.% GQD-LH nanocomposite microneedle array. (C) Compressive force-displacement curves for chitosan-1 wt.% GQD microneedles. (Inset) Optical microscopy image of a chitosan-1 wt.% GQD microneedle array after compression testing to 10 N. The microneedles have not broken under the force applied.

The depth of penetration of the microneedle array was determined by inserting chitosan-GQD microneedles into chicken-skin and subsequently cross-sectioning the chicken skin (Figure 5.S3). Microneedle arrays were inserted by hand into chicken skin and left *in situ* for 1 h before examination. The microneedles were intact after insertion and the depth of penetration is typically 400-500 µm and the width of the channel 250-350 µm. This confirms that the microneedles are strong enough to insert into skins.
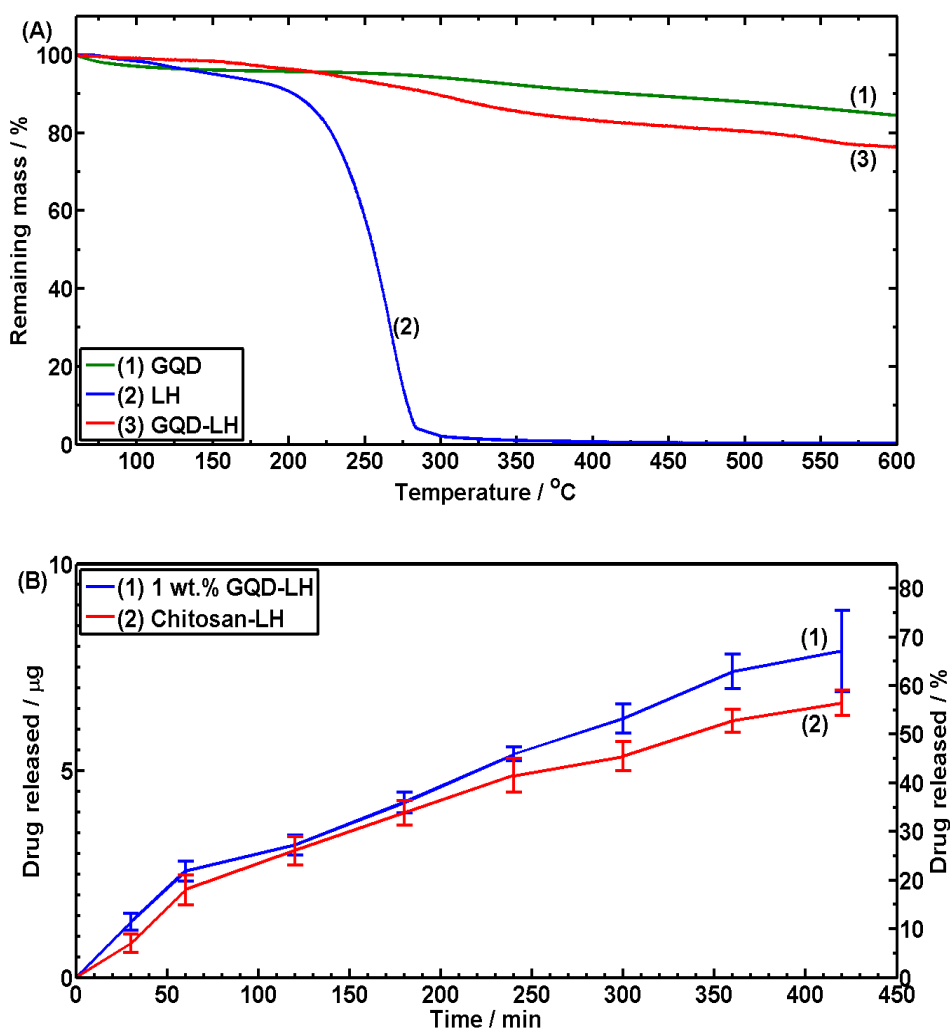
Figure 5.10: (A) TGA curves for GQDs, LH, and GQD-LH, and (B) the release rate of LH from chitosan and chitosan-1 wt.% GQD-LH microneedle shafts containing the same amount of LH.

Figure 5.10A shows TGA curves for the GQDs, LH, and GQD-LH. The loading of LH onto GQDs was determined to be 0.12:1 from the residual masses of GQDs (91.5%), LH (0.3%) and GQD-LH (81.6%) at 500 ^{o}C, accounting for the absorbed moisture of the three materials. Taking into consideration this loading ratio of LH to GQDs, a desired amount of GQD-LH was added to chitosan solution to prepare a chitosan-GQD-LH nanocomposite suspension at a concentration of 1 wt.% GQDs. This nanocomposite suspension was then used to form the microneedle shafts for drug delivery testing, with the base of the microneedle patch made from the same nanocomposite but without the drug. To make control microneedle shafts of chitosan-LH, a chitosan-LH solution was created with the same concentration of LH as in the chitosan-1 wt.% GQD-LH suspension. By restricting the LH to the microneedle shafts and not the base, all of the GQD-LH will enter the body through the bloodstream thus reducing the use of expensive drug in microneedle arrays.

Figure 5.10B shows the release rate of LH from the microneedle shafts of pristine chitosan and the chitosan-1 wt.% GQD nanocomposite containing the same amount of LH (11.5 μg). For the GQD-LH nanocomposite microneedles, the drug is bound to the surface of the GQDs, whereas in the chitosan-LH microneedles the drug was directly incorporated into chitosan. In the former, the GQD-LH was released together into the medium but it was shown in Chapter 4 that FL can diffuse away from rGO over time. After 1 h, ~23.0% (2.6 μg) of LH was released from the GQD-LH microneedle, with a maximum release of ~68.3% (7.9 μg) released after 7 h. This compares to ~18.1% (2.1 μg) of LH after 1 h from the chitosan-LH microneedle, with a maximum release of 57.4% (6.6 μg) released after 7 h. Up to 6 h, there is a similar drug release profile between the two sample types, but after 6 h the nanocomposite microneedles obtained a quicker and more substantial release than the polymer microneedles. Similar

improvements in the release of drugs from chitosan nanocomposites containing a drug with GO or rGO have been noted in Chapter 3 (Page 83) and Chapter 4 (Page 118); this was attributed to an increase in the diffusion coefficient of the drug when bonded to GO or rGO compared to the free drug, which is presumably the same cause of the improved drug delivery from the GQD-LH microneedle.
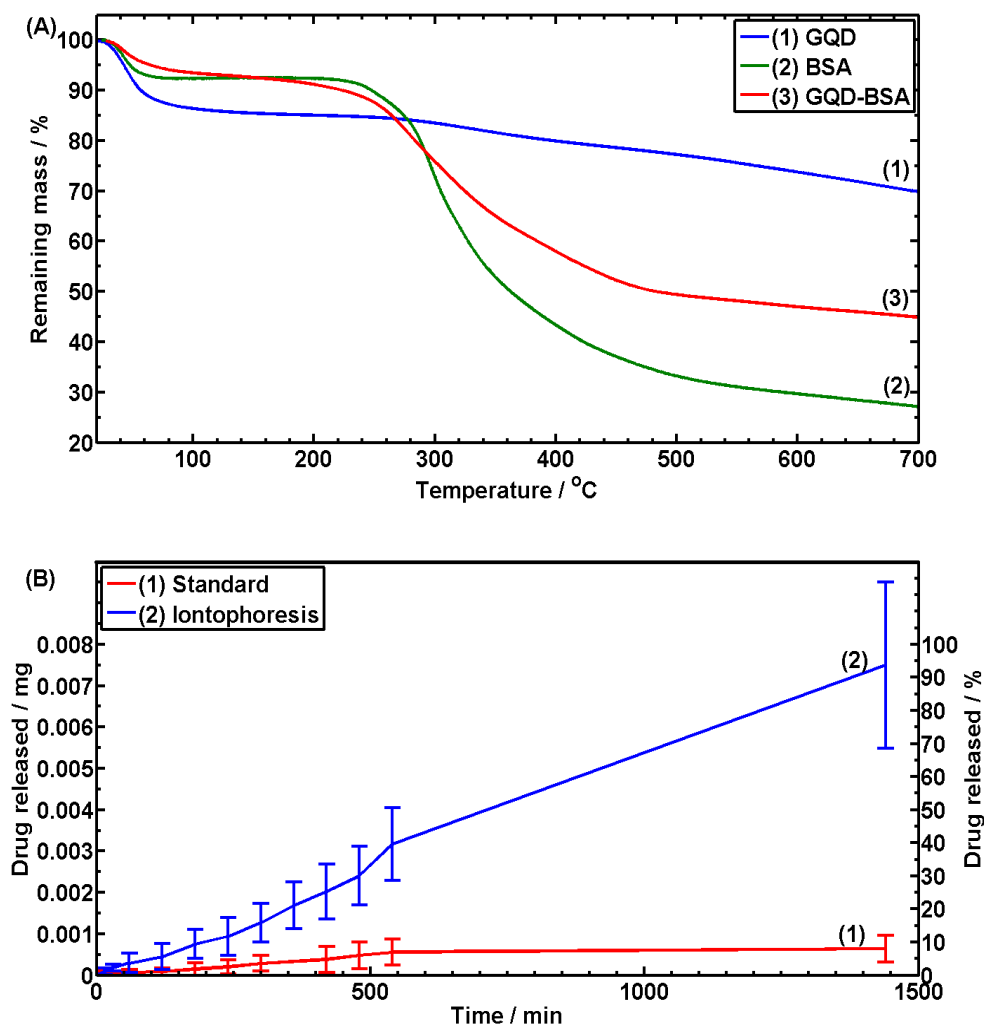
Figure 5.11: (A) TGA curves for GQD, BSA, and GQD-BSA and (B) release of BSA from chitosan-GQD microneedles, with and without the effect of iontophoresis.

LH is a drug with a low MWt of 288 Da. Another low MWt drug, FL, was shown to successfully diffuse from polymer films and microneedles in Chapter 3 and Chapter 4. Some therapeutics are of a much higher MWt than LH or FL, for example BSA with a MWt of ~60 kDa. Herein, the feasibility of releasing BSA bonded to GQD from a

microneedle array is assessed. The quantity of BSA bonded to the GQD was determined from TGA (Figure 5.11A). As a significant amount of BSA still remained even at 700 $^{\circ}$C, the mass losses for GQDs (8.9%), BSA (66.1%) and GQD-BSA (43.6%) during the major degradation step of BSA (220-500 $^{\circ}$C), taking into account of the absorbed moisture, were used to determine the loading ratio of BSA onto GQDs (BSA:GQD) of 0.29:1.

Curve 1 of Figure 5.11B shows the passive release of BSA from the microneedles into the release medium (distilled water) over 24 h. There was only minimal diffusion of the drug (7.6% of the available drug, or 0.6 μg) into the medium within the tested period of time. This is due to the difficulty in passive diffusion of large MWt therapeutics like BSA from its carrier; it was noted previously that the higher the MWt and the degree of deacetylation of chitosan, the lower the release of BSA from chitosan [549]. A similar low diffusion of BSA was noted from other polymer carriers, such as PMMA nanoparticles [550], with ~20% release over 24 h, and from alginate-montmorillonite microparticles, with ~13% over 175 min [551]. In order to improve the release of the large MWt therapeutic, a microneedle that uses iontophoresis, the electro-repulsion of charged molecules by an electrical field from one electrode towards the other electrode [62], was created as per Scheme 5.2. Iontophoresis has been previously used to improve upon the passive diffusion of low (dexamethasone, ~400 Da) [532] and medium (insulin, ~5800 Da) [133] MWt drugs and proteins/peptides [134,135] from microneedle arrays. Curve 2 of Figure 5.8B shows that for the iontophoresis-effect microneedle array (operating at 21.3 mV and 1.5 mA), the final drug release after 24 h was greatly improved in comparison to passive diffusion to 94.5%, or 7.4 μg of the available drug.
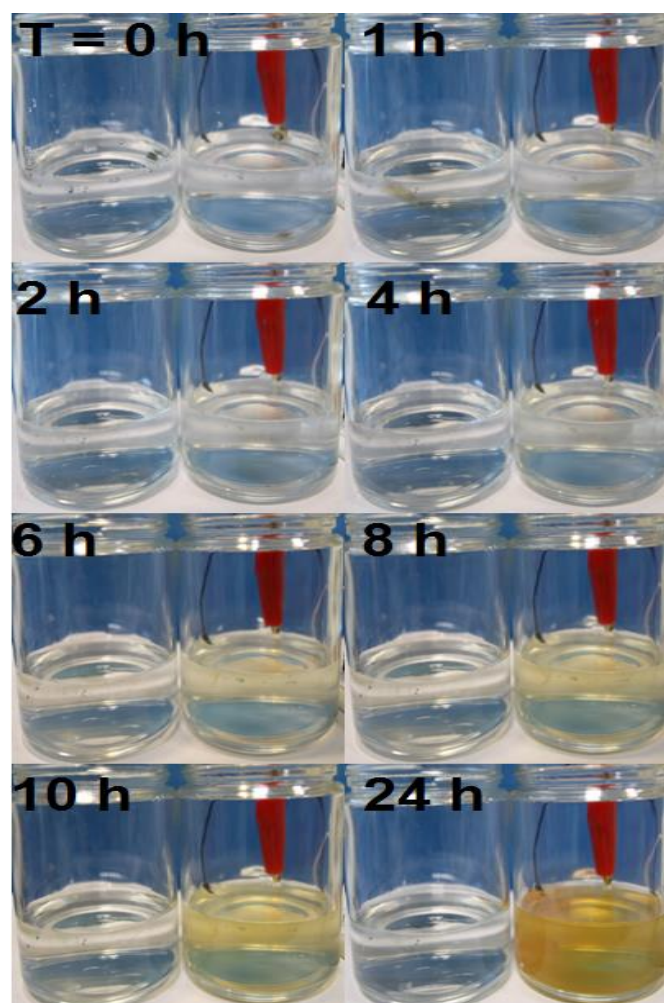
Figure 5.12: Digital photos showing the release of BSA from the microneedle into distilled water over 24 h for (left) passive diffusion and (right) electrically stimulated diffusion.

The effect of iontophoresis is shown visually in Figure 5.9, verifying the results of Figure 5.8. The left container contains a microneedle array made of chitosan-1 wt.% GQD-BSA which was submerged in the release medium (distilled water) and allowed to passively diffuse into the release medium over 24 h. The right-hand-side container contains a microneedle with the iontophoresis set-up. The strong, yellow staining of FL on the BSA (Figure 5.S4, Appendix 1) can be seen within the release medium after 6 h and this effect grows stronger over the 24 h with the iontophoresis. However, there is no obvious colour change in the standard set-up for passive diffusion. The iontophoresis-effect microneedle has released markedly more BSA into the medium

than the standard microneedle did, as seen by the stronger colour. This implies that iontophoresis offers an approach to deliver large MWt therapeutics through a microneedle array, and the chitosan-GQD nanocomposites are excellent candidates for this purpose.

5.3.4 Biostability of the GQD-drug released from the microneedle
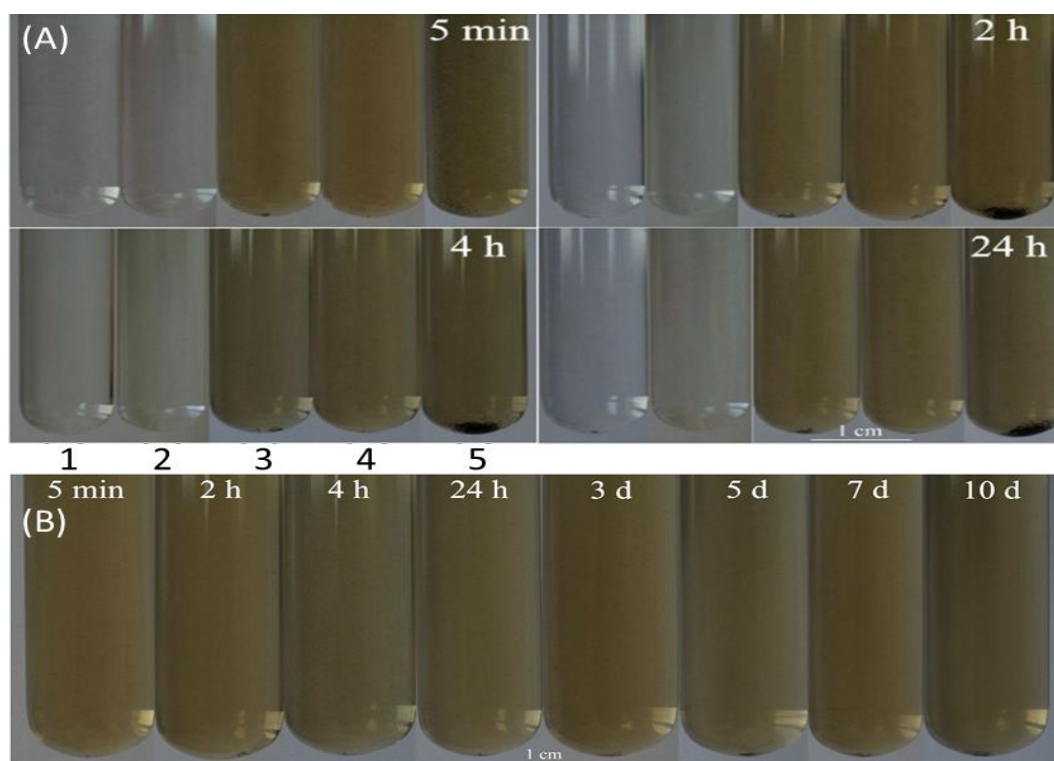
Figure 5.13: (A) The biostability of GQD (1-3), GQD-LH (4), and GQD-BSA (5), in (1) distilled water, (2) phosphate buffered saline (pH=7.4), and (3-5) foetal bovine serum. (B) Long term stability of GQD-LH in foetal bovine serum over 10 days, showing that the drug coated GQD remains relatively stable over 10 days.

After the GQD-drug is released into the fluid, it is important to assess their stability for future clinical applications. Figure 5.13A shows suspensions (0.3 mg ml^{-1}) of GQD (A, B, C), GQD-LH (D), and GQD-BSA (E), in (A) distilled water, (B) PBS (pH=7.4), (C-E) FBS. GQDs can be seen to remain stable in water up to 4 h and with negligible aggregation of larger particles after 24 h, and to experience no aggregation in PBS for up to 24 h. There was a small aggregation of GQDs in FBS after 5 min, possibly due to the aggregation of larger particles or due to the crosslinking of GQDs via hydrogen

bonding of –COOH of GQDs with the proteins in the FBS [522], but the quantity of aggregation does not increase up to 24 h. In contrast, the GQD-LH was stable up to 3 days in FBS (Figure 5.13B), experiencing barely any aggregation due to electrostatic repulsion from the positive ionic charge of LH [63]. This suspension remained relatively stable between 3 days and 10 days, with only little aggregation. As chitosan is also cationic, it is expected to enhance the stability of GQDs too, like what we previously found for chitosan-coated rGO nanosheets [552]. GQD-BSA was stable up to 5 min and then agglomerated heavily before 2 h. This is presumably due to the crosslinking between GQD-BSA nanoparticles themselves, forming larger particles; albumin is a protein found in blood serum, and the same hydrogen bonding that allowed GQD to bond to BSA may cause physical crosslinking between GQD-BSA.

Chitosan-GQD microneedles were also tested for their biostability in FBS over 6 h. The results (Figure 5.S5) show that the chitosan within the microneedle array is stable within FBS, similar to previous reports [553].

5.4 Conclusions

Graphene quantum dots, created by the hydrothermal reduction of a graphene oxide aqueous suspension, were 50-55 nm in diameter and ~1.5 nm in height, possessed photoluminescent properties and were shown to be minimally cytotoxic to adipose derived MSCs and be able to act as a contrast agent for fluorescent imaging of cells.

Chitosan – GQD nanocomposites were prepared by solution casting. The addition of GQDs increased the electrical conductivity relative to pristine chitosan by 7.9 times. The enzymatic degradation rate of the chitosan – GQD nanocomposite was similar to pristine chitosan 28 days after the test started. The UTS of chitosan increased from 62.5 MPa to 84.8 MPa and the elongation to break from 15.5% to 21.2% by the addition of 1 wt.% GQDs, with the Young's modulus remaining consistent. The

presence of GQD did not impede the enzymatic degradation of chitosan, with similar masses remaining after 28 days for both pristine chitosan and the nanocomposite, though initially the nanocomposite had a quicker enzymatic degradation rate than chitosan.

When formed into microneedles, the chitosan − 1 wt.% GQD nanocomposite shows promise as a transdermal drug delivery device. The microneedle arrays withstood the force of insertion into the body and released the painkiller lidocaine hydrochloride more substantially than pristine chitosan microneedles (68.3% of the available drug was released compared to 57.4%). Large molecular weight drugs like bovine serum albumin could be released from the nanocomposite microneedle under electrical stimulation, with an increase from 7.6% to 94.5% of the available drug released after 24 h for standard and iontophoresis-effect microneedles respectively.

GQDs and GQD-LH were shown to be stable in distilled water, phosphate buffered saline, and foetal calf serum over 24 h. GQD-LH remained stable in foetal bovine serum for up to 10 days, due to the LH imparting an electrostatic repulsion effect on the GQDs.

Bonding therapeutics to photoluminescent, electrically-conductive GQDs and integrating the drug-laden GQDs into a degradable polymer such as chitosan forms a nanocomposite that can be used in a microneedle array, creating a universal, multifunctional drug delivery platform for enhanced and controlled drug delivery that can be potentially utilised to deliver both small and large molecular weight therapeutics and be monitored through bio-imaging.

Chapter 6. Magnetic iron oxide-reduced graphene oxide quantum dots

6.1 Introduction

The chitosan-GQD nanocomposites in Chapter 5 were an improvement over the chitosan-GO and chitosan-rGO nanocomposites of Chapters 3 and 4 as they offered increases in electrical conductivity and mechanical properties over pristine chitosan, while also offering new functionality with the imaging/tracking of the drug within the body. In the form of microneedles, chitosan-GQD nanocomposites could release small and large (under electrical stimulation) MWt drugs. The GQDs, however, only possess one mode of imaging (fluorescent) and cannot be targeted to a specific site through external means. Ideally, the nanoparticles would have multiple modes of imaging as the depth of tissue penetration and the resolution of different imaging methods varies; for example, fluorescent imaging has a poorer depth of penetration in comparison to M.R.I., while M.R.I. has a lower resolution than fluorescent imaging [554,555]. They should also be responsive to external stimulation to allow for targeted drug delivery, and should have low cytotoxicity.

The aim of this chapter was to synthesise a new type of graphene based nanoparticle that will add these desired new functionalities to the nanocomposites. Superparamagnetic iron oxide-reduced graphene oxide quantum dots (from herein known as magnetic graphene quantum dots, or MGQDs) with these properties were synthesized through a green, hydrothermal method which simultaneously reduced and shattered nanoparticles of GO coated with IO. The structure and morphology of the MGQDs were analysed. MGQDs were assessed for their ability to offer dual-modality imaging through M.R.I. and fluorescent imaging, as well as the targeting of the delivery site of MGQD-bound drugs by their superparamagnetic

159

properties. Owing to their strong NIR irradiation absorbance, the MGQDs were also investigated as cancer photothermal therapy agents.
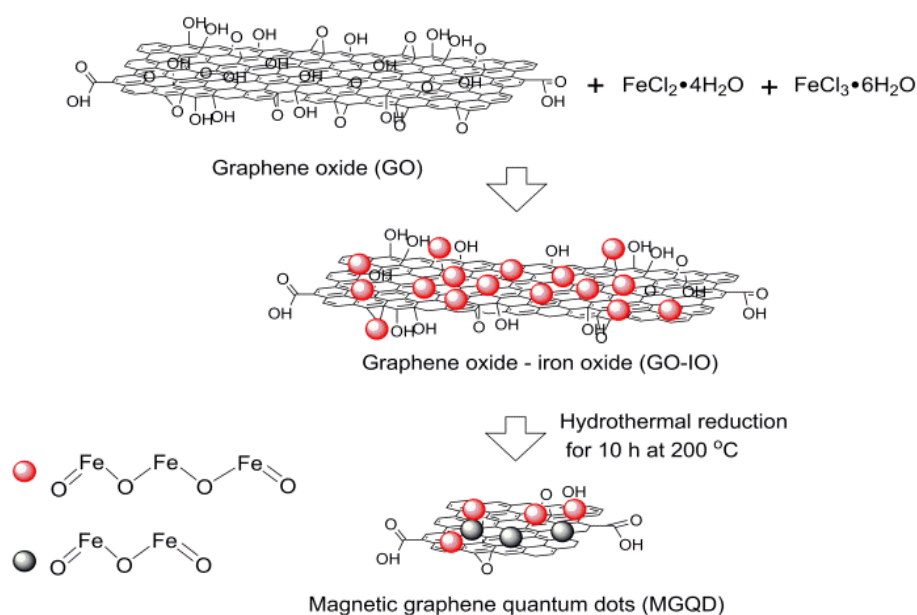
Scheme 6.1: Synthesis procedure for magnetic graphene quantum dots (MGQD). Aqueous solutions of ferrous chloride tetrahydrate and ferric chloride hexahydrate are stirred into a GO aqueous suspension; the mixture is reacted for 2 h under a nitrogen atmosphere at ambient temperature to form GO-IO nanoparticles. The GO-IO aqueous suspension undergoes hydrothermal reduction in an autoclave for 10 h at 200 $^{\circ}$C to create MGQDs.

6.2 Experimental section

6.2.1 Materials

The following chemicals were used as purchased from Sigma Aldrich; sulfuric acid (95-98%), hydrogen peroxide (29-32% in water), potassium permanganate (97%), sodium nitrate (> 99%), ferrous chloride tetrahydrate (> 99%), hydrochloric acid (36.5%), ferric chloride hexahydrate (97%), fluorescein sodium, graphite powder ($\leq$ 20 μm), rhodamine B, norharmane, lidocaine hydrochloride (> 99%), porcine trypsin (BioReagent), 3-[4,5-dimethylthiazol-2-yl]-2,5-diphenyltetrazolium bromide (MTT) solution (1 mg ml^{-1} in phosphate buffered saline (PBS)), and ethylenediaminetetraacetic acid (EDTA, BioReagent). Dulbecco's modified eagle medium (DMEM, 500 ml, Gibco Invitrogen (Paisley, UK) was used with fetal calf serum (FCS, Advanced Protein Products, Brierley Hill, UK), penicillin (100

units ml^{-1}), streptomycin (100 μg ml^{-1}), and fungizone (630 ng ml^{-1}) from Gibco Invitrogen (Paisley, UK). Isopropanol alcohol (reagent grade) and PBS tablets (pH = 7.4) were acquired from Fisher Scientific UK.

6.2.2 Preparation of graphene oxide-iron oxide nanoparticles

Graphene oxide was synthesized from a modified Hummers method [33]. GO-IO was prepared according to methods described in the literature with some modifications [267,279]. The freeze-dried GO powder (1 g) was dispersed in 150 ml of distilled water through stirring and sonication for 1 h and the pH of the suspension was raised to pH = 8 with the addition of ammonium hydroxide NH_4OH. Separately, ferrous chloride tetrahydrate $FeCl_2$-$4H_2O$ (5.4 g) and ferric chloride hexahydrate $FeCl_3$-$6H_2O$ (4 g) were dissolved in 135 ml distilled water. The GO suspension and the solution of IO precursors were added together, ammonium hydroxide was added drop wise until a pH = 10 was reached, and then the mixture was stirred for 2 h under a nitrogen atmosphere at ambient temperature. The precipitate, IO coated graphene oxide (GO-IO), was washed with distilled water, ethanol and dichloromethane to remove residual chemicals before being re-dispersed in distilled water (~ 3 mg ml^{-1}) by sonication for 1 h in a Fisherbrand (230V 50Hz) sonication bath.

6.2.3 Preparation of reduced graphene oxide-iron oxide quantum dots

The aqueous GO-IO suspension (~ 3 mg ml^{-1}) was treated in a Parr Series 4000 autoclave at 200 °C for 10 h (pressure of boiling water at 201 °C = 1.6 MPa) to generate reduced graphene oxide-iron oxide quantum dots (MGQDs). The suspension was placed in a dialysis bag (Fisher Scientific Biodesign Dialysis tubing, Mw cut off = 3.5 kDa) and the residual chemicals were allowed to diffuse into the distilled water surrounding the dialysis bag. The MGQD were collected in an aqueous suspension from the dialysis bag and lyophilised in a Labconco FreeZone Triad freeze-dryer to be stored as a powder in a desiccator. As a control, IO (with a

raised pH of 8) was autoclaved at 200 °C for 10 h to produce autoclaved iron oxide (A-IO) for a comparison study. GQDs from Chapter 5 were also used as a control in this chapter.

6.2.4 Drug loading onto quantum dots

LH (0.1 mg) was added to a suspension of MGQDs (0.1 mg ml^{-1}) under stirring for 48 h. The suspension was centrifuged at 9000 rpm for 1 h, after which the supernatant (containing the unbound drug) was removed and the precipitate was re-dispersed in water. This process was repeated several times to remove the unbound drug. The MGQD-LH was then freeze-dried and stored in a desiccator.

6.2.5 Characterisation

Transmission electron microscopy (TEM), energy dispersive X-ray spectroscopy (EDS), and selected area electron diffraction (SAED) were achieved using a Philips Technai T20 electron microscope operating at an accelerating voltage of 200 kV. High resolution TEM (HR-TEM) was carried out using a JEOL 2010F field emission gun TEM operating at an accelerating voltage of 200 kV. TEM samples were prepared by evaporating a diluted suspension (~ 0.01 mg ml^{-1}) onto a holey amorphous carbon coated copper grid (mesh size = 400). Electron energy loss spectroscopy (EELS) spectra were acquired on the JEOL 2010F using a Gatan image filter in image coupled mode with an energy dispersion of 0.5 eV per pixel. Atomic force microscopy (AFM) was carried out on a Veeco Dimension 3100 with Olympus AC160TS probes in tapping mode at 0.5 Hz, using a diluted suspension (~ 0.01 mg ml^{-1}) evaporated onto a freshly cleaved mica substrate. Dynamic light scattering (DLS) was performed on a Brookhaven ZetaPALS (660 nm wavelength), with 3 cycles of 2 min runs on suspensions of 1 mg ml^{-1} MGQD in distilled water.

X-ray diffraction (XRD) was performed on a Stoe Stadi P with Cu K$_\alpha$ irradiation (0.154 nm wavelength), with operating parameters of 40 kV, 35 mA, and a scanning speed of 1° min^{-1}. Raman spectroscopy between 50-3000 cm^{-1} with a resolution of 0.5 cm^{-1} was achieved with

a Renishaw inVia Raman microscope using a 514.5 nm wavelength laser. Fourier transform infrared (FT-IR) spectroscopy between 400-4000 cm^{-1} with a resolution of 1 cm^{-1} was performed on a Perkin Elmer Spectrum 100 with a diamond attenuated total reflectance unit. Thermogravimetric analysis (TGA) from 40 to 1000 $^\circ$C at 5 $^\circ$C min^{-1} was implemented with a Perkin Elmer Pyris 1 with a nitrogen atmosphere (20 ml min^{-1}).. A Micromeritics AccuPyc II 1340 was used to measure the density of the MGQDs, achieved at room temperature (24 $^\circ$C) by using 10 purge cycles and 10 calculation cycles of helium gas.

UV-visible light (UV-Vis) spectroscopy of nanoparticle suspensions in distilled water (0.3 mg ml^{-1} concentration) from 200-800 nm with a 1 nm resolution was achieved with a Perkin Elmer Lambda 900 spectrometer. Photoluminescence spectroscopy was conducted using a Horiba Fluoromax 4 with excitation sources from 300-400 nm and emission readings from 360-600 nm with a wavelength resolution of 2 nm. Photoluminescence quantum yield measurements used fluorescein sodium in 0.1 NaOH, rhodamine B in ethanol and 0.01% HCl, and norharmane in 0.1 M H_2SO_4 as reference standards. Quantum yield measurements were taken by using Equation 1 [35], shown below:

$$\phi_{qd} = \phi_{st} \times \frac{Grad_{qd}}{Grad_{st}} \times \frac{\eta_{qd}^2}{\eta_{st}^2} \qquad (6.1)$$

where "ϕ" is the fluorescence quantum yield, "Grad" is the gradient of the curve of emission versus absorbance, "η" is the refractive index for the solvent used in the solution, and "qd" and "st" are quantum dots and the standards used (fluorescein sodium, rhodamine B and norharmane). PL lifetime analysis (time correlated single photon counting) was achieved with irradiation from a frequency doubled Mira 900 Ti-Sapphire laser (10 W), a single photon counting module (Becker and Hickl SPC-830), an electronic trigger (Becker & Hickl GmbH PHD-400-N High Speed Photodiode Module), and the emission was detected by an ID Quantique ID100-50 single photon detection module. The magnetic hysteresis loop was created using a Quantum Design MPMS-XL 5 superconducting quantum interference device (SQUID),

operating at 37 °C to simulate *in vivo* conditions and between +/- 20,000 Oe (2 T) in 200 Oe intervals. A Siemens Trio TIM 3 Tesla M.R.I. was used to measure the T2 relaxation times of the MGQDs, with the echo time, T_E = 15.2, 30.4, 45.6, 60.8, 76, 91.2, 106.4, 121.6, 136.8, 152, 167.2 milliseconds and the relaxation time T_R = 3000 milliseconds.

6.2.6 Cell viability and imaging

Human skin was obtained with ethical permission from patients undergoing abdominoplasties or breast reductions from the Department of Plastics, Burns and Reconstructive Surgery, Sheffield Teaching Hospitals. All tissue was collected and used on an anonymous basis under a Human Tissue Authority research bank tissue license number 08/H1308/39.

Dermal fibroblast cells were isolated and cultured, as described previously [36], in DMEM at 37 °C and 5% CO_2 environment. When the culture was 50% confluent, the cells were collected by treating with a trypsin solution for 10 min and centrifuging the cell suspension to form a pellet at 1000 rpm for 5 min using a Hettich Rotafix 32A centrifuge. Cells were counted, with cells seeded (10,000 per well) in a 48 well plate. Cells were incubated overnight in DMEM to allow for cell reattachment, after which the DMEM medium was replaced with MGQD suspensions (20, 50, 100, 200, 500 µg ml^{-1} in DMEM) for 6 and 24 h incubation times (each testing iteration was tested in triplicate). At the end of each incubation time, cells were washed with PBS and then incubated in fresh DMEM until 72 h post-treatment when cells were assessed by the MTT-assay of metabolic activity. Cells were incubated for 40 min at 37 °C, after which the formazan salt was eluded by acidified isopropanol. The optical densities of the resultant solutions were measured with a plate reader at 540 nm with a reference filter of 630 nm (Bio-Tek ELx800). Control samples of untreated cells in DMEM were taken as 100% viable, and the optical densities of the MGQD treated cells were compared to these values.

164

An Olympus CK40 microscope and a Leica TCS SP8 two-photon confocal microscope (excitation source 690 nm, emission filter 360 nm) were used for cell imaging. For the two-photon fluorescent imaging, the cells were incubated with either 50 µg ml^{-1} or 100 µg ml^{-1} MGQDs for 12 h before the cells were fixed with glutaraldehyde.

6.2.7 Drug release from MGQDs

A 10 ml PBS suspension (37 °C, pH = 7.4) of MGQD-LH (1 mg ml^{-1} MGQD-LH) was inserted into a Spectrum Labs Float-A-Lyzer G2 dialysis tube with pore sizes between 0.1-0.5 kDa. This dialysis tube was floated vertically in a sealed container of pristine PBS solution (550 ml, 37 °C, pH = 7.4). This container was placed within a Stuart SI500 bio-incubator, maintained at 37 °C and agitated at 100 rpm. At set time points, 3 ml of PBS solution was taken from the outer container (and subsequently replaced with 3 ml of fresh PBS) and analysed with a Perkin Elmer Lambda 900 (resolution of 1 nm). The acquired spectra were compared to the absorbance values of free LH of known concentration (ranging from 0.06-1 mg ml^{-1}) in PBS.

6.2.8 Photothermal measurements

The temperature of aqueous suspensions of MGQDs and GQDs (1.5 ml, concentration of 50 µg ml^{-1} and 100 µg ml^{-1}) under irradiation from a NIR continuous laser (wavelength: 808 nm; laser power: 2, 5, 7.5 W cm^{-2}) was measured as a function of time. Distilled water was also studied as a control.

Photothermal experiments on HeLa cells incubated with suspensions of MGQDs and GQDs were carried out with a near-infrared continuous laser (wavelength: 808 nm; laser power: 2.5 W cm^{-2}). HeLa cells were seeded to a density of 5000 cells per well of a 96 well culture plate (BD Falcon, U.S.). Cells were incubated at 37 °C in a 5% CO_2 atmosphere for 24 h to allow for reattachment. After incubation, the cell culture medium was replaced by the MGQD or GQD suspension (100 µl of cell medium with a 50 µg ml^{-1} suspension of MGQD or GQD). After 4 h incubation with the QDs, the cells were irradiated by a laser for 20 min or 30

min. After incubation overnight, the QD suspension medium was removed and the cells were washed twice with PBS. To test the viability of the cells after irradiation, 100 μl of CCK-8 solution was added to each well and the cells were incubated for 2 h. The optical density of the cell solution was read on a microplate reader (Varioskan Flash, Thermo Scientific), with measurements taken at 450 nm.

2.9 Biostability

MGQD and MGQD-LH were dispersed in distilled water, PBS and FCS at a concentration of 50 μg ml^{-1}. Suspensions were imaged using a digital camera after predetermined intervals.

6.2.10 Statistical analysis

Statistical analysis ($p < 0.05$) and graphing were completed through MatLab 2012a software. Size analysis of TEM images was conducted through ImageJ software, with 60 separate samples taken over several images.

6.3 Results and discussion

6.3.1 Structure

Figure 6.1 shows TEM (A-1 and A-2) and AFM (Figure 6.1B, Inset) images of MGQDs. The synthesized MGQDs have an average diameter of 41.8 (± 8.1) nm from the TEM images, and an average diameter of 45.2 (± 10.3 nm) and a height of 2.3 nm (± 0.07 nm) from AFM. The MGQDs are identifiable in the TEM images in dark contrast (Figure 6.1A1-1A2) on the amorphous carbon film support due to the presence of high density IO (4.9 – 5.2 g cm^{-3} for magnetite [556]) within the MGQDs as well as mass-thickness contrast, similar to the identification of IO on GO-IO reported in the literature [280]. DLS results (Figure 6.1) show a mean hydrodynamic diameter of 61.4 nm, with a significant count within the 45-90 nm range. It is larger than the average diameters obtained from AFM and TEM, which can be accounted for by the presence of larger nanoparticles (i.e. agglomerates) in the polydisperse MGQD water

suspension [557]. The diameter of the MGQDs is larger than hydrothermally reduced GQDs (5-25 nm) previously reported by other groups [217,558,559], but these papers use either a longer hydrothermal treatment time (24 h) [558,559] or an additional oxidation procedure to further reduce the size of their GO before the hydrothermal treatment [217]. The diameter is, however, similar to that of the GQDs (51.9 nm) prepared by the same oxidation and hydrothermal treatment method in Chapter 5.
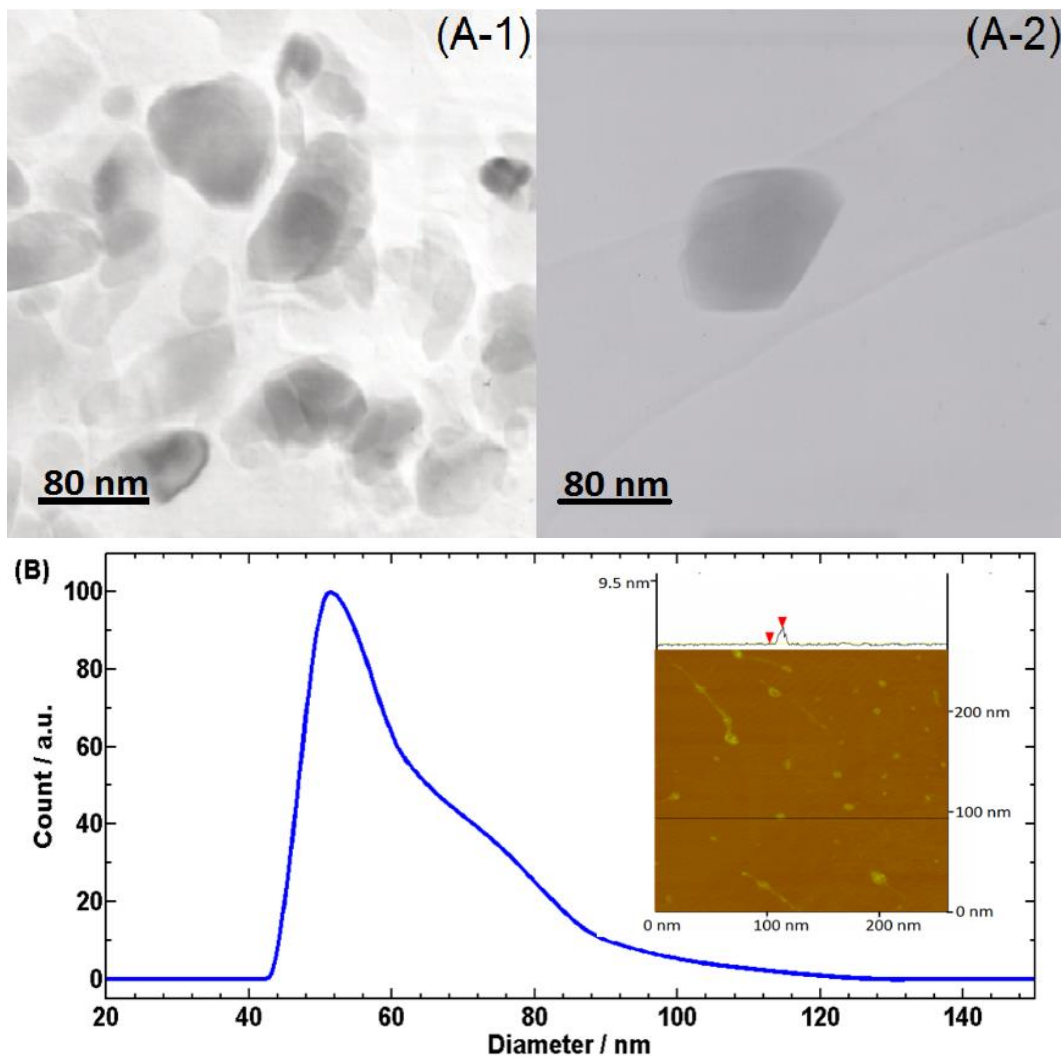
Figure 6.1: (A) TEM images of MGQDs, showing that the QDs are approximately 40-50 nm in diameter, (B) DLS size analysis of MGQD aqueous suspension, showing the majority of MGQDs are within the 45-90 nm diameter range; (Inset) AFM image of MGQDs, showing an average height of 2.3 nm and an average width of 45.2 nm.

As described previously, the average thickness of the MGQDs from AFM is 2.3 nm, which is thicker than the reported thickness of graphene (0.37 nm [500]), rGO (~0.8 nm [213])

or the GQDs prepared using the same hydrothermal reduction method (1.5 nm (Chapter 5)). This suggests that the IO coating on the MGQD surface is likely 0.8 – 1.9 nm thick. IO growth on GO was reported to be smaller than pristine IO growth due to the dispersed nucleation of Fe^{3+} by the oxygen functional groups (C=O) of GO [560], and a similar effect may have occurred during the synthesis of the IO on the GO-IO followed by reduction of GO into rGO during hydrothermal cutting.
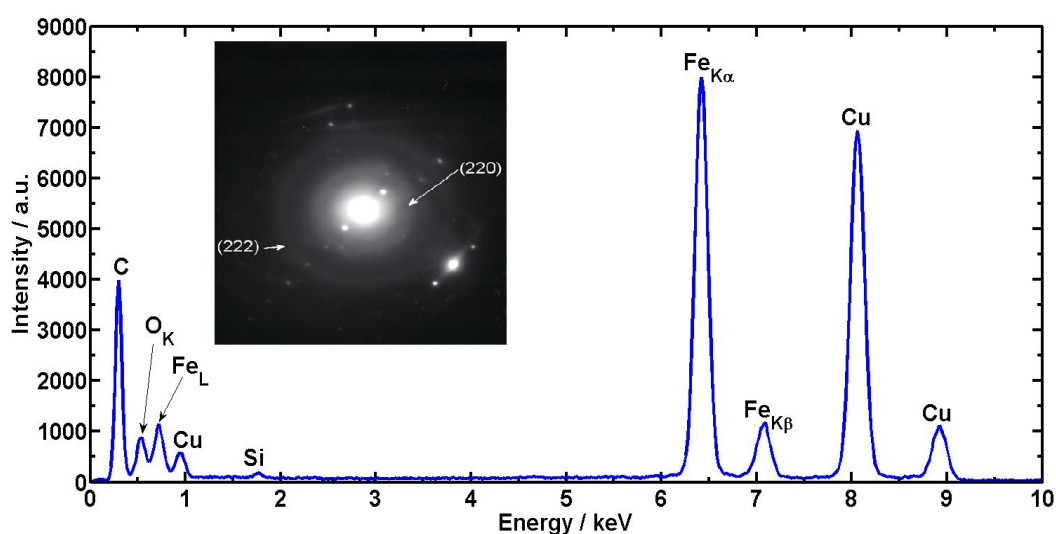
Figure 6.2: EDS spectrum of the MGQD presented in Figure 2 (A-2), showing a composition of carbon, oxygen, and iron; (inset) the SAED pattern of the MGQD, confirming the presence of iron oxide.

The composition of the MGQD in Figure 6.1A-2 can be seen in the EDS spectrum in Figure 6.2, which confirms the presence of iron (0.72, 6.42, and 7.08 keV) [561,562]. The oxygen (0.54 keV) was from the IO and the residual oxygenated groups in the hydrothermally reduced GO while carbon (0.3 keV) was from the rGO and carbon-coated copper grids (0.94, 8.06, and 8.92 keV) [561,563]. The SAED pattern (Figure 6.2, Inset) has the ring patterns associated with (220) and (104) diffraction peaks of magnetite and hematite (α-Fe_2O_3) respectively [564,565].
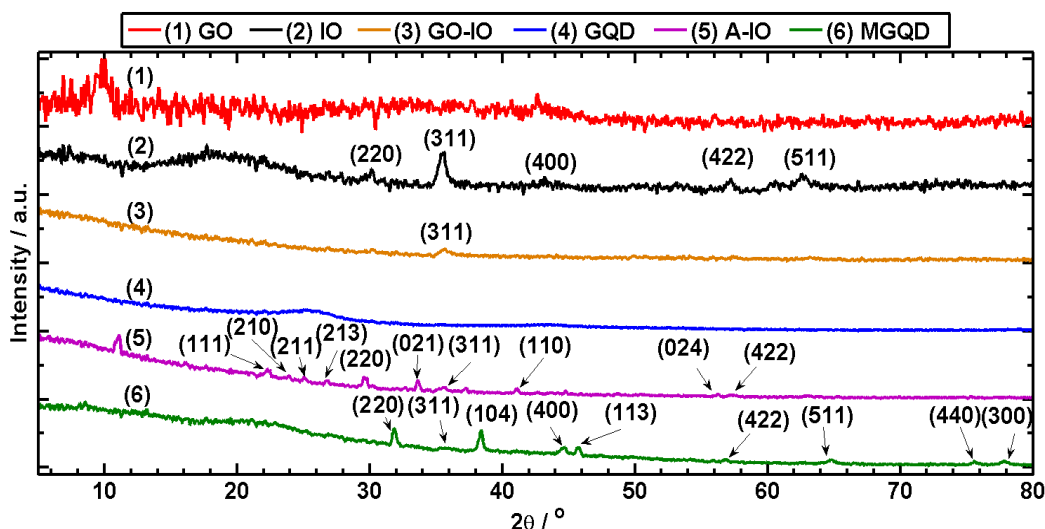
Figure **6.3**: XRD traces of GO, IO, GO-IO, GQDs, A-IO, and MGQDs.

The results from XRD (Figure 6.3) confirm that the MGQDs are characterized by both rGO and a mixture of magnetite, maghemite, and hematite. GO has been oxidized from graphite and is largely exfoliated (weak (002) peak at $2\theta = 10.6°$) [187]. IO is crystalline, with a (220) peak at $2\theta = 30.7°$, a strong (311) peak at $2\theta = 35.5°$, a (400) peak at $2\theta = 43.2°$, a (422) peak at $2\theta = 57.2°$, and a (511) peak at $2\theta = 62.5°$ [565–568]. This corresponds with the JCPDS 19-0629 card for magnetite, as IO possesses the (311), (220), (511) and (422) peaks that are common to both magnetite and maghemite but lacks of the characteristic (210), (211) and (213) peaks of maghemite (JCPDS 39-1346) [565,569]. GO-IO displays a distinct (311) peak from the IO, with the other peaks at a lower intensity, showing that the magnetite is formed before the hydrothermal treatment, as previously reported [279]. The GQDs were structurally characterised briefly in Chapter 5 as consisting of rGO. From Figure 6.3, GQDs are characteristic of rGO ((002) peak at $2\theta = 25.4°$) [399], which is almost a return to the value of pristine graphite $2\theta = 26°$ from Chapter 3. The value for GQD is closer than the value for rGO in Chapter 4, which was recorded as $2\theta = 23°$, as the hydrothermal reduction method is more efficient at reducing the GO than the biomolecule-method due to the higher reduction temperature. A-IO is a mixture of magnetite, maghemite, and hematite (the α- mineral form of maghemite), with the (311), (220), and (422) peaks from the

IO, maghemite specific peaks (210), (211), (213), and hematite characteristic peaks (021), (110), (024) (JCPDS 33-0664) indicated on the curve [565,570]. The presence of hematite is caused by the partial topotactic oxidation of magnetite at 200 °C during autoclaving [571]. The MGQD curve shows a change in structure from both GQD and A-IO. rGO can be identified by the weak (002) peak at $2\theta = 21.6°$. This peak has shifted by 3.8° when compared to the GQD curve, which may stem from the reaction of GO and IO during autoclaving that may have altered the crystalline structure (*vide infra*) [284]. The effect of rGO within the MGQDs has caused a reduction in intensity of the (311) and (511) peaks from IO, a new (440) peak at $2\theta = 76.0°$ common to magnetite and maghemite, and the introduction of a (104) peak at $2\theta = 38.3°$, a (113) peak at $2\theta = 45.5°$, and a (300) peak at $2\theta = 78.1°$, all from hematite [565].
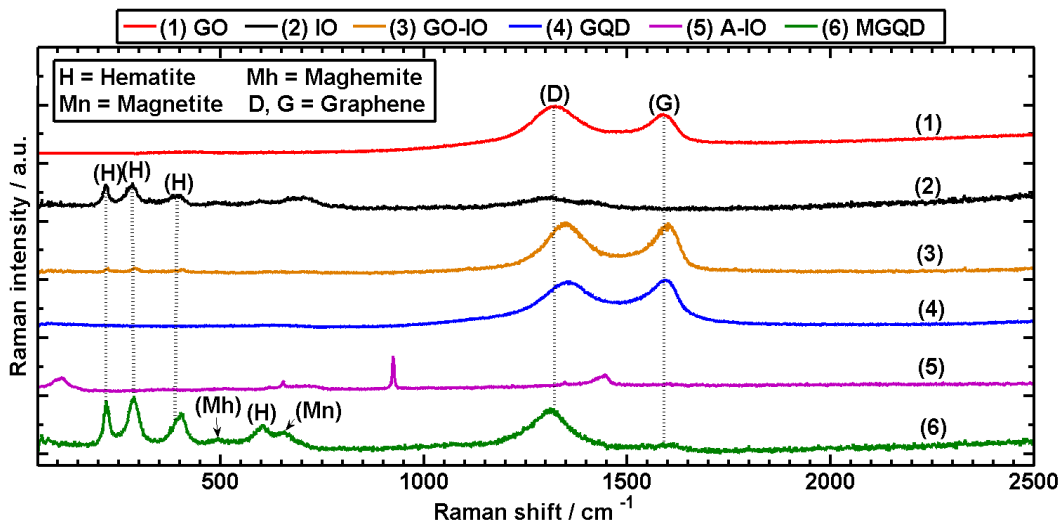
Figure 6.4: Raman spectra of GO, IO, GO-IO, GQDs, A-IO, and MGQDs.

A further analysis of the crystal structure of the MGQDs and the structural change during autoclaving was performed through Raman spectroscopy of GO, IO, GO-IO, GQDs, A-IO and MGQDs (Figure 6.4). GO can be identified by the G band at 1591 cm^{-1} (E$_{2g}$ mode) and the D band at 1322 cm^{-1} (A$_{1g}$) [210]. The IO is a mixture of magnetite and maghemite, with the maghemite caused by the local extreme heating of the IO powder by the laser source as it was not identified in the XRD analysis [572,573]. The peak at 300 cm^{-1} and the broad peak at 660 cm^{-1} are assigned to magnetite T$_{2g}$ and A$_{1g}$, while the peaks at 217, 283 and 401 cm^{-1} are

attributed to hematite $A_{1g}(1)$, $E_g(2 + 3)$, and $E_{2g}(4)$ [571,572,574]. The GO-IO spectrum is a combination of the characteristic peaks of the GO and IO spectra, again showing the successful seeding of IO crystals onto the GO nanosheets.

GQDs can be identified by the G band at 1594 cm^{-1} (E_{2g} mode) and the D band at 1359 cm^{-1} (a_{1g}), with the ratio of the intensities of the D peak to the G peak decreasing relative to GO, showing an increase in the sp^2 carbon structure of pristine graphene and graphite. It is noteworthy that the final values for the GQD are different, in particular the D peak, than those recorded for chitosan-reduced rGO from Chapter 4 (1359 cm^{-1} and 1594 cm^{-1} for GQD vs. 1313 cm^{-1} and 1597 cm^{-1} for rGO). The GQD D-peak at 1359 cm^{-1} is close to the accepted edge D-peak for pristine graphene (~1350 cm^{-1} [575,576]), confirming the result of XRD (Figure 6.3) that showed GQD as closer to pristine graphite than the chitosan-reduced rGO. A-IO is characterized as a mixture of magnetite and hematite, with a magnetite peak at 653 cm^{-1} [572,577] and a hematite peak at 619 cm^{-1} [565,572,577], and with additional goethite (α-FeOOH, the hydrated form of hematite) peaks at 924 cm^{-1} and at 1442 cm^{-1} [578]. MGQDs can be seen to be magnetite (656 cm^{-1}) [572,577], maghemite (broad peak at 500 cm^{-1}) [572,577], hematite (peaks at 218, 287, 402, and 604 cm^{-1}) and rGO (G peak at 1588 cm^{-1}) [210]. The Raman spectrum of the MGQDs is closer to GO-IO than to A-IO. Presumably this is because the IO within the MGQD is magnetite, like with GO-IO while the A-IO is mainly composed of maghemite and hematite. The IO of MGQD is in the form of a film on the surface of the MGQD as previously described, and only has one outer surface exposed to the effects of the hydrothermal treatment, unlike the A-IO particles which have all the surfaces exposed. This reduces the effect of the hydrothermal reaction on the IO on graphene surface, leading to a different chemical composition.
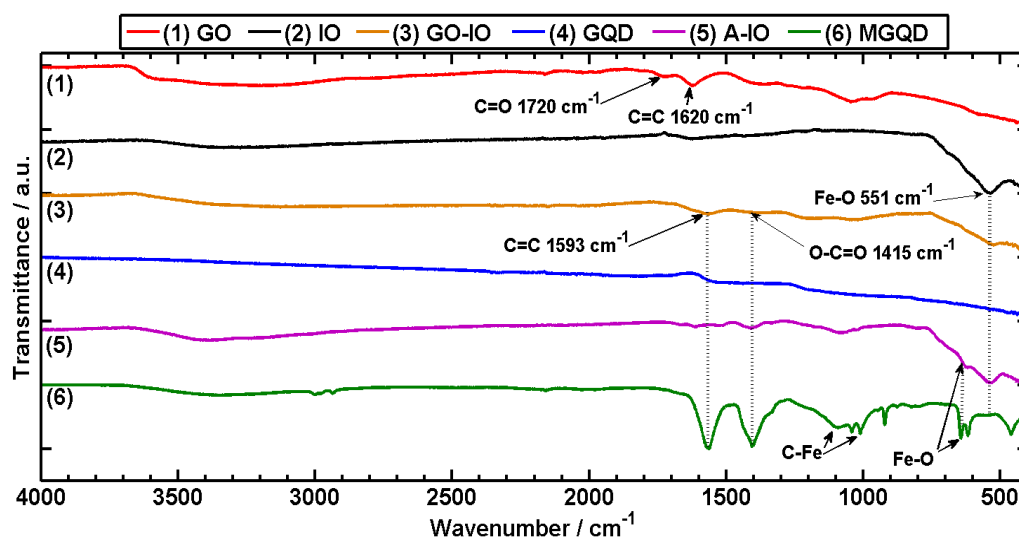
Figure 6.5: FT-IR spectra of GO, IO, GO-IO, GQDs, A-IO, and MGQDs.

The chemical bonds and chemical interactions within the nanoparticles can be identified through FT-IR spectra of the nanomaterials, as shown in Figure 6.5. GO has C-O bonds at 1043 cm^{-1}, C=C bonds at 1621 cm^{-1} and C=O bonds at 1720 cm^{-1}. On the IO spectrum, a peak for the Fe-O bond is present at 551 cm^{-1} [279]. For the GO-IO, the synthesis procedure of IO on the GO has led to the shift of the C=C aromatic bonds of the GO from 1621 cm^{-1} to 1593 cm^{-1} and to the creation of O-C=O bonds at 1415 cm^{-1} [579]. The Fe-O peak has been maintained and is at 527 cm^{-1}. The GQD curve shows a reduction in functional groups in comparison to GO, with the peaks barely visible on the curve, confirming the reduction of GO to rGO. A-IO possesses 622 and 537 cm^{-1} peaks attributed to Fe-O peaks [574]. MGQDs have 646, 619 and 462 cm^{-1} peaks attributed to Fe-O bonds from magnetite, maghemite and hematite, a C=C peak at 1564 cm^{-1} and O-C=O peak at 1406 cm^{-1} peak that are similar to GO-IO, and 1086 and 1012 cm^{-1} peaks attributed to C-Fe bonds confirming the chemical bonding between rGO and IO [574].
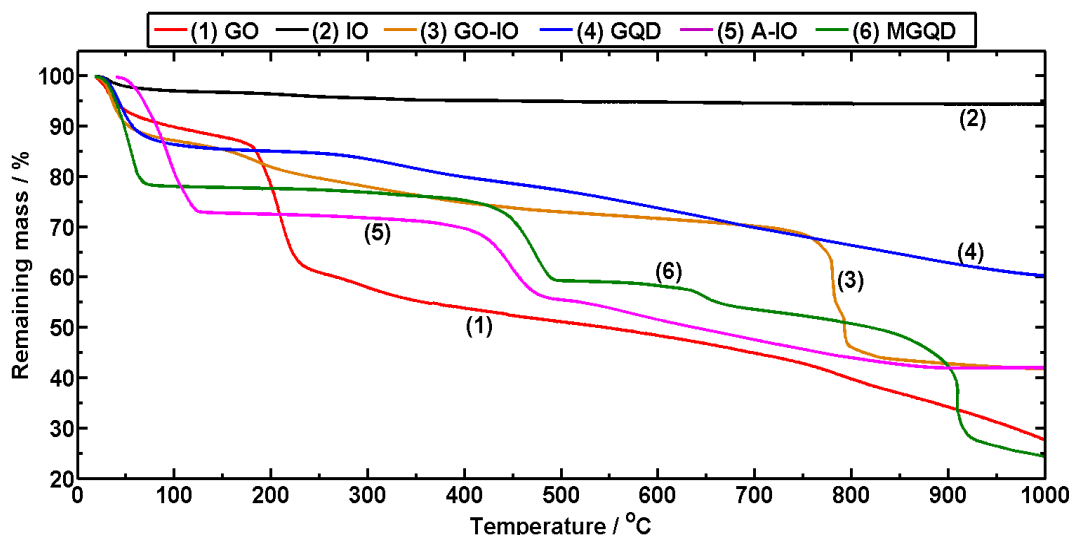
Figure 6.6: TGA curves of GO, IO, GO-IO, GQDs, A-IO, and MGQDs.

Figure 6.6 shows the TGA curves of the MGQD and its control samples in a nitrogen atmosphere. TGA suggests that GO is oxidized graphene (dissociation of epoxide and hydroxyl groups at ~200 °C is 23% of the total dry mass). IO has limited dissociation of ~5% (similar to magnetite) as it does not possess any functional groups on the surface to be dissociated [580]. GO-IO is a mixture of GO and IO with a main mass loss (27% of the dry mass) at ~780 °C, attributed to the reaction of IO with carbon from rGO to release CO and CO_2 gases [581]. GQD is rGO (reduced mass loss as compared to GO at ~200 °C, 0.5% of the total dry mass) [210]. The 0.5% mass loss compares favourably to the 13% mass loss for chitosan-reduced rGO for the same temperature range. A-IO has a major mass loss between 400 and 500 °C (~19% of the dry mass) that is attributable to the phase transformation from maghemite to hematite; this phase transformation may be accompanied by other transformations such as conversion of maghemite to an intermediate product magnetite [565,581–583]. Similar to A-IO, the MGQDs have a mass loss step at ~450 °C, with 20% of the dry mass. This mass loss does not occur in magnetite, so maghemite is not present on the IO or GO-IO as previously discussed. At ~620 °C, there is a minor mass loss (4% of the dry mass), which could be due to the reaction between α-Fe_2O_3 and carbon of graphene [583], resulting in the release of CO and CO_2. The major mass loss at ~780 °C in the curve for GO-IO has moved to ~910 °C (with a

loss of 24% of the dry mass), which may be the result of autoclaving that has caused phase transformation of the IO and the chemical bonding between IO and rGO.

The density of the MGQDs was measured through pycometry as 3.66 ($\pm$ 0.006) g cm^{-3} for MGQDs. In comparison, the density of GQDs was 1.66 ($\pm$ 0.006) g cm^{-3}, slightly higher than that for chitosan-reduced rGO (1.46 g cm^{-3}, Chapter 4) because of the absence of chitosan in the GQDs. The increase in density of the MGQDs over the value of GQDs is due to the higher density of the IO within the MGQD structure, e.g. 4.9 – 5.2 g cm^{-3} for magnetite [556]. By using the rule of mixture and considering the density of IO is 5 g cm^{-3}, the amount of IO in the MGQDs is estimated at 60 vol.% or about 82 wt.%.

6.3.2 Photoluminescent and magnetic properties
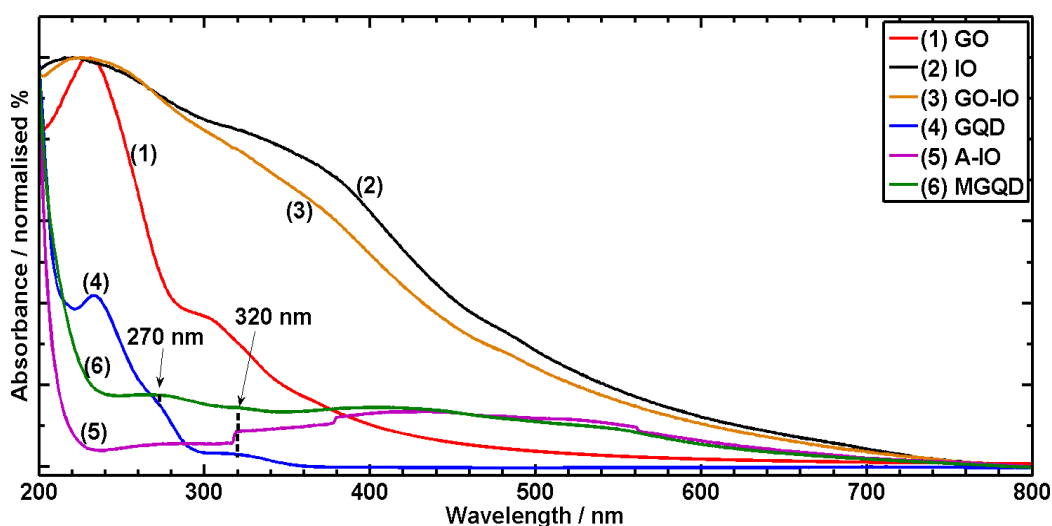
Figure 6.7: UV-Vis spectra for GO, IO, GO-IO, GQDs, A-IO and MGQDs (0.3 mg ml^{-1} concentration in distilled water).

The photo-physical properties of the nanoparticles were characterized using steady-state UV-Vis spectroscopy. As shown in Figure 6.7, MGQDs and GQDs have absorbance peaks at 270 nm and 320 nm, with the MGQDs also exhibiting the characteristic absorbance trait of A-IO in the wavelength region 400 to 500 nm.
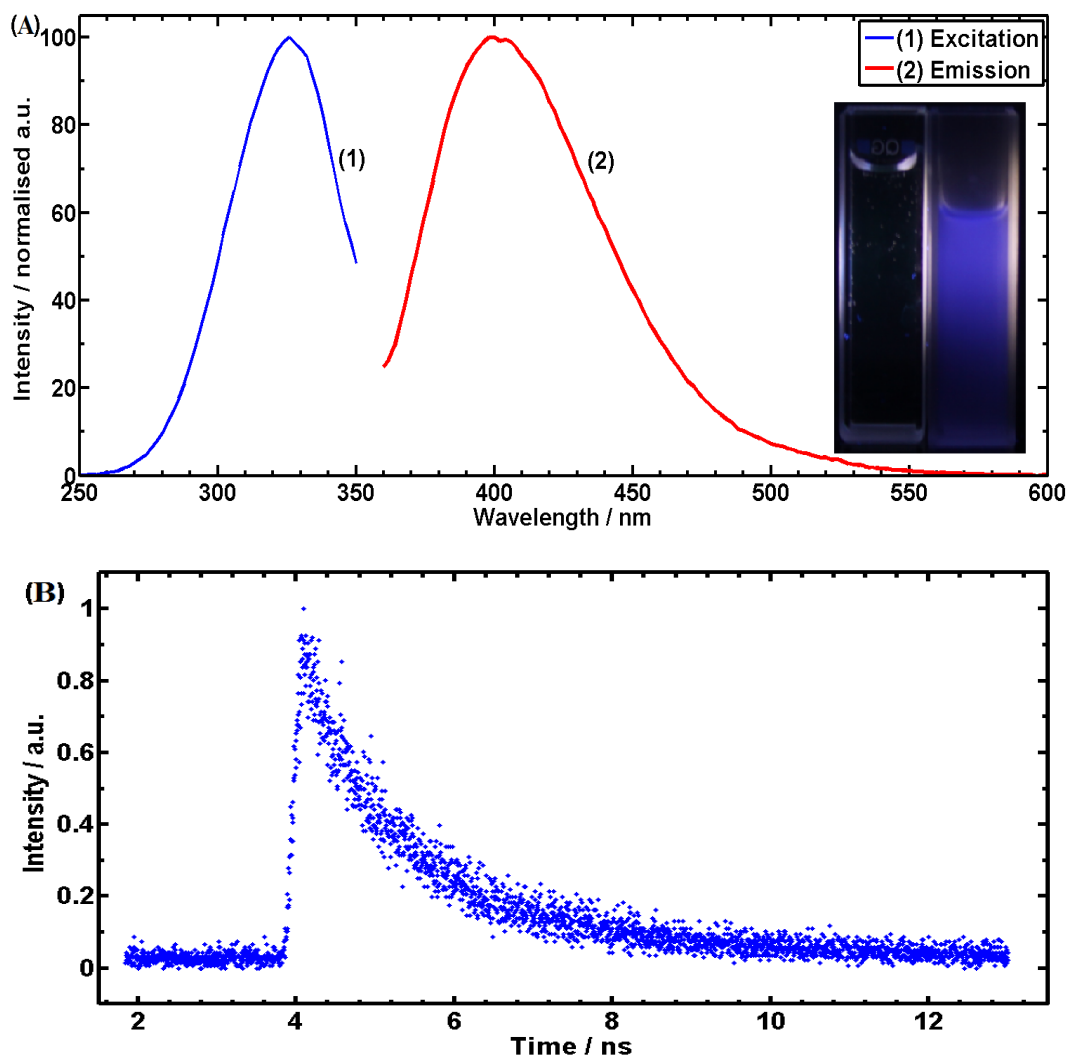
Figure 6.8: (A) Photoluminescence spectra of MGQDs showing the excitation wavelengths versus emission wavelengths; (Inset) Photoluminescent imaging of (left) PBS and (right) MGQDs in PBS under 360 nm light; (B) PL lifetime data for MGQDs in an aqueous suspension (1 mg ml^{-1}).

The emission characteristics of the MGQDs are presented in Figure 6.8A. Here, excitation of the MGQDs at 320 nm (corresponding to the peak in the excitation spectrum) yields an emission spectrum with a peak at 398 nm. This emission value is slightly lower than that (420 nm) observed for the GQDs prepared by the same hydrothermal method (Chapter 5). Quantum yield measurements (using Equation 6.1) gave a value of 7.9% for the MGQDs, similar to the published literature for GQDs (5.5-14%) prepared by other groups [15,337,338,539] and slightly lower than the GQDs prepared using the same method (9.4%) (Chapter 5). The MGQD result, in comparison to the GQD values, suggest the presence of IO

175

slightly quenches the luminescence of GQDs. The photos in the inset confirm the photoluminescence (PL) properties of the MGQDs (right), in contrast to the control sample of PBS solution. MGQDs, in a 1 mg ml^{-1} aqueous suspension, have a PL lifetime of 1.9 ns (Figure 6.8B), similar to GQDs and conventional QDs in the literature (range of 1-10 ns) [18,540–542], and slightly lower than the GQDs prepared using the same method (2.3 ns) (Chapter 5).

Previously reported GQDs with attached IO (GQD-IOs) did not possess PL properties as they synthesized GQDs first and then attached IO [584]. Coating of IO onto the GQDs quenched the fluorescence of GQDs, which is similar to the quenching behavior of gold nanoparticles bonded to semiconductor QDs [585]. It was theorized that a QD would have its fluorescence quenched by a non-radiative energy dissipation process from the bonded nanoparticles, and not explicitly through a decrease in the radiative (PL) properties of the QD itself [585,586]. In our process the GO-IO was synthesized first and then reduced to MGQDs; the reduction procedure broke the GO-IO into small QDs, with the edges of the core-GQD within the MGQD now exposed. These edges have a zigzag structure that contain triple carbenes [538] which are linked to the electron orbital transition at 320 nm [217], and so the PL properties of GQDs are preserved.

The magnetic hysteresis loop of MGQDs (Figure 6.9A), determined with a SQUID, illustrate that they possess no residual magnetization and are superparamagnetic. The saturation magnetization of the MGQDs was 7.31 emu g^{-1}, comparable to other magnetic nanoparticles (4.62 emu g^{-1}) [279]. As demonstrated in Figure 6.9A (Inset), the MGQDs can be drawn towards a magnet from a resting position. Figure 6.9B is the T2 relaxation time of MGQDs from M.R.I., with the slope of the relaxation time determined as 4.16 mM^{-1} s^{-1}. In comparison, the slope of the relaxation time of magnetite can vary from 35.48 to 114 mM^{-1} s^{-1} [587,588], maghemite had a slope of 43.3 mM^{-1} S^{-1} [589], and gadolinium-doped graphene and a GO-IO-manganese oxide nanoparticle had slopes of 108 mM^{-1} s^{-1} [590], and

$65.9 - 103$ mM^{-1} s^{-1} [591], respectively. The relaxation time slopes of nanoparticles that contain IO vary due to the different Fe concentrations of the nanoparticles used [587,588,591]. Figure 6.9B (Inset) shows digital images of MGQDs as contrast agents as a function of increasing Fe concentration. The results of the PL and magnetic properties tests confirm that the MGQDs can potentially be used for dual-modality fluorescent and M.R.I. applications.
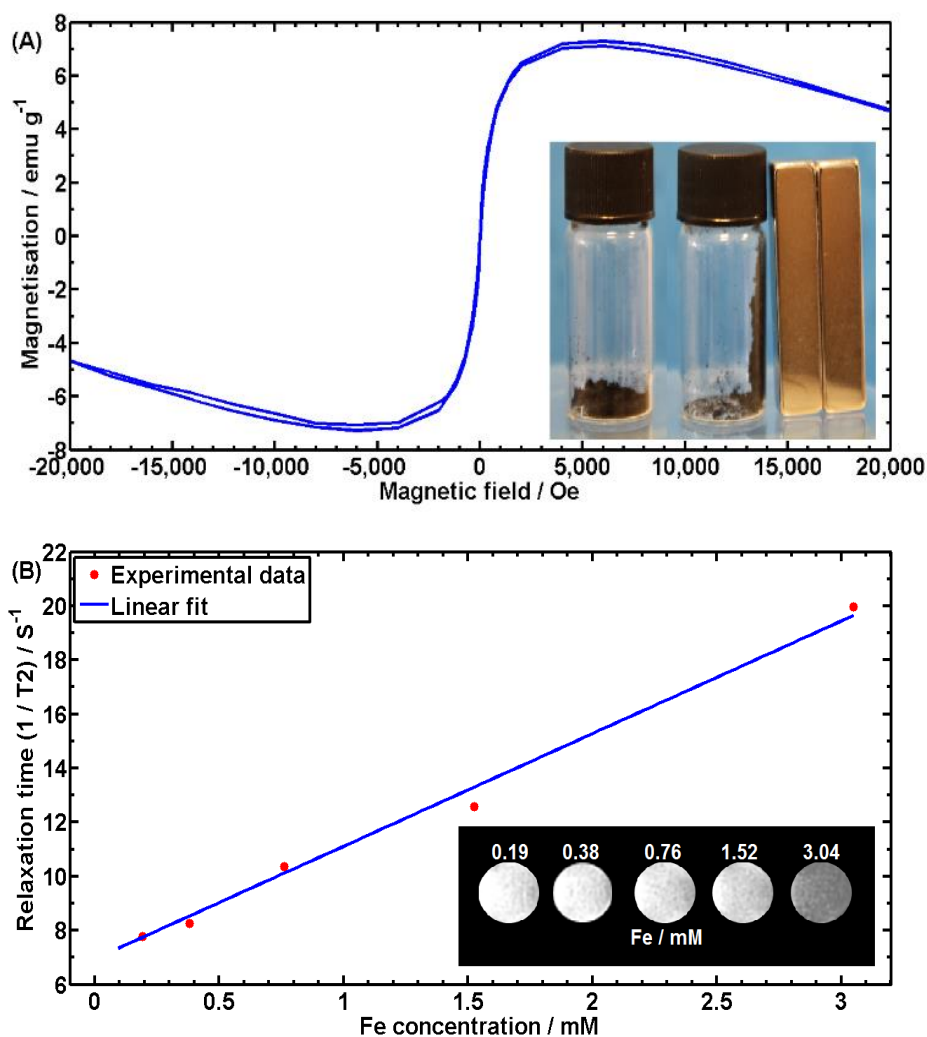
Figure 6.9: (A) Magnetic hysteresis loop of MGQDs and (Inset) digital images of the effect of external magnetic stimulation upon MGQD powder, (left) before and (right) after a magnet is placed beside it. (B) T2 relaxation time of MGQDs from M.R.I. and (Inset) digital images of MGQDs as contrast agents, as a function of increasing Fe concentration.

6.3.3 Cell viability and imaging
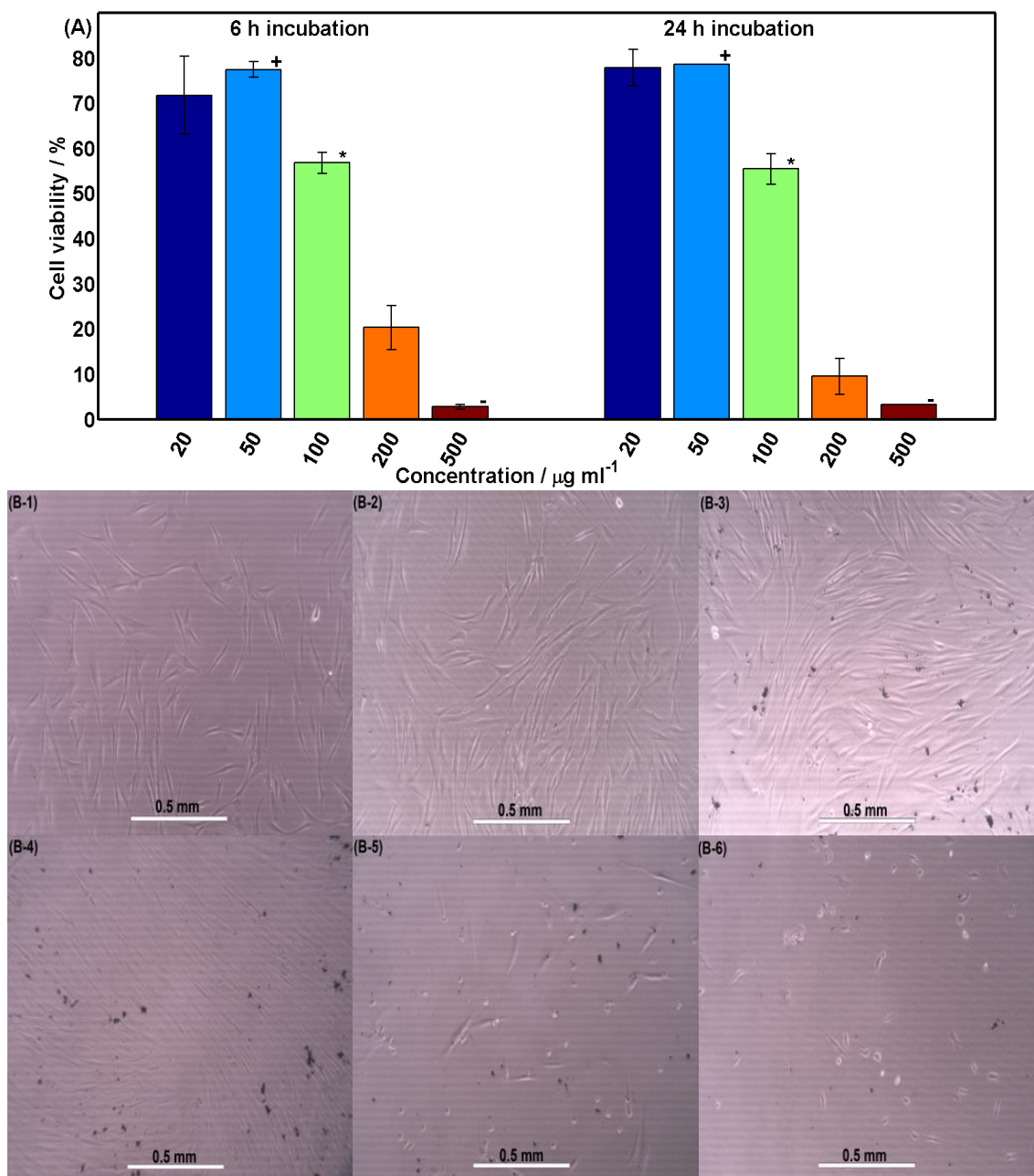
Figure 6.10: MTT cell viability results for MGQDs treated fibroblast cells. Concentrations used were 20, 50, 100, 200, and 500 µg ml^{-1} in DMEM medium and the initial incubation times were 6 h and 24 h. Cells were then washed and cultured for a further 72 h before viability was assessed. Bars with the same symbols (*, +, -) were statistically similar to each other (p < 0.05). Optical microscopy images of the cells were taken 72 h after an initial 6 h incubation with MGQDs. Concentrations used were (B-1) 0 (control), (B-2) 20, (B-3) 50, (B-4) 100, (B-5) 200, and (B-6) 500 µg ml^{-1}.

MGQDs were found to have limited cytotoxicity up to a concentration of 50 µg ml^{-1} in MTT cell viability tests (Figure 6.10A). Suspensions of MGQDs of 20 and 50 µg ml^{-1} in DMEM

gave cell viability levels of 70-75% compared to cell culture on tissue culture plastic at an initial 6 h and 24 h incubation times, suggesting that they have a low cytotoxicity. The cell viability values for MGQDs are similar to those recorded for pristine IO nanoparticles used for M.R.I. imaging (80% for 50 µg ml^{-1}) [275] and other GQDs reported before that are used for fluorescent imaging (70-80%) [15,309,338,339]. There is a dose dependent cytotoxic effect, with a decrease in cell viability when the concentration of MGQDs is raised from 50 µg ml^{-1} to 500 µg ml^{-1}. The visual effects of acute exposure (6 h incubation) to MGQDs shown in Figures 6.10B-1 to 6.10B-6 for cells which were subsequently cultured for a further 72 h. Cells which had encountered 20 and 50 µg ml^{-1} MGQDs grew well showing no long term adverse effects while cells which were exposed to concentrations of 100, 200 and 500 µg ml^{-1} did not recover and increase in number over the 72 h (Figures 6.10B-4 – 6.10B-6). Many of these cells are seen as the compact, white, and circular nodes: an appearance that was previously reported to indicate apoptosis [246]. The cell viability of nanoparticles can be improved upon by passivation with a coating of a biocompatible organic compound, with amine functionalized GQDs [337] and IO functionalized by pullulan [275] and dimercaptosuccinic acid [276] significantly improving the cell viability of the respective nanoparticles.

Figure 6.11 shows fibroblast cells under 345 nm irradiation that have been treated with (A-C) 50 µg ml^{-1} and (D-F) 100 µg ml^{-1} of MGQDs for 12 h. Figure 6.11 C and F are overlaid white light (Figure 6.11 A and D) and fluorescent light (Figure 6.11 B and E) images, showing that the emission of fluorescent light is from within the cells which suggests that the MGQDs entered the cells for both suspension concentrations. The emission is concentration dependent, with the emission from the cells stronger when treated with 100 µg ml^{-1} of MGQDs than with 50 µg ml^{-1}; the higher concentration of MGQDs in the suspension allowed for more MGQDs to be absorbed into the cells, but higher concentrations have been shown to be cytotoxic after a long period of incubation (Figure 6.10A). Nevertheless, at 50 µg ml^{-1} it is still possible to

image the nanoparticles. When surface-treated with a passivation agent, MGQDs at a higher concentration such as 100 μg ml^{-1} may also be used without incurring toxicity to cells.
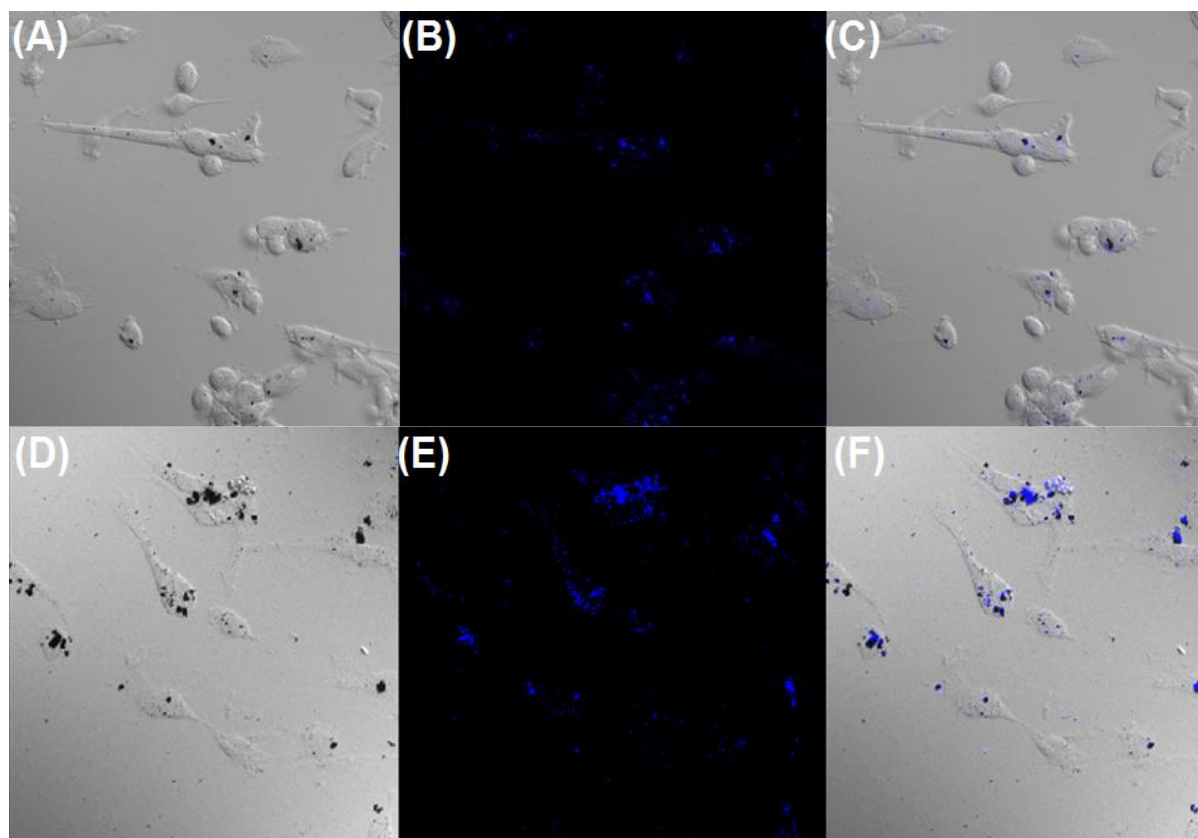
Figure 6.11: Optical microscopy images of fibroblast cells after an initial 12 h incubation with MGQDs. Concentrations used were (A-C) 50 μg ml^{-1} and (D-F) 100 μg ml^{-1}. (A) and (D) are the fibroblast cells under normal light, and (B) and (E) are under fluorescent light. (C) and (F) are an overlay of the white and fluorescent light images.

6.3.4 Drug delivery

The chemical bonding of the anesthetic lidocaine hydrochloride (LH) (Figure 6.12A, inset) onto MGQDs to form MGQD-LH is mainly through π-π stacking between the aromatic rings of the MGQDs and LH [592]. Figure 6.S2 shows the transposing of LH peaks onto MGQD in FT-IR (6.2S1A) and Raman (6.S1B) spectra, showing that the LH is adsorbed to the surface of the MGQDs. A comparison of TGA curves of MGQD-LH and LH (Figure 6.12A) and MGQD (Figure 6.5) allow for the quantity of the drug in MGQD-LH to be estimated as 23.8%, giving an estimated loading ratio of LH:MGQD of 0.31:1. The drug release profile (Figure 6.12B) determined that the release of LH from MGQD-LH into the PBS achieved ~100% (106.9 ±

13.1%) of the total drug available, or 5.09 ($\pm$ 0.63) mg ml^{-1}, at 8 h, after which the test was terminated.
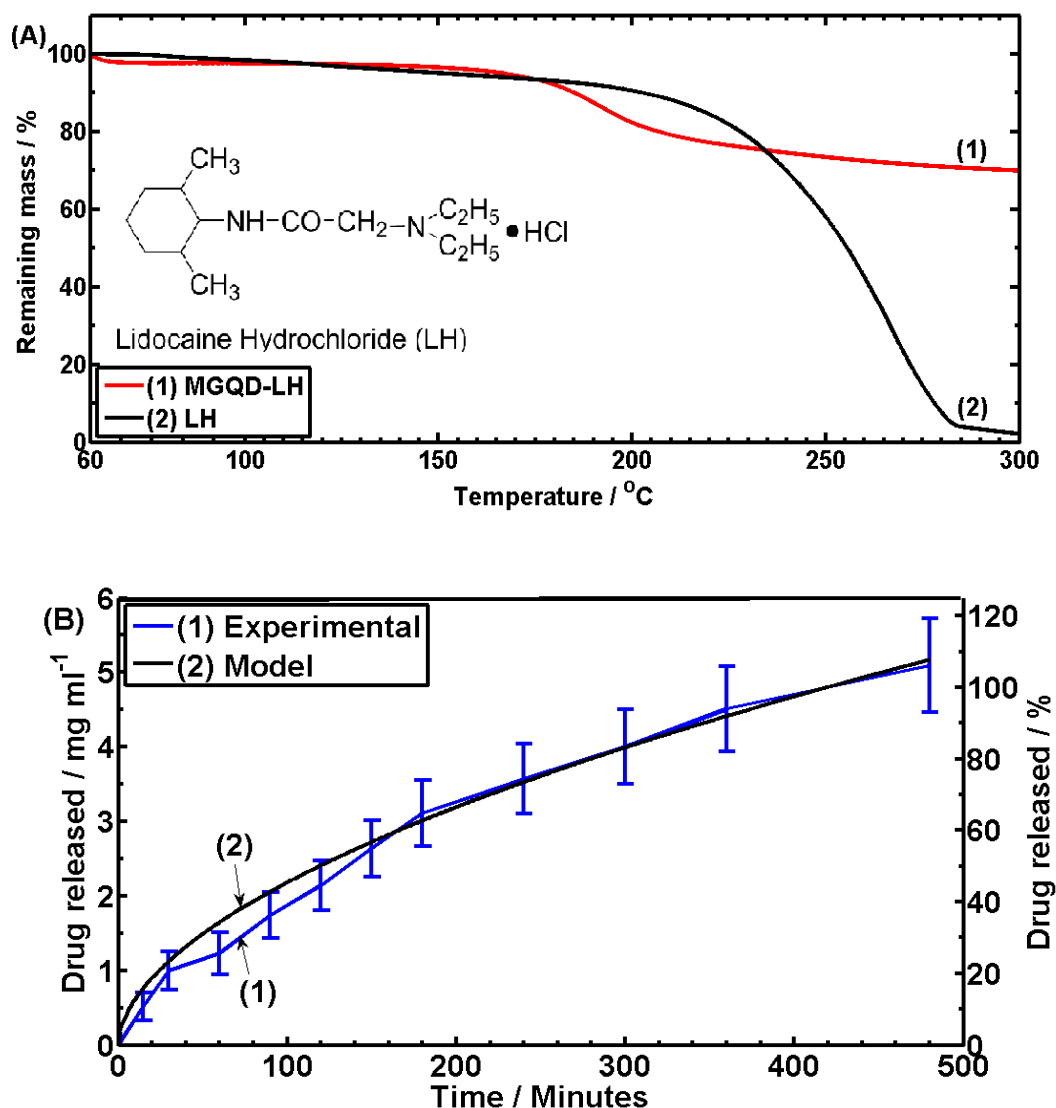
Figure 6.12: (A) TGA curves for MGQD-LH and LH (Inset: chemical structure of LH). (B) The release of LH from MGQD-LH over the course of 8 h.

To determine if the diffusion of LH from the MGQD follows Fickian law, Equation 6.2 was used [132]:

$$\frac{Q_t}{Q_T} = K \times t^n \tag{6.2}$$

in which Q_t is the amount of drug released at the time "t", Q_T is the total amount of drug released during the experiment, K is the diffusion coefficient and n is the diffusion release

exponent. It was found that the values of 0.56 μg s^{-1} and 0.55 for K and n best fit the experimental data presented in Figure 6.12B. This shows that the diffusion of the LH from the MGQD was not Fickian but anomalous [233] at pH = 7.4, similar to the diffusion of doxorubicin from GO [235] and rhodamine B from GO into a solution of pH = 4.5 [234]. These results indicate that a drug can be bonded to the surface of MGQDs and then be gradually released from the MGQDs into the body. It has been previously shown in the literature that similar nanoparticles like carbon QDs [340], GO [249] and IO [266] can be extracted from the blood and collect in the spleen/bladder to be excreted from the body through urine.

6.3.5 Photothermal properties

There is a possibility of using the MGQDs for cancer photothermal therapy, where the MGQDs absorb NIR light and convert it to heat that can be used to kill cancer cells locally [593]. To assess their potential for this application, suspensions of MGQDs in distilled water, together with GQD suspensions and distilled water control sample, were irradiated with a 2, 5, and 7.5 W cm^{-2} NIR laser (wavelength: 808 nm) for a period of time.
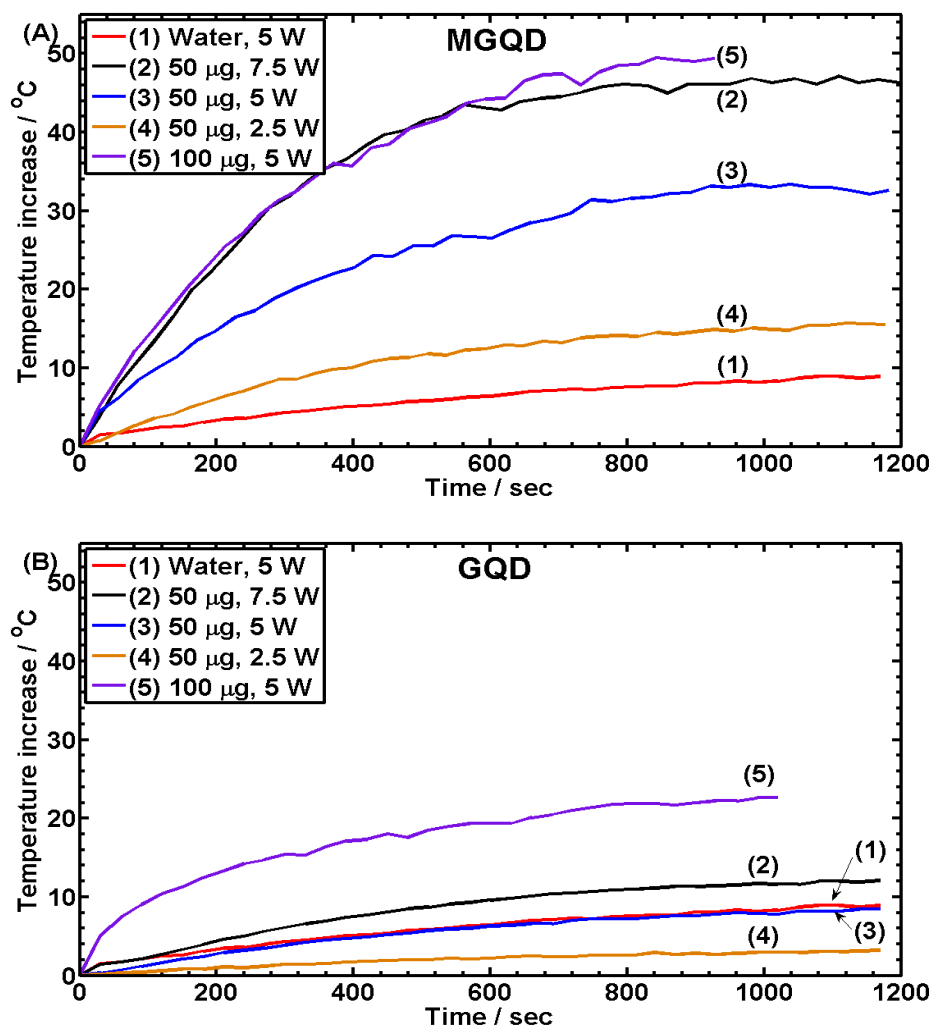
Figure 6.13: Temperature increase difference between (A) MGQD suspensions, (B) GQD suspensions, and distilled water (control) under NIR 808 nm laser irradiation with varying power.

The results (Figure 6.13) show that the temperature of the QD suspension increases with increasing laser power as well as QD concentration. After 20 min under 5 W cm^{-2} irradiation power, it can be seen that the temperature of the 50 μg ml^{-1} MGQD suspension increases by 32.6 °C, compared to 8.9 °C for the water control sample and 8.4 °C for the 50 μg ml^{-1} GQD suspension. This can be attributed to the higher absorption of the MGQDs in the NIR range (700-800 nm, Figure 6.6) than the GQDs; this higher absorption is due to the presence of IO on the MGQDs. After 20 min, the suspension of 50 μg ml^{-1} MGQDs at 7.5 W cm^{-2} achieved a temperature increase of 46.3 °C; this is comparable to the increase of the 100 μg ml^{-1} MGQD suspension (49.4 °C) after 16 min at 5 W cm^{-2} irradiation. This concentration and laser power

dependent result shows that the MGQDs can be used as an effective photothermal ablation agent at a low concentration that was determined to have low cytotoxicity (Figure 6.10). The differences in suspension concentration, irradiation time, and irradiation power make direct comparisons between previously reported photothermal therapy agents difficult. But, generally MGQDs compare well to other nanoparticles that are structurally and elementally similar, in particular GO-poly(ethylene glycol) (PEG) [245], rGO-PEG [245], GO-IO [280], and IO [587]. MQGDs also compare well to other photothermal agents such as carbon nanotubes [159] and gold nanoparticles [594].
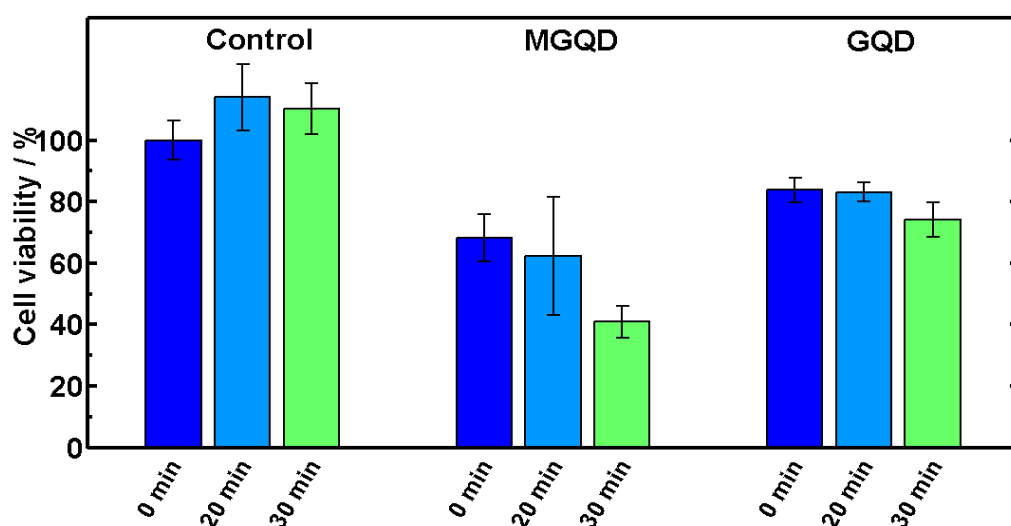
Figure 6.14: CCK-8 cell viability of HeLa cells incubated with 50 µg ml^{-1} MGQD or GQD suspensions and irradiated with a 2.5 W cm^{-2} NIR laser (wavelength: 808 nm) for 0 min, 20 min, or 30 min. Control cells were pristine HeLa cells without QD treatment.

The photothermal therapy results suggest that the MGQDs could be potentially used for the ablation of tumours, where the presence of MGQDs within the tumour will raise the temperature and kill tumour cells locally [593]. MGQDs and GQDs were incubated for 4 h with HeLa cells for *in vitro* photothermal ablation studies (Figure 6.14). Under 2.5 W cm^{-2} NIR laser irradiation, untreated HeLa cells can be seen to have a similar cell viability, with statistical insignificance, to the untreated, non-irradiated cells. This shows that laser irradiation alone at this power density will not reduce the viability of the HeLa cells. The presence of MGQDs, without irradiation, reduced the cell viability of HeLa cells to 68.2%, compared to 83.8% for

GQDs. These two values are lower than the values for fibroblast cells (Figure 6.10) due to different types of cell and incubation conditions used. MGQDs could have a higher cytotoxic effect on HeLa cells than on dermal fibroblast cells because of a higher susceptibility of HeLa cells to reactive oxide species than for the fibroblast cells, similar to the differing cell viability results for IO when incubated with mesothelioma cells and mice fibroblast that was attributed to reactive oxide species damage [273]. There is a time dependent decrease in cell viability, with a more substantial decrease in cell viability occurring when the HeLa cells that were treated with MGQDs were irradiated for 30 min than for 20 min (cell viability of 40.9% versus 62.3%, respectively). GQDs, under irradiation, did not reduce the cell viability of the HeLa cells by as much, achieving a reduction to 83.1% and 74.2% for 20 min and 30 min irradiation time, respectively. This difference between the GQDs and the MGQDs is in accordance with the temperature increases from the photothermal measurement.

Previously, QDs such as CuS [595,596] were used as photothermal ablation agents under irradiation with a 808 nm laser, with the QDs reducing the viability of HeLa cells [595] and of U87 glioblastoma cells [596]. When irradiated for 5 min with a 12 W cm^{-2} NIR laser, around ~65% of the tumour tissue in mice treated with CuS QDs showed signs of necrosis [596]. rGO-IO nanosheets achieved the full ablation of 4T1 tumours in mice that were treated with a 5 min exposure of 0.5 W cm^{-2} near-infrared laser irradiation [282]. In comparison to these results, our MGQDs are not as efficient as photothermal ablation agents under the laser irradiation conditions that we use, but they do offer bimodal imaging, with intrinsic M.R.I and fluorescent imaging capability. Also by increasing the laser power density (but still within the safe-use range), the photothermal ablation effect of the MGQDs may be improved.

3.5 Biostability

The stability of the MGQDs in biological fluids, including water, PBS and FCS, was assessed and the results are shown in Figure 6.15. It can be seen that pristine MGQDs partially aggregate

185

in distilled water and PBS (pH = 7.4) within 2 h, with larger particles falling to the bottom of the container, but the remaining particles remained stable in suspension as the quantity of aggregates did not increase with time up to 24 h. The IO on the surface of MGQD is hydrophobic [597] and aggregates in water and in PBS. MGQDs in FCS aggregated significantly within 2 h, presumably due to the crosslinking of MGQDs by hydrogen bonding of the proteins in the FCS with the remaining –COOH groups on MGQD edges [522].
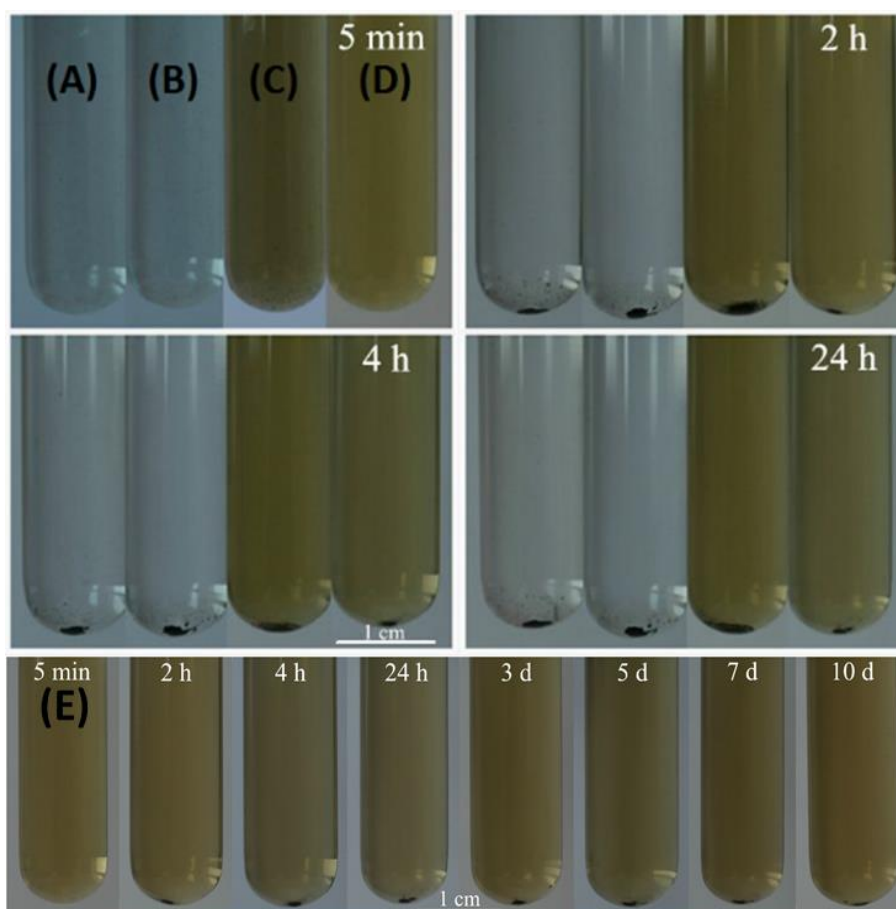
Figure 6.15: The biostability of (A-C) MGQDs and (D) MGQD-LH suspensions in solutions of (A) distilled water, (B) PBS (pH=7.4), (C-D) FCS. (E) MGQD-LH biostability in FCS over 10 days, showing that the drug coated MGQD is relatively stable in biological fluid over the test period of time.

The coating of LH onto the MGQD surface has reduced this crosslinking effect and greatly improved the biostability of the MGQD over 10 days (Figure 6.15E), with minimal further aggregation of the MGQD-LH after the initial 2 h. In solution, LH maintains a positive ionic charge [63], and in FCS the LH coating prevents the MGQDs from aggregating through

electrostatic repulsion. Coating the MGQDs with another ionic biopolymer, such as chitosan, may also improve the stability of the MGQDs, similar to the improvement afforded to chitosan-coated rGO (Chapter 4), as well as decreasing the cytotoxicity of the MGQDs [253].

6.4 Conclusions

The synthesis of MGQDs through the hydrothermal reduction of a water suspension of GO-IO nanoparticles was shown. The MGQDs were found to be around 45 nm in diameter and 2.3 nm high from TEM and AFM, with a composition of carbon, oxygen, and iron identified from EDS and EELS. Iron oxide was coated onto the graphene surface as a thin film and maybe also as individual particles within the bulk MGQDs. A mixture of iron oxides (magnetite, maghemite, and hematite) and rGO was formed during the hydrothermal reduction process, as determined from XRD, Raman spectroscopy, FT-IR and TGA. MGQDs emitted violet light with a wavelength of 398 nm when excited at 320 nm, showing excellent photoluminescent properties. They were also superparamagnetic, as determined by magnetic hysteresis analysis, and could act as a T2 contrast agent in M.R.I. applications.

Dermal fibroblast cells which had encountered a concentration of 50 µg ml^{-1} or lower of MGQDs grew well and showed no long term adverse effects. The MGQDs (50 µg ml^{-1} or 100 µg ml^{-1}) entered the cells after incubation for 12 h and could be detected by fluorescent imaging. A model drug was successfully bonded to the MGQDs, with a loading ratio of 0.31:1 (LH:MGQD), as characterized by FT-IR, Raman spectroscopy and TGA. The full release of the drug from the MGQD surface was achieved within 8 h. MGQDs, under NIR irradiation, generated a higher temperature than GQDs or distilled water due to the presence of iron oxide which is a more effective NIR absorber, and could achieve more significant temperature increases at a low concentration and laser power. This higher NIR absorption allowed for the MGQDs to reduce the cell viability of cancer cells during *in vitro* laser ablation experiments by a greater amount than was possible with GQDs. Ionic drug coated MGQDs were shown to

have a better stability in FCS than uncoated MGQDs, which showed the coated MGQDs were relatively stable in FCS over the test period (10 days).

These results demonstrate that the MGQDs have a low cytotoxicity and they retained the photoluminescent properties of GQDs which, in conjunction with the superparamagnetic properties from IO nanoparticles, would allow for fluorescent and M.R.I. dual-modality imaging in biomedical applications without the need to use an additional fluorescent dye. Meanwhile, the MGQDs could be used as a targeted drug carrier via the physical bonding of a therapeutic to the MGQDs and the subsequent release of the therapeutic at the desired site by external magnetic stimulation, and as an effective potential agent for cancer photothermal therapy.

Chapter 7. Chitosan-magnetic graphene quantum dot nanocomposites

7.1 Introduction

In Chapter 6, magnetic graphene quantum dots (MGQDs) were synthesised and characterised. The MGQDs offered additional functionality when compared to graphene quantum dots (GQDs); the MGQDs were both photoluminescent and superparamagnetic which allows for the MGQDs to be used for dual-modality imaging (fluorescent and M.R.I.) and they could be manipulated for targeted drug delivery purposes. Furthermore, the reduction of the GO during the MQGD formation process should return some of the ideal mechanical and electrical conductivity properties of pristine graphene that GO loses during the oxidation procedure. For these reasons, the addition of MGQDs to chitosan to form chitosan-MGQD nanocomposites should be an interesting material for use within microneedle arrays.

In Chapter 5, microneedle arrays made from chitosan-GQD nanocomposites proved to be successful, with the added electrical conductivity of the nanocomposite allowing the microneedle arrays to be used for iontophoresis-stimulated drug delivery of large MWt drugs. In this chapter, the chitosan-MGQD nanocomposites will be tested for their suitability to use within a microneedle array as their superparamagnetic and PL properties would make the microneedle arrays capable of delivering MGQD-bound small and large MWt drugs that could be tracked and manipulated *in vivo*.

An additional aim of this chapter is to improve the usability of the microneedle arrays. The release of the encapsulated therapeutic from polymer microneedle arrays typically is dependent upon the enzymatic degradation or the dissolution rate of the polymer. If the enzymatic degradation or dissolution time is too long, the use of a

microneedle array may be impractical, and the placement of a patch on the skin for a substantial amount of time may also cause irritation [598]. To counter this problem, this chapter will assess the design of a microneedle array that allows for the quick separation of the microneedle shafts from the base within 5 min. This was achieved by the introduction of a disc section at the base of the microneedle shaft that was made from the water soluble polymer PEG; when the PEG is dissolved, the microneedles are no longer attached to the base of the array and can therefore remain within the skin after the base patch has been removed. The structural effect that this design change had to the microneedle array rigidity was assessed and it was shown that the modification did not impede the mechanical or drug release properties of the original microneedle array.

7.2 Experimental section

7.2.1 Materials

The following chemicals were reagent grade and used as purchased from Sigma Aldrich; acetic acid ($> 99.7\%$), sulphuric acid (95-98%), hydrogen peroxide (29-32% in H_2O), potassium permanganate (97%), sodium nitrate ($> 99\%$), lidocaine hydrochloride (LH, $> 99\%$), ferrous chloride tetrahydrate ($FeCl_2\text{-}4H_2O$, $> 99\%$), ferric chloride hexahydrate ($FeCl_3\text{-}6H_2O$, 97%), fluorescein sodium (FL), lysozyme (from chicken egg white, $\sim 100,000$ U mg^{-1}), fluorescein sodium labelled – bovine serum albumin (BSA, BioReagent grade), polyethylene glycol (PEG, of 10k Da, 20k Da, and 35k Da MWt) and graphite powder (≤ 20 µm). Chitosan powder ($M_w = 100,000\text{-}300,000$, Acros Scientific) was used as purchased from Fisher Scientific. Phosphate buffered saline (PBS) tablets (pH = 7.4) were purchased from Thermo Fisher Scientific.

7.2.2 Preparation of magnetic graphene quantum dots

The method to prepare MGQDs has been discussed previously in Chapter 6. Briefly, GO was synthesised from graphite using a modified Hummers method [187], purified by washing with distilled water, exfoliated in distilled water, and lyophilised in a freeze drier (Labconco FreeZone Triad). $FeCl_2$-$4H_2O$ (5.4 g) and $FeCl_3$-$6H_2O$ (4 g) were dissolved in 135 ml distilled water. GO (1 g) was stirred and sonicated in 150 ml distilled water for 1 h, and ammonium hydroxide was used to raise the pH to 8. The two solutions were added together and the pH was raised to 10 by ammonium hydroxide. Under a nitrogen atmosphere, the solution was stirred for 2 h. The resultant precipitate, GO-IO, was washed with distilled water and ethanol. GO-IO was dispersed in distilled water, (~ 3 mg ml^{-1}), and the solution was hydrothermally reduced in a Parr Series 4000 autoclave (200 °C for 10 h at 1.6 MPa). A dialysis bag (Fisher Scientific Biodesign Dialysis tubing, Mw cut off = 3.5 kDa) was used to separate the quantum dots from larger particles. MGQDs were collected from the surrounding solution and lyophilised for storage.

7.2.3 Drug loading onto magnetic graphene quantum dots

Equal quantities of MGQD and either LH or BSA were added to distilled water to form an aqueous suspension of 0.1 mg ml^{-1} and stirred for 48 h. To remove the unbound therapeutic, the suspension was centrifuged (8000 rpm for 1 h) and dispersed in fresh distilled water several times. The resultant powder was lyophilised for storage.

7.2.4 Preparation of nanocomposites

The required amount (to form 0.25-5 wt.% nanocomposites) of the QDs (whether they be MGQD, MGQD-LH, or MGQD-BSA) was dispersed with stirring and sonication in distilled water. Simultaneously, chitosan powder was added to 2 wt.% acetic acid in distilled water to form a 2 wt.% solution. When the chitosan was fully dissolved

(typically left overnight at room temperature under stirring), the MGQD suspension was added under intense stirring and left stirring to allow the suspension to increase in viscosity (chitosan concentration of ~80 mg ml^{-1}). The mixture was degassed in a vacuum oven for 1 h at room temperature and poured into a mould to air dry.

7.2.5 Characterisation of chitosan-MGQD nanocomposites

Fourier transform infra-red (FT-IR) spectroscopy was achieved with a resolution of 1 cm^{-1} between 400-4000 cm^{-1} on a Perkin Elmer Spectrum 100 with a diamond attenuated total reflectance (ATR) unit. X-ray diffraction (XRD) analysis on a Stoe Stadi P with Cu K$_\alpha$ irradiation (0.154 nm wavelength) was used with the following operating parameters: 40 kV, 35 mA, and a scanning speed of 1° min^{-1}.

A Hounsfield twin column universal testing machine was used to mechanically test the nanocomposites with a 1 kN load cell and a 1 mm min^{-1} strain rate in accordance with ISO-527. Test specimens (number of specimens per material (n) = 5) were punched from nanocomposite film and were dog-bone shaped (neck section = 20 mm long, 2.6 mm wide, and 1 mm thick). Electrical conductivity was measured with an Agilent Technologies 34401A digital multimeter (n = 5) with electrode contact points painted using silver paint (RS 186-3600). The samples used were the dog-bone tensile specimens, prior to mechanical testing, with the electrode contact points placed at either end of the neck section. Mass loss due to enzymatic degradation over 8 weeks of nanocomposite specimens (n = 5) in 37 $^\circ$C PBS solution (pH = 7.4) with a 1.5 μg ml^{-1} concentration of lysozyme [499], was recorded with an analytical balance (Sartorius M-power AZ124) and a Stuart SI500 bioincubator agitating at 100 rpm. After each time step, the specimens were washed with distilled water and dried in a vacuum oven overnight before weighing, after which they were placed into fresh PBS and lysozyme solution.

7.2.6 Production of nanocomposite microneedles
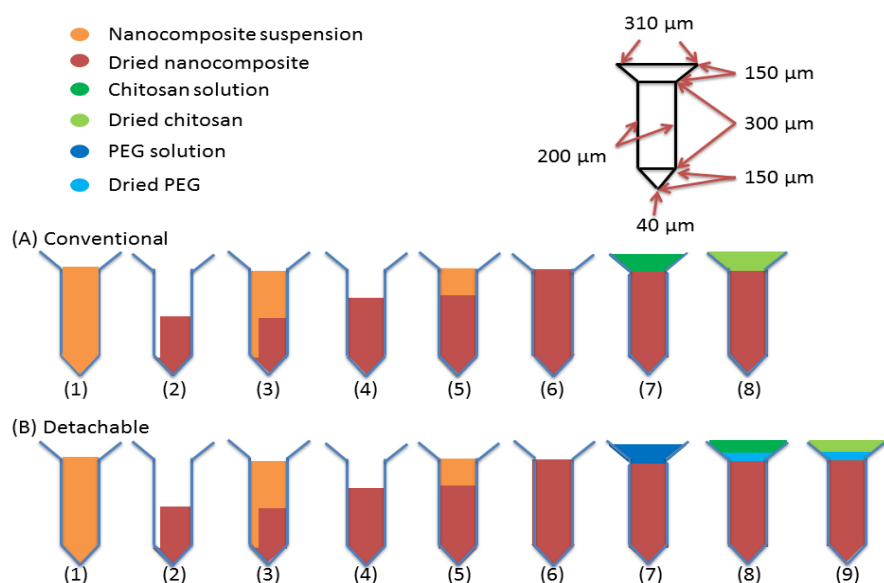
Scheme 7.1: Experimental procedure to create a (A) conventional and (B) detachable chitosan-MGQD microneedle arrays.

Conventional microneedle arrays were created in a two-step process as outlined in Scheme 7.1 [151,152], with the filling of the main needle shaft and the filling of the needle base as two separate processes. First, viscous nanocomposite solution (~80 mg ml^{-1}) was used to fill the moulds (Scheme 7.1A-2). To ensure that the solution filled the full microneedle (tip and shaft), the moulds were centrifuged at 8000 rpm for 1 h. Excess solution was cleaned from the surface and the moulds were left to air dry (Scheme 7.1A-3). The process of filling, centrifuging and drying the mould was repeated twice more to ensure the shaft was fully formed (Scheme 7.1A-(4-7)). Secondly, the base was filled with a viscous pristine chitosan solution, centrifuged for 1 h at 8000 rpm and dried in a vacuum oven (Scheme 7.1A-8). Upon drying, the microneedles were gently removed from the female mould and stored in desiccators.

To allow for the rapid detachment of the microneedle shaft from the base in the presence of bodily fluid, detachable microneedle arrays (Scheme 7.1B) were created with a ring of PEG at the base of the shaft. These arrays were created in a manner similar

to the standard microneedle arrays (Scheme 7.1B), but with one extra step: after the microneedle shaft has been filled with the nanocomposite mixture and dried, a highly viscous water solution of PEG is applied to the mould and excess solution scraped off. The moulds are then centrifuged for 1 h at 8000 rpm and dried in a vacuum oven. The base of the microneedles was created as standard, i.e. filled with high viscosity pristine chitosan solution, centrifuged for 1 h at 8000 rpm and dried in a vacuum oven.

7.2.7 Characterisation testing of microneedles

A Swift M10L microscope was used for optical microscopy images. Compression testing of the microneedles was carried out with a Hounsfield twin column universal testing machine with a 10 N load cell. The compression rate was 1 mm min^{-1}. Two metal plates were used as the platens; the microneedle array was attached to a fixed platen and a second platen was attached to the load cell and was used to uniformly compress the microneedle arrays (n = 5) [120]. The penetration of the microneedle arrays was measured in full-thickness chicken by cross-sectioning the specimen using a microtome (Brunel bench microtome) after they were embedded in a Labonord Q-Path paraffin embedding medium.

Chitosan – 2 wt.% MGQD-LH microneedle arrays (n = 5) were placed in 30 ml of PBS solution (37 °C, pH = 7.4) and agitated at 100 rpm. LH drug release was measured at set time points by collecting 3 ml of the solution and analysing it with UV-Vis spectroscopy (Perkin Elmer Lambda 900 operating at a resolution of 1nm), having replaced the taken solution with 3 ml of fresh PBS. The curves for each time point were compared to curves of free LH in PBS of known concentrations.

Chitosan – 2 wt.% MGQD-BSA microneedle arrays were tested for both passive diffusion and electrically stimulated diffusion of MGQD-BSA. For passive diffusion,

the microneedle array (n = 5) was placed in 100 ml of distilled water (37 ºC). BSA drug release was measured using UV-Vis spectroscopy, similar to the procedure to measure LH release. Electrically stimulated testing of chitosan − 2 wt.% MGQD-BSA microneedles was outlined previously in Chapter 5. Briefly, microneedle arrays were mounted to a microscopy slide using double-sided tape, with contacts made from silver paint to connect the microneedle array to the outer edge of the microscopy slide. The circuit, based on a prototyping circuit board, consists of a PP3 9 V 280 mAH nickel − metal hydride battery, a 2 kΩ resistor, an on/off switch, and two electrodes. The positive electrode was a crocodile clip that was used to connect the silver paint at the outer edge of the microneedle array to the circuit (the crocodile clip was not in direct contact with the microneedle array, and instead was in contact with the silver paint that touched the side of the microneedle array). The second electrode was submerged in the container of distilled water. The glass-slide was submerged vertically to a point where only the microneedle array was in the water and not the silver paint or the crocodile clip. The electrical flow, therefore, was through the microneedle array and not through the crocodile clip or the silver paint.

7.3 Results and discussion

7.3.1 Characterisation of nanocomposites

Characterisation of the MGQD nanoparticles was reported in Chapter 6. MGQDs were shown to possess PL and superparamagnetic properties for fluorescent imaging and M.R.I., and to respond to external magnetic stimulation for targeted drug delivery. The MGQDs were ~40 nm in diameter and 2-2.5 nm thick, and consisted of a core of a GQD coated with a shell containing a mixture of several IOs, namely maghemite, magnetite and hematite.
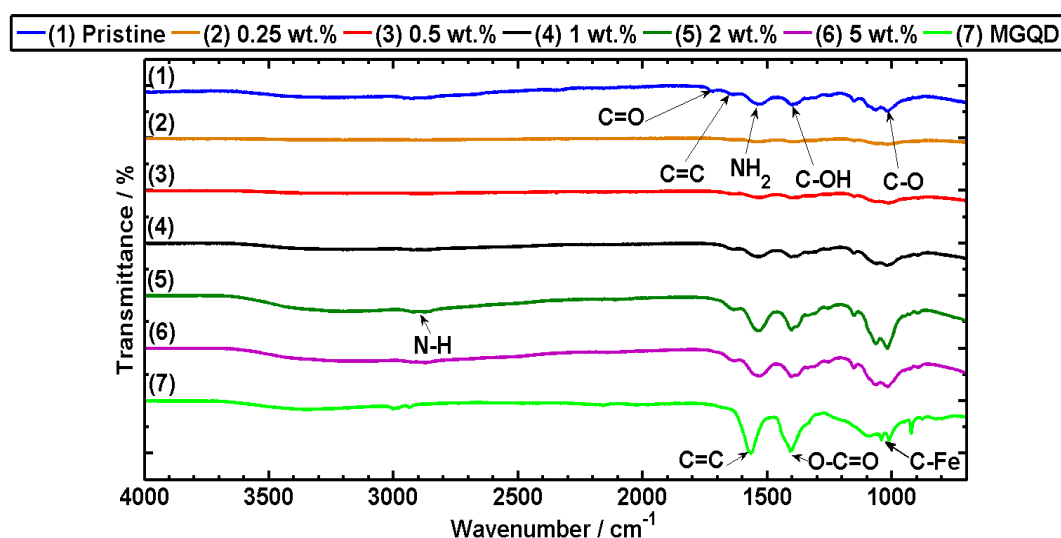
Figure 7.1: (A) FT-IR spectra and (B) XRD traces of chitosan-MGQD nanocomposites.

MGQDs were dispersed within chitosan at concentrations of 0.25-5 wt.%. FT-IR spectra are shown in Figure 7.1A, showing the characteristic peaks of chitosan (N-H peaks at 2800 cm^{-1}, C=O peak at 1720 cm^{-1}, C=C peak at 1640 cm^{-1}, amino peak at 1535-1546 cm^{-1}, C-OH peak at 1405 cm^{-1} and C-O at 1050-1100 cm^{-1}) [482]. The characteristic peaks of MGQDs are shown as C=C at 1564 cm^{-1}, O-C=O at 1406 cm^{-1}, and C-Fe peaks at 1086 cm^{-1} and 1012 cm^{-1} [574]. There are shifts in certain bonds when MGQDs are added to chitosan, for example the amino peak shifts from 1545 cm^{-1} for pristine chitosan to 1538 cm^{-1} for 1 wt.% MGQD, the C=C peak shifts from 1636 cm^{-1} for pristine chitosan to 1631 cm^{-1} for 1 wt.% MGQD and the C-O peak shifts from 1060 cm^{-1} for pristine chitosan to 1063 cm^{-1} for 1 wt.% MGQD. These

shifts can be attributed to both the hydrogen bonding that occurs between the chitosan (amino group) [396,482] and the MGQDs (Fe-O and O-C=O) and for the C-O peak shift there is the possible overlapping of peaks between the C-O peaks of chitosan and the C-Fe peaks of the MGQDs. The shifts are accompanied by a change in intensity of the C=C, amino, C-OH and C-O peaks for the nanocomposites, with the absorbance of all the peaks increasing from 0.25 wt.% to 2 wt.% as the MGQD wt.% increased.
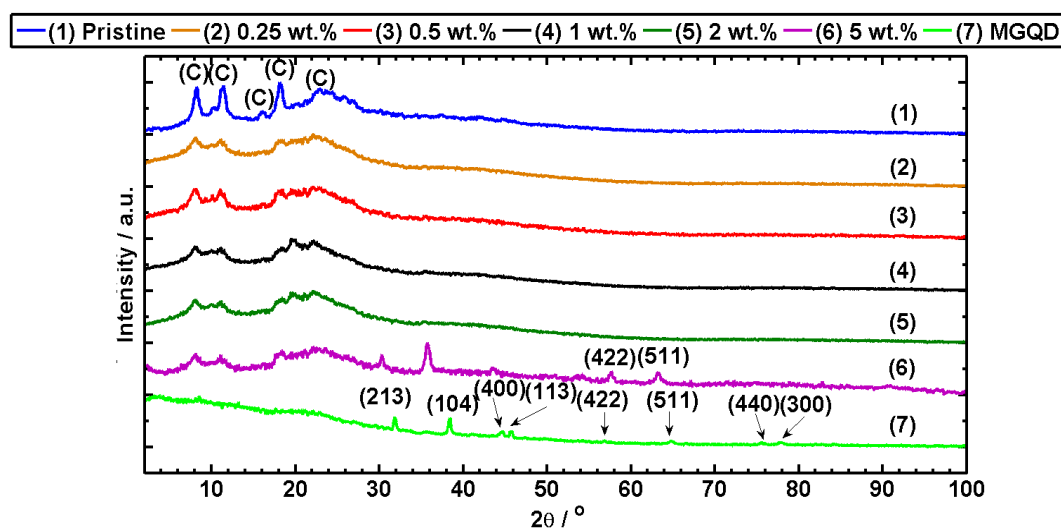
Figure 7.2: XRD traces of chitosan-MGQD nanocomposites.

In Figure 7.2, XRD traces of the nanocomposites can be seen. Typically, the chitosan peaks (crystalline and amorphous) are the only peaks present for both the pristine chitosan and the nanocomposites up to 2 wt.% MGQDs. The diffraction peaks from the MGQDs can be seen in the 5 wt.% nanocomposite due to the high wt.% of MGQDs present. These peaks are the (213) peak from maghemite, the (104) from hematite, and (422) and (511) from magnetite (Chapter 6). The other MGQD specific peaks may be present but too weak to clearly identify at this wt.%. From the chitosan-specific crystalline peaks that are identified on curve 1 of Figure 7.2, the crystallinity percentage can be determined from Equation 3.1 (Chapter 3). This gives crystallinity values for 0-5 wt.% MGQDs nanocomposites of 34.1%, 27.3%, 27.3%, 27.1%, 26.3%, and 25.5% respectively, showing a decrease in crystallinity with increasing wt.% of MGQDs. Graphene based nanoparticles have been shown previously to reduce the

crystallinity of chitosan-GO in Chapter 3 and chitosan-GQD nanocomposites in Chapter 5; in this instance, the decrease is presumably due to MGQDs restricting the chitosan chain movement due to the surface absorption and bonding [504].
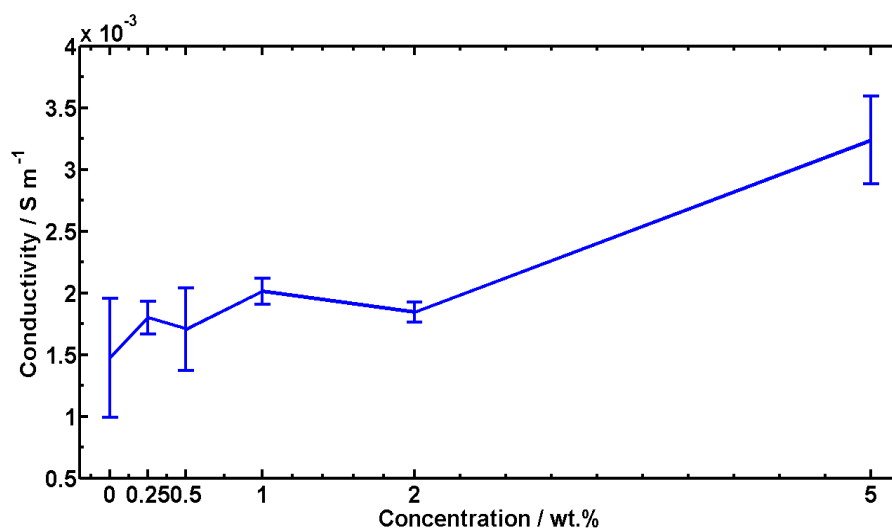
Figure 7.3: Electrical conductivity of chitosan-MGQD nanocomposites.

The electrical conductivity of the nanocomposites was measured, with a maximum conductivity of 0.0035 S m^{-1} achieved at 5 wt.% MGQD versus 0.0018 S m^{-1} for pristine chitosan (Figure 7.3). There was no significant increase in conductivity when the MGQDs wt.% increased from 0.25 wt.% to 2 wt.% MGQDs. The conductivity of the 5 wt.% MGQD nanocomposite is lower than that recorded for chitosan-GQD nanocomposites (e.g. 1 wt.% GQD = 0.0161 S m^{-1}, Chapter 5). The difference between nanocomposites formed of highly reduced GQD and of MGQD is due to the presence of IO on the surface of the MGQDs. IO can improve the conductivity of polymers [417,420,421], but graphene is more conductive than IO [179,599]. The shape, size, the dispersion degree of the MGQD and the volume fraction of graphene in the nanocomposite are other important factors that affect the electrical conductivity of a nanocomposite [366]. From Chapter 6, it can be seen that MGQDs are both thicker than GQDs at ~2.5 nm versus ~1.5 nm and of a higher density than the GQDs which means that there is a lower volume fraction of MGQDs within the nanocomposite for a given wt.% (3.66 g cm^{-3} for MGQD in comparison to 1.66 g cm^{-3} for GQD).
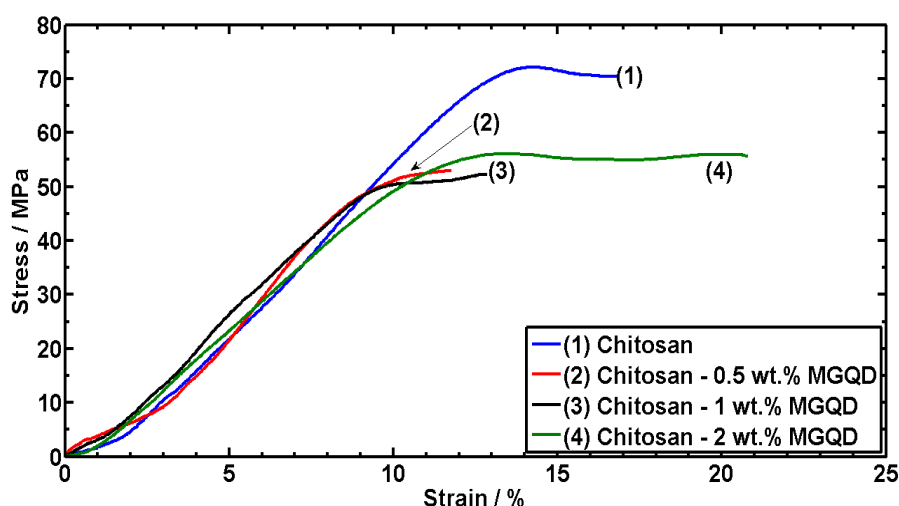
Figure 7.4: (A) Representative tensile curves and (B) enzymatic degradation rate for pristine chitosan and 0.5 wt.%, 1 wt.%, and 2 wt.% MGQD nanocomposites.

Figure 7.4 shows representative tensile stress-strain curves for pristine chitosan and chitosan nanocomposites. The Young's modulus (E) is 1.48 (± 0.38) GPa, the UTS is 62.5 (± 9.4) MPa, and ε_b is 15.5 (± 4.2) % for pristine chitosan. The 0.5 wt.% and 1 wt.% MGQD nanocomposites can be seen to have a lower UTS than pristine chitosan, with average values of 48.9 (± 3.4) MPa and 49.8 (± 4.1) MPa, respectively. The E of the 0.5 wt.% and 1 wt.% MGQD nanocomposites are 1.19 (± 0.07) GPa and 1.32 (± 0.16) GPa respectively. The 2 wt.% MGQD nanocomposite has a UTS and E that is statistically similar (p < 0.05 confidence level) to pristine chitosan, with an E of 1.45 (± 0.27) GPa and a UTS of 60.6 (± 7.25) MPa. The 5 wt.% MGQD nanocomposite was found to be too brittle to be mechanically tested.

The influential factors are the crystallinity of the chitosan and the effectiveness of the MGQDs as reinforcing nanofillers. The crystallinity of a polymer can affect its mechanical properties [483], and the nanocomposites of 0.25-2 wt.% have a lower crystallinity than the pristine chitosan, potentially reducing the strength and stiffness of the nanocomposites. As discussed previously, QDs such as MGQDs and GQDs may not be as effective a nanofiller as GO or rGO due to its smaller aspect ratio (they have both got a smaller diameter than GO or rGO and are both thicker than GO). MGQDs are also denser than rGO and GQD which means

199

that there is a lower volume fraction of MGQD nanoparticles within the nanocomposite for a given wt.% of nanofiller. MGQDs do, however, have a rGO backbone (reported E of 185 GPa [527] to 250 GPa [528] to 305 GPa [390]) and a shell of IO (E reported as 200-250 GPa depending on the crystal orientation [600]). There is also a strong bonding interface between the MGQDs and the chitosan (as shown in Figure 7.1). At a 2 wt.% loading, there is a sufficient concentration of MGQDs to efficiently transfer the load through the chitosan (which may not have been the case with the 0.5 wt.% and 1 wt.% nanocomposites).

The effect of crystallinity upon the chitosan and the effectiveness of the MGQD can be seen to effectively cancel each other out for the 2 wt.% nanocomposite. The ε_b is 13.3 ($\pm$ 3.9) % for 0.5 wt.%, 15.5 ($\pm$ 4.5) % for 1 wt.%, and 18.2 ($\pm$ 4.6) % for 2 wt.% MGQD nanocomposites. The 17.4% increase in ε_b for the 2 wt.% MGQD nanocomposite over chitosan is not as big an increase as for the ε_b increase (37%) for the chitosan-1 wt.% GQD nanocomposite from Chapter 5, which also had a 36% increase in UTS unlike the chitosan-MGQD nanocomposite, which is presumably due to the differences between MGQD and GQD in terms of size and density, as discussed previously. In comparison to chitosan, the increase in ε_b can be explained by the reduction in the crystallinity of the chitosan in the chitosan-MGQD nanocomposite and the MGQDs may possess a degree of mobility within the nanocomposite when the nanocomposite is under tension, which will absorb energy [369,400,505].
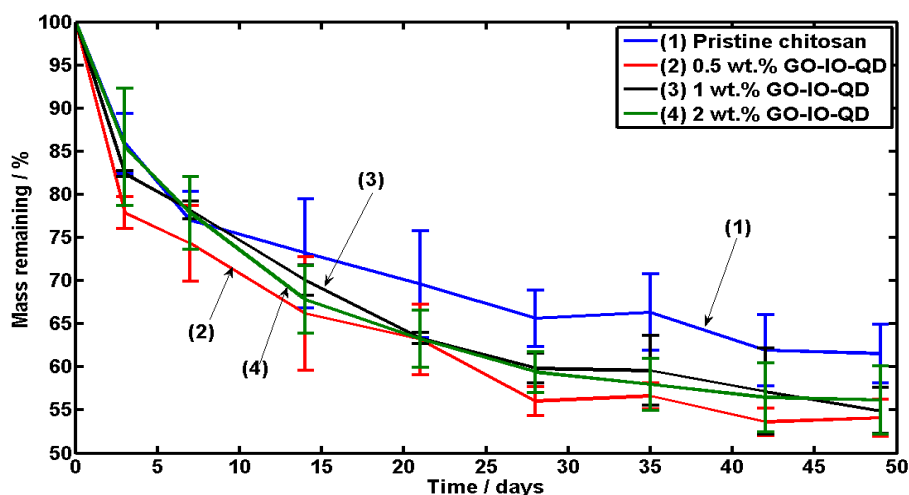
Figure 7.5: Enzymatic degradation rate for pristine chitosan and 0.5 wt.%, 1 wt.%, and 2 wt.% MGQD nanocomposites.

Pristine chitosan and the 0.5 wt.%, 1 wt.% and 2 wt.% nanocomposites were subjected to a enzymatic degradation test to determine the effect of MGQD concentration on the enzymatic degradation rate of chitosan. Figure 7.5 shows the effect that increasing the MGQD concentration has upon the remaining mass of chitosan at each time-step when subjected to enzymatic degradation. Chitosan samples were reduced to 61.6% of their original mass after 49 days, while 0.5 wt.%, 1 wt.% and 2 wt.% were reduced to 54.1%, 54.9% and 56.2% respectively.

It was previously noted in Chapters 3 and 4 that the inclusion of graphene nanosheets impeded the enzymatic degradation rate of nanocomposites through the previously discussed "tortuous path" model. This was not the case with the smaller MGQDs, as the nanocomposites can be seen in Figure 7.2B to have a higher enzymatic degradation rate than pristine chitosan and therefore the MGQDs did not impede the enzyme from permeating through the chitosan, similar to the chitosan-GQD nanocomposites in Chapter 5. For the chitosan-MGQD nanocomposites, the difference in the final mass of the samples is statistically insignificant, showing that the enzymatic degradation rate is not concentration dependent. The decrease in remaining mass between pristine chitosan and the MGQD nanocomposites is due to the lower

crystallinity of the nanocomposites compared to pristine chitosan and the possible diffusion of some of the MGQDs from the nanocomposite into the PBS solution [486,601].

7.3.2 Chitosan-2 wt.% microneedle arrays
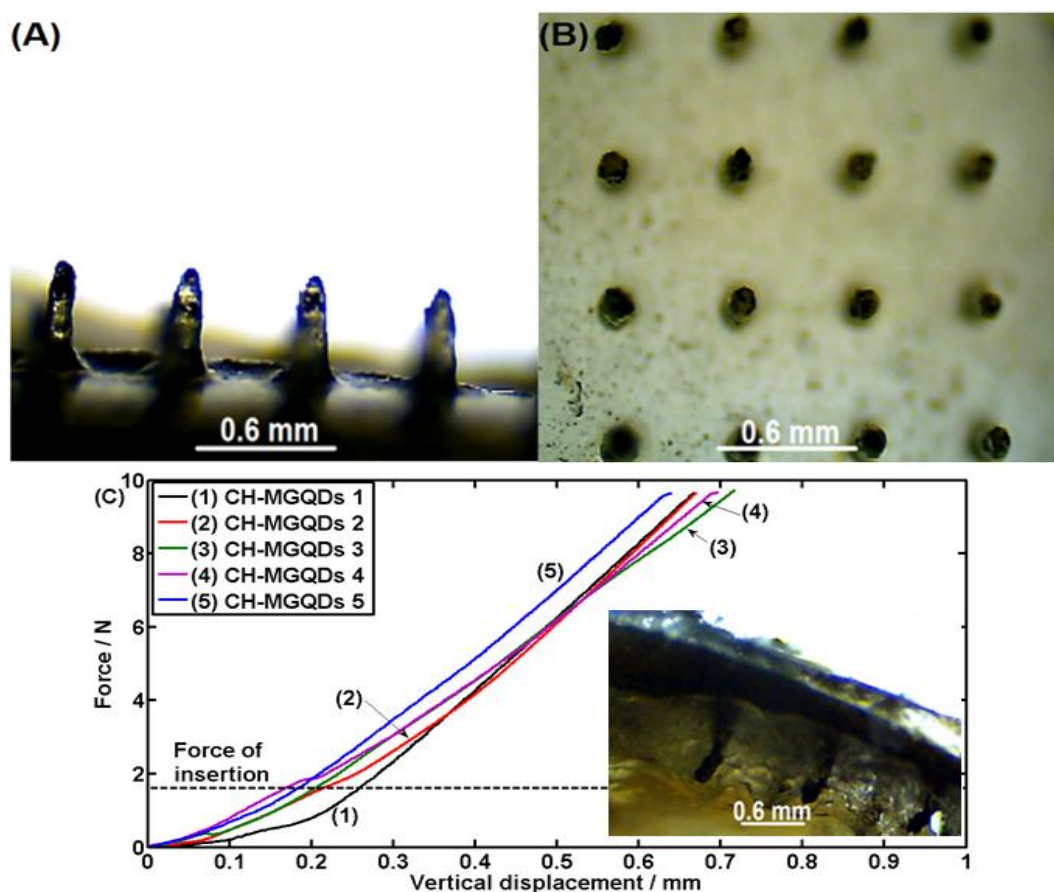
Figure 7.6: Optical microscopy images of the CH-MGQDs microneedle array; (A) side view, (B) plan view of the microneedle array, and (C) compression testing of CH-MGQDs microneedle arrays. (Inset) Side view of CH-MGQDs microneedle array after insertion into chicken skin.

The 2 wt.% MGQD nanocomposite was selected for use as a microneedle array as the nanocomposite had better mechanical properties than the other nanocomposites, close to pristine chitosan, while the high wt.% did not hinder the enzymatic degradation characteristics and would allow for a higher quantity of drug to be loaded into the nanocomposite relative to lower wt.% nanocomposites. Chitosan-2 wt.% MGQDs nanocomposites were used to form microneedle arrays for the delivery of small and large MWt drugs into the body via transdermal drug delivery. Figure 7.6A and 7.6B show optical microscopy images of the chitosan-2 wt.%

MGQD microneedle array (from here on known as CH-MGQD microneedle array), showing the plan and side profile of the microneedle arrays. The microneedle arrays were tested by compressive testing to 10 N to verify their structural integrity under the force of insertion, as seen in Figure 7.6C. A failure of the microneedle shaft would be seen as a substantial drop in the compressive force required to compress the microneedle array. The inset of Figure 7.6C shows the CH-MGQDs microneedle arrays during insertion into chicken skin by hand, confirming that these CH-MGQDs microneedle arrays were strong enough to survive the force of insertion into the skin. The depth of penetration of the microneedle array into the chicken skin can be determined as approximately 500 μm, similar to previously reported penetration values for chitosan-GQD microneedles in Chapter 5.

To allow for the microneedles to detach from the microneedle array base, a disc of the water soluble polymer PEG was included at the base of the microneedle shaft. Incorporating a section of pristine PEG to the base of the microneedle may have a negative impact upon the microneedle rigidity. Different MWt PEG polymers (MWt = 10 kDa, 20 kDa, and 35 kDa) were investigated for the effect that they would have on the structural integrity of the microneedle arrays. Higher MWt PEG was not tested as the systemic clearance of PEG from the body is reduced as the MWt increases [602] and there is a reduced dissolution rate when the MWt increases [603]. Figure 7.7A shows representative curves of the compressive testing of pristine chitosan microneedle arrays with the addition of a small ring of PEG between the main microneedle shaft and the base. It can be seen that the 10k Da MWt PEG microneedle array deformed substantially in comparison to pristine chitosan; the low MWt PEG offered limited mechanical strength to the base of the microneedle when under compression. The 20k Da microneedle arrays retained similar levels of deformation to the pristine chitosan sample due to the stronger mechanical properties of the 20k Da PEG relative to the 10k Da PEG.
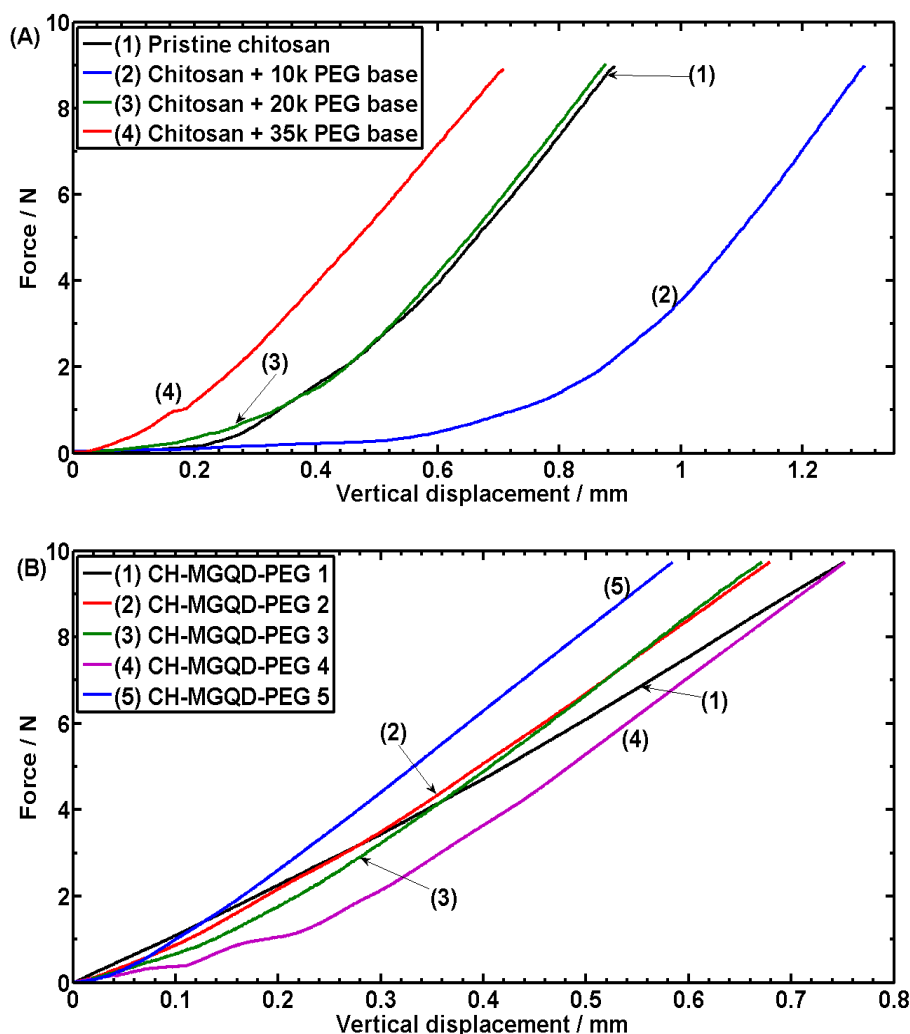
Figure 7.7: Compression testing of (A) chitosan and various MWt PEG and (B) CH-MGQDs with 35k Da PEG microneedle arrays.

The microneedle arrays containing 35k Da PEG were less ductile than the pristine chitosan microneedle arrays, due to the rigidity of the high MWt PEG. A strong base is important to the usability of microneedle arrays, preventing the fracture or bending during insertion. The 35k Da PEG proved to be the strongest base material of the materials tested and the force versus displacement curve of the chitosan-35 k Da PEG microneedle was similar to the pristine chitosan-2 wt.% MGQD microneedle array in Figure 7.6C. With this in mind, the 35k Da PEG was chosen to be used in this nanocomposite microneedle array.

The compressive testing results of the CH-MGQD with 35k Da PEG (from here on known as CH-MGQD-PEG) microneedle arrays are shown in Figure 7.7B, which shows that

the addition of a PEG ring to the base of the microneedle main shaft does not deteriorate the strength of the microneedle array in comparison to conventional CH-MGQD microneedle arrays, and the compression curves are similar to the CH-MGQD microneedle arrays without PEG.
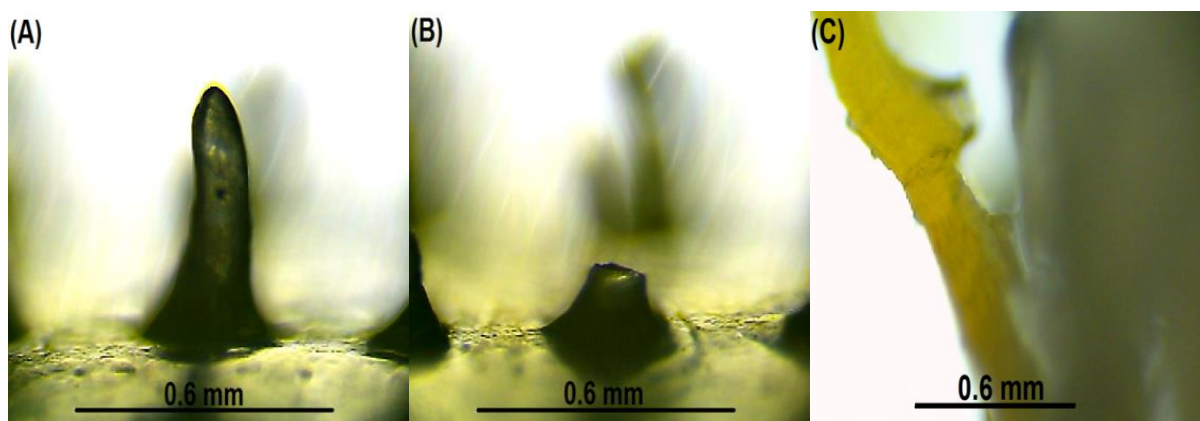
Figure 7.8: Side view of a CH-MGQD-PEG microneedle array, with (A) before and (B) after 5 min in the presence of water, showing the successful detachment of the microneedle shaft from the base. (C) After insertion of the microneedle array into chicken skin for 5 min, the successful detachment of the microneedle shaft from the base can be seen again.

Figure 7.8 shows the detachment of the microneedle main shaft from the array base when the CH-MGQD-PEG microneedle array was mounted to a glass slide and had two drops of distilled water applied to the upper surface. After 5 min, the water had caused the microneedle to swell and upon further inspection the microneedle shafts were no longer connected to the microneedle base. The mounds at the base of the microneedle shaft can be seen to have remained, as seen in Figure 7.8B. The region where PEG was deposited would have been between the mound and the main shaft. This shows that the microneedles can be detached within 5 min when in the presence of water or bodily fluid within skins by placing a ring of PEG between the main shaft and the base. Other images of microneedle separation are shown in Figure 7.S1 (Appendix 1). As a further proof of concept test, the CH-MGQD-PEG microneedle array was inserted into chicken skin (Figure 7.8 C) for 5 min, and it can be seen

that the microneedles have separated from the main base. This further confirms that the PEG separation method can work after insertion into skin.
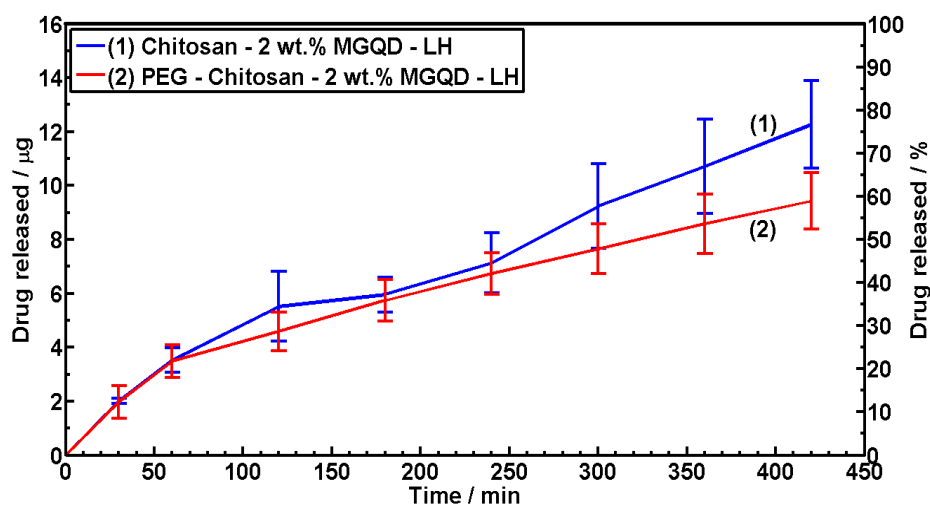
Figure 7.9: Release of LH from microneedle arrays of CH-MGQD or CH-MGQD-PEG over 7 h. The release from both microneedle types can be seen to be very similar in profile.

For the delivery of small MWt therapeutics, LH (288 Da) was chosen as the model drug. The drug was bonded (via hydrogen bonding and π-π stacking) to the surface of the MGQDs, with a loading ratio of 0.31:1 (LH:MGQD) determined from Chapter 6. Microneedle arrays containing chitosan and 2 wt.% MGQD with bonded LH were tested for the release of LH (Figure 7.9). Two types of microneedle arrays were tested; CH-MGQD-PEG and CH-MGQD. It can be seen that the two types of microneedle array are initially (up to 4 h) very similar in terms of quantity of drug released and the rate at which it was released, after which the CH-MGQD-PEG released less LH than the CH-MGQD microneedle array (after 6 h, CH-MGQD released 12.3 µg or 76.6% of the available drug and CH-MGQD-PEG released 9.4 µg or 59.4%). After this time-point, the microneedles were no longer fully intact and the test was stopped. The difference in final delivery quantity between the two types of microneedle array is presumably due to the separation of the microneedles from the base, as the same amount of drug-containing chitosan-2wt.% MGQD was used in both types of microneedles (i.e. three centrifuge cycles) and therefore the results should be identical. It is

206

possible that some of the microneedle shafts for the CH-MGQD-PEG may have become buoyant after 4 h after detaching from the base and floated to the surface of the PBS. This problem would not occur during *in vivo* treatment as the microneedles would be embedded in the skin prior to the separation. This test focused on the release of MGQD-LH from the microneedle array; it has been shown in Chapter 6 that LH could be fully released from MGQDs over 6 h.
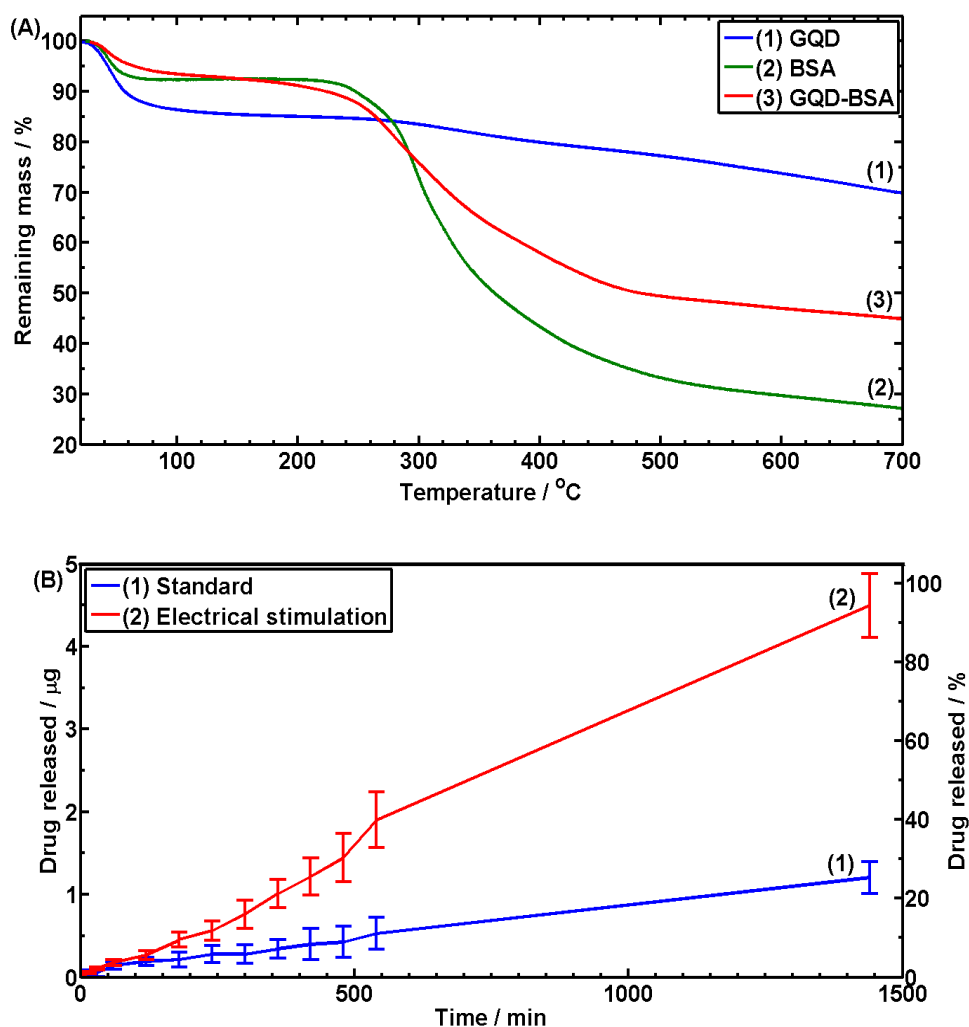
Figure 7.10: (A) TGA curves for the determination of the loading of BSA onto MGQDs and (B) the passive diffusion and electrically stimulated release of BSA from microneedle arrays.

To study the release of large MWt drugs from the CH-MGQD microneedles, MGQDs were bonded to the therapeutic BSA (~60k Da MWt). Iontophoresis could not be achieved

with CH-MGQD-PEG microneedles as the PEG ring would cause the detachment of the main microneedle shaft containing the drug before the drug could be released. Figure 7.10A shows the TGA curves of MGQDs, BSA, and MGQD-BSA. This shows that there is a 9.5%, or 0.10:1 BSA:MGQD, loading of BSA in MGQD-BSA, as determined from the mass loss of MGQD-BSA between 220-400 °C, accounting for both the loss of BSA over this temperature range (52.8%) and for absorbed water, in both cases. This MGQD-BSA was used to form CH-MGQD microneedles which were subsequently tested for passive diffusion release of BSA over 1440 min (24 h), as shown in Figure 7.10B. The passive diffusion release of BSA was limited, with only 0.5 μg or 10.7% released after 8 h and 1.2 μg or 25.7% released over 24 h. Similar passive drug release performance from the BSA loaded CH-MGQD-PEG microneedle array is expected.

This low level of release can be improved by using electrical stimulation, as shown in Chapter 5, where the use of electrical stimulation offered a significant improvement over standard diffusion release of BSA from chitosan-GQD microneedles. A similar improvement was noted for the CH-MGQD microneedles, with 1.9 μg or 40.7% released over 8 h and 4.5 μg or 96.4% released over 24 h, with the final value markedly higher than the 1.2 μg after 24 h for the passive diffusion microneedle array. Figure 7.11 shows the difference in release visually, with passive diffusion shown in the left container and electrically stimulated release in the right hand container. The yellow colour of the FL labelled BSA (Figure 5.S2, Appendix 1) can be seen in the right hand container after 4 h, with the colour becoming more vibrant at 6 h and 8 h. After 24 h, the colour of the right hand container is a combination of the strong yellow from the FL release and the black of the MGQD (Figure 6.4, inset). The water in the left container does not exhibit a strong yellow colour as the amount of BSA released from the passive diffusion microneedle array was substantially lower. The results of the drug test in Figure 7.10B show that chitosan

- 2 wt.% MGQD microneedle arrays can be used for the release of large MWt drugs through electrically stimulated diffusion; this ability is due to the nanocomposites being electrical conductive which allows for the current to flow through the nanocomposite in order to transfer the therapeutic from the nanocomposite into the target medium, such as with normal iontophoretic devices and their electrodes [62]. The results shown in Figure 7.9 and Figure 7.10 show that chitosan-MGQD nanocomposites are capable of the efficient and strong release of small and large MWt drugs when in the form of a microneedle array.
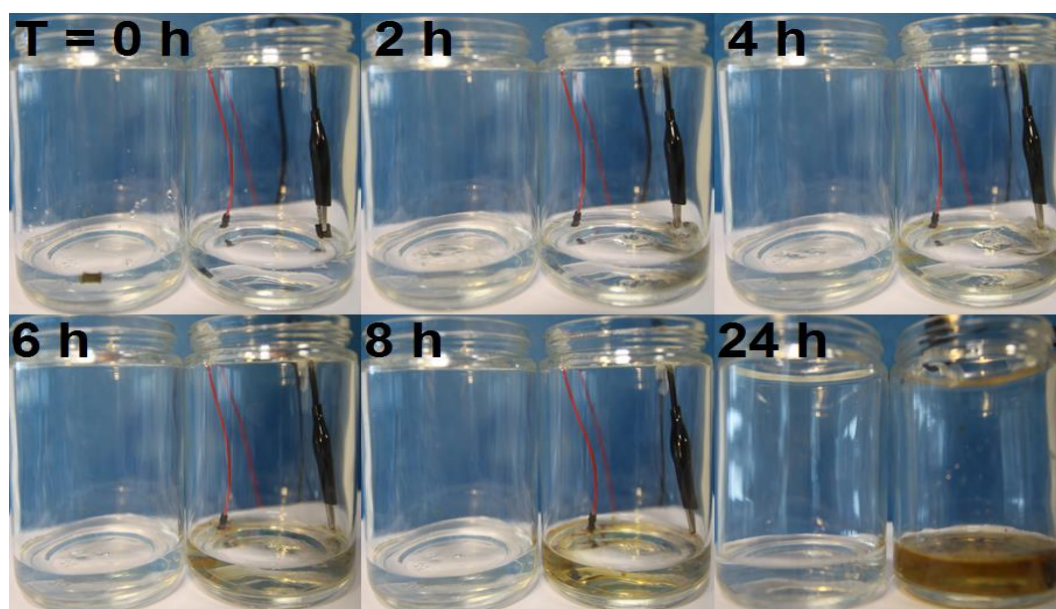
Figure 7.11: Visual representation of the difference in release of BSA by either passive (left) or electrically stimulated (right) release.

7.4 Conclusions

Iron oxide - reduced graphene oxide QDs (MGQDs) were shown in Chapter 6 to be capable of dual-modality imaging, targeted drug delivery, and photothermal ablation. Polymer nanocomposites of chitosan-MGQDs were developed for transdermal drug delivery applications such as a combined iontophoretic-microneedle array device where the nanocomposites would need to be both electrically conductive and mechanically

strong to survive insertion into the skin; the MGQDs would be used after release from the microneedle for the imaging/tracking of the drug.

The addition of 2 wt.% MGQDs to chitosan increased the electrical conductivity by 25%. The 2 wt.% MGQD nanocomposites has a statistically similar UTS and E to chitosan and a higher ε_b. Microneedle arrays need to be biodegradable and the 2 wt.% MGQD nanocomposite has a quicker initial enzymatic degradation rate than pristine chitosan. These results show that, while the MGQD may not offer an improvement to the mechanical properties, the added benefits of combining MGQDs with chitosan (such as improved electrical conductivity and increased enzymatic degradation) are not met with the disadvantage of a reduction in mechanical properties. Compression testing of the chitosan-MGQD nanocomposite microneedles confirmed that they were strong enough to survive the force of insertion into the skin layers. Cross-sections of chicken skin samples were used to determine the depth of penetration of the microneedle array as 500 μm.

Drug release from polymer-based microneedles is dependent upon the enzymatic degradation or the dissolution rate within bodily fluids of the polymer, which may be prohibitively long. Chitosan-MGQD nanocomposite microneedles were modified with a ring of PEG at the microneedle base; the microneedles were shown to rapidly detach from the base within 5 min in the presence of water or bodily fluid, with no effect on the mechanical strength of the microneedle arrays under compressive loading. The microneedles can stay in the body and release the MGQD-bound drug.

The chitosan-MGQD microneedle arrays, both conventional and detachable, were tested for their ability to release a small MWt drug. The conventional chitosan-MGQD microneedle array released 76.6% within 6 h, more than the detachable microneedle array (59.4%), proving that the chitosan-MGQD nanocomposite can be

used for drug delivery. There was a marked improvement in the delivery of large MWt drugs when the conventional microneedles were electrically stimulated to create a microneedle array-iontophoretic type device. The total percentage of drug released increased from 25.7% for passive diffusion to 96.4% over 24 h for the microneedle array-iontophoretic type device; showing that the ability to efficiently release large MWt drugs from the nanocomposite was only achievable by using electrical stimulation of the conductive films.

Microneedles formed from chitosan-MGQD nanocomposites have potential for use in medicine; the use of MGQDs as a drug carrier allows for therapeutics of small or large MWt to be bonded to the nanoparticle, subsequently targeted by an external magnetic field to a site of release whilst being monitored by M.R.I. or fluorescent imaging. The electrical conductivity of chitosan-MGQD nanocomposites can be used for the electrically stimulated release of large MWt drugs, allowing for chitosan-MGQD microneedle arrays to be a universal delivery platform for therapeutics of many different sizes and their subsequent targeting and monitoring.

Chapter 8. Overall conclusions and future work

8.1 Overall conclusions

This thesis has focused on the synthesis and characterisation of graphene derivatives and chitosan-graphene nanocomposites, and on quantifying the changes in material properties that adding these graphene derivatives into pristine chitosan can achieve. In each individual chapter, key findings have been discussed at that level but certain findings and trends are common throughout the thesis. From these common trends, one major conclusion can be ascertained: graphene can alter the mechanical properties, the electrical conductivity, the crystallinity, the enzymatic degradation rates, and the drug release rates of the nanocomposites relative to the pristine polymer.

Graphene acted as an effective reinforcement filler to increase the mechanical properties of chitosan, with changes in the E, UTS, and ε_b recorded for the chitosan-graphene nanocomposites attributed to the high aspect ratios, high surface areas, and high Young's modulus of graphene. Graphene is also a very electrically conductive nanoparticle, and when incorporated into a polymer nanocomposite, the resultant nanocomposites have improved electrical conductivity when compared to pristine chitosan and percolation thresholds were achieved at low graphene concentration levels.

Graphene affects the crystallinity of the nanocomposites, relative to pristine chitosan, which can influence the mechanical properties and the enzymatic degradation rate. The lowering of the crystallinity is attributed to the restriction of the chitosan chains by the graphene derivatives through surface absorption and bonding between the graphene and the chitosan, preventing the rearrangement of chitosan chains into ordered molecular chains for crystallisation. An increase in crystallinity was attributed to the crystallite nucleation effect of the graphene. Additionally, the presence of nanoparticles within a nanocomposite can

influence the enzymatic degradation of the nanocomposite by increasing the barrier properties due to the tortuous path model, where the high aspect ratio sheets are effective nanoparticles to limit the permeation of enzymes through the nanocomposite.

The release of the drug from a nanocomposite was both quicker and more substantial than that recorded for pristine chitosan; this improvement was attributed to the increase in the diffusion coefficient of the drug as a result of bonding the drug to graphene. Improvements in stimulus response were also noted for the chitosan-graphene nanocomposites in comparison to the pristine chitosan; the nanocomposites displayed a pH sensitive release of the drug, with a considerably lower drug release when the nanocomposite was in an acidic environment, as well as the electrically stimulated release of large MWt drugs that microneedles containing chitosan-graphene nanocomposites can be used for the delivery of both small and large MWt drugs. The increase in conductivity for the chitosan-graphene nanocomposites as if the nanocomposites were not conductive, iontophoretic stimulation would not be possible and subsequently the nanocomposites could not be used to deliver large MWt drugs.

Due to the improvements in mechanical, electrical conductivity, and drug release/delivery/tracking performance, chitosan-graphene nanocomposites are ideal materials for use in biomedical applications such as microneedle arrays or drug-release films and coatings, and the graphene derivatives themselves may find use as drug carriers that are capable of tracking and targeting a drug to a target site *in vivo*.

8.2 Future work

The design of the microneedle array could be improved in future work. These improvements could be an increase in the number of microneedles in an array (from 10×10 to 50×50, for example). This is the obvious way to increase the graphene-bound delivery dosage per microneedle array administration, but this can be met by usability issues; future research work

may focus on whether all of the microneedles in a larger array could be applied evenly at once by hand alone, and if not, how to achieve this with an a applicator instead of a hand.

Other possible improvements in the design could be to the depth of penetration of the microneedles; this might be through lengthening the microneedle shaft, but this would require compression studies to determine if buckling or bending is now a possible failure mode. Additional studies could also analyse the pain felt by patients when this particular design of microneedle is applied, if human trials could be arranged. If the microneedle is too long, it might interact with the nerves below the viable epidermis, and therefore cause pain.

The design of the microneedle array may be modified by widening the gap between microneedles in the array. This would benefit the insertion of the microneedles by preventing clogging by debris that might accumulate during insertion. It may also reduce the damage to the skin, with further spaced microneedles more likely to cleanly puncture the skin than to tear the skin. The effect that widening the spacing would have would require further *in vitro* skin penetration analysis and possible human or relevant animal trials to determine the effect that microneedle spacing has on skin healing. Testing would also be needed to determine whether all of the microneedles could be applied at once by hand, or whether the array is too large and an applicator is needed.

Alternative tip shapes might improve cutting performance and make the microneedle sharper, requiring a lower force to insert the array. These changes would need human or relevant animal trials to determine the effect that microneedle spacing has on skin healing. The best design could be determined and then utilised in future iteration of the microneedle array.

Within this thesis, polymer-graphene nanocomposites have been typically studied for drug testing at 1 wt.% or 2 wt.% ,and with the loading of drugs onto graphene typically in the 20-40% range, this means that the quantity of drug within a nanocomposite is limited. A solution to this problem may be to introduce unbound drug into the nanocomposite. The effect

of graphene on the release of this free drug from the polymer could be studied. In this scenario, graphene would not be bound to the drug but may still affect the drug release rate by decreasing the permeability of the release medium through the polymer, and the drug loading within the nanocomposite would be higher than that possible for graphene-bound drug loaded nanocomposites. This drug release testing will show if graphene will inhibit or improve the free drug release from nanocomposites with, for example, a ~40% loading versus pristine chitosan with the same drug quantity, but without graphene. This may overcome some of the problems with low graphene content and still allow graphene to be a structural reinforcement and to be used to make electrically conductive nanocomposites to allow for electrically stimulated drug release.

In vivo testing of the microneedle arrays and the release of the nanoparticles may be required to study the effects of nanoparticles delivered through this route. Although the literature states that graphene can be removed from the body, the application of graphene through the dermal layers has not been sufficiently studied as of yet. This testing might take the form of a 'bio-distribution' test where the quantity of accumulated graphene is measured at certain points of the body over the course of several weeks, as well as in the excretions of the test subject.

In this thesis, *in vitro* testing and characterisation analysis showed the potential of the MQGDs, but i*n vivo* testing would be required to fully study the combined targeting and imaging/tracking of the MGQDs and to assess their usefulness to biomedicine.

The GQDs and MGQDs could be developed further, with their cytotoxicity lowered by passivation with biomolecules. An *in vitro* biostability test will determine which biomolecules enhance the biostability of the QDs in bodily fluids when coated to the surface. The biomolecules may, however, hamper the fluorescent imaging capability of the QDs by fluorescence quenching, which will need to be investigated.

The magnetic properties of the MGQDs could be improved. Currently, the magnetic portion of the MGQDs is a mixture of iron oxides with varying magnetic strengths. Ideally, the magnetic properties of the MGQDs could be optimised by keeping the iron oxide solely magnetite. This may require an alteration in the production parameters (such as a lower autoclave temperature or the use of inert gases in the hydrothermal treatment to prevent oxidation to other forms) to prevent the production of different IO types that may be less magnetic than magnetite.

The hydrothermal treatment might also be modified by increasing the pressure of the inert gases beyond that which is possible with steam from the 200 $^{\circ}$C water. The increase in gas pressure within the autoclave may reduce the size of the QDs to a smaller size than currently possible. This may also allow the treatment temperature to be reduced from 200 $^{\circ}$C to a lower temperature.

Bibliography

[1] J. R. Wilmoth, "Increase of Maximum Life-Span in Sweden, 1861-1999," *Science (80-.).*, vol. 289, no. 5488, pp. 2366–2368, 2000.

[2] J. Oeppen and J. W. Vaupel, "Demography: Broken limits to life expectancy," *Science (80-.).*, vol. 296, no. 5570, pp. 1029–1031, 2002.

[3] J. Appleby, "Spending on health and social care over the next 50 years: why think long tem?" The King's Fund, London, pp. 1–68, 2013.

[4] Deloitte, "2014 Global Health Care Outook." Deloitte, London, pp. 1–28, 2014.

[5] J. A. Poisal, C. Truffer, S. Smith, A. Sisko, C. Cowan, S. Keehan, and B. Dickensheets, "Health spending projections through 2016: modest changes obscure part D's impact.," *Health Aff. (Millwood).*, vol. 26, no. 2, pp. 242–253, 2007.

[6] F. Lienert, J. J. Lohmueller, A. Garg, and P. A. Silver, "Synthetic biology in mammalian cells: next generation research tools and therapeutics.," *Nat. Rev. Mol. Cell Biol.*, vol. 15, no. 2, pp. 95–107, 2014.

[7] C. Alvarez-Lorenzo and A. Concheiro, "Smart drug delivery systems: from fundamentals to the clinic.," *Chem. Commun. (Camb).*, vol. 50, no. 58, pp. 7743–7765, 2014.

[8] S. Hehir and N. R. Cameron, "Recent advances in drug delivery systems based on polypeptides prepared from N -carboxyanhydrides," *Polym. Int.*, vol. 63, no. 6, pp. 943–954, 2014.

[9] W. Passl, "Synthetic polymers in modern pharmacy," *Prog. Polym. Sci.*, vol. 14, pp. 629–677, 1989.

[10] L. G. Ost, "Blood and injection phobia: background and cognitive, physiological, and behavioral variables," *J. Abnorm. Psychol.*, vol. 101, pp. 68–74, 1992.

[11] Y. Mizuno, K. Suzuki, M. Mori, K. Hayashi, T. Owaki, H. Hayashi, K. Kumada, K. Ohba, and M. Mizokami, "Study of needlestick accidents and hepatitis C virus infection in healthcare workers by molecular evolutionary analysis.," *J. Hosp. Infect.*, vol. 35, no. 2, pp. 149–154, 1997.

[12] M. R. Prausnitz and R. Langer, "Transdermal drug delivery.," *Nat. Biotechnol.*, vol. 26, no. 11, pp. 1261–1268, 2008.

[13] A. Ahad, M. Aqil, K. Kohli, Y. Sultana, M. Mujeeb, and A. Ali, "Transdermal drug delivery: the inherent challenges and technological advancements," *J. Pharmacol. Sci.*, vol. 5, no. 6, pp. 276–288, 2010.

[14] Z. Liu, J. T. Robinson, X. Sun, and H. Dai, "PEGylated nanographene oxide for delivery of water-insoluble cancer drugs.," *J. Am. Chem. Soc.*, vol. 130, no. 33, pp. 10876–10877, 2008.

[15] S. K. Bhunia, A. Saha, A. R. Maity, S. C. Ray, and N. R. Jana, "Carbon nanoparticle-based fluorescent bioimaging probes.," *Sci. Rep.*, vol. 3, pp. 1–7, 2013.

[16] S. Cheong, P. Ferguson, K. W. Feindel, I. F. Hermans, P. T. Callaghan, C. Meyer, A. Slocombe, C.-H. Su, F.-Y. Cheng, C.-S. Yeh, B. Ingham, M. F. Toney, and R. D. Tilley, "Simple synthesis and functionalization of iron nanoparticles for magnetic resonance imaging.," *Angew. Chem. Int. Ed. Engl.*, vol. 50, no. 18, pp. 4206–4209, 2011.

[17] D. R. Larson, W. R. Zipfel, R. M. Williams, S. W. Clark, M. P. Bruchez, F. W. Wise, and W. W. Webb, "Water-soluble quantum dots for multiphoton fluorescence imaging in vivo." *Science*, vol. 300, no. 5624, pp. 1434–1436, 2003.

[18] M.-L. Chen, Y.-J. He, X.-W. Chen, and J.-H. Wang, "Quantum-dot-conjugated graphene as a probe for simultaneous cancer-targeted fluorescent imaging, tracking, and monitoring drug delivery.," *Bioconjug. Chem.*, vol. 24, no. 3, pp. 387–397, 2013.

[19] C. Alexiou, R. Jurgons, R. Schmid, a Hilpert, C. Bergemann, F. Parak, and H. Iro, "In vitro and in vivo investigations of targeted chemotherapy with magnetic nanoparticles," *J. Magn. Magn. Mater.*, vol. 293, no. 1, pp. 389–393, 2005.

[20] K. H. Bae, M. Park, M. J. Do, N. Lee, J. H. Ryu, G. W. Kim, C. G. Kim, T. G. Park, and T. Hyeon, "Chitosan Oligosaccharide-Stabilized Ferrimagnetic Iron Oxide Nanocubes for Magnetically Modulated Cancer Hyperthermia.," *ACS Nano*, vol. 26, pp. 5266–5273, 2012.

[21] Dorland, *Dorland's Illustrated Medical Dictionary*, 32nd ed., no. 32E. Philadelphia: Saunders (Elsevier), 2011.

[22] R. A. Kleinknecht, R. M. Thorndike, and M. M. Walls, "Factorial dimensions and correlates of blood, injury, injection and related medical fears: Cross validation of the Medical Fear Survey," *Behav. Res. Ther.*, vol. 34, no. 4, pp. 323–331, 1996.

[23] B. Deacon and J. Abramowitz, "Fear of needles and vasovagal reactions among phlebotomy patients.," *J. Anxiety Disord.*, vol. 20, no. 7, pp. 946–960, 2006.

[24] J. L. Gerberding, "Incidence and prevalence of human immunodeficiency virus, hepatitis B virus, hepatitis C virus, and cytomegalovirus among health care personnel at risk for blood exposure: final report from a longitudinal study.," *J. Infect. Dis.*, vol. 170, no. 6, pp. 1410–1417, 1994.

[25] B. Gumodoka, J. Vos, Z. a Berege, H. a van Asten, W. M. Dolmans, and M. W. Borgdorff, "Injection practices in Mwanza Region, Tanzania: prescriptions, patient demand and sterility.," *Trop. Med. Int. Health*, vol. 1, no. 6, pp. 874–880, 1996.

[26] Manmohan, T. Shukla, A. Mathur, N. Upadhyay, and S. Sharma, "A review on gastro retentive drug delivery system: an emerging approach to improve the gastric residence time of solid dosage forms," *J. Pharmacol. Sci.*, vol. 8, no. 2, pp. 176–182, 2011.

[27] A. Sosnik, J. das Neves, and B. Sarmento, "Mucoadhesive polymers in the design of nano-drug delivery systems for administration by non-parenteral routes: A review," *Prog. Polym. Sci.*, vol. 39, no. 12, pp. 2030–2075, 2014.

[28] U. A. Meyer and U. M. Zanger, "Molecular mechanisms of genetic polymorphisms of drug metabolism.," *Annu. Rev. Pharmacol. Toxicol.*, vol. 37, pp. 269–296, 1997.

[29] J. A. Mikszta, V. J. Sullivan, C. Dean, A. M. Waterston, J. B. Alarcon, J. P. Dekker, J. M. Brittingham, J. Huang, C. R. Hwang, and M. Ferriter, "Protective immunization against inhalational anthrax: a comparison of minimally invasive delivery platforms," *J. Infect. Dis.*, vol. 191, no. 2, pp. 278–288, 2005.

[30] R. C. Dhakar, S. D. Maurya, V. K. Tilak, and A. K. Gupta, "A review on factors affecting the design of nasal drug delivery system," *International Journal of Drug Delivery*, vol. 3, no. 2. pp. 194–208, 2011.

[31] A. Alexander, S. Dwivedi, Ajazuddin, T. K. Giri, S. Saraf, S. Saraf, and D. K. Tripathi, "Approaches for breaking the barriers of drug permeation through transdermal drug delivery.," *J. Control. Release*, vol. 164, no. 1, pp. 26–40, 2012.

[32] T. W. Wong, "Electrical, magnetic, photomechanical and cavitational waves to overcome skin barrier for transdermal drug delivery.," *J. Control. Release*, vol. 193, pp. 257–269, 2014.

[33] A. I. Minchinton and I. F. Tannock, "Drug penetration in solid tumours.," *Nat. Rev. Cancer*, vol. 6, no. 8, pp. 583–592, 2006.

[34] O. Trédan, C. M. Galmarini, K. Patel, and I. F. Tannock, "Drug resistance and the solid tumor microenvironment.," *J. Natl. Cancer Inst.*, vol. 99, no. 19, pp. 1441–1454, 2007.

[35] S. Henry, D. McAllister, M. Allen, and M. Prausnitz, "Microfabricated microneedles: A novel approach to transdermal drug delivery," *J. Pharmacol. Sci.*, vol. 87, no. 8, pp. 922–925, 1998.

[36] A. Joshi and J. Raje, "Sonicated transdermal drug transport.," *J. Control. Release*, vol. 83, no. 1, pp. 13–22, 2002.

[37] G. Widera, J. Johnson, L. Kim, L. Libiran, K. Nyam, P. E. Daddona, and M. Cormier, "Effect of delivery parameters on immunization to ovalbumin following intracutaneous administration by a coated microneedle array patch system.," *Vaccine*, vol. 24, no. 10, pp. 1653–1664, 2006.

[38] D. G. Koutsonanos, M. del Pilar Martin, V. G. Zarnitsyn, S. P. Sullivan, R. W. Compans, M. R. Prausnitz, and I. Skountzou, "Transdermal influenza immunization with vaccine-coated microneedle arrays.," *PLoS One*, vol. 4, no. 3, pp. 4773–4782, 2009.

[39] H. J. Dean, D. Fuller, and J. E. Osorio, "Powder and particle-mediated approaches for delivery of DNA and protein vaccines into the epidermis.," *Comp. Immunol. Microbiol. Infect. Dis.*, vol. 26, no. 5–6, pp. 373–388, 2003.

[40] K. van der Maaden, W. Jiskoot, and J. Bouwstra, "Microneedle technologies for (trans)dermal drug and vaccine delivery.," *J. Control. Release*, vol. 161, no. 12, pp. 645–655, 2012.

[41] R. J. Feldmann and H. I. Maibach, "Regional variation in percutaneous penetration of 14C cortisol in man.," *J. Invest. Dermatol.*, vol. 48, no. 2, pp. 181–183, 1967.

[42] A. Gupta and P. B. Myrdal, "Development of a perillyl alcohol topical cream formulation," *Int. J. Pharm.*, vol. 269, no. 2, pp. 373–383, 2004.

[43] H. Petering, C. Breuer, R. Herbst, A. Kapp, and T. Werfel, "Comparison of localized high-dose UVA1 irradiation versus topical cream psoralen-UVA for treatment of chronic vesicular dyshidrotic eczema," *J. Am. Acad. Dermatol.*, vol. 50, no. 1, pp. 68–72, 2004.

[44] M. G. Lebwohl, D. L. Breneman, B. S. Goffe, J. R. Grossman, M. R. Ling, J. Milbauer, S. H. Pincus, R. G. Sibbald, L. J. Swinyer, G. D. Weinstein, D. A. Lew-Kaya, J. C. Lue, J. R. Gibson, and J. Sefton, "Tazarotene 0.1% gel plus corticosteroid cream in the treatment of plaque psoriasis," *J. Am. Acad. Dermatol.*, vol. 39, no. 4, pp. 590–596, 1998.

[45] D. W. Osborne, A. J. I. Ward, and K. J. O'Neill, "Microemulsions as topical drug delivery vehicles: in-vitro transdermal studies of a model hydrophilic drug," *J. Pharm. Pharmacol.*, vol. 43, no. 6, pp. 451–454, 1991.

[46] C. C. Lyon, A. J. Smith, C. E. Griffiths, and M. H. Beck, "Peristomal dermatoses: a novel indication for topical steroid lotions.," *J. Am. Acad. Dermatol.*, vol. 43, no. 4, pp. 679–682, 2000.

[47] H. Schreier and J. Bouwstra, "Liposomes and niosomes as topical drug carriers: dermal and transdermal drug delivery," *J. Control. Release*, vol. 30, no. 1, pp. 1–15, 1994.

[48] M. Mezei and V. Gulasekharam, "Liposomes-A selective drug delivery system for the topical route of administration: gel dosage form," *J. Pharm. Pharmacol.*, vol. 34, no. 7, pp. 473–474, 1982.

[49] M. Mezei and V. Gulasekharam, "Liposomes - a selective drug delivery system for the topical route of administration I. Lotion dosage form," *Life Sci.*, vol. 26, no. 18, pp. 1473–1477, 1980.

[50] A. Azagury, L. Khoury, G. Enden, and J. Kost, "Ultrasound mediated transdermal drug delivery.," *Adv. Drug Deliv. Rev.*, vol. 72, pp. 127–143, 2014.

[51] J. E. Riviere and M. G. Papich, "Potential and problems of developing transdermal patches for veterinary applications," *Adv. Drug Deliv. Rev.*, vol. 50, no. 3, pp. 175–203, 2001.

[52] A.-R. Denet, R. Vanbever, and V. Préat, "Skin electroporation for transdermal and topical delivery.," *Adv. Drug Deliv. Rev.*, vol. 56, no. 5, pp. 659–674, 2004.

[53] J. C. Weaver and Y. A. Chizmadzhev, "Theory of electroporation: A review," *Bioelectrochemistry Bioenerg.*, vol. 41, no. 2, pp. 135–160, 1996.

[54] T. Blagus, B. Markelc, M. Cemazar, T. Kosjek, V. Preat, D. Miklavcic, and G. Sersa, "In vivo real-time monitoring system of electroporation mediated control of transdermal and topical drug delivery.," *J. Control. Release*, vol. 172, no. 3, pp. 862–871, 2013.

[55] M. R. Prausnitz, V. G. Bose, R. Langer, and J. C. Weaver, "Electroporation of mammalian skin: a mechanism to enhance transdermal drug delivery.," *Proc. Natl. Acad. Sci.*, vol. 90, no. 22, pp. 10504–10508, 1993.

[56] S. A. Molokhia, E.-K. Jeong, W. I. Higuchi, and S. K. Li, "Transscleral iontophoretic and intravitreal delivery of a macromolecule: study of ocular distribution in vivo and postmortem with MRI.," *Exp. Eye Res.*, vol. 88, no. 3, pp. 418–425, 2009.

[57] J. E. Riviere, N. A. Monteiro-Riviere, R. A. Rogers, D. Bommannan, J. A. Tamada, and R. O. Potts, "Pulsatile transdermal delivery of LHRH using electroporation: Drug delivery and skin toxicology," *J. Control. Release*, vol. 36, no. 3, pp. 229–233, 1995.

[58] J. W. Hooper, J. W. Golden, A. M. Ferro, and A. D. King, "Smallpox DNA vaccine delivered by novel skin electroporation device protects mice against intranasal poxvirus challenge.," *Vaccine*, vol. 25, no. 10, pp. 1814–1823, 2007.

[59] H. Aihara and J. Miyazaki, "Gene transfer into muscle by electroporation in vivo.," *Nat. Biotechnol.*, vol. 16, no. 9, pp. 867–870, 1998.

[60] M. R. M. R. Prausnitz, "The effects of electric current applied to skin: A review for transdermal drug delivery," *Adv. Drug Deliv. Rev.*, vol. 18, no. 3, pp. 395–425, 1996.

[61] M. S. Wallace, B. Ridgeway, E. Jun, G. Schulteis, D. Rabussay, and L. Zhang, "Topical delivery of lidocaine in healthy volunteers by electroporation, electroincorporation, or iontophoresis: an evaluation of skin anesthesia.," *Reg. Anesth. Pain Med.*, vol. 26, no. 3, pp. 229–238, 2001.

[62] M. B. Brown, M. J. Traynor, G. P. Martin, and F. K. Akomeah, "Transdermal drug delivery systems: skin perturbation devices.," *Methods Mol. Biol.*, vol. 437, pp. 119–139, 2008.

[63] Y. N. Kalia, A. Naik, J. Garrison, and R. H. Guy, "Iontophoretic drug delivery.," *Adv. Drug Deliv. Rev.*, vol. 56, no. 5, pp. 619–658, 2004.

[64] M. J. Pikal, "The role of electroosmotic flow in transdermal iontophoresis," *Adv. Drug Deliv. Rev.*, vol. 9, no. 2–3, pp. 201–237, 1992.

[65] J. P. Howard, T. R. Drake, and D. L. Kellogg, "Effects of alternating current iontophoresis on drug delivery," *Arch. Phys. Med. Rehabil.*, vol. 76, no. 5, pp. 463–466, 1995.

[66] E. Eljarrat-Binstock, F. Raiskup, J. Frucht-Pery, and A. J. Domb, "Hydrogel probe for iontophoresis drug delivery to the eye," *J. Biomater. Sci. Polym. Ed.*, vol. 15, no. 4, pp. 397–413, 2012.

[67] T. Gratieri, E. Pujol-Bello, G. M. Gelfuso, J. G. de Souza, R. F. V Lopez, and Y. N. Kalia, "Iontophoretic transport kinetics of ketorolac in vitro and in vivo: demonstrating local enhanced topical drug delivery to muscle.," *Eur. J. Pharm. Biopharm.*, vol. 86, no. 2, pp. 219–226, 2014.

[68] M. Halhal, G. Renard, Y. Courtois, D. BenEzra, and F. Behar-Cohen, "Iontophoresis: from the lab to the bed side," *Exp. Eye Res.*, vol. 78, no. 3, pp. 751–757, 2004.

[69] S. N. Murthy, S. M. Sammeta, and C. Bowers, "Magnetophoresis for enhancing transdermal drug delivery: Mechanistic studies and patch design.," *J. Control. Release*, vol. 148, no. 2, pp. 197–203, 2010.

[70] S. M. Sammeta, M. A. Repka, and S. Narasimha Murthy, "Magnetophoresis in combination with chemical enhancers for transdermal drug delivery.," *Drug Dev. Ind. Pharm.*, vol. 37, no. 9, pp. 1076–1082, 2011.

[71] G. Krishnan, J. Edwards, and Y. Chen, "Enhanced skin permeation of naltrexone by pulsed electromagnetic fields in human skin in vitro," *J. Pharm. Sci.*, vol. 99, no. 6, pp. 2724–2731, 2010.

[72] S. Mitragotri and J. Kost, "Low-frequency sonophoresis: a review.," *Adv. Drug Deliv. Rev.*, vol. 56, no. 5, pp. 589–601, 2004.

[73] D. Bommannan, H. Okuyama, P. Stauffer, and R. H. Guy, "Sonophoresis. I. The Use of High-Frequency Ultrasound to Enhance Transdermal Drug Delivery," *Pharm. Res.*, vol. 9, no. 4, pp. 559–564, 1992.

[74] N. B. Smith, S. Lee, E. Maione, R. B. Roy, S. McElligott, and K. K. Shung, "Ultrasound-mediated transdermal transport of insulin in vitro through human skin using novel transducer designs.," *Ultrasound Med. Biol.*, vol. 29, no. 2, pp. 311–317, 2003.

[75] H. Liu, S. Li, W. Pan, Y. Wang, F. Han, and H. Yao, "Investigation into the potential of low-frequency ultrasound facilitated topical delivery of Cyclosporin A.," *Int. J. Pharm.*, vol. 326, no. 1–2, pp. 32–38, 2006.

[76] S. Mitragotri and J. Kost, "Transdermal Delivery of Heparin and Low-Molecular Weight Heparin Using Low-Frequency Ultrasound," *Pharm. Res.*, vol. 18, no. 8, pp. 1151–1156, 2001.

[77] A. Dahlan, H. O. Alpar, and S. Murdan, "An investigation into the combination of low frequency ultrasound and liposomes on skin permeability.," *Int. J. Pharm.*, vol. 379, no. 1, pp. 139–142, 2009.

[78] S. Mitragotri, D. Blankschtein, and R. Langer, "Ultrasound-mediated transdermal protein delivery," *Science (80-.).*, vol. 269, no. 5225, pp. 850–853, 1995.

[79] A. Tezel, A. Sens, J. Tuchscherer, and S. Mitragotri, "Synergistic effect of low-frequency ultrasound and surfactants on skin permeability.," *J. Pharm. Sci.*, vol. 91, no. 1, pp. 91–100, 2002.

[80] R. Alvarez-Román, G. Merino, Y. N. Kalia, A. Naik, and R. H. Guy, "Skin permeability enhancement by low frequency sonophoresis: lipid extraction and transport pathways.," *J. Pharm. Sci.*, vol. 92, no. 6, pp. 1138–1146, 2003.

[81] B. E. Polat, D. Hart, R. Langer, and D. Blankschtein, "Ultrasound-mediated transdermal drug delivery: mechanisms, scope, and emerging trends.," *J. Control. Release*, vol. 152, no. 3, pp. 330–348, 2011.

[82] J. Bramson, K. Dayball, C. Evelegh, Y. H. Wan, D. Page, and A. Smith, "Enabling topical immunization via microporation: a novel method for pain-free and needle-free delivery of adenovirus-based vaccines.," *Gene Ther.*, vol. 10, no. 3, pp. 251–260, 2003.

[83] A. V Badkar, A. M. Smith, J. a Eppstein, and A. K. Banga, "Transdermal delivery of interferon alpha-2B using microporation and iontophoresis in hairless rats.," *Pharm. Res.*, vol. 24, no. 7, pp. 1389–1395, 2007.

[84] A. Arora, M. R. Prausnitz, and S. Mitragotri, "Micro-scale devices for transdermal drug delivery.," *Int. J. Pharm.*, vol. 364, no. 2, pp. 227–236, 2008.

[85] M. Paranjape, J. Garra, S. Brida, T. Schneider, R. White, and J. Currie, "A PDMS dermal patch for non-intrusive transdermal glucose sensing," *Sensors Actuators A Phys.*, vol. 104, no. 3, pp. 195–204, 2003.

[86] U. Hohenleutner, S. Hohenleutner, W. Bäumler, and M. Landthaler, "Fast and effective skin ablation with an Er:YAG laser: determination of ablation rates and thermal damage zones.," *Lasers Surg. Med.*, vol. 20, no. 3, pp. 242–247, 1997.

[87] J. W. Lee, P. Gadiraju, J.-H. Park, M. G. Allen, and M. R. Prausnitz, "Microsecond thermal ablation of skin for transdermal drug delivery.," *J. Control. Release*, vol. 154, no. 1, pp. 58–68, 2011.

[88] G. Levin, A. Gershonowitz, H. Sacks, M. Stern, A. Sherman, S. Rudaev, I. Zivin, and M. Phillip, "Transdermal delivery of human growth hormone through RF-microchannels.," *Pharm. Res.*, vol. 22, no. 4, pp. 550–555, 2005.

[89] A. C. Sintov, I. Krymberk, D. Daniel, T. Hannan, Z. Sohn, and G. Levin, "Radiofrequency-driven skin microchanneling as a new way for electrically assisted transdermal delivery of hydrophilic drugs.," *J. Control. Release*, vol. 89, no. 2, pp. 311–320, 2003.

[90] J. B. Alarcon, A. W. Hartley, N. G. Harvey, and J. A. Mikszta, "Preclinical evaluation of microneedle technology for intradermal delivery of influenza vaccines.," *Clin. Vaccine Immunol.*, vol. 14, no. 4, pp. 375–381, 2007.

[91] Q. Zhu, V. G. Zarnitsyn, L. Ye, Z. Wen, Y. Gao, L. Pan, I. Skountzou, H. S. Gill, M. R. Prausnitz, C. Yang, and R. W. Compans, "Immunization by vaccine-coated microneedle arrays protects against lethal influenza virus challenge.," *Proc. Natl. Acad. Sci. USA*, vol. 106, no. 19, pp. 7968–7973, 2009.

[92] S. P. Sullivan, D. G. Koutsonanos, P. Martin, J. W. Lee, V. Zarnitsyn, S. Choi, N. Murthy, R. W. Compans, I. Skountzou, and M. R. Prausnitz, "Dissolving polymer microneedle patches for influenza vaccination," *Nat. Med.*, vol. 16, no. 8, pp. 915–920, 2010.

[93] S. Kaushik, a H. Hord, D. D. Denson, D. V McAllister, S. Smitra, M. G. Allen, and M. R. Prausnitz, "Lack of pain associated with microfabricated microneedles.," *Anesth. Analg.*, vol. 92, no. 2, pp. 502–504, 2001.

[94] S. Indermun, R. Luttge, Y. E. Choonara, P. Kumar, L. C. du Toit, G. Modi, and V. Pillay, "Current advances in the fabrication of microneedles for transdermal delivery.," *J. Control. Release*, vol. 185C, pp. 130–138, 2014.

[95] D. V McAllister, P. M. Wang, S. P. Davis, J.-H. Park, P. J. Canatella, M. G. Allen, and M. R. Prausnitz, "Microfabricated needles for transdermal delivery of macromolecules and nanoparticles: fabrication methods and transport studies.," *Proc. Natl. Acad. Sci. USA*, vol. 100, no. 24, pp. 13755–13760, 2003.

[96] Y.-C. Kim, J.-H. Park, and M. R. Prausnitz, "Microneedles for drug and vaccine delivery.," *Adv. Drug Deliv. Rev.*, vol. 64, no. 14, pp. 1547–1568, 2012.

[97] H. J. Corbett, G. J. P. Fernando, X. Chen, I. H. Frazer, and M. A. F. Kendall, "Skin vaccination against cervical cancer associated human papillomavirus with a novel micro-projection array in a mouse model.," *PLoS One*, vol. 5, no. 10, pp. 1–9, 2010.

[98] C. H. Dean, J. B. Alarcon, A. M. Waterston, K. Draper, R. Early, F. Guirakhoo, and J. A. Mikszta, "Cutaneous Delivery of a Live, Attenuated Chimeric Flavivirus Vaccine against japanese encephalitis," *Hum. Vaccin.*, vol. 1, no. 3, pp. 106–111, 2005.

[99] P. C. DeMuth, X. Su, R. E. Samuel, P. T. Hammond, and D. J. Irvine, "Nano-layered microneedles for transcutaneous delivery of polymer nanoparticles and plasmid DNA.," *Adv. Mater*, vol. 22, no. 43, pp. 4851–4856, 2010.

[100] M. Cormier, B. Johnson, M. Ameri, K. Nyam, L. Libiran, D. D. Zhang, and P. Daddona, "Transdermal delivery of desmopressin using a coated microneedle array patch system." *J. Control. Release*, vol. 97, no. 3, pp. 503–511, 2004.

[101] D. P. Wermeling, S. L. Banks, D. a Hudson, H. S. Gill, J. Gupta, M. R. Prausnitz, and A. L. Stinchcomb, "Microneedles permit transdermal delivery of a skin-impermeant medication to humans.," *Proc. Natl. Acad. Sci. USA*, vol. 105, no. 6, pp. 2058–2063, 2008.

[102] R. K. Sivamani, B. Stoeber, G. C. Wu, H. Zhai, D. Liepmann, and H. Maibach, "Clinical microneedle injection of methyl nicotinate: stratum corneum penetration," *Ski. Res. Technol.*, vol. 11, no. 2, pp. 152–156, 2005.

[103] S. P. Davis, W. Martanto, M. G. Allen, and M. R. Prausnitz, "Hollow metal microneedles for insulin delivery to diabetic rats.," *IEEE Trans. Biomed. Eng.*, vol. 52, no. 5, pp. 909–915, 2005.

[104] J. W. Lee, J.-H. Park, and M. R. Prausnitz, "Dissolving microneedles for transdermal drug delivery.," *Biomaterials*, vol. 29, no. 13, pp. 2113–2124, 2008.

[105] S. P. Sullivan, N. Murthy, and M. R. Prausnitz, "Minimally Invasive Protein Delivery with Rapidly Dissolving Polymer Microneedles," *Adv. Mater*, vol. 20, no. 5, pp. 933–938, 2008.

[106] Y. Zhang, K. Brown, K. Siebenaler, A. Determan, D. Dohmeier, and K. Hansen, "Development of lidocaine-coated microneedle product for rapid, safe, and prolonged local analgesic action.," *Pharm. Res.*, vol. 29, no. 1, pp. 170–177, 2012.

[107] H. S. Gill, J. Söderholm, M. R. Prausnitz, and M. Sällberg, "Cutaneous vaccination using microneedles coated with hepatitis C DNA vaccine.," *Gene Ther.*, vol. 17, no. 6, pp. 811–814, 2010.

[108] S. Coulman, D. Barrow, A. Anstey, C. Gateley, A. Morrissey, N. Wilke, C. Allender, K. Brain, and J. C. Birchall, "Minimally invasive cutaneous delivery of macromolecules and plasmid DNA via microneedles.," *Curr. Drug Deliv.*, vol. 3, no. 1, pp. 65–75, 2006.

[109] J. a Mikszta, J. B. Alarcon, J. M. Brittingham, D. E. Sutter, R. J. Pettis, and N. G. Harvey, "Improved genetic immunization via micromechanical disruption of skin-barrier function and targeted epidermal delivery.," *Nat. Med.*, vol. 8, no. 4, pp. 415–419, 2002.

[110] L. Simonsen, A. Kane, J. Lloyd, M. Zaffran, and M. Kane, "Unsafe injections in the developing world and transmission of bloodborne pathogens," *Bull. World Health Organ.*, vol. 77, no. 10, pp. 789–800, 1999.

[111] P. M. Wang, M. Cornwell, J. Hill, and M. R. Prausnitz, "Precise microinjection into skin using hollow microneedles.," *J. Invest. Dermatol.*, vol. 126, no. 5, pp. 1080–1087, 2006.

[112] B. Stoeber and D. Liepmann, "Arrays of Hollow Out-of-Plane Microneedles for Drug Delivery," *J. Microelecctromechanical Syst.*, vol. 14, no. 3, pp. 472–479, 2005.

[113] M. W. Ashraf, N. Afzulpurkar, A. Nisar, and S. Tayyaba, "Fabrication and analysis of hollow microneedles and polymeric piezoelectric valveless micropump for transdermal drug-delivery system," *IET Commun.*, vol. 6, no. 18, pp. 3248–3256, 2012.

[114] B. Ma, S. Liu, Z. Gan, G. Liu, X. Cai, H. Zhang, and Z. Yang, "A PZT insulin pump integrated with a silicon microneedle array for transdermal drug delivery," *Microfluid. Nanofluidics*, vol. 2, no. 5, pp. 417–423, 2006.

[115] K. Kurita, "Chemistry and application of chitin and chitosan," *Polym. Degrad. Stab.*, vol. 59, no. 1–3, pp. 117–120, 1998.

[116] M. Frydrych and B. Chen, "Large three-dimensional poly(glycerol sebacate)-based scaffolds – a freeze-drying preparation approach," *J. Mater. Chem. B*, vol. 1, no. 48, pp. 6650–6661, 2013.

[117] M. Bai, B. Wilske, F. Buegger, J. Esperschütz, M. Bach, H.-G. Frede, and L. Breuer, "Relevance of nonfunctional linear polyacrylic acid for the biodegradation of superabsorbent polymer in soils.," *Environ. Sci. Pollut. Res. Int.*, pp. 1–9, 2014.

[118] P. Bertoglio, S. E. Jacobo, and M. E. Daraio, "Preparation and Characterization of PVA Films with Magnetic Nanoparticles : The Effect of Particle Loading on Drug Release Behavior," *J. Appl. Polym. Sci.*, vol. 115, pp. 1859–1865, 2009.

[119] P. C. Demuth, W. F. Garcia-Beltran, M. L. Ai-Ling, P. T. Hammond, and D. J. Irvine, "Composite dissolving microneedles for coordinated control of antigen and adjuvant

delivery kinetics in transcutaneous vaccination.," *Adv. Funct. Mater.*, vol. 23, no. 2, pp. 161–172, 2013.

[120] K. Tsioris, W. K. Raja, E. M. Pritchard, B. Panilaitis, D. L. Kaplan, and F. G. Omenetto, "Fabrication of Silk Microneedles for Controlled-Release Drug Delivery," *Adv. Funct. Mater.*, vol. 22, no. 2, pp. 330–335, 2012.

[121] W. K. Raja, S. Maccorkle, I. M. Diwan, A. Abdurrob, J. Lu, F. G. Omenetto, and D. L. Kaplan, "Transdermal delivery devices: fabrication, mechanics and drug release from silk.," *Small*, vol. 9, no. 21, pp. 3704–3713, 2013.

[122] S. Liu, M. Jin, Y. Quan, F. Kamiyama, K. Kusamori, H. Katsumi, T. Sakane, and A. Yamamoto, "Transdermal delivery of relatively high molecular weight drugs using novel self-dissolving microneedle arrays fabricated from hyaluronic acid and their characteristics and safety after application to the skin.," *Eur. J. Pharm. Biopharm.*, vol. 86, no. 2, pp. 267–276, 2014.

[123] Y. Ito, A. Murakami, T. Maeda, N. Sugioka, and K. Takada, "Evaluation of self-dissolving needles containing low molecular weight heparin (LMWH) in rats.," *Int. J. Pharm.*, vol. 349, no. 1–2, pp. 124–129, 2008.

[124] Y. Ito, E. Hagiwara, A. Saeki, N. Sugioka, and K. Takada, "Feasibility of microneedles for percutaneous absorption of insulin.," *J. Pharmacol. Sci.*, vol. 29, no. 1, pp. 82–88, 2006.

[125] M.-H. Ling and M.-C. Chen, "Dissolving polymer microneedle patches for rapid and efficient transdermal delivery of insulin to diabetic rats.," *Acta Biomater.*, vol. 9, no. 11, pp. 8952–8961, 2013.

[126] A. P. Raphael, T. W. Prow, M. L. Crichton, X. Chen, G. J. P. Fernando, and M. A. F. Kendall, "Targeted, needle-free vaccinations in skin using multilayered, densely-packed dissolving microprojection arrays.," *Small*, vol. 6, no. 16, pp. 1785–1793, 2010.

[127] H. J. H. B. Hirschberg, G. G. P. van de Wijdeven, A. B. Kelder, G. P. J. M. van den Dobbelsteen, and G. F. A. Kersten, "Bioneedles as vaccine carriers.," *Vaccine*, vol. 26, no. 19, pp. 2389–2397, 2008.

[128] G. Li, A. Badkar, S. Nema, C. S. Kolli, and A. K. Banga, "In vitro transdermal delivery of therapeutic antibodies using maltose microneedles.," *Int. J. Pharm.*, vol. 368, no. 1–2, pp. 109–115, 2009.

[129] J. R. Wendorf, E. B. Ghartey-Tagoe, S. C. Williams, E. Enioutina, P. Singh, and G. W. Cleary, "Transdermal delivery of macromolecules using solid-state biodegradable microstructures.," *Pharm. Res.*, vol. 28, no. 1, pp. 22–30, 2011.

[130] P. C. DeMuth, Y. Min, B. Huang, J. A. Kramer, A. D. Miller, D. H. Barouch, P. T. Hammond, and D. J. Irvine, "Polymer multilayer tattooing for enhanced DNA vaccination.," *Nat. Mater.*, vol. 12, no. 4, pp. 367–376, 2013.

[131] P. Colombo, R. Bettini, G. Massimo, P. L. Catellani, P. Santi, and N. A. Peppas, "Drug diffusion front movement is important in drug release control from swellable matrix tablets," *J. Pharm. Sci.*, vol. 84, no. 8, pp. 991–997, 1995.

[132] R. W. Korsmeyer, R. Gurny, E. Doelker, P. Buri, and N. A. Peppas, "Mechanisms of solute release from porous hydrophilic polymers," *Int. J. Pharm.*, vol. 15, no. 1, pp. 25–35, 1983.

[133] H. Chen, H. Zhu, J. Zheng, D. Mou, J. Wan, J. Zhang, T. Shi, Y. Zhao, H. Xu, and X. Yang, "Iontophoresis-driven penetration of nanovesicles through microneedle-induced skin microchannels for enhancing transdermal delivery of insulin.," *J. Control. Release*, vol. 139, no. 1, pp. 63–72, 2009.

[134] M. J. Garland, E. Caffarel-Salvador, K. Migalska, A. D. Woolfson, and R. F. Donnelly, "Dissolving polymeric microneedle arrays for electrically assisted transdermal drug delivery.," *J. Control. Release*, vol. 159, no. 1, pp. 52–59, 2012.

[135] R. F. Donnelly, M. J. Garland, and A. Z. Alkilani, "Microneedle-iontophoresis combinations for enhanced transdermal drug delivery.," *Methods Mol. Biol.*, vol. 1141, pp. 121–132, 2014.

[136] N. Wilke, C. Hibert, J. O. Brien, A. Morrissey, and J. O'Brien, "Silicon microneedle electrode array with temperature monitoring for electroporation," *Sensors Actuators A Phys.*, vol. 123–124, pp. 319–325, 2005.

[137] L. Daugimont, N. Baron, G. Vandermeulen, N. Pavselj, D. Miklavcic, M.-C. Jullien, G. Cabodevila, L. M. Mir, and V. Préat, "Hollow microneedle arrays for intradermal drug delivery and DNA electroporation.," *J. Membr. Biol.*, vol. 236, no. 1, pp. 117–125, 2010.

[138] S.-O. Choi, Y. C. Kim, J.-H. Park, J. Hutcheson, H. S. Gill, Y.-K. Yoon, M. R. Prausnitz, and M. G. Allen, "An electrically active microneedle array for electroporation.," *Biomed. Microdevices*, vol. 12, no. 2, pp. 263–273, 2010.

[139] S.-O. Choi, Y.-C. Kim, J. W. Lee, J.-H. Park, M. R. Prausnitz, and M. G. Allen, "Intracellular protein delivery and gene transfection by electroporation using a microneedle electrode array.," *Small*, vol. 8, no. 7, pp. 1081–1091, 2012.

[140] K. Yan, H. Todo, and K. Sugibayashi, "Transdermal drug delivery by in-skin electroporation using a microneedle array.," *Int. J. Pharm.*, vol. 397, no. 1–2, pp. 77–83, 2010.

[141] J.-H. Park, M. G. Allen, and M. R. Prausnitz, "Biodegradable polymer microneedles: fabrication, mechanics and transdermal drug delivery.," *J. Control. Release*, vol. 104, no. 1, pp. 51–66, 2005.

[142] M. Kohler and W. Fritzsche, *Nanotechnology: an introduction to nanostructuring techniques*. Wiley VCH, 2007.

[143] Z. Cui, *Nanofabrication: Principles, capabilities and limits*. Springer, 2008.

[144] K. Gonsalves, C. Halberstadt, C. T. Laurencin, and L. Nair, *Biomedical nanostructures*. John Wiley & Sons, Ltd, 2008.

[145] S. Paik, "In-plane single-crystal-silicon microneedles for minimally invasive microfluid systems," *Sensors Actuators A Phys.*, vol. 114, no. 2–3, pp. 276–284, 2004.

[146] N. Wilke, a Mulcahy, S. Ye, and a Morrissey, "Process optimization and characterization of silicon microneedles fabricated by wet etch technology," *Microelectronics J.*, vol. 36, no. 7, pp. 650–656, 2005.

[147] M. Jackson, *Microfabrication and Nanomanufacturing*. CRC Press, 2006.

[148] V. Melissinaki, A. A. Gill, I. Ortega, M. Vamvakaki, A. Ranella, J. W. Haycock, C. Fotakis, M. Farsari, and F. Claeyssens, "Direct laser writing of 3D scaffolds for neural tissue engineering applications.," *Biofabrication*, vol. 3, no. 4, pp. 1–5, 2011.

[149] F. Claeyssens, E. A. Hasan, A. Gaidukeviciute, D. S. Achilleos, A. Ranella, C. Reinhardt, A. Ovsianikov, X. Shizhou, C. Fotakis, M. Vamvakaki, B. N. Chichkov, and M. Farsari, "Three-Dimensional Biodegradable Structures Fabricated by Two-Photon Polymerization," *Langmuir*, vol. 25, no. 5, pp. 3219–3223, 2009.

[150] B. H. Cumpston, S. P. Ananthavel, S. Barlow, D. L. Dyer, J. E. Ehrlich, L. L. Erskine, A. A. Heikal, S. M. Kuebler, I.-Y. S. Lee, D. McCord-Maughon, J. Qin, H. Rockel, M. Rumi, X.-L. Wu, S. R. Marder, and J. W. Perry, "Two-photon polymerization initiators for three-dimensional optical data storage and microfabrication," *Nature*, vol. 398, no. 6722, pp. 51–54, 1999.

[151] M.-C. Chen, M.-H. Ling, K.-Y. Lai, and E. Pramudityo, "Chitosan microneedle patches for sustained transdermal delivery of macromolecules.," *Biomacromolecules*, vol. 13, no. 12, pp. 4022–4031, 2012.

[152] M.-C. Chen, S.-F. Huang, K.-Y. Lai, and M.-H. Ling, "Fully embeddable chitosan microneedles as a sustained release depot for intradermal vaccination," *Biomaterials*, vol. 34, no. 12, pp. 3077–3086, 2013.

[153] H. Rhim and G. D. Dodd, "Radiofrequency thermal ablation of liver tumors.," *J. Clin. Ultrasound*, vol. 27, no. 5, pp. 221–229, 1999.

[154] L. Calderon-Garciduenas, B. Azzarelli, H. Acuna, R. Garcia, T. M. Gambling, N. Osnaya, S. Monroy, M. R. Del Tizapantzi, J. L. Carson, A. Villarreal-Calderon, and B. Rewcastle, "Air pollution and brain damage.," *Toxicol. Pathol.*, vol. 30, no. 3, pp. 373–389, 2002.

[155] A. Nemmar, M. F. Hoylaerts, P. H. M. Hoet, D. Dinsdale, T. Smith, H. Xu, J. Vermylen, and B. Nemery, "Ultrafine particles affect experimental thrombosis in an in vivo hamster model.," *Am. J. Respir. Crit. Care Med.*, vol. 166, no. 7, pp. 998–1004, 2002.

[156] A. Peters, B. Veronesi, L. Calderón-Garcidueñas, P. Gehr, L. C. Chen, M. Geiser, W. Reed, B. Rothen-Rutishauser, S. Schürch, and H. Schulz, "Translocation and potential neurological effects of fine and ultrafine particles a critical update," *Part. Fibre Toxicol.*, vol. 3, no. 1, pp. 1–13, 2006.

[157] R. P. Feazell, N. Nakayama-Ratchford, H. Dai, and S. J. Lippard, "Soluble single-walled carbon nanotubes as longboat delivery systems for platinum(IV) anticancer drug design.," *J. Am. Chem. Soc.*, vol. 129, no. 27, pp. 8438–8439, 2007.

[158] Z. Liu, W. Cai, L. He, N. Nakayama, K. Chen, X. Sun, X. Chen, and H. Dai, "In vivo biodistribution and highly efficient tumour targeting of carbon nanotubes in mice.," *Nat. Nanotechnol.*, vol. 2, no. 1, pp. 47–52, 2007.

[159] X. Liu, H. Tao, K. Yang, S. Zhang, S.-T. Lee, and Z. Liu, "Optimization of surface chemistry on single-walled carbon nanotubes for in vivo photothermal ablation of tumors.," *Biomaterials*, vol. 32, no. 1, pp. 144–151, 2011.

[160] A. K. Geim and K. S. Novoselov, "The rise of graphene.," *Nat. Mater.*, vol. 6, no. 3, pp. 183–191, 2007.

[161] Z. Zhang, X. Yang, Y. Zhang, B. Zeng, S. Wang, T. Zhu, R. B. S. Roden, Y. Chen, and R. Yang, "Delivery of telomerase reverse transcriptase small interfering RNA in complex with positively charged single-walled carbon nanotubes suppresses tumor growth.," *Clin. Cancer Res.*, vol. 12, no. 16, pp. 4933–4939, 2006.

[162] K. Welsher, S. P. Sherlock, and H. Dai, "Deep-tissue anatomical imaging of mice using carbon nanotube fluorophores in the second near-infrared window.," *Proc. Natl. Acad. Sci. USA*, vol. 108, no. 22, pp. 8943–8948, 2011.

[163] J. T. Robinson, K. Welsher, S. M. Tabakman, S. P. Sherlock, H. Wang, R. Luong, and H. Dai, "High Performance In Vivo Near-IR (>1 μm) Imaging and Photothermal Cancer Therapy with Carbon Nanotubes.," *Nano Res.*, vol. 3, no. 11, pp. 779–793, 2010.

[164] A. A. Shvedova, V. Castranova, E. R. Kisin, D. Schwegler-Berry, A. R. Murray, V. Z. Gandelsman, A. Maynard, and P. Baron, "Exposure to carbon nanotube material: assessment of nanotube cytotoxicity using human keratinocyte cells.," *J. Toxicol. Environ. Health. A*, vol. 66, no. 20, pp. 1909–1926, 2003.

[165] B. Halliwell, "Reactive oxygen species in living systems: Source, biochemistry, and role in human disease," *Am. J. Med.*, vol. 91, no. 3, pp. S14–S22, 1991.

[166] L. Packer, L. Prilipko, and Y. Christen, Eds., *Free Radicals in the Brain*. Berlin, Heidelberg: Springer Berlin Heidelberg, 1992.

[167] T. Ozben, "Oxidative stress and apoptosis: impact on cancer therapy.," *J. Pharm. Sci.*, vol. 96, no. 9, pp. 2181–2196, 2007.

[168] T. Finkel, "Oxidant signals and oxidative stress," *Curr. Opin. Cell Biol.*, vol. 15, no. 2, pp. 247–254, 2003.

[169] B. Halliwell and J. Gutteridge, *Free radicals in biology and medicine*, 3rd ed. Oxford: Oxford University Press, 1999.

[170] M. Valko, D. Leibfritz, J. Moncol, M. T. D. Cronin, M. Mazur, and J. Telser, "Free radicals and antioxidants in normal physiological functions and human disease.," *Int. J. Biochem. Cell Biol.*, vol. 39, no. 1, pp. 44–84, 2007.

[171] N. Singh, A. K. Dhalla, C. Seneviratne, and P. K. Singal, "Oxidative stress and heart failure," *Mol. Cell. Biochem.*, vol. 147, no. 1–2, pp. 77–81, 1995.

[172] N. A. Monteiro-Riviere, R. J. Nemanich, A. O. Inman, Y. Y. Wang, and J. E. Riviere, "Multi-walled carbon nanotube interactions with human epidermal keratinocytes.," *Toxicol. Lett.*, vol. 155, no. 3, pp. 377–384, 2005.

[173] A. Radomski, P. Jurasz, D. Alonso-Escolano, M. Drews, M. Morandi, T. Malinski, and M. W. Radomski, "Nanoparticle-induced platelet aggregation and vascular thrombosis.," *Br. J. Pharmacol.*, vol. 146, no. 6, pp. 882–893, 2005.

[174] Z. Li, T. Hulderman, R. Salmen, R. Chapman, S. S. Leonard, S.-H. Young, A. Shvedova, M. I. Luster, and P. P. Simeonova, "Cardiovascular Effects of Pulmonary Exposure to Single-Wall Carbon Nanotubes," *Environ. Health Perspect.*, vol. 115, no. 3, pp. 377–382, 2007.

[175] A. Yokoyama, Y. Sato, Y. Nodasaka, S. Yamamoto, T. Kawasaki, M. Shindoh, T. Kohgo, T. Akasaka, M. Uo, F. Watari, and K. Tohji, "Biological behavior of hat-stacked carbon nanofibers in the subcutaneous tissue in rats.," *Nano Lett.*, vol. 5, no. 1, pp. 157–161, 2005.

[176] S. Chen, Q. Wu, C. Mishra, J. Kang, H. Zhang, K. Cho, W. Cai, A. A. Balandin, and R. S. Ruoff, "Thermal conductivity of isotopically modified graphene.," *Nat. Mater.*, vol. 11, no. 3, pp. 203–207, 2012.

[177] C. Lee, X. Wei, J. W. Kysar, and J. Hone, "Measurement of the elastic properties and intrinsic strength of monolayer graphene.," *Science (80-.).*, vol. 321, no. 5887, pp. 385–388, 2008.

[178] K. S. Novoselov, A. K. Geim, S. V Morozov, D. Jiang, Y. Zhang, S. V Dubonos, I. V Grigorieva, and A. Firsov, "Electric field effect in atomically thin carbon films.," *Science (80-.).*, vol. 306, no. 5696, pp. 666–669, 2004.

[179] M. D. Stoller, S. Park, Y. Zhu, J. An, and R. S. Ruoff, "Graphene-based ultracapacitors.," *Nano Lett.*, vol. 8, no. 10, pp. 3498–3502, 2008.

[180] A. A. Balandin, S. Ghosh, W. Bao, I. Calizo, D. Teweldebrhan, F. Miao, and C. N. Lau, "Superior thermal conductivity of single-layer graphene.," *Nano Lett.*, vol. 8, no. 3, pp. 902–907, 2008.

[181] K. I. Bolotin, K. J. Sikes, Z. Jiang, M. Klima, G. Fudenberg, J. Hone, P. Kim, and H. L. Stormer, "Ultrahigh electron mobility in suspended graphene," *Solid State Commun.*, vol. 146, no. 9–10, pp. 351–355, 2008.

[182] R. Murali, K. Brenner, Y. Yang, T. Beck, and J. D. Meindl, "Resistivity of Graphene Nanoribbon Interconnects," *IEEE Electron Device Lett.*, vol. 30, no. 6, pp. 611–613, 2009.

[183] X. Wang, H. You, F. Liu, M. Li, L. Wan, S. Li, Q. Li, Y. Xu, R. Tian, Z. Yu, D. Xiang, and J. Cheng, "Large-Scale Synthesis of Few-Layered Graphene using CVD," *Chem. Vap. Depos.*, vol. 15, no. 1–3, pp. 53–56, 2009.

[184] J. Geng, B.-S. Kong, S. B. Yang, and H.-T. Jung, "Preparation of graphene relying on porphyrin exfoliation of graphite.," *Chem. Comm.*, vol. 46, no. 28, pp. 5091–5093, 2010.

[185] U. Khan, A. O'Neill, M. Lotya, S. De, and J. N. Coleman, "High-concentration solvent exfoliation of graphene.," *Small*, vol. 6, no. 7, pp. 864–871, 2010.

[186] W. Hummers and R. Offeman, "Preparation of graphitic oxide," *J. Am. Chem. Soc.*, vol. 208, pp. 1339–1339, 1958.

[187] D. C. Marcano, D. V Kosynkin, J. M. Berlin, A. Sinitskii, Z. Sun, A. Slesarev, L. B. Alemany, W. Lu, and J. M. Tour, "Improved synthesis of graphene oxide.," *ACS Nano*, vol. 4, no. 8, pp. 4806–4814, 2010.

[188] H.-P. Boehm and W. Scholz, "Der Verpuffungspunkt des Graphitoxids," *Zeitschrift Anorg. und Allg. Chemie*, vol. 335, no. 1–2, pp. 74–79, 1965.

[189] K. Krishnamoorthy, M. Veerapandian, K. Yun, and S.-J. Kim, "The chemical and structural analysis of graphene oxide with different degrees of oxidation," *Carbon N. Y.*, vol. 53, pp. 38–49, 2013.

[190] Y. Pan, H. Bao, and L. Li, "Noncovalently functionalized multiwalled carbon nanotubes by chitosan-grafted reduced graphene oxide and their synergistic reinforcing effects in chitosan films.," *ACS Appl. Mater. Interf.*, vol. 3, no. 12, pp. 4819–4830, 2011.

[191] J. I. Paredes, S. Villar-Rodil, A. Martínez-Alonso, and J. M. D. Tascón, "Graphene oxide dispersions in organic solvents.," *Langmuir*, vol. 24, no. 19, pp. 10560–10564, 2008.

[192] J. W. Suk, R. D. Piner, J. An, and R. S. Ruoff, "Mechanical properties of monolayer graphene oxide.," *ACS Nano*, vol. 4, no. 11, pp. 6557–6564, 2010.

[193] L. Liu, J. Zhang, J. Zhao, and F. Liu, "Mechanical properties of graphene oxides.," *Nanoscale*, vol. 4, no. 19, pp. 5910–5916, 2012.

[194] C. Gómez-Navarro, R. T. Weitz, A. M. Bittner, M. Scolari, A. Mews, M. Burghard, and K. Kern, "Electronic transport properties of individual chemically reduced graphene oxide sheets.," *Nano Lett.*, vol. 7, no. 11, pp. 3499–3503, 2007.

[195] H. A. Becerril, J. Mao, Z. Liu, R. M. Stoltenberg, Z. Bao, and Y. Chen, "Evaluation of solution-processed reduced graphene oxide films as transparent conductors.," *ACS Nano*, vol. 2, no. 3, pp. 463–470, 2008.

[196] O. C. Compton, D. A. Dikin, K. W. Putz, L. C. Brinson, and S. T. Nguyen, "Electrically conductive 'alkylated' graphene paper via chemical reduction of amine-functionalized graphene oxide paper.," *Adv. Mater.*, vol. 22, no. 8, pp. 892–896, 2010.

[197] J. Zhao, S. Pei, W. Ren, L. Gao, and H.-M. Cheng, "Efficient preparation of large-area graphene oxide sheets for transparent conductive films.," *ACS Nano*, vol. 4, no. 9, pp. 5245–5252, 2010.

[198] H. He, J. Klinowski, M. Forster, and A. Lerf, "A new structural model for graphite oxide," *Chem. Phys. Lett.*, vol. 287, no. 1–2, pp. 53–56, 1998.

[199] D. R. Dreyer, S. Park, C. W. Bielawski, and R. S. Ruoff, "The chemistry of graphene oxide.," *Chem. Soc. Rev.*, vol. 39, no. 1, pp. 228–240, 2010.

[200] N. I. Kovtyukhova, P. J. Ollivier, B. R. Martin, T. E. Mallouk, S. A. Chizhik, E. V. Buzaneva, and A. D. Gorchinskiy, "Layer-by-Layer Assembly of Ultrathin Composite Films from Micron-Sized Graphite Oxide Sheets and Polycations," *Chem. Mater.*, vol. 11, no. 3, pp. 771–778, 1999.

[201] S. Mao, H. Pu, and J. Chen, "Graphene oxide and its reduction: modeling and experimental progress," *RSC Adv.*, vol. 2, no. 7, pp. 2643–2662, 2012.

[202] T. Kuila, A. K. Mishra, P. Khanra, N. H. Kim, and J. H. Lee, "Recent advances in the efficient reduction of graphene oxide and its application as energy storage electrode materials.," *Nanoscale*, vol. 5, no. 1, pp. 52–71, 2013.

[203] S. Stankovich, D. A. Dikin, R. D. Piner, K. A. Kohlhaas, A. Kleinhammes, Y. Jia, Y. Wu, S. T. Nguyen, and R. S. Ruoff, "Synthesis of graphene-based nanosheets via chemical reduction of exfoliated graphite oxide," *Carbon N. Y.*, vol. 45, no. 7, pp. 1558–1565, 2007.

[204] H. Bao, Y. Pan, Y. Ping, N. G. Sahoo, T. Wu, L. Li, J. Li, and L. H. Gan, "Chitosan-functionalized graphene oxide as a nanocarrier for drug and gene delivery.," *Small*, vol. 7, no. 11, pp. 1569–1578, 2011.

[205] S. J. Wang, Y. Geng, Q. Zheng, and J.-K. Kim, "Fabrication of highly conducting and transparent graphene films," *Carbon N. Y.*, vol. 48, no. 6, pp. 1815–1823, 2010.

[206] H.-L. Guo, X.-F. Wang, Q.-Y. Qian, F.-B. Wang, and X.-H. Xia, "A green approach to the synthesis of graphene nanosheets.," *ACS Nano*, vol. 3, no. 9, pp. 2653–2659, 2009.

[207] C. Zhu, S. Guo, Y. Fang, and S. Dong, "Reducing sugar: new functional molecules for the green synthesis of graphene nanosheets.," *ACS Nano*, vol. 4, no. 4, pp. 2429–2437, 2010.

[208] M. Wojtoniszak, X. Chen, R. J. Kalenczuk, A. Wajda, J. Łapczuk, M. Kurzewski, M. Drozdzik, P. K. Chu, and E. Borowiak-Palen, "Synthesis, dispersion, and cytocompatibility of graphene oxide and reduced graphene oxide.," *Colloids Surf. B. Biointerfaces*, vol. 89, pp. 79–85, 2012.

[209] Y. Wang, Z. Shi, and J. Yin, "Facile synthesis of soluble graphene via a green reduction of graphene oxide in tea solution and its biocomposites.," *ACS Appl. Mater. Interf.*, vol. 3, no. 4, pp. 1127–1133, 2011.

[210] K. Liu, J.-J. Zhang, F.-F. Cheng, T.-T. Zheng, C. Wang, and J.-J. Zhu, "Green and facile synthesis of highly biocompatible graphene nanosheets and its application for cellular imaging and drug delivery," *J. Mater. Chem.*, vol. 21, no. 32, pp. 12034–12040, 2011.

[211] M. Fang, J. Long, W. Zhao, L. Wang, and G. Chen, "pH-Responsive chitosan-mediated graphene dispersions.," *Langmuir*, vol. 26, no. 22, pp. 16771–16774, 2010.

[212] M. J. Fernández-Merino, L. Guardia, J. I. Paredes, S. Villar-Rodil, P. Solís-Fernández, A. Martínez-Alonso, and J. M. D. Tascón, "Vitamin C Is an Ideal Substitute for Hydrazine in the Reduction of Graphene Oxide Suspensions," *J. Phys. Chem.*, vol. 114, no. 14, pp. 6426–6432, 2010.

[213] J. Zhang, H. Yang, G. Shen, P. Cheng, J. Zhang, and S. Guo, "Reduction of graphene oxide via L-ascorbic acid.," *Chem. Comm.*, vol. 46, no. 7, pp. 1112–1114, 2010.

[214] Y. Guo, X. Sun, Y. Liu, W. Wang, H. Qiu, and J. Gao, "One pot preparation of reduced graphene oxide (RGO) or Au (Ag) nanoparticle-RGO hybrids using chitosan as a reducing and stabilizing agent and their use in methanol electrooxidation," *Carbon N. Y.*, vol. 50, no. 7, pp. 2513–2523, 2012.

[215] J. Liu, S. Fu, B. Yuan, Y. Li, and Z. Deng, "Toward a universal 'adhesive nanosheet' for the assembly of multiple nanoparticles based on a protein-induced reduction/decoration of graphene oxide.," *J. Am. Chem. Soc.*, vol. 132, no. 21, pp. 7279–7281, 2010.

[216] V. K. Rana, M.-C. Choi, J.-Y. Kong, G. Y. Kim, M. J. Kim, S.-H. Kim, S. Mishra, R. P. Singh, and C.-S. Ha, "Synthesis and Drug-Delivery Behavior of Chitosan-Functionalized Graphene Oxide Hybrid Nanosheets," *Macromol. Mater. Eng.*, vol. 296, no. 2, pp. 131–140, 2011.

[217] D. Pan, J. Zhang, Z. Li, and M. Wu, "Hydrothermal route for cutting graphene sheets into blue-luminescent graphene quantum dots.," *Adv. Mater*, vol. 22, no. 6, pp. 734–738, 2010.

[218] Y. Zhou, Q. Bao, L. A. L. Tang, Y. Zhong, and K. P. Loh, "Hydrothermal Dehydration for the 'Green' Reduction of Exfoliated Graphene Oxide to Graphene and Demonstration of Tunable Optical Limiting Properties," *Chem. Mater.*, vol. 21, no. 13, pp. 2950–2956, 2009.

[219] Y. Zhang, T. R. Nayak, H. Hong, and W. Cai, "Graphene: a versatile nanoplatform for biomedical applications.," *Nanoscale*, vol. 4, no. 13, pp. 3833–3842, 2012.

[220] S. Goenka, V. Sant, and S. Sant, "Graphene-based nanomaterials for drug delivery and tissue engineering.," *J. Control. Release*, vol. 173, pp. 75–88, 2014.

[221] L. Feng, S. Zhang, and Z. Liu, "Graphene based gene transfection.," *Nanoscale*, vol. 3, no. 3, pp. 1252–1257, 2011.

[222] L. Zhang, Z. Lu, Q. Zhao, J. Huang, H. Shen, and Z. Zhang, "Enhanced chemotherapy efficacy by sequential delivery of siRNA and anticancer drugs using PEI-grafted graphene oxide.," *Small*, vol. 7, no. 4, pp. 460–464, 2011.

[223] L. Zhang, J. Xia, Q. Zhao, L. Liu, and Z. Zhang, "Functional graphene oxide as a nanocarrier for controlled loading and targeted delivery of mixed anticancer drugs.," *Small*, vol. 6, no. 4, pp. 537–544, 2010.

[224] L. Zhou, S. Wei, X. Ge, J. Zhou, H. Jiang, F. Li, and J. Shen, "Combination of chemotherapy and photodynamic therapy using graphene oxide as drug delivery system.," *J. Photochem. Photobiol. B.*, vol. 135, pp. 7–16, 2014.

[225] H. S. Jung, M.-Y. Lee, W. H. Kong, I. H. Do, and S. K. Hahn, "Nano graphene oxide–hyaluronic acid conjugate for target specific cancer drug delivery," *RSC Adv.*, vol. 4, no. 27, pp. 14197–14200, 2014.

[226] X. Yang, X. Zhang, Z. Liu, Y. Ma, Y. Huang, and Y. Chen, "High-Efficiency Loading and Controlled Release of Doxorubicin Hydrochloride on Graphene Oxide," *J. Phys. Chem.*, vol. 112, no. 45, pp. 17554–17558, 2008.

[227] J. Chen, H. Liu, C. Zhao, G. Qin, G. Xi, T. Li, X. Wang, and T. Chen, "One-step reduction and PEGylation of graphene oxide for photothermally controlled drug delivery.," *Biomaterials*, vol. 35, no. 18, pp. 4986–4995, 2014.

[228] W. Miao, G. Shim, S. Lee, S. Lee, Y. S. Choe, and Y.-K. Oh, "Safety and tumor tissue accumulation of pegylated graphene oxide nanosheets for co-delivery of anticancer drug and photosensitizer.," *Biomaterials*, vol. 34, no. 13, pp. 3402–3410, 2013.

[229] H. Kim, D. Lee, J. Kim, T.-I. Kim, and W. J. Kim, "Photothermally triggered cytosolic drug delivery via endosome disruption using a functionalized reduced graphene oxide.," *ACS Nano*, vol. 7, no. 8, pp. 6735–6746, 2013.

[230] F. Zhi, H. Dong, X. Jia, W. Guo, H. Lu, Y. Yang, H. Ju, X. Zhang, and Y. Hu, "Functionalized graphene oxide mediated adriamycin delivery and miR-21 gene silencing to overcome tumor multidrug resistance in vitro.," *PLoS One*, vol. 8, no. 3, pp. 1–9, 2013.

[231] W. Miao, G. Shim, C. M. Kang, S. Lee, Y. S. Choe, H.-G. Choi, and Y.-K. Oh, "Cholesteryl hyaluronic acid-coated, reduced graphene oxide nanosheets for anti-cancer drug delivery.," *Biomaterials*, vol. 34, no. 37, pp. 9638–9647, 2013.

[232] X. Zhao, L. Liu, X. Li, J. Zeng, X. Jia, and P. Liu, "Biocompatible graphene oxide nanoparticle-based drug delivery platform for tumor microenvironment-responsive triggered release of Doxorubicin.," *Langmuir*, vol. 30, no. 34, pp. 10419–10429, 2014.

[233] H. Pandey, V. Parashar, R. Parashar, R. Prakash, P. W. Ramteke, and A. C. Pandey, "Controlled drug release characteristics and enhanced antibacterial effect of graphene nanosheets containing gentamicin sulfate.," *Nanoscale*, vol. 3, no. 10, pp. 4104–4108, 2011.

[234] R. Zhang, M. Hummelgård, G. Lv, and H. Olin, "Real time monitoring of the drug release of rhodamine B on graphene oxide," *Carbon N. Y.*, vol. 49, no. 4, pp. 1126–1132, 2011.

[235] D. Ma, J. Lin, Y. Chen, W. Xue, and L.-M. Zhang, "In situ gelation and sustained release of an antitumor drug by graphene oxide nanosheets," *Carbon N. Y.*, vol. 50, no. 8, pp. 3001–3007, 2012.

[236] R. Zhang and H. Olin, "Carbon nanomaterials as drug carriers: Real time drug release investigation," *Mater. Sci. Eng. C*, vol. 32, no. 5, pp. 1247–1252, 2012.

[237] C.-H. Lu, C.-L. Zhu, J. Li, J.-J. Liu, X. Chen, and H.-H. Yang, "Using graphene to protect DNA from cleavage during cellular delivery.," *Chem. Comm.*, vol. 46, no. 18, pp. 3116–3118, 2010.

[238] M. Wu, R. Kempaiah, P.-J. J. Huang, V. Maheshwari, and J. Liu, "Adsorption and desorption of DNA on graphene oxide studied by fluorescently labeled oligonucleotides.," *Langmuir*, vol. 27, no. 6, pp. 2731–2738, 2011.

[239] L. Feng, X. Yang, X. Shi, X. Tan, R. Peng, J. Wang, and Z. Liu, "Polyethylene glycol and polyethylenimine dual-functionalized nano-graphene oxide for photothermally enhanced gene delivery.," *Small*, vol. 9, no. 11, pp. 1989–1997, 2013.

[240] H. Kim and W. J. Kim, "Photothermally controlled gene delivery by reduced graphene oxide-polyethylenimine nanocomposite.," *Small*, vol. 10, no. 1, pp. 117–126, 2014.

[241] H. Hu, C. Tang, and C. Yin, "Folate conjugated trimethyl chitosan/graphene oxide nanocomplexes as potential carriers for drug and gene delivery," *Mater. Lett.*, vol. 125, pp. 82–85, 2014.

[242] Y. Wang, Z. Li, D. Hu, C.-T. Lin, J. Li, and Y. Lin, "Aptamer/graphene oxide nanocomplex for in situ molecular probing in living cells.," *J. Am. Chem. Soc.*, vol. 132, no. 27, pp. 9274–9276, 2010.

[243] Z. M. Markovic, L. M. Harhaji-Trajkovic, B. M. Todorovic-Markovic, D. P. Kepić, K. M. Arsikin, S. P. Jovanović, A. C. Pantovic, M. D. Dramićanin, and V. S. Trajkovic, "In vitro comparison of the photothermal anticancer activity of graphene nanoparticles and carbon nanotubes.," *Biomaterials*, vol. 32, no. 4, pp. 1121–1129, 2011.

[244] K. Yang, S. Zhang, G. Zhang, X. Sun, S.-T. Lee, and Z. Liu, "Graphene in mice: ultrahigh in vivo tumor uptake and efficient photothermal therapy.," *Nano Lett.*, vol. 10, no. 9, pp. 3318–3323, 2010.

[245] J. T. Robinson, S. M. Tabakman, Y. Liang, H. Wang, H. S. Casalongue, D. Vinh, and H. Dai, "Ultrasmall reduced graphene oxide with high near-infrared absorbance for photothermal therapy.," *J. Am. Chem. Soc.*, vol. 133, no. 17, pp. 6825–6831, 2011.

[246] K. Wang, J. Ruan, H. Song, J. Zhang, Y. Wo, S. Guo, and D. Cui, "Biocompatibility of Graphene Oxide," *Nanoscale*, pp. 1–8, 2010.

[247] X. Zhang, J. Yin, C. Peng, W. Hu, Z. Zhu, W. Li, C. Fan, and Q. Huang, "Distribution and biocompatibility studies of graphene oxide in mice after intravenous administration," *Carbon N. Y.*, vol. 49, no. 3, pp. 986–995, 2011.

[248] A. Schinwald, F. A. Murphy, A. Jones, W. Macnee, and K. Donaldson, "Graphene-Based Nanoplatelets: A New Risk to the Respiratory System as a Consequence of Their Unusual Aerodynamic Properties.," *ACS Nano*, vol. 6, no. 1, pp. 736–746, 2012.

[249] K. Yang, Ḱ. J. Wan, Ḱ. S. Zhang, Y. Zhang, S. Lee, and Z. Liu, "In Vivo Pharmacokinetics, Long-Term Biodistribution, and Toxicology of PEGylated Graphene in Mice," *ACS Nano*, vol. 5, no. 1, pp. 516–522, 2010.

[250] C. Cheng, S. Li, S. Nie, W. Zhao, H. Yang, S. Sun, and C. Zhao, "General and biomimetic approach to biopolymer-functionalized graphene oxide nanosheet through adhesive dopamine.," *Biomacromolecules*, vol. 13, no. 12, pp. 4236–4246, 2012.

[251] H. Zhang, G. Grüner, and Y. Zhao, "Recent advancements of graphene in biomedicine," *J. Mater. Chem. B*, vol. 1, no. 20, pp. 2542–2567, 2013.

[252] L. Ma, H. Qin, C. Cheng, Y. Xia, C. He, C. Nie, L. Wang, and C. Zhao, "Mussel-inspired self-coating at macro-interface with improved biocompatibility and bioactivity via dopamine grafted heparin-like polymers and heparin," *J. Mater. Chem. B*, vol. 2, no. 4, pp. 363–375, 2014.

[253] J. Kim, Y.-R. Kim, Y. Kim, K. T. Lim, H. Seonwoo, S. Park, S.-P. Cho, B. H. Hong, P.-H. Choung, T. D. Chung, Y.-H. Choung, and J. H. Chung, "Graphene-incorporated chitosan substrata for adhesion and differentiation of human mesenchymal stem cells," *J. Mater. Chem. B*, vol. 1, no. 7, pp. 933–938, 2013.

[254] D. Depan, T. C. Pesacreta, and R. D. K. Misra, "The synergistic effect of a hybrid graphene oxide–chitosan system and biomimetic mineralization on osteoblast functions," *Biomater. Sci.*, vol. 2, no. 2, pp. 264–274, 2014.

[255] D. Ling and T. Hyeon, "Chemical design of biocompatible iron oxide nanoparticles for medical applications.," *Small*, vol. 9, no. 9–10, pp. 1450–1466, 2013.

[256] A. Figuerola, R. Di Corato, L. Manna, and T. Pellegrino, "From iron oxide nanoparticles towards advanced iron-based inorganic materials designed for biomedical applications.," *Pharmacol. Res.*, vol. 62, no. 2, pp. 126–143, 2010.

[257] M. Arruebo, R. Fernández-pacheco, M. R. Ibarra, and J. Santamaría, "Magnetic nanoparticles for drug delivery," *Rev. Lit. Arts Am.*, vol. 2, no. 3, pp. 22–32, 2007.

[258] S.-H. Hu, C.-H. Tsai, C.-F. Liao, D.-M. Liu, and S.-Y. Chen, "Controlled rupture of magnetic polyelectrolyte microcapsules for drug delivery.," *Langmuir*, vol. 24, no. 20, pp. 11811–11818, 2008.

[259] H. Xu, L. Cheng, C. Wang, X. Ma, Y. Li, and Z. Liu, "Polymer encapsulated upconversion nanoparticle/iron oxide nanocomposites for multimodal imaging and magnetic targeted drug delivery," *Biomaterials*, vol. 32, no. 35, pp. 9364–9373, 2011.

[260] S. Purushotham and R. Ramanujan, "Thermoresponsive magnetic composite nanomaterials for multimodal cancer therapy.," *Acta Biomater.*, vol. 6, no. 2, pp. 502–510, 2010.

[261] K. Cai, Z. Luo, Y. Hu, X. Chen, Y. Liao, L. Yang, and L. Deng, "Magnetically Triggered Reversible Controlled Drug Delivery from Microfabricated Polymeric Multireservoir Devices," *Adv. Mater*, vol. 21, no. 40, pp. 4045–4049, 2009.

[262] T.-Y. Liu, S.-H. Hu, T.-Y. Liu, D.-M. Liu, and S.-Y. Chen, "Magnetic-sensitive behavior of intelligent ferrogels for controlled release of drug.," *Langmuir*, vol. 22, no. 14, pp. 5974–5978, 2006.

[263] T. Hoare, J. Santamaria, G. F. Goya, S. Irusta, D. Lin, S. Lau, R. Padera, R. Langer, and D. S. Kohane, "A Magnetically Triggered Composite Membrane for On-Demand Drug Delivery," *Nano Lett.*, vol. 9, no. 10, pp. 3651–3657, 2009.

[264] N. Morishita, H. Nakagami, R. Morishita, S. Takeda, F. Mishima, BungoTerazono, S. Nishijima, Y. Kaneda, and N. Tanaka, "Magnetic nanoparticles with surface modification enhanced gene delivery of HVJ-E vector," *Biochem. Biophys. Res. Commun.*, vol. 334, no. 4, pp. 1121–1126, 2005.

[265] S. a. Corr, A. O' Byrne, Y. K. Gun'ko, S. Ghosh, D. F. Brougham, S. Mitchell, Y. Volkov, and A. Prina-Mello, "Magnetic-fluorescent nanocomposites for biomedical multitasking," *Chem. Comm.*, no. 43, pp. 4474–4476, 2006.

[266] R. Weissleder, A. Bogdanov, E. A. Neuwelt, and M. Papisov, "Long-circulating iron oxides for MR imaging," *Adv. Drug Deliv. Rev.*, vol. 16, no. 2–3, pp. 321–334, 1995.

[267] E. H. Kim, Y. Ahn, and H. S. Lee, "Biomedical applications of superparamagnetic iron oxide nanoparticles encapsulated within chitosan," *J. Alloys Compd.*, vol. 434–435, pp. 633–636, 2007.

[268] E.-K. Lim, Y.-M. Huh, J. Yang, K. Lee, J.-S. Suh, and S. Haam, "pH-Triggered Drug-Releasing Magnetic Nanoparticles for Cancer Therapy Guided by Molecular Imaging by MRI.," *Adv. Mater*, vol. 23, no. 21, pp. 2436–2442, 2011.

[269] J.-H. Park, G. von Maltzahn, L. Zhang, M. P. Schwartz, E. Ruoslahti, S. N. Bhatia, and M. J. Sailor, "Magnetic Iron Oxide Nanoworms for Tumor Targeting and Imaging.," *Adv. Mater*, vol. 20, no. 9, pp. 1630–1635, 2008.

[270] J. Chatterjee, Y. Haik, and C. Chen, "Size dependent magnetic properties of iron oxide nanoparticles," *J. Magn. Magn. Mater.*, vol. 257, pp. 113–118, 2003.

[271] K. Donadel, M. D. V. Felisberto, V. T. Fávere, M. Rigoni, N. J. Batistela, and M. C. M. Laranjeira, "Synthesis and characterization of the iron oxide magnetic particles coated with chitosan biopolymer," *Mater. Sci. Eng. C*, vol. 28, no. 4, pp. 509–514, 2008.

[272] M. Babincova, V. Altanerov, C. Altaner, C. Bergemann, and P. Babinec, "In vitro analysis of cisplatin functionalized magnetic nanoparticles in combined cancer chemotherapy and electromagnetic hyperthermia.," *IEEE Trans. Nanobioscience*, vol. 7, no. 1, pp. 15–19, 2008.

[273] T. J. Brunner, P. Wick, P. Manser, P. Spohn, R. N. Grass, L. K. Limbach, A. Bruinink, and W. J. Stark, "In vitro cytotoxicity of oxide nanoparticles: comparison to asbestos, silica, and the effect of particle solubility.," *Environ. Sci. Technol.*, vol. 40, no. 14, pp. 4374–4381, 2006.

[274] Y. Zhang, N. Kohler, and M. Zhang, "Surface modification of superparamagnetic magnetite nanoparticles and their intracellular uptake.," *Biomaterials*, vol. 23, no. 7, pp. 1553–1561, 2002.

[275] A. K. Gupta and M. Gupta, "Cytotoxicity suppression and cellular uptake enhancement of surface modified magnetic nanoparticles.," *Biomaterials*, vol. 26, no. 13, pp. 1565–1573, 2005.

[276] M. Auffan, L. Decome, J. Rose, T. Orsiere, M. De Meo, V. Briois, C. Chaneac, L. Olivi, J.-L. Berge-Lefranc, A. Botta, M. R. Wiesner, and J.-Y. Bottero, "In vitro interactions between DMSA-coated maghemite nanoparticles and human fibroblasts: A physicochemical and cyto-genotoxical study.," *Environ. Sci. Technol.*, vol. 40, no. 14, pp. 4367–4373, 2006.

[277] J. S. Kim, T.-J. Yoon, K. N. Yu, B. G. Kim, S. J. Park, H. W. Kim, K. H. Lee, S. B. Park, J.-K. Lee, and M. H. Cho, "Toxicity and tissue distribution of magnetic nanoparticles in mice.," *Toxicol. Sci.*, vol. 89, no. 1, pp. 338–347, 2006.

[278] R. Weissleder, D. D. Stark, B. L. Engelstad, B. R. Bacon, C. C. Compton, D. L. White, P. Jacobs, and J. Lewis, "Superparamagnetic iron oxide: pharmacokinetics and toxicity.," *Ajr Am. J. Roentgenol.*, vol. 152, no. 1, pp. 167–173, 1989.

[279] X. Yang, X. Zhang, Y. Ma, Y. Huang, Y. Wang, and Y. Chen, "Superparamagnetic graphene oxide–Fe3O4 nanoparticles hybrid for controlled targeted drug carriers," *J. Mater. Chem.*, vol. 19, no. 18, pp. 2710–2714, 2009.

[280] X. Ma, H. Tao, K. Yang, L. Feng, L. Cheng, X. Shi, Y. Li, L. Guo, and Z. Liu, "A functionalized graphene oxide-iron oxide nanocomposite for magnetically targeted drug delivery, photothermal therapy, and magnetic resonance imaging," *Nano Res.*, vol. 5, no. 3, pp. 199–212, 2012.

[281] X. Shi, H. Gong, Y. Li, C. Wang, L. Cheng, and Z. Liu, "Graphene-based magnetic plasmonic nanocomposite for dual bioimaging and photothermal therapy.," *Biomaterials*, vol. 34, no. 20, pp. 4786–4793, 2013.

[282] K. Yang, L. Hu, X. Ma, S. Ye, L. Cheng, X. Shi, C. Li, Y. Li, and Z. Liu, "Multimodal imaging guided photothermal therapy using functionalized graphene nanosheets anchored with magnetic nanoparticles.," *Adv. Mater.*, vol. 24, no. 14, pp. 1868–1872, 2012.

[283] X. Fan, G. Jiao, W. Zhao, P. Jin, and X. Li, "Magnetic Fe3O4-graphene composites as targeted drug nanocarriers for pH-activated release.," *Nanoscale*, vol. 5, no. 3, pp. 1143–1152, 2013.

[284] G. Wang, G. Chen, Z. Wei, X. Dong, and M. Qi, "Multifunctional Fe3O4/graphene oxide nanocomposites for magnetic resonance imaging and drug delivery," *Mater. Chem. Phys.*, vol. 141, no. 2–3, pp. 997–1004, 2013.

[285] K. Turcheniuk, M. Khanal, A. Motorina, P. Subramanian, A. Barras, V. Zaitsev, V. Kuncser, A. Leca, A. Martoriati, K. Cailliau, J.-F. Bodart, R. Boukherroub, and S.

Szunerits, "Insulin loaded iron magnetic nanoparticle–graphene oxide composites: synthesis, characterization and application for in vivo delivery of insulin," *RSC Adv.*, vol. 4, no. 2, pp. 865–875, 2014.

[286] X. Yang, Y. Wang, X. Huang, Y. Ma, Y. Huang, R. Yang, H. Duan, and Y. Chen, "Multi-functionalized graphene oxide based anticancer drug-carrier with dual-targeting function and pH-sensitivity," *J. Mater. Chem.*, vol. 21, no. 10, pp. 3448–3454, 2011.

[287] C. Wang, S. Ravi, U. S. Garapati, M. Das, M. Howell, J. Mallela, S. Alwarappan, S. S. Mohapatra, and S. Mohapatra, "Multifunctional chitosan magnetic-graphene (CMG) nanoparticles: a theranostic platform for tumor-targeted co-delivery of drugs, genes and MRI contrast agents," *J. Mater. Chem. B*, vol. 1, no. 35, pp. 4396–4405, 2013.

[288] Y. Gao, X. Zou, J. X. Zhao, Y. Li, and X. Su, "Graphene oxide-based magnetic fluorescent hybrids for drug delivery and cellular imaging.," *Colloids Surf. B. Biointerfaces*, vol. 112, pp. 128–133, 2013.

[289] Z. Wang, C. Zhou, J. Xia, B. Via, Y. Xia, F. Zhang, Y. Li, and L. Xia, "Fabrication and characterization of a triple functionalization of graphene oxide with Fe3O4, folic acid and doxorubicin as dual-targeted drug nanocarrier.," *Colloids Surf. B. Biointerfaces*, vol. 106, pp. 60–65, 2013.

[290] J.-M. Shen, F.-Y. Gao, L.-P. Guan, W. Su, Y.-J. Yang, Q.-R. Li, and Z.-C. Jin, "Graphene oxide–Fe3O4 nanocomposite for combination of dual-drug chemotherapy with photothermal therapy," *RSC Adv.*, vol. 4, no. 35, pp. 18473–18484, 2014.

[291] S. Garg, A. De, T. Nandi, and S. Mozumdar, "Synthesis of a smart gold nano-vehicle for liver specific drug delivery.," *AAPS PharmSciTech*, vol. 14, no. 3, pp. 1219–1226, 2013.

[292] H. Takahashi, Y. Niidome, and S. Yamada, "Controlled release of plasmid DNA from gold nanorods induced by pulsed near-infrared light.," *Chem. Comm.*, no. 17, pp. 2247–2249, 2005.

[293] Z. Zhang, J. Jia, Y. Lai, Y. Ma, J. Weng, and L. Sun, "Conjugating folic acid to gold nanoparticles through glutathione for targeting and detecting cancer cells.," *Bioorg. Med. Chem.*, vol. 18, no. 15, pp. 5528–5534, 2010.

[294] X. Huang, I. H. El-Sayed, W. Qian, and M. A. El-Sayed, "Cancer cell imaging and photothermal therapy in the near-infrared region by using gold nanorods.," *J. Am. Chem. Soc.*, vol. 128, no. 6, pp. 2115–2120, 2006.

[295] J. Alper, M. Crespo, and K. Hamad-Schifferli, "Release Mechanism of Octadecyl Rhodamine B Chloride from Au Nanorods by Ultrafast Laser Pulses," *J. Phys. Chem.*, vol. 113, no. 15, pp. 5967–5973, 2009.

[296] Y. Huang, F. Yu, Y.-S. Park, J. Wang, M.-C. Shin, H. S. Chung, and V. C. Yang, "Co-administration of protein drugs with gold nanoparticles to enable percutaneous delivery.," *Biomaterials*, vol. 31, no. 34, pp. 9086–9091, 2010.

[297] S. D. Brown, P. Nativo, J.-A. Smith, D. Stirling, P. R. Edwards, B. Venugopal, D. J. Flint, J. A. Plumb, D. Graham, and N. J. Wheate, "Gold nanoparticles for the improved anticancer drug delivery of the active component of oxaliplatin.," *J. Am. Chem. Soc.*, vol. 132, no. 13, pp. 4678–4684, 2010.

[298] R. Hong, G. Han, J. M. Fernández, B. Kim, N. S. Forbes, and V. M. Rotello, "Glutathione-mediated delivery and release using monolayer protected nanoparticle carriers.," *J. Am. Chem. Soc.*, vol. 128, no. 4, pp. 1078–1079, 2006.

[299] Y. Cheng, A. C Samia, J. D. Meyers, I. Panagopoulos, B. Fei, and C. Burda, "Highly efficient drug delivery with gold nanoparticle vectors for in vivo photodynamic therapy of cancer." *J. Am. Chem. Soc.*, vol. 130, no. 32, pp. 10643–10647, 2008.

[300] J. D. Gibson, B. P. Khanal, and E. R. Zubarev, "Paclitaxel-functionalized gold nanoparticles.," *J. Am. Chem. Soc.*, vol. 129, no. 37, pp. 11653–11661, 2007.

[301] M. A. Polizzi, N. A. Stasko, and M. H. Schoenfisch, "Water-soluble nitric oxide-releasing gold nanoparticles.," *Langmuir*, vol. 23, no. 9, pp. 4938–4943, 2007.

[302] D. C. Hone, P. I. Walker, R. Evans-Gowing, S. FitzGerald, A. Beeby, I. Chambrier, M. J. Cook, and D. A. Russell, "Generation of Cytotoxic Singlet Oxygen via Phthalocyanine-Stabilized Gold Nanoparticles: A Potential Delivery Vehicle for Photodynamic Therapy," *Langmuir*, vol. 18, no. 8, pp. 2985–2987, 2002.

[303] A. Barhoumi, R. Huschka, R. Bardhan, M. W. Knight, and N. J. Halas, "Light-induced release of DNA from plasmon-resonant nanoparticles: Towards light-controlled gene therapy," *Chem. Phys. Lett.*, vol. 482, no. 4–6, pp. 171–179, 2009.

[304] S. E. Lee, G. L. Liu, F. Kim, and L. P. Lee, "Remote optical switch for localized and selective control of gene interference.," *Nano Lett.*, vol. 9, no. 2, pp. 562–570, 2009.

[305] G. Han, N. S. Chari, A. Verma, R. Hong, C. T. Martin, and V. M. Rotello, "Controlled recovery of the transcription of nanoparticle-bound DNA by intracellular concentrations of glutathione.," *Bioconjug. Chem.*, vol. 16, no. 6, pp. 1356–1359, 2005.

[306] X. Huang, W. Qian, I. H. El-Sayed, and M. A. El-Sayed, "The potential use of the enhanced nonlinear properties of gold nanospheres in photothermal cancer therapy.," *Lasers Surg. Med.*, vol. 39, no. 9, pp. 747–53, 2007.

[307] M. S. Yavuz, Y. Cheng, J. Chen, C. M. Cobley, Q. Zhang, M. Rycenga, J. Xie, C. Kim, K. H. Song, A. G. Schwartz, L. V Wang, and Y. Xia, "Gold nanocages covered by smart polymers for controlled release with near-infrared light.," *Nat. Mater.*, vol. 8, no. 12, pp. 935–939, 2009.

[308] H. Park, H. Tsutsumi, and H. Mihara, "Cell penetration and cell-selective drug delivery using α-helix peptides conjugated with gold nanoparticles.," *Biomaterials*, vol. 34, no. 20, pp. 4872–4879, 2013.

[309] M. Zhang, L. Bai, W. Shang, W. Xie, H. Ma, Y. Fu, D. Fang, H. Sun, L. Fan, M. Han, C. Liu, and S. Yang, "Facile synthesis of water-soluble, highly fluorescent graphene quantum dots as a robust biological label for stem cells," *J. Mater. Chem.*, vol. 22, no. 15, pp. 7461–7467, 2012.

[310] A. I. Ekimov, A. L. Efros, and A. A. Onushchenko, "Quantum size effect in semiconductor microcrystals," *Solid State Commun.*, vol. 56, no. 11, pp. 921–924, 1985.

[311] M. Reed, J. Randall, R. Aggarwal, R. Matyi, T. Moore, and A. Wetsel, "Observation of discrete electronic states in a zero-dimensional semiconductor nanostructure," *Phys. Rev. Lett.*, vol. 60, no. 6, pp. 535–537, 1988.

[312] T. Jamieson, R. Bakhshi, D. Petrova, R. Pocock, M. Imani, and A. M. Seifalian, "Biological applications of quantum dots.," *Biomaterials*, vol. 28, no. 31, pp. 4717–4732, 2007.

[313] W. C. . Chan, D. J. Maxwell, X. Gao, R. E. Bailey, M. Han, and S. Nie, "Luminescent quantum dots for multiplexed biological detection and imaging," *Curr. Opin. Biotechnol.*, vol. 13, no. 1, pp. 40–46, 2002.

[314] A. M. Derfus, W. C. W. Chan, and S. N. Bhatia, "Probing the Cytotoxicity of Semiconductor Quantum Dots," *Nano Lett.*, vol. 4, no. 1, pp. 11–18, 2004.

[315] G. Guo, W. Liu, J. Liang, Z. He, H. Xu, and X. Yang, "Probing the cytotoxicity of CdSe quantum dots with surface modification," *Mater. Lett.*, vol. 61, no. 8–9, pp. 1641–1644, 2007.

[316] M. Green and E. Howman, "Semiconductor quantum dots and free radical induced DNA nicking.," *Chem. Comm.*, no. 1, pp. 121–123, 2005.

[317] H. Mattoussi, G. Palui, and H. Bin Na, "Luminescent quantum dots as platforms for probing in vitro and in vivo biological processes.," *Adv. Drug Deliv. Rev.*, vol. 64, no. 2, pp. 138–166, 2012.

[318] Y.-P. Gu, R. Cui, Z.-L. Zhang, Z.-X. Xie, and D.-W. Pang, "Ultrasmall near-infrared Ag2Se quantum dots with tunable fluorescence for in vivo imaging.," *J. Am. Chem. Soc.*, vol. 134, no. 1, pp. 79–82, 2012.

[319] Y. Du, B. Xu, T. Fu, M. Cai, F. Li, Y. Zhang, and Q. Wang, "Near-infrared photoluminescent Ag2S quantum dots from a single source precursor.," *J. Am. Chem. Soc.*, vol. 132, no. 5, pp. 1470–1471, 2010.

[320] S. Shen, Y. Zhang, L. Peng, Y. Du, and Q. Wang, "Matchstick-shaped Ag2S-ZnS heteronanostructures preserving both UV/blue and near-infrared photoluminescence.," *Angew. Chem. Int. Ed. Engl.*, vol. 50, no. 31, pp. 7115–7118, 2011.

[321] J. P. Zimmer, S.-W. Kim, S. Ohnishi, E. Tanaka, J. V Frangioni, and M. G. Bawendi, "Size series of small indium arsenide-zinc selenide core-shell nanocrystals and their application to in vivo imaging.," *J. Am. Chem. Soc.*, vol. 128, no. 8, pp. 2526–2527, 2006.

[322] U. Banin, "Growth and Properties of Semiconductor Core/Shell Nanocrystals with InAs Cores," *J. Am. Chem. Soc.*, vol. 122, no. 40, pp. 9692–9702, 2000.

[323] Y. Cao and U. Banin, "Synthesis and Characterization of InAs/InP and InAs/CdSe Core/Shell Nanocrystals.," *Angew. Chem. Int. Ed. Engl.*, vol. 38, no. 24, pp. 3692–3694, 1999.

[324] S. Haubold, M. Haase, A. Kornowski, and H. Weller, "Strongly luminescent InP/ZnS core-shell nanoparticles.," *Chemphyschem*, vol. 2, no. 5, pp. 331–334, 2001.

[325] R. Xie, D. Battaglia, and X. Peng, "Colloidal InP nanocrystals as efficient emitters covering blue to near-infrared.," *J. Am. Chem. Soc.*, vol. 129, no. 50, pp. 15432–15433, 2007.

[326] K.-T. Yong, "Mn-doped near-infrared quantum dots as multimodal targeted probes for pancreatic cancer imaging.," *Nanotechnology*, vol. 20, no. 1, pp. 15102–15112, 2009.

[327] W. Zheng, P. Kumar, A. Washington, Z. Wang, N. S. Dalal, G. F. Strouse, and K. Singh, "Quantum phase transition from superparamagnetic to quantum superparamagnetic state in ultrasmall Cd(1-x)Cr(II)(x)Se quantum dots?," *J. Am. Chem. Soc.*, vol. 134, no. 4, pp. 2172–2179, 2012.

[328] P. I. Archer, S. A. Santangelo, and D. R. Gamelin, "Direct Observation of sp-d exchange interactions in colloidal Mn2+- and Co2+-doped CdSe quantum dots.," *Nano Lett.*, vol. 7, no. 4, pp. 1037–1043, 2007.

[329] N. Singh, S. Charan, K. Sanjiv, S.-H. Huang, Y.-C. Hsiao, C.-W. Kuo, F.-C. Chien, T.-C. Lee, and P. Chen, "Synthesis of tunable and multifunctional Ni-doped near-infrared QDs for cancer cell targeting and cellular sorting.," *Bioconjug. Chem.*, vol. 23, no. 3, pp. 421–430, 2012.

[330] H. Yang, S. Santra, G. A. Walter, and P. H. Holloway, "GdIII-Functionalized Fluorescent Quantum Dots as Multimodal Imaging Probes," *Adv. Mater.*, vol. 18, no. 21, pp. 2890–2894, 2006.

[331] V. Salgueiriño-Maceira, M. A. Correa-Duarte, M. Spasova, L. M. Liz-Marzán, and M. Farle, "Composite Silica Spheres with Magnetic and Luminescent Functionalities," *Adv. Funct. Mater.*, vol. 16, no. 4, pp. 509–514, 2006.

[332] S. T. Selvan, P. K. Patra, C. Y. Ang, and J. Y. Ying, "Synthesis of silica-coated semiconductor and magnetic quantum dots and their use in the imaging of live cells.," *Angew. Chem. Int. Ed. Engl.*, vol. 46, no. 14, pp. 2448–2452, 2007.

[333] S. Wang, B. R. Jarrett, S. M. Kauzlarich, and A. Y. Louie, "Core/shell quantum dots with high relaxivity and photoluminescence for multimodality imaging.," *J. Am. Chem. Soc.*, vol. 129, no. 13, pp. 3848–3856, 2007.

[334] J. Kim, J. E. Lee, J. Lee, J. H. Yu, B. C. Kim, K. An, Y. Hwang, C.-H. Shin, J.-G. Park, J. Kim, and T. Hyeon, "Magnetic fluorescent delivery vehicle using uniform

mesoporous silica spheres embedded with monodisperse magnetic and semiconductor nanocrystals.," *J. Am. Chem. Soc.*, vol. 128, no. 3, pp. 688–689, 2006.

[335] X. Zhang, S. Wang, C. Zhu, M. Liu, Y. Ji, L. Feng, L. Tao, and Y. Wei, "Carbon-dots derived from nanodiamond: photoluminescence tunable nanoparticles for cell imaging.," *J. Colloid Interface Sci.*, vol. 397, pp. 39–44, 2013.

[336] S. Zhuo, M. Shao, and S.-T. Lee, "Upconversion and downconversion fluorescent graphene quantum dots: ultrasonic preparation and photocatalysis.," *ACS Nano*, vol. 6, no. 2, pp. 1059–1064, 2012.

[337] F. Jiang, D. Chen, R. Li, Y. Wang, G. Zhang, S. Li, J. Zheng, N. Huang, Y. Gu, C. Wang, and C. Shu, "Eco-friendly synthesis of size-controllable amine-functionalized graphene quantum dots with antimycoplasma properties.," *Nanoscale*, vol. 5, no. 3, pp. 1137–1142, 2013.

[338] H. Sun, L. Wu, N. Gao, J. Ren, and X. Qu, "Improvement of photoluminescence of graphene quantum dots with a biocompatible photochemical reduction pathway and its bioimaging application.," *ACS Appl. Mater. Interf.*, vol. 5, no. 3, pp. 1174–1179, 2013.

[339] M. Nurunnabi, Z. Khatun, K. M. Huh, S. Y. Park, D. Y. Lee, K. J. Cho, and Y.-K. Lee, "In vivo biodistribution and toxicology of carboxylated graphene quantum dots.," *ACS Nano*, vol. 7, no. 8, pp. 6858–6867, 2013.

[340] X. Huang, F. Zhang, L. Zhu, K. Y. Choi, N. Guo, J. Guo, K. Tackett, P. Anilkumar, G. Liu, Q. Quan, H. S. Choi, G. Niu, Y.-P. Sun, S. Lee, and X. Chen, "Effect of injection routes on the biodistribution, clearance, and tumor uptake of carbon dots.," *ACS Nano*, vol. 7, no. 7, pp. 5684–5693, 2013.

[341] M. Nurunnabi, Z. Khatun, M. Nafiujjaman, D.-G. Lee, and Y.-K. Lee, "Surface coating of graphene quantum dots using mussel-inspired polydopamine for biomedical optical imaging.," *ACS Appl. Mater. Interfaces*, vol. 5, no. 16, pp. 8246–8253, 2013.

[342] M. Yu, Y. Yang, R. Han, Q. Zheng, L. Wang, Y. Hong, Z. Li, and Y. Sha, "Polyvalent lactose-quantum dot conjugate for fluorescent labeling of live leukocytes." *Langmuir*, vol. 26, no. 11, pp. 8534–8539, 2010.

[343] W. Liu, M. Howarth, A. B. Greytak, Y. Zheng, D. G. Nocera, A. Y. Ting, and M. G. Bawendi, "Compact biocompatible quantum dots functionalized for cellular imaging.," *J. Am. Chem. Soc.*, vol. 130, no. 4, pp. 1274–1284, 2008.

[344] K. Susumu, H. T. Uyeda, I. L. Medintz, T. Pons, J. B. Delehanty, and H. Mattoussi, "Enhancing the stability and biological functionalities of quantum dots via compact multifunctional ligands.," *J. Am. Chem. Soc.*, vol. 129, no. 45, pp. 13987–13996, 2007.

[345] B. C. Mei, K. Susumu, I. L. Medintz, J. B. Delehanty, T. J. Mountziaris, and H. Mattoussi, "Modular poly(ethylene glycol) ligands for biocompatible semiconductor and gold nanocrystals with extended pH and ionic stability," *J. Mater. Chem.*, vol. 18, no. 41, pp. 4949–4958, 2008.

[346] H. T. Uyeda, I. L. Medintz, J. K. Jaiswal, S. M. Simon, and H. Mattoussi, "Synthesis of compact multidentate ligands to prepare stable hydrophilic quantum dot fluorophores.," *J. Am. Chem. Soc.*, vol. 127, no. 11, pp. 3870–3878, 2005.

[347] D. Hull and T. W. Clyne, *An Introduction to Composite Materials*, 1st ed. Cambridge: Cambridge University Press, 1981.

[348] R. Simon, S. P. Prosen, and J. Duffy, "Carbon Fibre Composites," *Nature*, vol. 213, no. 5081, pp. 1113–1114, 1967.

[349] B. Chen and J. R. G. Evans, "Impact and tensile energies of fracture in polymer–clay nanocomposites," *Polymer (Guildf).*, vol. 49, no. 23, pp. 5113–5118, 2008.

[350] W. Tang, M. H. Santare, and S. G. Advani, "Melt processing and mechanical property characterization of multi-walled carbon nanotube/high density polyethylene (MWNT/HDPE) composite films," *Carbon N. Y.*, vol. 41, no. 14, pp. 2779–2785, 2003.

[351] C. A. Sobon, H. K. Bowen, A. Broad, and P. D. Calvert, "Precipitation of magnetic oxides in polymers," *J. Mater. Sci. Lett.*, vol. 6, no. 8, pp. 901–904, 1987.

[352] H. Kim, A. A. Abdala, and C. W. Macosko, "Graphene/Polymer Nanocomposites," *Macromolecules*, vol. 43, no. 16, pp. 6515–6530, 2010.

[353] T. Kuilla, S. Bhadra, D. Yao, N. H. Kim, S. Bose, and J. H. Lee, "Recent advances in graphene based polymer composites," *Prog. Polym. Sci.*, vol. 35, no. 11, pp. 1350–1375, 2010.

[354] A. Y. W. Sham and S. M. Notley, "A review of fundamental properties and applications of polymer–graphene hybrid materials," *Soft Matter*, vol. 9, no. 29, pp. 6645–6653, 2013.

[355] Y. Sun and G. Shi, "Graphene/polymer composites for energy applications," *J. Polym. Sci. Part B Polym. Phys.*, vol. 51, no. 4, pp. 231–253, 2013.

[356] K. Hu, D. D. Kulkarni, I. Choi, and V. V. Tsukruk, "Graphene-polymer nanocomposites for structural and functional applications," *Prog. Polym. Sci.*, vol. 39, no. 11, pp. 1934–1972, 2014.

[357] N. Yousefi, X. Sun, X. Lin, X. Shen, J. Jia, B. Zhang, B. Tang, M. Chan, and J.-K. Kim, "Highly aligned graphene/polymer nanocomposites with excellent dielectric properties for high-performance electromagnetic interference shielding.," *Adv. Mater.*, vol. 26, no. 31, pp. 5480–5487, 2014.

[358] S. F. Medeiros, A. M. Santos, H. Fessi, and A. Elaissari, "Stimuli-responsive magnetic particles for biomedical applications.," *Int. J. Pharm.*, vol. 403, no. 1–2, pp. 139–161, 2011.

[359] T. Ramanathan, A. a Abdala, S. Stankovich, D. a Dikin, M. Herrera-Alonso, R. D. Piner, D. H. Adamson, H. C. Schniepp, X. Chen, R. S. Ruoff, S. T. Nguyen, I. a Aksay, R. K. Prud'Homme, L. C. Brinson, and others, "Functionalized graphene sheets for polymer nanocomposites," *Nat. Nanotechnol.*, vol. 3, no. 6, pp. 327–331, 2008.

[360] L. Lee, C. Zeng, X. Cao, X. Han, J. Shen, and G. Xu, "Polymer nanocomposite foams," *Compos. Sci. Technol.*, vol. 65, no. 15–16, pp. 2344–2363, 2005.

[361] R. A. Vaia and E. P. Giannelis, "Polymer Nanocomposites: Status and Opportunities," *MRS Bull.*, vol. 26, no. 05, pp. 394–401, 2011.

[362] R. K. Layek, S. Samanta, and A. K. Nandi, "Graphene sulphonic acid/chitosan nano biocomposites with tunable mechanical and conductivity properties," *Polymer (Guildf).*, vol. 53, no. 11, pp. 2265–2273, 2012.

[363] H. W. Ha, A. Choudhury, T. Kamal, D.-H. Kim, and S.-Y. Park, "Effect of chemical modification of graphene on mechanical, electrical, and thermal properties of polyimide/graphene nanocomposites.," *ACS Appl. Mater. Interfaces*, vol. 4, no. 9, pp. 4623–4630, 2012.

[364] H.-D. Huang, P.-G. Ren, J. Chen, W.-Q. Zhang, X. Ji, and Z.-M. Li, "High barrier graphene oxide nanosheet/poly(vinyl alcohol) nanocomposite films," *J. Memb. Sci.*, vol. 409–410, pp. 156–163, 2012.

[365] C.-C. Teng, C.-C. M. Ma, C.-H. Lu, S.-Y. Yang, S.-H. Lee, M.-C. Hsiao, M.-Y. Yen, K.-C. Chiou, and T.-M. Lee, "Thermal conductivity and structure of non-covalent functionalized graphene/epoxy composites," *Carbon N. Y.*, vol. 49, no. 15, pp. 5107–5116, 2011.

[366] J. R. Potts, D. R. Dreyer, C. W. Bielawski, and R. S. Ruoff, "Graphene-based polymer nanocomposites," *Polymer (Guildf).*, vol. 52, no. 1, pp. 5–25, 2011.

[367] Y. Xu, W. Hong, H. Bai, C. Li, and G. Shi, "Strong and ductile poly(vinyl alcohol)/graphene oxide composite films with a layered structure," *Carbon N. Y.*, vol. 47, no. 15, pp. 3538–3543, 2009.

[368] J.-H. Chang, T.-G. Jang, K. J. Ihn, W.-K. Lee, and G. S. Sur, "Poly(vinyl alcohol) nanocomposites with different clays: Pristine clays and organoclays," *J. Appl. Polym. Sci.*, vol. 90, no. 12, pp. 3208–3214, 2003.

[369] C. Wan, M. Frydrych, and B. Chen, "Strong and bioactive gelatin–graphene oxide nanocomposites," *Soft Matter*, vol. 7, no. 13, pp. 6159–6166, 2011.

[370] Y. Rao, "Gelatin–clay nanocomposites of improved properties," *Polymer (Guildf).*, vol. 48, no. 18, pp. 5369–5375, 2007.

[371] J. F. Martucci, A. Vázquez, and R. A. Ruseckaite, "Nanocomposites based on gelatin and montmorillonite," *J. Therm. Anal. Calorim.*, vol. 89, no. 1, pp. 117–122, 2007.

[372] H. Kim, Y. Miura, and C. W. Macosko, "Graphene/Polyurethane Nanocomposites for Improved Gas Barrier and Electrical Conductivity," *Chem. Mater.*, vol. 22, no. 11, pp. 3441–3450, 2010.

[373] J. Liang, Y. Xu, Y. Huang, L. Zhang, Y. Wang, Y. Ma, F. Li, T. Guo, and Y. Chen, "Infrared-Triggered Actuators from Graphene-Based Nanocomposites," *J. Phys. Chem. C*, vol. 113, no. 22, pp. 9921–9927, 2009.

[374] S. Stankovich, D. a Dikin, G. H. B. Dommett, K. M. Kohlhaas, E. J. Zimney, E. a Stach, R. D. Piner, S. T. Nguyen, and R. S. Ruoff, "Graphene-based composite materials.," *Nature*, vol. 442, no. 7100, pp. 282–286, 2006.

[375] B. Das, K. Eswar Prasad, U. Ramamurty, and C. N. R. Rao, "Nano-indentation studies on polymer matrix composites reinforced by few-layer graphene.," *Nanotechnology*, vol. 20, no. 12, pp. 125705–12709, 2009.

[376] G. D. Barber, B. H. Calhoun, and R. B. Moore, "Poly(ethylene terephthalate) ionomer based clay nanocomposites produced via melt extrusion," *Polymer (Guildf).*, vol. 46, no. 17, pp. 6706–6714, 2005.

[377] L. Liu, Z. Qi, and X. Zhu, "Studies on nylon 6/clay nanocomposites by melt-intercalation process," *J. Appl. Polym. Sci.*, vol. 71, no. 7, pp. 1133–1138, 1999.

[378] H. Kim and C. W. Macosko, "Morphology and Properties of Polyester/Exfoliated Graphite Nanocomposites," *Macromolecules*, vol. 41, no. 9, pp. 3317–3327, 2008.

[379] H. Kim and C. W. Macosko, "Processing-property relationships of polycarbonate/graphene composites," *Polymer (Guildf).*, vol. 50, no. 15, pp. 3797–3809, 2009.

[380] C. H. Dan, M. H. Lee, Y. D. Kim, B. H. Min, and J. H. Kim, "Effect of clay modifiers on the morphology and physical properties of thermoplastic polyurethane/clay nanocomposites," *Polymer (Guildf).*, vol. 47, no. 19, pp. 6718–6730, 2006.

[381] M. Song, V. Mittal, and P. O'Brien, *Polymer-Graphene Nanocomposites*, 1st ed. Cambridge: Royal Society of Chemistry, 2012.

[382] J.-M. Thomassin, M. Trifkovic, W. Alkarmo, C. Detrembleur, C. Jérôme, and C. Macosko, "Poly(methyl methacrylate)/Graphene Oxide Nanocomposites by a Precipitation Polymerization Process and Their Dielectric and Rheological Characterization," *Macromolecules*, vol. 47, no. 6, pp. 2149–2155, 2014.

[383] H. Hu, X. Wang, J. Wang, L. Wan, F. Liu, H. Zheng, R. Chen, and C. Xu, "Preparation and properties of graphene nanosheets–polystyrene nanocomposites via in situ emulsion polymerization," *Chem. Phys. Lett.*, vol. 484, no. 4–6, pp. 247–253, 2010.

[384] J. Zhu, A. B. Morgan, F. J. Lamelas, and C. A. Wilkie, "Fire Properties of Polystyrene−Clay Nanocomposites," *Chem. Mater.*, vol. 13, no. 10, pp. 3774–3780, 2001.

[385] Y.-H. Yu, C.-Y. Lin, J.-M. Yeh, and W.-H. Lin, "Preparation and properties of poly(vinyl alcohol)–clay nanocomposite materials," *Polymer (Guildf).*, vol. 44, no. 12, pp. 3553–3560, 2003.

[386] M. A. Rafiee, J. Rafiee, Z. Wang, H. Song, Z.-Z. Yu, and N. Koratkar, "Enhanced mechanical properties of nanocomposites at low graphene content.," *ACS Nano*, vol. 3, no. 12, pp. 3884–3890, 2009.

[387] H.-L. Ma, Y. Zhang, Q.-H. Hu, S. He, X. Li, M. Zhai, and Z.-Z. Yu, "Enhanced mechanical properties of poly(vinyl alcohol) nanocomposites with glucose-reduced graphene oxide," *Mater. Lett.*, vol. 102–103, pp. 15–18, 2013.

[388] X. Yang, S. Shang, and L. Li, "Layer-structured poly(vinyl alcohol)/graphene oxide nanocomposites with improved thermal and mechanical properties," *J. Appl. Polym. Sci.*, vol. 120, no. 3, pp. 1355–1360, 2011.

[389] M. Tian, L. Qu, X. Zhang, K. Zhang, S. Zhu, X. Guo, G. Han, X. Tang, and Y. Sun, "Enhanced mechanical and thermal properties of regenerated cellulose/graphene composite fibers.," *Carbohydr. Polym.*, vol. 111, pp. 456–462, 2014.

[390] H.-K. Jang, H.-I. Kim, T. Dodge, P. Sun, H. Zhu, J.-D. Nam, and J. Suhr, "Interfacial shear strength of reduced graphene oxide polymer composites," *Carbon N. Y.*, vol. 77, pp. 390–397, 2014.

[391] C. Bao, Y. Guo, L. Song, Y. Kan, X. Qian, and Y. Hu, "In situ preparation of functionalized graphene oxide/epoxy nanocomposites with effective reinforcements," *J. Mater. Chem.*, vol. 21, no. 35, pp. 13290–13298, 2011.

[392] M. Fang, Z. Zhang, J. Li, H. Zhang, H. Lu, and Y. Yang, "Constructing hierarchically structured interphases for strong and tough epoxy nanocomposites by amine-rich graphene surfaces," *J. Mater. Chem.*, vol. 20, no. 43, pp. 9635–9643, 2010.

[393] Y. Chen, Y. Qi, Z. Tai, X. Yan, F. Zhu, and Q. Xue, "Preparation, mechanical properties and biocompatibility of graphene oxide/ultrahigh molecular weight polyethylene composites," *Eur. Polym. J.*, vol. 48, no. 6, pp. 1026–1033, 2012.

[394] O. M. Istrate, K. R. Paton, U. Khan, A. O'Neill, A. P. Bell, and J. N. Coleman, "Reinforcement in melt-processed polymer–graphene composites at extremely low graphene loading level," *Carbon N. Y.*, vol. 78, pp. 243–249, 2014.

[395] W. Kai, Y. Hirota, L. Hua, and Y. Inoue, "Thermal and mechanical properties of a poly(ε-caprolactone)/graphite oxide composite," *J. Appl. Polym. Sci.*, vol. 107, no. 3, pp. 1395–1400, 2008.

[396] X. Yang, Y. Tu, L. Li, S. Shang, and X.-M. Tao, "Well-dispersed chitosan/graphene oxide nanocomposites.," *ACS Appl. Mater. Interf.*, vol. 2, no. 6, pp. 1707–1713, 2010.

[397] Y. Pan, T. Wu, H. Bao, and L. Li, "Green fabrication of chitosan films reinforced with parallel aligned graphene oxide," *Carbohydr. Polym.*, vol. 83, no. 4, pp. 1908–1915, 2011.

[398] A. M. Pandele, S. Dinescu, M. Costache, E. Vasile, C. Obreja, H. Iovu, and M. Ionita, "Preparation and in vitro, bulk, and surface investigation of chitosan/graphene oxide composite films," *Polym. Compos.*, vol. 34, no. 12, pp. 2116–2124, 2013.

[399] X. Wang, H. Bai, Z. Yao, A. Liu, and G. Shi, "Electrically conductive and mechanically strong biomimetic chitosan/reduced graphene oxide composite films," *J. Mater. Chem.*, vol. 20, no. 41, pp. 9032–9036, 2010.

[400] C. Wan and B. Chen, "Reinforcement and interphase of polymer/graphene oxide nanocomposites," *J. Mater. Chem.*, vol. 22, no. 8, pp. 3637–3646, 2012.

[401] L. Gong, I. A. Kinloch, R. J. Young, I. Riaz, R. Jalil, and K. S. Novoselov, "Interfacial stress transfer in a graphene monolayer nanocomposite.," *Adv. Mater*, vol. 22, no. 24, pp. 2694–2697, 2010.

[402] X. Zhao, Q. Zhang, D. Chen, and P. Lu, "Enhanced Mechanical Properties of Graphene-Based Poly(vinyl alcohol) Composites," *Macromolecules*, vol. 43, no. 5, pp. 2357–2363, 2010.

[403] Y. Huang, Y. Qin, Y. Zhou, H. Niu, Z.-Z. Yu, and J.-Y. Dong, "Polypropylene/Graphene Oxide Nanocomposites Prepared by In Situ Ziegler−Natta Polymerization," *Chem. Mater.*, vol. 22, no. 13, pp. 4096–4102, 2010.

[404] D. Wang, X. Zhang, J.-W. Zha, J. Zhao, Z.-M. Dang, and G.-H. Hu, "Dielectric properties of reduced graphene oxide/polypropylene composites with ultralow percolation threshold," *Polymer (Guildf).*, vol. 54, no. 7, pp. 1916–1922, 2013.

[405] X.-Y. Qi, D. Yan, Z. Jiang, Y.-K. Cao, Z.-Z. Yu, F. Yavari, and N. Koratkar, "Enhanced electrical conductivity in polystyrene nanocomposites at ultra-low graphene content.," *ACS Appl. Mater. Interfaces*, vol. 3, no. 8, pp. 3130–3133, 2011.

[406] H.-B. Zhang, W.-G. Zheng, Q. Yan, Y. Yang, J.-W. Wang, Z.-H. Lu, G.-Y. Ji, and Z.-Z. Yu, "Electrically conductive polyethylene terephthalate/graphene nanocomposites prepared by melt compounding," *Polymer (Guildf).*, vol. 51, no. 5, pp. 1191–1196, 2010.

[407] S. Sayyar, E. Murray, B. C. Thompson, S. Gambhir, D. L. Officer, and G. G. Wallace, "Covalently linked biocompatible graphene/polycaprolactone composites for tissue engineering," *Carbon N. Y.*, vol. 52, pp. 296–304, 2013.

[408] Y. A. Balogun and R. C. Buchanan, "Enhanced percolative properties from partial solubility dispersion of filler phase in conducting polymer composites (CPCs)," *Compos. Sci. Technol.*, vol. 70, no. 6, pp. 892–900, 2010.

[409] L. Sun, W.-J. Boo, A. Clearfield, H.-J. Sue, and H. Q. Pham, "Barrier properties of model epoxy nanocomposites," *J. Membr. Sci.*, vol. 318, no. 1–2, pp. 129–136, 2008.

[410] J. S. Bunch, S. S. Verbridge, J. S. Alden, A. M. van der Zande, J. M. Parpia, H. G. Craighead, and P. L. McEuen, "Impermeable atomic membranes from graphene sheets.," *Nano Lett.*, vol. 8, no. 8, pp. 2458–2462, 2008.

[411] P. LeBaron, "Polymer-layered silicate nanocomposites: an overview," *Appl. Clay Sci.*, vol. 15, no. 1–2, pp. 11–29, 1999.

[412] J. Kim, C. Hu, R. Woo, and M. Sham, "Moisture barrier characteristics of organoclay epoxy nanocomposites," *Compos. Sci. Technol.*, vol. 65, no. 5, pp. 805–813, 2005.

[413] L. E. Nielsen, "Models for the Permeability of Filled Polymer Systems," *J Macromol Sci, Part A. Pure Appl Chem*, vol. 1, no. 5, pp. 929–942, 1967.

[414] H. Liu, T. Kuila, N. H. Kim, B.-C. Ku, and J. H. Lee, "In situ synthesis of the reduced graphene oxide–polyethyleneimine composite and its gas barrier properties," *J. Mater. Chem. A*, vol. 1, no. 11, pp. 3739–3746, 2013.

[415] I.-H. Tseng, Y.-F. Liao, J.-C. Chiang, and M.-H. Tsai, "Transparent polyimide/graphene oxide nanocomposite with improved moisture barrier property," *Mater. Chem. Phys.*, vol. 136, no. 1, pp. 247–253, 2012.

[416] O. C. Compton, S. Kim, C. Pierre, J. M. Torkelson, and S. T. Nguyen, "Crumpled graphene nanosheets as highly effective barrier property enhancers.," *Adv. Mater*, vol. 22, no. 42, pp. 4759–4763, 2010.

[417] J. Gass, P. Poddar, J. Almand, S. Srinath, and H. Srikanth, "Superparamagnetic Polymer Nanocomposites with Uniform Fe3O4 Nanoparticle Dispersions," *Adv. Funct. Mater.*, vol. 16, no. 1, pp. 71–75, 2006.

[418] L. Raymond, J.-F. Revol, D. H. Ryan, and R. H. Marchessault, "Precipitation of ferrites in Nafion membranes," *J. Appl. Polym. Sci.*, vol. 59, no. 7, pp. 1073–1086, 1996.

[419] A. A. Novakova, V. Y. Lanchinskaya, A. V. Volkov, T. S. Gendler, T. Y. Kiseleva, M. A. Moskvina, and S. B. Zezin, "Magnetic properties of polymer nanocomposites containing iron oxide nanoparticles," *J. Magn. Magn. Mater.*, vol. 258–259, pp. 354–357, 2003.

[420] D. C. Sun and D. S. Sun, "The synthesis and characterization of electrical and magnetic nanocomposite: PEDOT/PSS–Fe3O4," *Mater. Chem. Phys.*, vol. 118, no. 2–3, pp. 288–292, 2009.

[421] S. Taccola, F. Greco, A. Zucca, C. Innocenti, C. de J. Fernández, G. Campo, C. Sangregorio, B. Mazzolai, and V. Mattoli, "Characterization of free-standing PEDOT:PSS/iron oxide nanoparticle composite thin films and application as conformable humidity sensors.," *ACS Appl. Mater. Interfaces*, vol. 5, no. 13, pp. 6324–6332, 2013.

[422] K. Agarwal, M. Prasad, R. B. Sharma, and D. K. Setua, "Studies on Microstructural and Thermophysical properties of polymer nanocomposite based on polyphenylene oxide and Ferrimagnetic iron oxide," *Polym. Test.*, vol. 30, no. 1, pp. 155–160, 2011.

[423] X.-J. Li, Q. Wei, and X. Wang, "Preparation of magnetic polyimide/maghemite nanocomposite fibers by electrospinning," *High Perform. Polym.*, vol. 26, no. 7, pp. 810–816, 2014.

[424] J. Zhang, J. Wang, T. Lin, C. H. Wang, K. Ghorbani, J. Fang, and X. Wang, "Magnetic and mechanical properties of polyvinyl alcohol (PVA) nanocomposites with hybrid nanofillers – Graphene oxide tethered with magnetic Fe3O4 nanoparticles," *Chem. Eng. J.*, vol. 237, pp. 462–468, 2014.

[425] M. T. Ramesan, "Dynamic mechanical properties, magnetic and electrical behavior of iron oxide/ethylene vinyl acetate nanocomposites," *Polym. Compos.*, vol. 35, no. 10, pp. 1989–1996, 2014.

[426] X. Geng, L. Niu, Z. Xing, R. Song, G. Liu, M. Sun, G. Cheng, H. Zhong, Z. Liu, Z. Zhang, L. Sun, H. Xu, L. Lu, and L. Liu, "Aqueous-processable noncovalent chemically converted graphene-quantum dot composites for flexible and transparent optoelectronic films.," *Adv. Mater.*, vol. 22, no. 5, pp. 638–642, 2010.

[427] M. Mahmoudifard, A. M. Shoushtari, and M. Shanehsaz, "Quantum dot/polyvinyl alcohol composite nanofibers membrane as highly sensitive fluorescence quenching-based sensors," *Fibers Polym.*, vol. 15, no. 9, pp. 1797–1803, 2014.

[428] R. Liang, D. Yan, R. Tian, X. Yu, W. Shi, C. Li, M. Wei, D. G. Evans, and X. Duan, "Quantum Dots-Based Flexible Films and Their Application as the Phosphor in White Light-Emitting Diodes," *Chem. Mater.*, vol. 26, no. 8, pp. 2595–2600, 2014.

[429] B. Suo, X. Su, J. Wu, D. Chen, A. Wang, and Z. Guo, "Poly (vinyl alcohol) thin film filled with CdSe–ZnS quantum dots: Fabrication, characterization and optical properties," *Mater. Chem. Phys.*, vol. 119, no. 1–2, pp. 237–242, 2010.

[430] F. Jin, M.-L. Zheng, M.-L. Zhang, Z.-S. Zhao, and X.-M. Duan, "A facile layer-by-layer assembly method for the fabrication of fluorescent polymer/quantum dot nanocomposite thin films," *RSC Adv.*, vol. 4, no. 63, pp. 33206–33214, 2014.

[431] B. O. Dabbousi, M. G. Bawendi, O. Onitsuka, and M. F. Rubner, "Electroluminescence from CdSe quantum-dot/polymer composites," *Appl. Phys. Lett.*, vol. 66, no. 11, pp. 1316–1318, 1995.

[432] H. C. Kim, H.-G. Hong, C. Yoon, H. Choi, I.-S. Ahn, D. C. Lee, Y.-J. Kim, and K. Lee, "Fabrication of high quantum yield quantum dot/polymer films by enhancing dispersion of quantum dots using silica particles.," *J. Colloid Interface Sci.*, vol. 393, pp. 74–79, 2013.

[433] A. Pucci, M. Boccia, F. Galembeck, C. A. de P. Leite, N. Tirelli, and G. Ruggeri, "Luminescent nanocomposites containing CdS nanoparticles dispersed into vinyl alcohol based polymers," *React. Funct. Polym.*, vol. 68, no. 7, pp. 1144–1151, 2008.

[434] S. A. McDonald, G. Konstantatos, S. Zhang, P. W. Cyr, E. J. D. Klem, L. Levina, and E. H. Sargent, "Solution-processed PbS quantum dot infrared photodetectors and photovoltaics.," *Nat. Mater.*, vol. 4, no. 2, pp. 138–142, 2005.

[435] L. Zhu, P. Huo, Q. Wang, F. Liang, C. Zhang, J. Li, X. Qu, G. Wang, and Z. Yang, "Photoluminescent poly(ether ether ketone)-quantum dot composite films.," *Chem. Commun.*, vol. 49, no. 46, pp. 5283–5285, 2013.

[436] S. Mallakpour and V. Behranvand, "Optical, mechanical, and thermal behavior of poly(vinyl alcohol) composite films embedded with biosafe and optically active poly(amide–imide)-ZnO quantum dot nanocomposite as a novel reinforcement," *Colloid Polym. Sci.*, vol. 292, no. 11, pp. 2857–2867, 2014.

[437] G. Wu, L. Zhou, S. Yan, X. Xia, Y. Xiong, and W. Xu, "Transparent, fluorescent, and mechanical enhanced elastomeric composites formed with poly (styrene-butadiene-styrene) and SiO2-hybridized CdTe quantum dots," *J. Appl. Polym. Sci.*, vol. 122, no. 4, pp. 2325–2330, 2011.

[438] S. Agrawal, D. Patidar, and N. S. Saxena, "Investigation of temperature-dependent mechanical properties of CdS/PMMA nanocomposites," *J. Compos. Mater.*, vol. 45, no. 24, pp. 2507–2514, 2011.

[439] S. N. Raja, A. C. K. Olson, K. Thorkelsson, A. J. Luong, L. Hsueh, G. Chang, B. Gludovatz, L. Lin, T. Xu, R. O. Ritchie, and A. P. Alivisatos, "Tetrapod nanocrystals as fluorescent stress probes of electrospun nanocomposites.," *Nano Lett.*, vol. 13, no. 8, pp. 3915–3922, 2013.

[440] M. N. . Ravi Kumar, "A review of chitin and chitosan applications," *React. Funct. Polym.*, vol. 46, no. 1, pp. 1–27, 2000.

[441] M. N. V. R. Kumar, R. A. A. Muzzarelli, C. Muzzarelli, H. Sashiwa, and A. J. Domb, "Chitosan chemistry and pharmaceutical perspectives.," *Chem. Rev.*, vol. 104, no. 12, pp. 6017–6084, 2004.

[442] S. Rao and C. Sharma, "Use of chitosan as a biomaterial: studies on its safety and hemostatic potential.," *J Biomed Mater Res.*, vol. 34, no. 1, pp. 21–28, 1997.

[443] R. A. A. Muzzarelli, *Polymer Science: A Comprehensive Reference*, vol. 10. Elsevier BV, 2012.

[444] R. A. A. Muzzarelli, J. Boudrant, D. Meyer, N. Manno, M. DeMarchis, and M. G. Paoletti, "Current views on fungal chitin/chitosan, human chitinases, food preservation, glucans, pectins and inulin: A tribute to Henri Braconnot, precursor of the carbohydrate polymers science, on the chitin bicentennial," *Carbohydr. Polym.*, vol. 87, no. 2, pp. 995–1012, 2012.

[445] K. Okuyama, K. Noguchi, T. Miyazawa, T. Yui, and K. Ogawa, "Molecular and Crystal Structure of Hydrated Chitosan," *Macromolecules*, vol. 30, no. 19, pp. 5849–5855, 1997.

[446] T. Yui, K. Imada, K. Okuyama, Y. Obata, K. Suzuki, and K. Ogawa, "Molecular and crystal structure of the anhydrous form of chitosan," *Macromolecules*, vol. 27, no. 26, pp. 7601–7605, 1994.

[447] T. Kean and M. Thanou, "Biodegradation, biodistribution and toxicity of chitosan.," *Adv. Drug Deliv. Rev.*, vol. 62, no. 1, pp. 3–11, 2010.

[448] A. Göpferich, "Mechanisms of polymer degradation and erosion," *Biomaterials*, vol. 17, no. 2, pp. 103–114, 1996.

[449] B. Porstmann, K. Jung, H. Schmechta, U. Evers, M. Pergande, T. Porstmann, H.-J. Kramm, and H. Krause, "Measurement of lysozyme in human body fluids: Comparison of various enzyme immunoassay techniques and their diagnostic application," *Clin. Biochem.*, vol. 22, no. 5, pp. 349–355, 1989.

[450] J. D. Funkhouser and N. N. Aronson, "Chitinase family GH18: evolutionary insights from the genomic history of a diverse protein family.," *BMC Evol. Biol.*, vol. 7, no. 1, pp. 96–112, 2007.

[451] H. Onishi and Y. Machida, "Biodegradation and distribution of water-soluble chitosan in mice.," *Biomaterials*, vol. 20, no. 2, pp. 175–182, 1999.

[452] S. Richardson, "Potential of low molecular mass chitosan as a DNA delivery system: biocompatibility, body distribution and ability to complex and protect DNA," *Int. J. Pharm.*, vol. 178, no. 2, pp. 231–243, 1999.

[453] D. Agudelo, S. Sanyakamdhorn, S. Nafisi, and H.-A. Tajmir-Riahi, "Transporting antitumor drug tamoxifen and its metabolites, 4-hydroxytamoxifen and endoxifen by chitosan nanoparticles.," *PLoS One*, vol. 8, no. 3, p. e60250, 2013.

[454] R. Vivek, V. Nipun Babu, R. Thangam, K. S. Subramanian, and S. Kannan, "pH-responsive drug delivery of chitosan nanoparticles as Tamoxifen carriers for effective anti-tumor activity in breast cancer cells.," *Colloids Surf. B. Biointerfaces*, vol. 111C, pp. 117–123, 2013.

[455] F. S. Majedi, M. M. Hasani-Sadrabadi, J. J. VanDersarl, N. Mokarram, S. Hojjati-Emami, E. Dashtimoghadam, S. Bonakdar, M. A. Shokrgozar, A. Bertsch, and P. Renaud, "On-Chip Fabrication of Paclitaxel-Loaded Chitosan Nanoparticles for Cancer Therapeutics," *Adv. Funct. Mater.*, vol. 24, no. 4, pp. 432–441, 2014.

[456] Y.-S. Wang, L.-R. Liu, Q. Jiang, and Q.-Q. Zhang, "Self-aggregated nanoparticles of cholesterol-modified chitosan conjugate as a novel carrier of epirubicin," *Eur. Polym. J.*, vol. 43, no. 1, pp. 43–51, 2007.

[457] Y. Son, "Biodistribution and anti-tumor efficacy of doxorubicin loaded glycol-chitosan nanoaggregates by EPR effect," *J. Control. Release*, vol. 91, no. 1–2, pp. 135–145, 2003.

[458] Q. Tian, C.-N. Zhang, X.-H. Wang, W. Wang, W. Huang, R.-T. Cha, C.-H. Wang, Z. Yuan, M. Liu, H.-Y. Wan, and H. Tang, "Glycyrrhetinic acid-modified chitosan/poly(ethylene glycol) nanoparticles for liver-targeted delivery.," *Biomaterials*, vol. 31, no. 17, pp. 4748–4756, 2010.

[459] H. A. Tajmir-Riahi, S. Nafisi, S. Sanyakamdhorn, D. Agudelo, and P. Chanphai, "Applications of chitosan nanoparticles in drug delivery.," *Methods Mol. Biol.*, vol. 1141, pp. 165–184, 2014.

[460] Z. Yuan, Y. Ye, F. Gao, H. Yuan, M. Lan, K. Lou, and W. Wang, "Chitosan-graft-β-cyclodextrin nanoparticles as a carrier for controlled drug release.," *Int. J. Pharm.*, vol. 446, no. 1–2, pp. 191–198, 2013.

[461] W. J. Trickler, J. Khurana, A. A. Nagvekar, and A. K. Dash, "Chitosan and glyceryl monooleate nanostructures containing gemcitabine: potential delivery system for pancreatic cancer treatment.," *AAPS PharmSciTech*, vol. 11, no. 1, pp. 392–401, 2010.

[462] K. . Leong, H.-Q. Mao, V. . Truong-Le, K. Roy, S. . Walsh, and J. . August, "DNA-polycation nanospheres as non-viral gene delivery vehicles," *J. Control. Release*, vol. 53, no. 1–3, pp. 183–193, 1998.

[463] A. Azadi, M. Hamidi, and M.-R. Rouini, "Methotrexate-loaded chitosan nanogels as 'Trojan Horses' for drug delivery to brain: preparation and in vitro/in vivo characterization.," *Int. J. Biol. Macromol.*, vol. 62, pp. 523–530, 2013.

[464] J. Akbuğa and G. Durmaz, "Preparation and evaluation of cross-linked chitosan microspheres containing furosemide," *Int. J. Pharm.*, vol. 111, no. 3, pp. 217–222, 1994.

[465] S. R. Jameela and A. Jayakrishnan, "Glutaraldehyde cross-linked chitosan microspheres as a long acting biodegradable drug delivery vehicle: studies on the in vitro release of mitoxantrone and in vivo degradation of microspheres in rat muscle," *Biomaterials*, vol. 16, no. 10, pp. 769–775, 1995.

[466] M. . Lorenzo-Lamosa, C. Remuñán-López, J. . Vila-Jato, and M. . Alonso, "Design of microencapsulated chitosan microspheres for colonic drug delivery," *J. Control. Release*, vol. 52, no. 1–2, pp. 109–118, 1998.

[467] J.-P. Nam, S.-C. Park, T.-H. Kim, J.-Y. Jang, C. Choi, M.-K. Jang, and J.-W. Nah, "Encapsulation of paclitaxel into lauric acid-O-carboxymethyl chitosan-transferrin

micelles for hydrophobic drug delivery and site-specific targeted delivery.," *Int. J. Pharm.*, vol. 457, no. 1, pp. 124–135, 2013.

[468] X.-Y. Gong, Y.-H. Yin, Z.-J. Huang, B. Lu, P.-H. Xu, H. Zheng, F.-L. Xiong, H.-X. Xu, X. Xiong, and X.-B. Gu, "Preparation, characterization and in vitro release study of a glutathione-dependent polymeric prodrug Cis-3-(9H-purin-6-ylthio)-acrylic acid-graft-carboxymethyl chitosan.," *Int. J. Pharm.*, vol. 436, no. 1–2, pp. 240–247, 2012.

[469] S. Ahn, I.-H. Lee, E. Lee, H. Kim, Y.-C. Kim, and S. Jon, "Oral delivery of an anti-diabetic peptide drug via conjugation and complexation with low molecular weight chitosan.," *J. Control. Release*, vol. 170, no. 2, pp. 226–232, 2013.

[470] E. Lee, J. Lee, and S. Jon, "A novel approach to oral delivery of insulin by conjugating with low molecular weight chitosan.," *Bioconjug. Chem.*, vol. 21, no. 10, pp. 1720–1723, 2010.

[471] E. Lee, J. Lee, I.-H. Lee, M. Yu, H. Kim, S. Y. Chae, and S. Jon, "Conjugated chitosan as a novel platform for oral delivery of paclitaxel.," *J. Med. Chem.*, vol. 51, no. 20, pp. 6442–6449, 2008.

[472] L. Yang, R. Zeng, C. Li, G. Li, R. Qiao, L. Hu, and Z. Li, "Novel synthesis and in vitro drug release of polymeric prodrug: Chitosan-O-isopropyl-5'-O-d4T monophosphate conjugate.," *Bioorg. Med. Chem. Lett.*, vol. 19, no. 9, pp. 2566–2569, 2009.

[473] J. Kristl, J. Šmid-Korbar, E. Štruc, M. Schara, and H. Rupprecht, "Hydrocolloids and gels of chitosan as drug carriers," *Int. J. Pharm.*, vol. 99, no. 1, pp. 13–19, 1993.

[474] J. Yang, J. Chen, D. Pan, Y. Wan, and Z. Wang, "pH-sensitive interpenetrating network hydrogels based on chitosan derivatives and alginate for oral drug delivery.," *Carbohydr. Polym.*, vol. 92, no. 1, pp. 719–725, 2013.

[475] J. Knapczyk, "Chitosan hydrogel as a base for semisolid drug forms," *Int. J. Pharm.*, vol. 93, no. 1–3, pp. 233–237, 1993.

[476] M. Ishihara, K. Obara, T. Ishizuka, M. Fujita, M. Sato, K. Masuoka, Y. Saito, H. Yura, T. Matsui, H. Hattori, M. Kikuchi, and A. Kurita, "Controlled release of fibroblast growth factors and heparin from photocrosslinked chitosan hydrogels and subsequent effect on in vivo vascularization.," *J. Biomed. Mater. Res., Part A*, vol. 64, no. 3, pp. 551–559, 2003.

[477] A. Portero, C. Remuñán-López, and J. . Vila-Jato, "Effect of chitosan and chitosan glutamate enhancing the dissolution properties of the poorly water soluble drug nifedipine," *Int. J. Pharm.*, vol. 175, no. 1, pp. 75–84, 1998.

[478] Y. Xie, B. Xu, and Y. Gao, "Controlled transdermal delivery of model drug compounds by MEMS microneedle array.," *Nanomedicine*, vol. 1, no. 2, pp. 184–190, 2005.

[479] J. Akbuğa, "The effect of the physicochemical properties of a drug on its release from chitosonium malate matrix tablets," *Int. J. Pharm.*, vol. 100, no. 1–3, pp. 257–261, 1993.

[480] H. Tozaki, J. Komoike, C. Tada, T. Maruyama, A. Terabe, T. Suzuki, A. Yamamoto, and S. Muranishi, "Chitosan capsules for colon-specific drug delivery: improvement of insulin absorption from the rat colon.," *J. Pharmacol. Sci.*, vol. 86, no. 9, pp. 1016–1021, 1997.

[481] W. M. Hou, S. Miyazaki, M. Takada, and T. Komai, "Sustained release of indomethacin from chitosan granules.," *Chem. Pharm. Bull.*, vol. 33, no. 9, pp. 3986–3992, 1985.

[482] D. Han, L. Yan, W. Chen, and W. Li, "Preparation of chitosan/graphene oxide composite film with enhanced mechanical strength in the wet state," *Carbohydr. Polym.*, vol. 83, no. 2, pp. 653–658, 2011.

[483] J. C. Halpin, "Moduli of Crystalline Polymers Employing Composite Theory," *J. Appl. Phys.*, vol. 43, no. 5, pp. 2235–2241, 1972.

[484] Y. Wan, K. A. . Creber, B. Peppley, and V. T. Bui, "Ionic conductivity of chitosan membranes," *Polymer (Guildf).*, vol. 44, no. 4, pp. 1057–1065, 2003.

[485] B. Carreño-Gómez and R. Duncan, "Evaluation of the biological properties of soluble chitosan and chitosan microspheres," *Int. J. Pharm.*, vol. 148, no. 2, pp. 231–240, 1997.

[486] D. Depan, A. Pratheep Kumar, R. P. Singh, and R. D. K. Misra, "Stability of chitosan/montmorillonite nanohybrid towards enzymatic degradation on grafting with poly(lactic acid)," *Mater. Sci. Technol.*, vol. 30, no. 5, pp. 587–592, 2014.

[487] H. Fan, L. Wang, K. Zhao, N. Li, Z. Shi, Z. Ge, and Z. Jin, "Fabrication, mechanical properties, and biocompatibility of graphene-reinforced chitosan composites.," *Biomacromolecules*, vol. 11, no. 9, pp. 2345–2351, 2010.

[488] A. M. Pandele, M. Ionita, L. Crica, S. Dinescu, M. Costache, and H. Iovu, "Synthesis, characterization, and in vitro studies of graphene oxide/chitosan-polyvinyl alcohol films.," *Carbohydr. Polym.*, vol. 102, pp. 813–820, 2014.

[489] Y. Chen, Y. Qi, X. Yan, H. Ma, J. Chen, B. Liu, and Q. Xue, "Green fabrication of porous chitosan/graphene oxide composite xerogels for drug delivery," *J. Appl. Polym. Sci.*, vol. 131, no. 6, pp. 40006–40016, 2014.

[490] L. He, H. Wang, G. Xia, J. Sun, and R. Song, "Chitosan/graphene oxide nanocomposite films with enhanced interfacial interaction and their electrochemical applications," *Appl. Surf. Sci.*, vol. 314, pp. 510–515, 2014.

[491] S. Walker and H. Straw, *Spectrocopy*, 1st ed., vol. 2. London: Chapman & Hall, 1962.

[492] G. Lampman, D. Pavia, G. Kriz, and J. Vyvyan, *Spectroscopy*, 4th ed. Belmont: Cengage Learning, 2009.

[493] B. Fultz and J. Howe, *Transmission electron microscopy and diffractometry of materials*, 3rd ed. New York: Springer, 2007.

[494] D. Williams and C. Carter, *Transmission electron microscopy*. New York: Springer, 1996.

[495] S. J. Reed, *Electron Microprobe Analysis and Scanning Electron Microscopy in Geology*. Cambridge: Cambridge University Press, 2005.

[496] P. Eaton, *Atomic force microscopy*. Oxford: Oxford University Press, 2010.

[497] T. Freier, H. S. Koh, K. Kazazian, and M. S. Shoichet, "Controlling cell adhesion and degradation of chitosan films by N-acetylation.," *Biomaterials*, vol. 26, no. 29, pp. 5872–5878, 2005.

[498] K. Tomihata and Y. Ikada, "In vitro and in vivo degradation of films of chitin and its deacetylated derivatives," *Biomaterials*, vol. 18, no. 7, pp. 567–575, 1997.

[499] J. Brouwer, T. van Leeuwen-Herberts, and M. O. de Ruit, "Determination of lysozyme in serum, urine, cerebrospinal fluid and feces by enzyme immunoassay," *Clin. Chim. Acta*, vol. 142, no. 1, pp. 21–30, 1984.

[500] Y. K. Koh, M.-H. Bae, D. G. Cahill, and E. Pop, "Reliably counting atomic planes of few-layer graphene (n > 4).," *ACS Nano*, vol. 5, no. 1, pp. 269–274, 2011.

[501] A. Galvan-Sanchez, F. Urena-Nunez, H. Flores-Llamas, and R. Lopez-Castanares, "Determination of the crystallinity index of iron polymethacrylate," *J. Appl. Polym. Sci.*, vol. 74, no. 4, pp. 995–1002, 1999.

[502] C. Nunes, A. Mahendrasingam, and R. Suryanarayanan, "Quantification of crystallinity in substantially amorphous materials by synchrotron X-ray powder diffractometry.," *Pharm. Res.*, vol. 22, no. 11, pp. 1942–1953, 2005.

[503] J.-E. An and Y. G. Jeong, "Structure and electric heating performance of graphene/epoxy composite films," *Eur. Polym. J.*, vol. 49, no. 6, pp. 1322–1330, 2013.

[504] A. U. Chaudhry and V. Mittal, "High-density polyethylene nanocomposites using masterbatches of chlorinated polyethylene/graphene oxide," *Polym. Eng. Sci.*, vol. 53, no. 1, pp. 78–88, 2013.

[505] A. Dasari, Z.-Z. Yu, and Y.-W. Mai, "Transcrystalline Regions in the Vicinity of Nanofillers in Polyamide-6," *Macromolecules*, vol. 1, pp. 123–130, 2007.

[506] B. Chen and J. R. G. Evans, "Nominal and Effective Volume Fractions in Polymer−Clay Nanocomposites," *Macromolecules*, vol. 39, no. 5, pp. 1790–1796, 2006.

[507] L.-C. Tang, Y.-J. Wan, D. Yan, Y.-B. Pei, L. Zhao, Y.-B. Li, L.-B. Wu, J.-X. Jiang, and G.-Q. Lai, "The effect of graphene dispersion on the mechanical properties of graphene/epoxy composites," *Carbon N. Y.*, vol. 60, pp. 16–27, 2013.

[508] M. M. Sari, "Fluorescein isothiocyanate conjugated graphene oxide for detection of dopamine," *Mater. Chem. Phys.*, vol. 138, no. 2, pp. 843–849, 2013.

[509] X. Sun, Z. Liu, K. Welsher, J. T. Robinson, A. Goodwin, S. Zaric, and H. Dai, "Nano-Graphene Oxide for Cellular Imaging and Drug Delivery.," *Nano Res.*, vol. 1, no. 3, pp. 203–212, 2008.

[510] T. Higuchi, "Rate of release of medicaments from ointment bases containing drugs in suspension," *J. Pharmacol. Sci.*, vol. 50, no. 10, pp. 874–875, 1961.

[511] T. Higuchi, "Mechanism of sustained-action medication. Theoretical analysis of rate of release of solid drugs dispersed in solid matrices," *J. Pharmacol. Sci.*, vol. 52, no. 12, pp. 1145–1149, 1963.

[512] T. Casalini, M. Salvalaglio, G. Perale, M. Masi, and C. Cavallotti, "Diffusion and aggregation of sodium fluorescein in aqueous solutions.," *J. Phys. Chem. B*, vol. 115, no. 44, pp. 12896–12904, 2011.

[513] H. Bai, C. Li, X. Wang, and G. Shi, "A pH-sensitive graphene oxide composite hydrogel.," *Chem. Comm.*, vol. 46, no. 14, pp. 2376–2378, 2010.

[514] Y. Xu, K. Sheng, C. Li, and G. Shi, "Self-assembled graphene hydrogel via a one-step hydrothermal process.," *ACS Nano*, vol. 4, no. 7, pp. 4324–4330, 2010.

[515] R. Nordtveit, K. M. Vårum, and O. Smidsrød, "Degradation of partially N-acetylated chitosans with hen egg white and human lysozyme," *Carbohydr. Polym.*, vol. 29, no. 2, pp. 163–167, 1996.

[516] R. J. Nordtveit, K. M. Vårum, and O. Smidsrød, "Degradation of fully water-soluble, partially N-acetylated chitosans with lysozyme," *Carbohydr. Polym.*, vol. 23, no. 4, pp. 253–260, 1994.

[517] H. Sashiwa, H. Saimoto, Y. Shigemasa, R. Ogawa, and S. Tokura, "Lysozyme susceptibility of partially deacetylated chitin," *Int. J. Biol. Macromol.*, vol. 12, no. 5, pp. 295–296, 1990.

[518] R. Liu, S. Liang, X.-Z. Tang, D. Yan, X. Li, and Z.-Z. Yu, "Tough and highly stretchable graphene oxide/polyacrylamide nanocomposite hydrogels," *J. Mater. Chem.*, vol. 22, no. 28, pp. 14160–14167, 2012.

[519] Y. Hong, H. Song, Y. Gong, Z. Mao, C. Gao, and J. Shen, "Covalently crosslinked chitosan hydrogel: properties of in vitro degradation and chondrocyte encapsulation.," *Acta Biomater.*, vol. 3, no. 1, pp. 23–31, 2007.

[520] D. Li, M. B. Müller, S. Gilje, R. B. Kaner, and G. G. Wallace, "Processable aqueous dispersions of graphene nanosheets.," *Nat. Nanotechnol.*, vol. 3, no. 2, pp. 101–105, 2008.

[521] S. Cooppan, Y. E. Choonara, L. C. du Toit, P. Kumar, V. M. K. Ndesendo, and V. Pillay, "A novel gastric release PEG-enclatherated polymethacrylate-based memblet system," *J. Appl. Polym. Sci.*, vol. 128, no. 6, pp. 4327–4338, 2013.

[522] Y. Lu, H. Kong, F. Wen, S. Zhang, and X. Zhang, "Lab-on-graphene: graphene oxide as a triple-channel sensing device for protein discrimination.," *Chem. Comm.*, vol. 49, no. 1, pp. 81–83, 2013.

[523] Y. Dong, Y. Ruan, H. Wang, Y. Zhao, and D. Bi, "Studies on glass transition temperature of chitosan with four techniques," *J. Appl. Polym. Sci.*, vol. 93, no. 4, pp. 1553–1558, 2004.

[524] B. Sreedhar, D. K. Chattopadhyay, and V. Swapna, "Thermal and surface characterization of polyurethane–urea clay nanocomposite coatings," *J. Appl. Polym. Sci.*, vol. 100, no. 3, pp. 2393–2401, 2006.

[525] A. Leszczynska and K. Pielichowski, "Application of thermal analysis methods for characterization of polymer/montmorillonite nanocomposites," *J. Therm. Anal. Calorim.*, vol. 93, no. 3, pp. 677–687, 2008.

[526] Z. Wang, Q. Hu, R. Fei, J. Ke, and J. Shen, "Chitosan rod reinforced by self-crosslinking through thermal treatment," *Front. Mater. Sci. China*, vol. 2, no. 2, pp. 205–208, 2008.

[527] J. T. Robinson, M. Zalalutdinov, J. W. Baldwin, E. S. Snow, Z. Wei, P. Sheehan, and B. H. Houston, "Wafer-scale reduced graphene oxide films for nanomechanical devices.," *Nano Lett.*, vol. 8, no. 10, pp. 3441–3445, 2008.

[528] C. Gómez-Navarro, M. Burghard, and K. Kern, "Elastic properties of chemically derived single graphene sheets.," *Nano Lett.*, vol. 8, no. 7, pp. 2045–2049, 2008.

[529] J. C. Halpin and J. L. Kardos, "The Halpin-Tsai equations: A review," *Polym. Eng. Sci.*, vol. 16, no. 5, pp. 344–352, 1976.

[530] S. Ramakrishna, T. C. Lim, R. Inai, and K. Fujihara, "Modified Halpin-Tsai Equation for Clay-Reinforced Polymer Nanofiber," *Mech. Adv. Mater. Struc.*, vol. 13, no. 1, pp. 77–81, 2006.

[531] S. Morariu, C.-E. Brunchi, and M. Bercea, "The Behavior of Chitosan in Solvents with Different Ionic Strengths," *Ind. Eng. Chem. Res.*, vol. 51, no. 39, pp. 12959–12966, 2012.

[532] C. L. Weaver, J. M. LaRosa, X. Luo, and X. T. Cui, "Electrically controlled drug delivery from graphene oxide nanocomposite films.," *ACS Nano*, vol. 8, no. 2, pp. 1834–1843, 2014.

[533] P. Aggarwal, "Geometrical effects in mechanical characterizing of microneedle for biomedical applications," *Sensors Actuators B Chem.*, vol. 102, no. 2, pp. 226–234, 2004.

[534] K. A. Blackwood, R. McKean, I. Canton, C. O. Freeman, K. L. Franklin, D. Cole, I. Brook, P. Farthing, S. Rimmer, J. W. Haycock, A. J. Ryan, and S. MacNeil, "Development of biodegradable electrospun scaffolds for dermal replacement.," *Biomaterials*, vol. 29, no. 21, pp. 3091–3104, 2008.

[535] A. T. R. Williams, S. A. Winfield, and J. N. Miller, "Relative fluorescence quantum yields using a computer-controlled luminescence spectrometer," *Analyst*, vol. 108, no. 1290, pp. 1067–1071, 1983.

[536] V. D. Frolov, P. A. Pivovarov, E. V. Zavedeev, A. A. Khomich, A. N. Grigorenko, and V. I. Konov, "Laser-induced local profile transformation of multilayered graphene on a substrate," *Opt. Laser Technol.*, vol. 69, pp. 34–38, 2015.

[537] A. Gupta, G. Chen, P. Joshi, S. Tadigadapa, and P. C. Eklund, "Raman scattering from high-frequency phonons in supported n-graphene layer films.," *Nano Lett.*, vol. 6, no. 12, pp. 2667–2673, 2006.

[538] L. R. Radovic and B. Bockrath, "On the chemical nature of graphene edges: origin of stability and potential for magnetism in carbon materials.," *J. Am. Chem. Soc.*, vol. 127, no. 16, pp. 5917–5927, 2005.

[539] K. Habiba, V. I. Makarov, J. Avalos, M. J. F. Guinel, B. R. Weiner, and G. Morell, "Luminescent graphene quantum dots fabricated by pulsed laser synthesis," *Carbon N. Y.*, vol. 64, pp. 341–350, 2013.

[540] J. Peng, W. Gao, B. K. Gupta, Z. Liu, R. Romero-Aburto, L. Ge, L. Song, L. B. Alemany, X. Zhan, G. Gao, S. A. Vithayathil, B. A. Kaipparettu, A. A. Marti, T. Hayashi, J.-J. Zhu, and P. M. Ajayan, "Graphene quantum dots derived from carbon fibers.," *Nano Lett.*, vol. 12, no. 2, pp. 844–849, 2012.

[541] S. Zhu, J. Zhang, S. Tang, C. Qiao, L. Wang, H. Wang, X. Liu, B. Li, Y. Li, W. Yu, X. Wang, H. Sun, and B. Yang, "Surface Chemistry Routes to Modulate the Photoluminescence of Graphene Quantum Dots: From Fluorescence Mechanism to Up-Conversion Bioimaging Applications," *Adv. Funct. Mater.*, vol. 22, no. 22, pp. 4732–4740, 2012.

[542] J.-H. Song, T. Atay, S. Shi, H. Urabe, and A. V Nurmikko, "Large enhancement of fluorescence efficiency from CdSe/ZnS quantum dots induced by resonant coupling to spatially controlled surface plasmons.," *Nano Lett.*, vol. 5, no. 8, pp. 1557–1561, 2005.

[543] D. Pan, L. Guo, J. Zhang, C. Xi, Q. Xue, H. Huang, J. Li, Z. Zhang, W. Yu, Z. Chen, Z. Li, and M. Wu, "Cutting sp2 clusters in graphene sheets into colloidal graphene quantum dots with strong green fluorescence," *J. Mater. Chem.*, vol. 22, no. 8, pp. 3314–3318, 2012.

[544] Y. Wan, K. A. M. Creber, B. Peppley, and V. T. Bui, "Ionic conductivity and related properties of crosslinked chitosan membranes," *J. Appl. Polym. Sci.*, vol. 89, no. 2, pp. 306–317, 2003.

[545] J. Liang, Y. Wang, Y. Huang, Y. Ma, Z. Liu, J. Cai, C. Zhang, H. Gao, and Y. Chen, "Electromagnetic interference shielding of graphene/epoxy composites," *Carbon N. Y.*, vol. 47, no. 3, pp. 922–925, 2009.

[546] D. S. McLachlan, C. Chiteme, C. Park, K. E. Wise, S. E. Lowther, P. T. Lillehei, E. J. Siochi, and J. S. Harrison, "AC and DC percolative conductivity of single wall carbon nanotube polymer composites," *J. Polym. Sci. Part B Polym. Phys.*, vol. 43, no. 22, pp. 3273–3287, 2005.

[547] B. Chen and J. R. G. Evans, "Impact strength of polymer-clay nanocomposites," *Soft Matter*, vol. 5, no. 19, pp. 3572–3584, 2009.

[548] T. D. Fornes and D. R. Paul, "Modeling properties of nylon 6/clay nanocomposites using composite theories," *Polymer (Guildf).*, vol. 44, no. 17, pp. 4993–5013, 2003.

[549] Y. Xu and Y. Du, "Effect of molecular structure of chitosan on protein delivery properties of chitosan nanoparticles," *Int. J. Pharm.*, vol. 250, no. 1, pp. 215–226, 2003.

[550] M. E. Ali and A. Lamprecht, "Polyethylene glycol as an alternative polymer solvent for nanoparticle preparation.," *Int. J. Pharm.*, vol. 456, no. 1, pp. 135–142, 2013.

[551] H. Kaygusuz and F. B. Erim, "Alginate/BSA/montmorillonite composites with enhanced protein entrapment and controlled release efficiency," *React. Funct. Polym.*, vol. 73, no. 11, pp. 1420–1425, 2013.

[552] R. Justin and B. Chen, "Body temperature reduction of graphene oxide through chitosan functionalisation and its application in drug delivery," *Mater. Sci. Eng. C.*, vol. 34, no. 1, pp. 50–53, 2014.

[553] Z. Cui and R. J. Mumper, "Chitosan-based nanoparticles for topical genetic immunization," *J. Control. Release*, vol. 75, no. 3, pp. 409–419, 2001.

[554] J. Rao, A. Dragulescu-Andrasi, and H. Yao, "Fluorescence imaging in vivo: recent advances.," *Curr. Opin. Biotechnol.*, vol. 18, no. 1, pp. 17–25, 2007.

[555] M. F. Kircher, U. Mahmood, R. S. King, R. Weissleder, and L. Josephson, "A Multimodal Nanoparticle for Preoperative Magnetic Resonance Imaging and Intraoperative Optical Brain Tumor Delineation," *Cancer Res.*, vol. 63, no. 23, pp. 8122–8125, 2003.

[556] X. Li, H. Yang, W. Fu, C. Wu, S. Liu, H. Zhu, and X. Pang, "Preparation of low-density superparamagnetic microspheres by coating glass microballoons with magnetite nanoparticles," *Mater. Sci. Eng. B*, vol. 135, no. 1, pp. 38–43, 2006.

[557] V. Filipe, A. Hawe, and W. Jiskoot, "Critical evaluation of Nanoparticle Tracking Analysis (NTA) by NanoSight for the measurement of nanoparticles and protein aggregates.," *Pharm. Res.*, vol. 27, no. 5, pp. 796–810, 2010.

[558] J. Shen, Y. Zhu, X. Yang, J. Zong, J. Zhang, and C. Li, "One-pot hydrothermal synthesis of graphenequantum dots surface-passivated by polyethylene glycol and their photoelectric conversion under near-infrared light," *New J. Chem.*, vol. 36, no. 1, pp. 97–101, 2012.

[559] Y. Li, Y. Zhao, H. Cheng, Y. Hu, G. Shi, L. Dai, and L. Qu, "Nitrogen-Doped Graphene Quantum Dots with Oxygen-Rich Functional Groups," *J. Am. Chem. Soc.*, vol. 134, no. 1, pp. 15–18, 2011.

[560] Q. Qu, S. Yang, and X. Feng, "2D sandwich-like sheets of iron oxide grown on graphene as high energy anode material for supercapacitors.," *Adv. Mater.*, vol. 23, no. 46, pp. 5574–5580, 2011.

[561] V. Chandra, J. Park, Y. Chun, J. W. Lee, I.-C. Hwang, and K. S. Kim, "Water-dispersible magnetite-reduced graphene oxide composites for arsenic removal.," *ACS Nano*, vol. 4, no. 7, pp. 3979–3986, 2010.

[562] D. Carta, A. Corrias, A. Falqui, R. Brescia, E. Fantechi, F. Pineider, and C. Sangregorio, "EDS, HRTEM/STEM, and X-ray Absorption Spectroscopy Studies of Co-Substituted Maghemite Nanoparticles," *J. Phys. Chem. C*, vol. 117, no. 18, pp. 9496–9506, 2013.

[563] J. Ji, G. Zhang, H. Chen, S. Wang, G. Zhang, F. Zhang, and X. Fan, "Sulfonated graphene as water-tolerant solid acid catalyst," *Chem. Sci.*, vol. 2, no. 3, pp. 484–487, 2011.

[564] A. Bharde, D. Rautaray, V. Bansal, A. Ahmad, I. Sarkar, S. M. Yusuf, M. Sanyal, and M. Sastry, "Extracellular biosynthesis of magnetite using fungi.," *Small*, vol. 2, no. 1, pp. 135–141, 2006.

[565] R. M. Cornell and U. Schwertmann, *The Iron Oxides*. Weinheim: Wiley - VCH, 1996.

[566] T. T. Tung, J.-F. Feller, T. Kim, H. Kim, W. S. Yang, and K. S. Suh, "Electromagnetic properties of Fe3O4-functionalized graphene and its composites with a conducting polymer," *J. Polym. Sci. Part A Polym. Chem.*, vol. 50, no. 5, pp. 927–935, 2012.

[567] F. He, K. Lam, D. Ma, J. Fan, L. H. Chan, and L. Zhang, "Fabrication of graphene nanosheet (GNS)–Fe3O4 hybrids and GNS–Fe3O4/syndiotactic polystyrene composites with high dielectric permittivity," *Carbon N. Y.*, vol. 58, pp. 175–184, 2013.

[568] Y. Sun, M. Ma, Y. Zhang, and N. Gu, "Synthesis of nanometer-size maghemite particles from magnetite," *Colloids Surfaces A Physicochem. Eng. Asp.*, vol. 245, no. 1–3, pp. 15–19, 2004.

[569] W. Kim, C.-Y. Suh, S.-W. Cho, K.-M. Roh, H. Kwon, K. Song, and I.-J. Shon, "A new method for the identification and quantification of magnetite-maghemite mixture using conventional X-ray diffraction technique.," *Talanta*, vol. 94, pp. 348–352, 2012.

[570] C.-J. Jia, L.-D. Sun, Z.-G. Yan, L.-P. You, F. Luo, X.-D. Han, Y.-C. Pang, Z. Zhang, and C.-H. Yan, "Single-Crystalline Iron Oxide Nanotubes," *Angew. Chemie*, vol. 117, no. 28, pp. 4402–4407, 2005.

[571] N. Pinna, S. Grancharov, P. Beato, P. Bonville, M. Antonietti, and M. Niederberger, "Magnetite Nanocrystals: Nonaqueous Synthesis, Characterization, and Solubility," *Chem. Mater.*, vol. 17, no. 11, pp. 3044–3049, 2005.

[572] O. N. Shebanova and P. Lazor, "Raman spectroscopic study of magnetite (FeFe2O4): a new assignment for the vibrational spectrum," *J. Solid State Chem.*, vol. 174, no. 2, pp. 424–430, 2003.

[573] I. R. Beattie and T. R. Gilson, "The single crystal Raman Spectra of Nearly Opaque Materials: Iron (III) oxide and Chromium (III) oxide," *J. Am. Chem. Soc.*, pp. 980–986, 1970.

[574] M. Ramalakshmi, P. Shakkthivel, M. Sundrarajan, and S. M. Chen, "Novel method of room temperature ionic liquid assisted Fe3O4 nanocubes and nanoflakes synthesis," *Mater. Res. Bull.*, vol. 48, no. 8, pp. 2758–2765, 2013.

[575] L. M. Malard, M. A. Pimenta, G. Dresselhaus, and M. S. Dresselhaus, "Raman spectroscopy in graphene," *Phys. Rep.*, vol. 473, no. 5–6, pp. 51–87, 2009.

[576] A. C. Ferrari, J. C. Meyer, V. Scardaci, C. Casiraghi, M. Lazzeri, F. Mauri, S. Piscanec, D. Jiang, K. S. Novoselov, S. Roth, and A. K. Geim, "Raman Spectrum of Graphene and Graphene Layers," *Phys. Rev. Lett.*, vol. 97, no. 18, pp. 187401–187405, 2006.

[577] Y.-S. Li, J. S. Church, and A. L. Woodhead, "Infrared and Raman spectroscopic studies on iron oxide magnetic nano-particles and their surface modifications," *J. Magn. Magn. Mater.*, vol. 324, no. 8, pp. 1543–1550, 2012.

[578] W. D. Chemelewski, H.-C. Lee, J.-F. Lin, A. J. Bard, and C. B. Mullins, "Amorphous FeOOH oxygen evolution reaction catalyst for photoelectrochemical water splitting.," *J. Am. Chem. Soc.*, vol. 136, no. 7, pp. 2843–2850, 2014.

[579] X. Yang, C. Chen, J. Li, G. Zhao, X. Ren, and X. Wang, "Graphene oxide-iron oxide and reduced graphene oxide-iron oxide hybrid materials for the removal of organic and inorganic pollutants," *RSC Adv.*, vol. 2, no. 23, pp. 8821–8826, 2012.

[580] D. Morillo, A. Uheida, G. Pérez, M. Muhammed, and M. Valiente, "Arsenate removal with 3-mercaptopropanoic acid-coated superparamagnetic iron oxide nanoparticles.," *J. Colloid Interface Sci.*, vol. 438, pp. 227–234, 2015.

[581] U. Schwertmann, *Iron Oxides in the Laboratory Preparation and Characterization*, 2nd ed. Wiley Online Library, 2008.

[582] X. N. Xu, Y. Wolfus, A. Shaulov, Y. Yeshurun, I. Felner, I. Nowik, Y. Koltypin, and A. Gedanken, "Annealing study of Fe2O3 nanoparticles: Magnetic size effects and phase transformations," *J. Appl. Phys.*, vol. 91, no. 7, pp. 4611–4616, 2002.

[583] K. Mondal, H. Lorethova, E. Hippo, T. Wiltowski, and S. B. Lalvani, "Reduction of iron oxide in carbon monoxide atmosphere—reaction controlled kinetics," *Fuel Process. Technol.*, vol. 86, no. 1, pp. 33–47, 2004.

[584] X. Wu, Y. Zhang, T. Han, H. Wu, S. Guo, and J. Zhang, "Composite of graphene quantum dots and Fe3O4 nanoparticles: peroxidase activity and application in phenolic compound removal," *RSC Adv.*, vol. 4, no. 7, pp. 3299–3305, 2014.

[585] T. Pons, I. L. Medintz, K. E. Sapsford, S. Higashiya, A. F. Grimes, D. S. English, and H. Mattoussi, "On the quenching of semiconductor quantum dot photoluminescence by proximal gold nanoparticles.," *Nano Lett.*, vol. 7, no. 10, pp. 3157–3164, 2007.

[586] A. Samanta, Y. Zhou, S. Zou, H. Yan, and Y. Liu, "Fluorescence quenching of quantum dots by gold nanoparticles: a potential long range spectroscopic ruler.," *Nano Lett.*, vol. 14, no. 9, pp. 5052–5057, 2014.

[587] L.-S. Lin, Z.-X. Cong, J.-B. Cao, K.-M. Ke, Q.-L. Peng, J. Gao, H.-H. Yang, G. Liu, and X. Chen, "Multifunctional Fe3O4-polydopamine core-shell nanocomposites for intracellular mRNA detection and imaging-guided photothermal therapy.," *ACS Nano*, vol. 8, no. 4, pp. 3876–3883, 2014.

[588] X.-D. Li, X.-L. Liang, X.-L. Yue, J.-R. Wang, C.-H. Li, Z.-J. Deng, L.-J. Jing, L. Lin, E.-Z. Qu, S.-M. Wang, C.-L. Wu, H.-X. Wu, and Z.-F. Dai, "Imaging guided photothermal therapy using iron oxide loaded poly(lactic acid) microcapsules coated with graphene oxide," *J. Mater. Chem. B*, vol. 2, no. 2, pp. 217–223, 2014.

[589] A. G. Malyutin, R. Easterday, Y. Lozovyy, A. Spilotros, H. Cheng, O. R. Sanchez-Felix, B. D. Stein, D. G. Morgan, D. I. Svergun, B. Dragnea, and L. M. Bronstein, "Viruslike Nanoparticles with Maghemite Cores Allow for Enhanced MRI Contrast Agents," *Chem. Mater.*, vol. 27, no. 1, pp. 327–335, 2014.

[590] A. Gizzatov, V. Keshishian, A. Guven, A. M. Dimiev, F. Qu, R. Muthupillai, P. Decuzzi, R. G. Bryant, J. M. Tour, and L. J. Wilson, "Enhanced MRI relaxivity of aquated Gd3+ ions by carboxyphenylated water-dispersed graphene nanoribbons.," *Nanoscale*, vol. 6, no. 6, pp. 3059–3063, 2014.

251

[591] Y. Chen, P. Xu, Z. Shu, M. Wu, L. Wang, S. Zhang, Y. Zheng, H. Chen, J. Wang, Y. Li, and J. Shi, "Multifunctional Graphene Oxide-based Triple Stimuli-Responsive Nanotheranostics," *Adv. Funct. Mater.*, vol. 24, no. 28, pp. 4386–4396, 2014.

[592] H.-W. Liu, S.-H. Hu, Y.-W. Chen, and S.-Y. Chen, "Characterization and drug release behavior of highly responsive chip-like electrically modulated reduced graphene oxide–poly(vinyl alcohol) membranes," *J. Mater. Chem.*, vol. 22, no. 33, pp. 17311–17320, 2012.

[593] D. Jaque, L. Martínez Maestro, B. del Rosal, P. Haro-Gonzalez, A. Benayas, J. L. Plaza, E. Martín Rodríguez, and J. García Solé, "Nanoparticles for photothermal therapies.," *Nanoscale*, vol. 6, no. 16, pp. 9494–9530, 2014.

[594] J. M. Stern, J. Stanfield, W. Kabbani, J.-T. Hsieh, and J. A. Cadeddu, "Selective prostate cancer thermal ablation with laser activated gold nanoshells.," *J. Urol.*, vol. 179, no. 2, pp. 748–753, 2008.

[595] Y. Li, W. Lu, Q. Huang, M. Huang, C. Li, and W. Chen, "Copper sulfide nanoparticles for photothermal ablation of tumor cells.," *Nanomedicine*, vol. 5, no. 8, pp. 1161–1171, 2010.

[596] M. Zhou, R. Zhang, M. Huang, W. Lu, S. Song, M. P. Melancon, M. Tian, D. Liang, and C. Li, "A chelator-free multifunctional [64Cu]CuS nanoparticle platform for simultaneous micro-PET/CT imaging and photothermal ablation therapy.," *J. Am. Chem. Soc.*, vol. 132, no. 43, pp. 15351–8, 2010.

[597] Y. Xu, Y. Qin, S. Palchoudhury, and Y. Bao, "Water-soluble iron oxide nanoparticles with high stability and selective surface functionality.," *Langmuir*, vol. 27, no. 14, pp. 8990–8997, 2011.

[598] J. Gupta, H. S. Gill, S. N. Andrews, and M. R. Prausnitz, "Kinetics of skin resealing after insertion of microneedles in human subjects.," *J. Control. Release*, vol. 154, no. 2, pp. 148–155, 2011.

[599] N. Guskos, G. . Papadopoulos, V. Likodimos, S. Patapis, D. Yarmis, A. Przepiera, K. Przepiera, J. Majszczyk, J. Typek, M. Wabia, K. Aidinis, and Z. Drazek, "Photoacoustic, EPR and electrical conductivity investigations of three synthetic mineral pigments: hematite, goethite and magnetite," *Mater. Res. Bull.*, vol. 37, no. 6, pp. 1051–1061, 2002.

[600] E. Kester, U. Rabe, L. Presmanes, P. Tailhades, and W. Arnold, "Measurement of Young's modulus of nanocrystalline ferrites with spinel structures by atomic force acoustic microscopy," *J. Phys. Chem. Solids*, vol. 61, no. 8, pp. 1275–1284, 2000.

[601] J.-K. Francis Suh and H. W. . Matthew, "Application of chitosan-based polysaccharide biomaterials in cartilage tissue engineering: a review," *Biomaterials*, vol. 21, no. 24, pp. 2589–2598, 2000.

[602] M J Knauf, D. P. Bell, P. Hirtzer, Z. P. Luo, J. D. Young, and N. V Katre, "Relationship of effective molecular size to systemic clearance in rats of recombinant interleukin-2 chemically modified with water-soluble polymers.," *J. Biol. Chem.*, no. 263, pp. 15064–15070, 1988.

[603] S. Okonogi and S. Puttipipatkhachorn, "Dissolution improvement of high drug-loaded solid dispersion.," *AAPS PharmSciTech*, vol. 7, no. 2, p. E52, 2006.
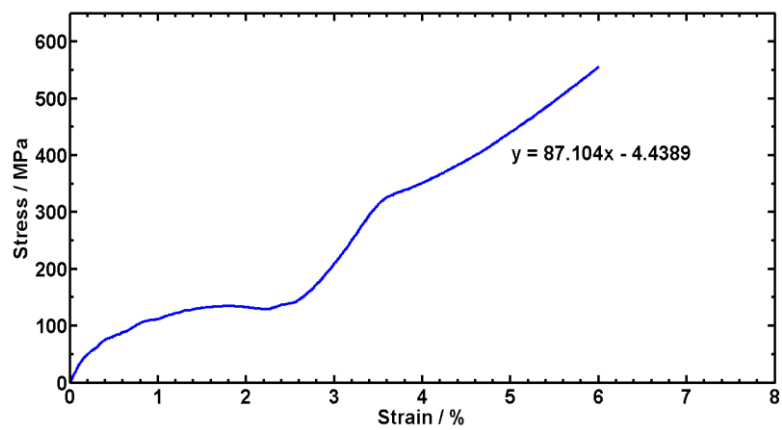
Appendix 1. Supplemental figures

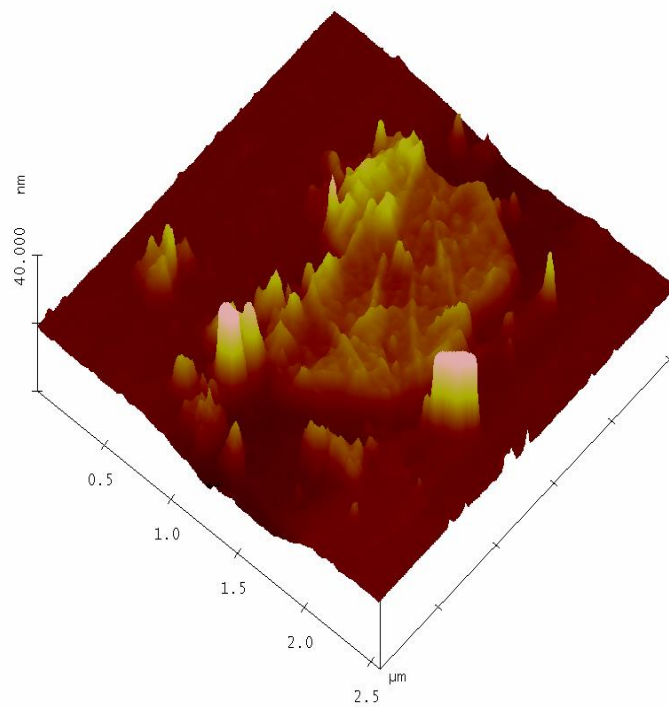**Figure 3.S1**: Tensile test of a steel specimen.

Figure 3.S2: 3D-AFM image of GO-FL sheet from Figure 3.5, emphasising the roughness and unevenness of the FL coating on the GO.
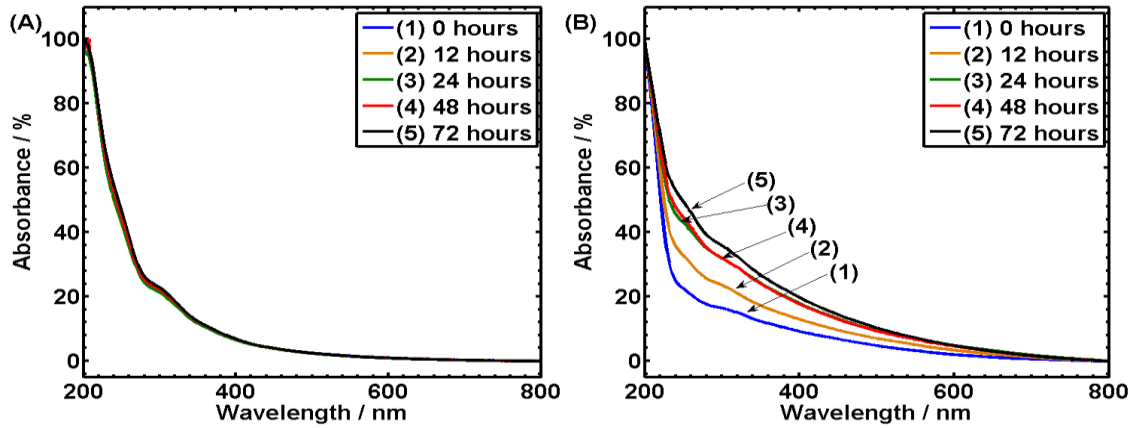
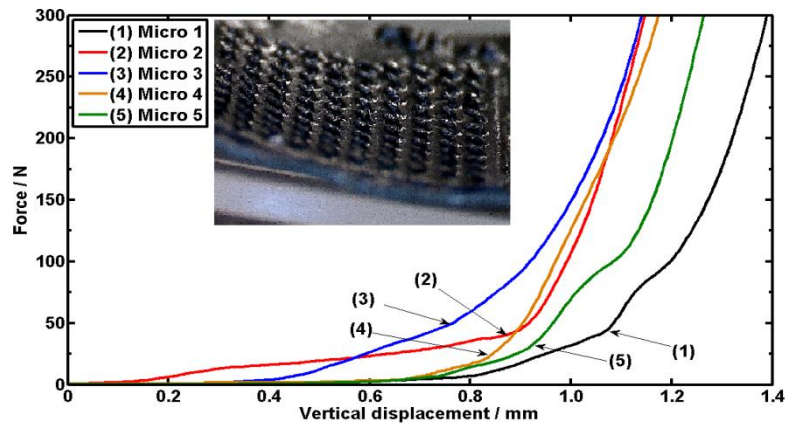**Figure 4.S1**: UV-Vis spectra of rGO over 72 h at (A) 20 °C and (B) 37 °C.

Figure 4.S2: Compression testing to failure of microneedle arrays using a 1 kN load cell with no limitation on maximum loads or minimum depths. The point where the microneedles are believed to have fully failed is indicated by the relevant arrow. After this point, the individual microneedles are being crushed to a horizontal position after having failed by bending means. (Inset) One of the fully failed microneedle arrays can be seen with the individual needles at an orientation closer to horizontal than to vertical.
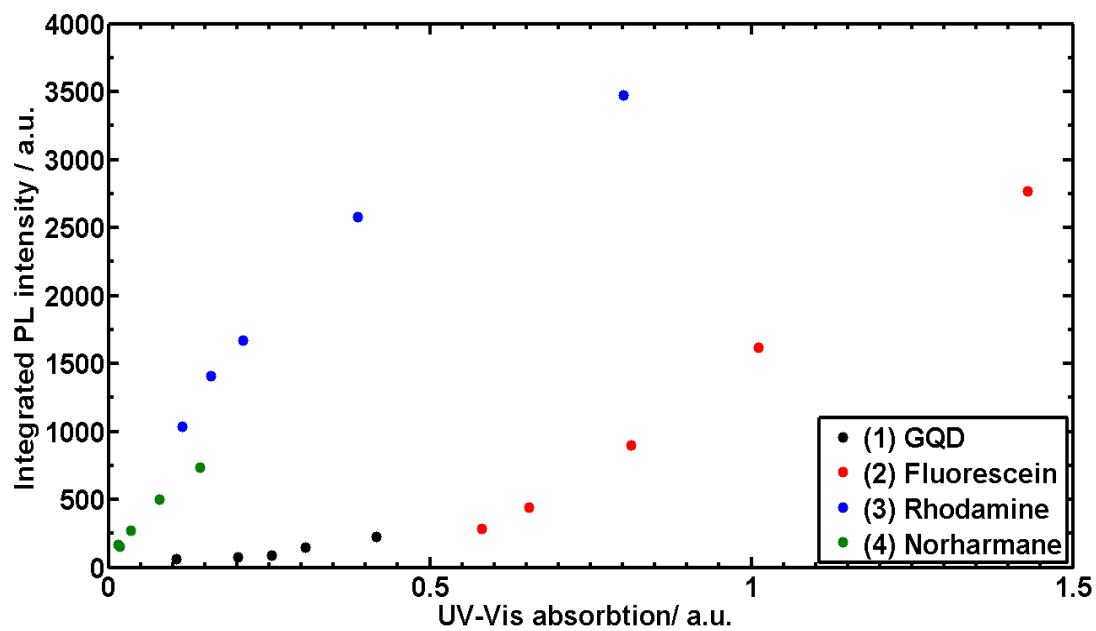
Figure 5.S1: Data for photoluminescence (PL) quantum yield measurements.
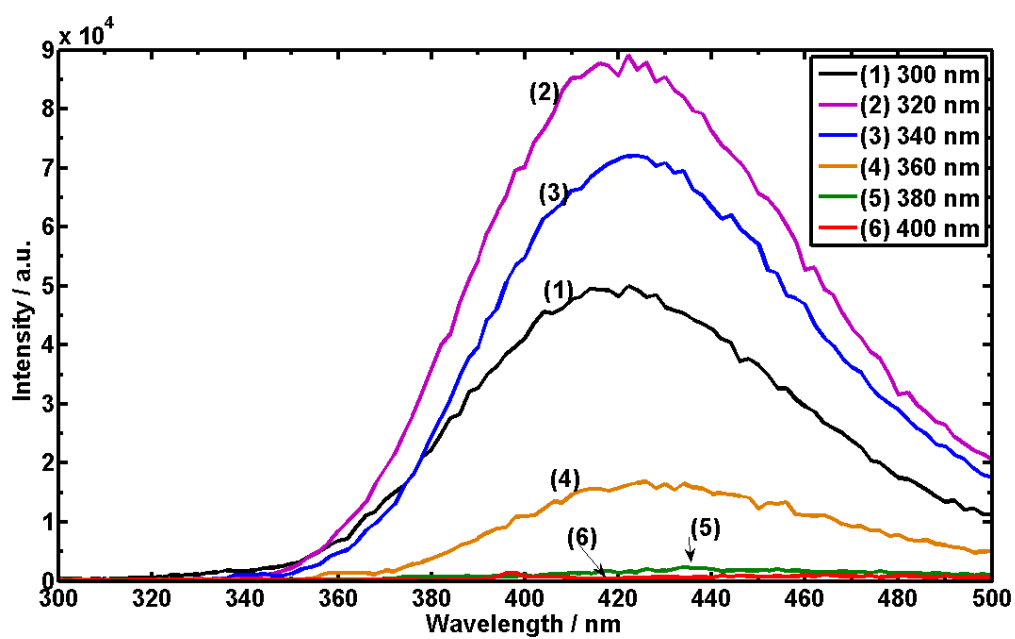
Figure 5.S2: PL spectra showing the selectivity of GQD emission to the excitation wavelength.
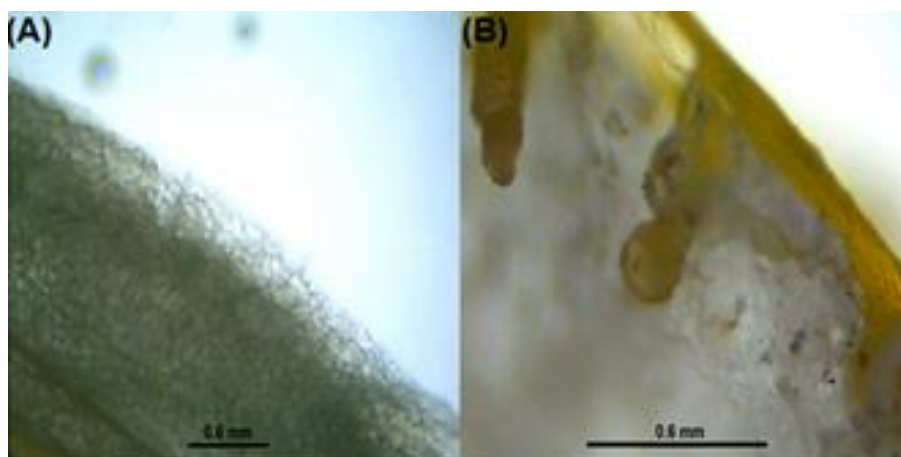
Figure 5.S3: Optical microscopy images of chitosan - 1 wt.% fluorescein sodium coated graphene quantum dot (GQD-FL) nanocomposite microneedle arrays that were inserted into full thickness chicken skin: (A) pristine chicken skin, (B) after the insertion of a chitosan - 1 wt.% GQD microneedle array. Microneedle arrays were inserted into full-thickness chicken skin by hand and were kept for 1 h, after which the skin was prepared for cross-sectioning by treating with ethanol for 10 min to displace water and then embedding in Labonord Q-Path paraffin embedding medium (melting temperature is 57 ^{o}C). The samples were then cross-sectioned using a microtome (Brunel bench microtome) and the cross sectioned samples were transferred to microscopy glass slides and re-heated to 57 ^{o}C to remove the embedding medium from the samples. Optical microscopy was through an optical microscope (Swift M10L, Swift Optical Instruments).
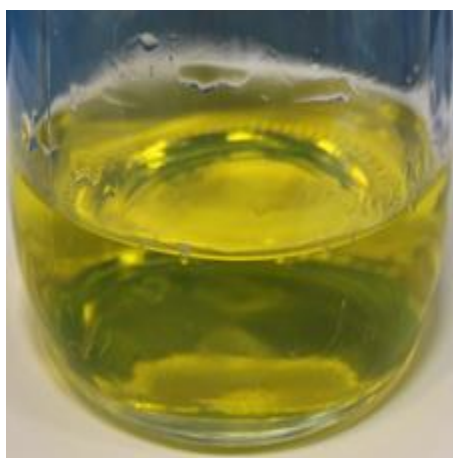

Figure 5.S4: Digital image of fluorescein sodium labelled bovine serum albumin (BSA) (~0.08 µg ml^{-1}, similar to curve 2 after 24 h in Figure 5.7B), showing the characteristic colour of BSA-FL and confirming the medium solutions presented in Figure 5.8 (after 24 h) mainly contain the BSA coated FL.
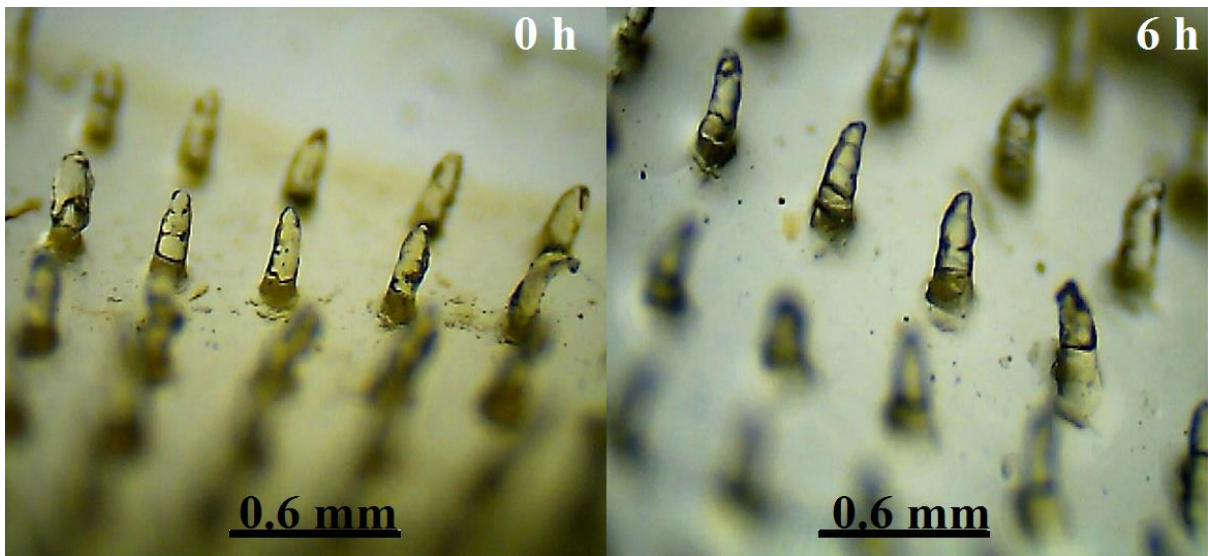
Figure 5.S5 Optical microscopy image of microneedle arrays before and after submersion in foetal bovine serum (FBS) and subsequent air drying. By comparing the 0 h and 6 h images, the size of the microneedles remains similar after immersion showing no stability problems for the microneedles in FBS.
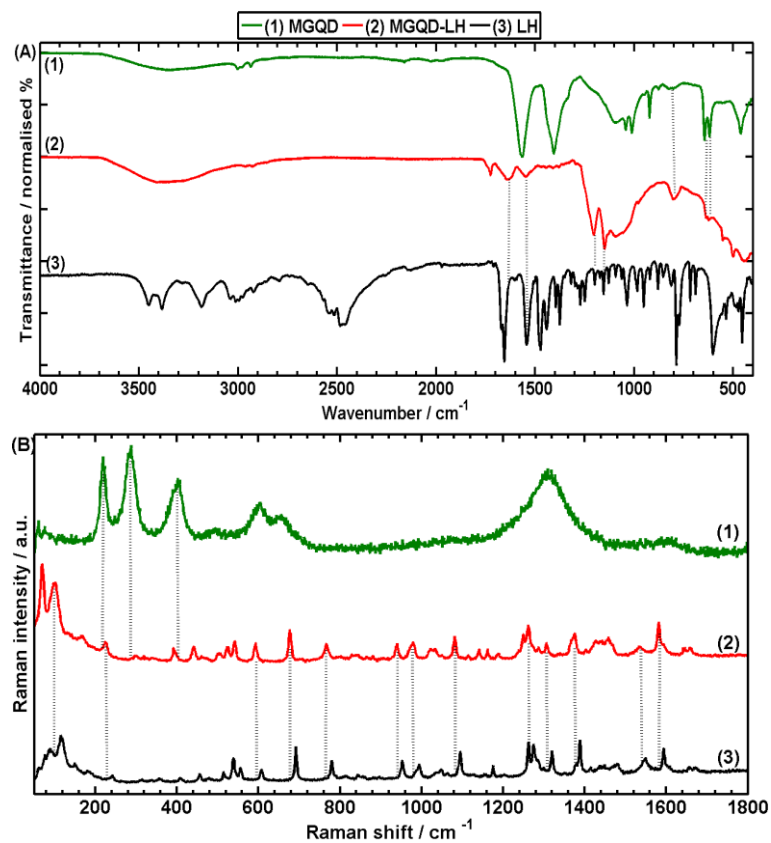

Figure 6.S1 (A) FT-IR spectra and (B) Raman spectra for LH, MGQDs, and MGQD-LH.
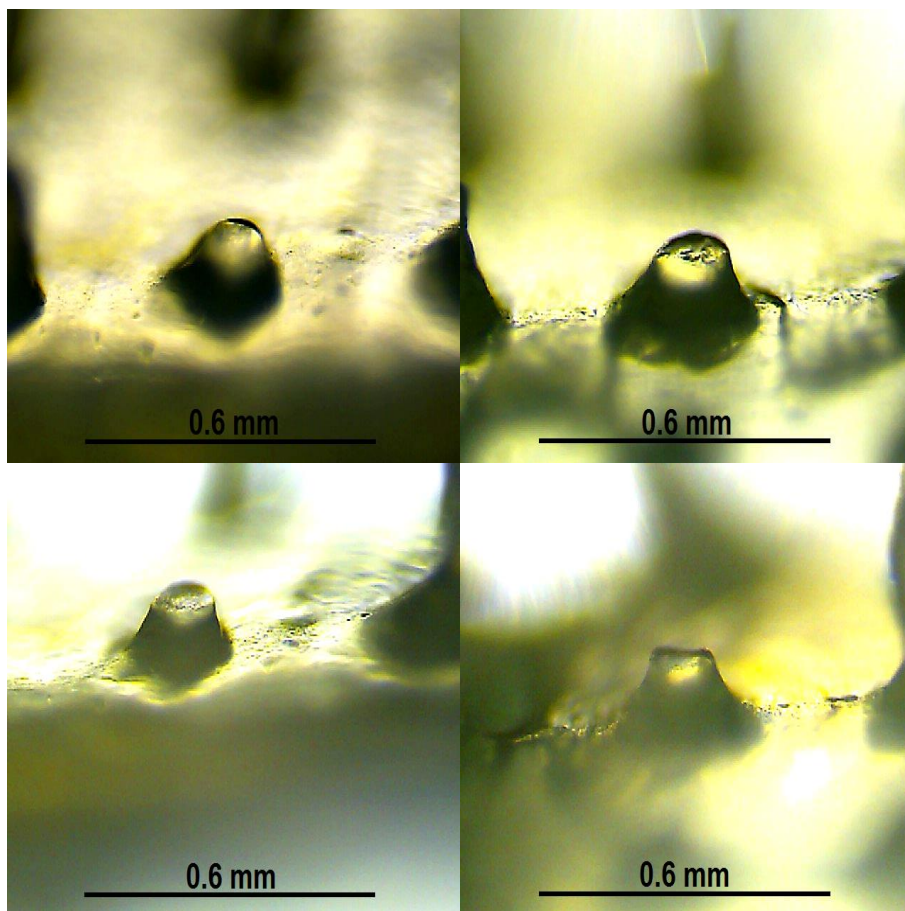
Figure 7.S1: Optical microscopy images of four separate microneedles of the CH-MGQD-PEG microneedle arrays, after 5 min in the presence of water. The main shaft detached after the PEG dissolved in the presence of water.